Imperial College London
Department of Electrical and Electronic Engineering

Methods and Microelectronics for Proprioceptive Neural Feedback

Ian Williams

October 29, 2014

Supervised by Dr Timothy Constandinou

Submitted in part fulfilment of the requirements for the degree of
Doctor of Philosophy in Electrical and Electronic Engineering of Imperial College London
and the Diploma of Imperial College London

Declaration

I herewith certify that all material in this dissertation which is not my own work has been properly acknowledged.

Ian Williams

Thanks to Natalie and my family who supported me throughout and to my supervisor and friends at Imperial who made it possible.

Abstract

A neural implant giving an amputee a sense of feeling back in their prosthetic limb could help millions of people live happier, more productive lives. Tactile feedback is commonly targeted, however, it is the lesser known sense of proprioception that is crucial for smooth, coordinated limb control and non-visual limb awareness – both of which are high priorities for amputees.

This thesis describes research carried out to progress the development and creation of a proprioceptive neural prosthesis targeted at trans-humeral upper limb amputees.

Firstly a review of proprioceptive neural prosthesis design considerations and challenges is presented. The purpose of which is to identify areas requiring further development and to identify a prototype target system that focuses and scopes design effort.

Then 3 technical chapters cover research into:

(1) Combining efficient implementations of biomechanical and proprioceptor models in order to generate signals that mimic human muscular proprioceptive patterns. A neuro-musculoskeletal model of the upper limb with 7 degrees of freedom and 17 muscles is presented and generates real time estimates of muscle spindle and Golgi Tendon Organ neural firing patterns.

(2) An 8 channel energy-efficient neural stimulator for generating charge-balanced asymmetric pulses. Power consumption is reduced by implementing a fully-integrated DC-DC converter that uses a reconfigurable switched capacitor topology to provide 4 output voltages for Dynamic Voltage Scaling (DVS). A novel charge balancing method is implemented which has a low level of accuracy on a single pulse and a much higher accuracy over a series of pulses. The method used is robust to process and component variation and does not require any initial or ongoing calibration.

(3) A non-invasive proprioceptive feedback trial platform (using vibration induced proprioception) for testing modelled neural signals. A low cost vibration device is designed and tested, identifying key issues with this form of non-invasive feedback.

Copyright

The copyright of this thesis rests with the author and is made available under a Creative Commons Attribution Non-Commercial No Derivatives licence. Researchers are free to copy, distribute or transmit the thesis on the condition that they attribute it, that they do not use it for commercial purposes and that they do not alter, transform or build upon it. For any reuse or redistribution, researchers must make clear to others the licence terms of this work

Contents

1 Introduction **20**

1.1 What is proprioception . . . 20
1.2 Inspiration . . . 20
1.2.1 History of proprioceptive neural prostheses . . . 21
1.3 Motivation . . . 22
1.3.1 Target group . . . 22
1.3.2 Prosthetic limbs . . . 23
1.3.3 Benefit provided by proprioceptive feedback . . . 25
1.4 Research approach . . . 27
1.4.1 Document structure . . . 27

2 Proprioception: Physiology, Pathophysiology and Functional Replacement **33**

2.1 Proprioceptors . . . 33
2.1.1 Muscle spindles . . . 33
2.1.2 Golgi Tendon Organs . . . 35
2.1.3 Cutaneous receptors . . . 37
2.1.4 Articular receptors . . . 37
2.2 Neural pathways . . . 37
2.2.1 The peripheral pathway . . . 38
2.2.2 Central pathway . . . 41
2.3 Proprioception pathophysiology following amputation . . . 43
2.3.1 Neural changes . . . 43
2.3.2 Phantom limb pain . . . 43
2.3.3 Viability for neural stimulation . . . 44
2.4 Proprioception integration . . . 44
2.5 Proprioceptive performance . . . 45
2.6 Key unknowns . . . 46
2.6.1 Unconscious proprioception . . . 46
2.6.2 Cerebellar and deep brain changes post-amputation . . . 46
2.6.3 Descending proprioceptive signals . . . 46
2.6.4 Human neural firing patterns . . . 47
2.7 Artificial Proprioceptive Feedback . . . 47
2.7.1 Sensory substitution . . . 48
2.7.2 Modality matched feedback . . . 49

2.7.3 Direct neural stimulation . . . 50
2.8 Summary . . . 50

3 Design of a Proprioceptive Neural Prosthesis 57
3.0.1 Previous reviews . . . 57
3.0.2 Chapter content . . . 59
3.1 Implant Site . . . 60
3.1.1 The brain . . . 60
3.1.2 The spine . . . 61
3.1.3 The DRG . . . 61
3.1.4 The PNS . . . 62
3.1.5 Overview . . . 62
3.2 Neural feedback . . . 63
3.2.1 Mapping prosthetic state to a human model . . . 63
3.2.2 Nerve receptor selection . . . 64
3.2.3 Neural Signal Modelling . . . 65
3.2.4 Portable Processing . . . 65
3.3 Neuromodulation . . . 66
3.3.1 Action potential generation . . . 66
3.3.2 Modulation methods . . . 66
3.3.3 Electrical Neural Stimulation . . . 69
3.3.4 Electrode physics . . . 71
3.3.5 Electrode types . . . 72
3.3.6 Influencing neuron recruitment . . . 74
3.3.7 Electrode choice . . . 78
3.3.8 Neural stimulator design . . . 78
3.4 Implant . . . 81
3.5 Sensors . . . 82
3.5.1 Position and motion sensors . . . 83
3.5.2 Force measurement . . . 83
3.5.3 Practical implementation . . . 84
3.6 Discussion . . . 84
3.6.1 Gaps and areas of further work . . . 84

4 Computationally Efficient Modelling of Proprioceptive Signals in the Upper Limb 93
4.1 Introduction . . . 93
4.2 Neuro-musculoskeletal modelling . . . 95
4.2.1 Musculoskeletal modelling . . . 95
4.2.2 Muscle activation estimation . . . 98
4.2.3 Receptor modelling . . . 99
4.3 Models and Methods . . . 101
4.3.1 Musculoskeletal model . . . 103

4.3.2 Biomechanical modelling . . . 105
4.3.3 Proprioceptor modelling . . . 107
4.4 Results . . . 110
4.4.1 Model validation . . . 110
4.4.2 Computational efficiency . . . 114
4.5 Discussion . . . 118
4.5.1 Generating proprioceptive feedback for a prosthesis . . . 118
4.5.2 Approximations . . . 119
4.5.3 Issues and areas for further work . . . 120
4.5.4 Conclusion . . . 121

5 Energy efficient neural stimulation for proprioceptive feedback 127
5.1 Charge Balanced Stimulation . . . 128
5.2 Power Consumption . . . 129
5.2.1 Switched capacitor DC-DC converter design . . . 133
5.2.2 DC-DC converter parameters . . . 136
5.3 Circuit Implementation . . . 138
5.3.1 Technology selection . . . 139
5.3.2 Controller . . . 139
5.3.3 DC-DC converter . . . 140
5.3.4 Current Sink . . . 143
5.3.5 H-bridge . . . 145
5.3.6 Core Supply DC-DC converter . . . 146
5.3.7 ESD and pad ring . . . 146
5.4 Experimental Results . . . 146
5.4.1 Simulated Results . . . 147
5.4.2 Measured results . . . 148
5.4.3 Ex-Vivo Results . . . 153
5.5 Discussion and Future Work . . . 154
5.5.1 Future Work . . . 155

6 Vibratory proprioceptive feedback 160
6.1 Introduction . . . 160
6.2 Artificial feedback . . . 161
6.2.1 Proprioceptive illusion . . . 161
6.2.2 Vibrotactile feedback . . . 162
6.3 Vibration mechanisms . . . 163
6.3.1 Vibrotactile devices . . . 163
6.3.2 Tendon vibration devices . . . 164
6.4 Materials & Methods . . . 164
6.4.1 Trial setup . . . 165
6.4.2 Subjects . . . 165
6.4.3 Vibration devices . . . 165

6.4.4 Vibration modulation . . . 167
6.4.5 Trials . . . 169
6.5 Results . . . 171
6.5.1 Subjective sensations . . . 171
6.5.2 Tendon vibrator performance . . . 171
6.6 Discussion . . . 172
6.6.1 Results discussion . . . 172
6.6.2 Feasibility of non-invasive proprioception and recommendations . . . 174

7 Conclusion **178**
7.1 Summary . . . 178
7.1.1 Introductory and background information chapters . . . 178
7.1.2 Design of a proprioceptive neural prosthesis . . . 178
7.1.3 Real time naturalistic patterns . . . 179
7.1.4 Efficient neural stimulation . . . 179
7.1.5 Non-invasive proprioceptive feedback . . . 180
7.2 Contributions . . . 180
7.3 Future directions . . . 181
7.3.1 Disruptive technologies . . . 181
7.3.2 Way ahead . . . 182
7.4 Concluding Remarks . . . 183

List of Figures

1.1 Some of the possible levels of amputation for the upper limb. 22
1.2 A body powered and a modern myoelectric prosthetic arm 23
1.3 Key prosthetic developments. 24
1.4 Targeted Muscle Reinnervation involves deinnervating unused muscles and surgical redirection of nerves from the amputated limb to reinnervate these muscles. 25
1.5 Results from a movement task in a patient with no proprioception and with varying delays on visual feedback 26
1.6 Outline of a proprioceptive neural prosthesis, with the areas addressed in this thesis highlighted. 27

2.1 Axon types and diameters 34
2.2 The main proprioceptive receptors and their locations in skin, muscles and joints. 35
2.3 Cross section of a muscle spindle and its innervation by fusimotor and afferent axons. 36
2.4 Gamma motor neuron action 36
2.5 The location of a Dorsal Root Ganglion and an example of the unipolar cell bodies found within it. 38
2.6 The brachial plexus – showing the formation of the major nerves from the spinal roots (adapted from wikipedia.org). 38
2.7 Cross-section of a peripheral nerve showing the layers and fascicular arrangement. 39
2.8 Innervation from the spinal roots: outer pictures are maps of skin innervation (dermatome) and inner are maps of muscle innervation (myotome). 39
2.9 Innervation from the major nerves: outer pictures are maps of skin innervation (dermatome) and inner are maps of muscle innervation (myotome). . . 41
2.10 Muscle innervations of the major arm nerves (reproduced from orthopaedicsone.com). 41
2.11 The proprioceptive neural pathway in the CNS. 42
2.12 A proposed role for the descending corollary discharge is that it is used to highlight differences between expected and actual motion. 44
2.13 An overview of 6 possible feedback paths for prosthetic limb users. 47
2.14 Devices for vibrotactile and electrocutaneous feedback. 48
2.15 Modality matched sensory feedback systems. 49

3.1 Generic concept of a proprioceptive prosthesis. 57
3.2 The proposed system design process with arrows showing dependencies. Below each headline is an overview of the choices discussed in this chapter. . . 60
3.3 Action potential generation. (a) – The phospholipid cell membrane, ionic charges and an ion channel. (b) – A typical action potential 66
3.4 Optogenetics - the action of opsins in the cell membrane 68
3.5 Electrical stimulation of a neuron generating an action potential 70
3.6 Solvated ions forming an electrical double layer at the electrode-electrolyte boundary and the electrical potential across the boundary. 72
3.7 Examples of charge balanced waveforms 73
3.8 Cross sections through a nerve bundle indicating the interfaces provided by some common electrode types. 73
3.9 Pictures of the 5 main types of electrodes. 74
3.10 The operation of a Flat Interface Nerve Electrode in comparison to a standard cuff electrode 75
3.11 Alternative representations of the challenge of stimulating target neurons. . 75
3.12 Electric field shaping. 77
3.13 Diagrammatic representation of electrode type selectivity. 78
3.14 Current, voltage and charge controlled stimulation 79
3.15 Conceptual diagram of a Voltage Controlled Stimulator with DC blocking capacitors and electrode shorting. 79
3.16 Current Controlled Stimulators. Φ_1 switches are closed during anodic stimulation and Φ_2 during cathodic. 80
3.17 Charge Controlled Stimulators. Φ_1 is closed during anodic stimulation and Φ_2 during cathodic. 81
3.18 The sensor fit for two research prostheses 82
3.19 Outline proposed system design 85

4.1 Outline of the modelling presented here, showing inputs from sensors (left) being translated into predictions of neural firing patterns (right). 95
4.2 A selection of muscle architectures illustrating how pennation angles vary. . 97
4.3 The structure of a muscle 97
4.4 The Hill model. 99
4.5 Outline depiction of the models. 102
4.6 The musculoskeletal model 103
4.7 The articular span of the muscles in this model. 104
4.8 Predicted muscle activations for an actor brushing his teeth. 111
4.9 Comparison of proposed spindle model with original Mileusnic et Al results 112
4.10 Second comparison of proposed spindle model with original Mileusnic et Al results 113
4.11 Comparison of proposed spindle model with Mileusnic spindle model and recorded data 114
4.12 Human muscle spindle firing patterns for imposed motions. 115

4.13 Predicted proprioceptor firing patterns for the actor brushing his teeth. . . 116
4.14 Stability and sensitivity of the model to rapid perturbation 117

5.1 Biphasic waveforms and current stimulator designs 128
5.2 H-bridge configuration for biphasic current control. Switches allow bi-directional flow of current through a load. 129
5.3 The proposed charge balancing scheme. 130
5.4 Lumped circuit models of the electrode-tissue interface. 130
5.5 Electrical neural stimulation waveforms 131
5.6 Power consumption for a sub-maximal current stimulation using various power saving methods. 132
5.7 Current waveform generated using a switching DC-DC converter 132
5.8 A simplified DC-DC converter 133
5.9 Asymptotic limits for switched capacitor performance. FSL – Fast Switching Limit, SSL – Slow Switching Limit 134
5.10 Interleaving multiple converters together to reduce ripple 136
5.11 Effect of number of converter voltage outputs on power savings, energy per stimulation and required converter efficiency 137
5.12 A reconfigurable multi-topology switched capacitor DC converter. 137
5.13 Overview of the proposed neural stimulator. 138
5.14 State diagram for the neural stimulator controller. 139
5.15 The DC-DC converter 141
5.16 Charging and discharging cycles of the DC-DC converter 143
5.17 Circuit schematic of the current reference, DAC and regulated cascode current mirror. 144
5.18 Simulations of the output impedance. 145
5.19 Microphotograph of the neural stimulator, measuring 2 mm × 2.7 mm. . . . 146
5.20 Transient analysis of the neural stimulator for a full-scale stimulus 147
5.21 Simulated DC converter efficiency for different target stimuli (i.e. output currents) for 3 V, 9 V and 12 V compliances. 148
5.22 Monte Carlo simulations of charge balancing. 148
5.23 Sample results of the neural stimulator. 149
5.24 Charge imbalance results. 150
5.25 Energy per stimulation. 151
5.26 Voltages across the electrode and the current controlling transistors. 151
5.27 Experimental setup for the *ex-vivo* test. 153
5.28 *ex-vivo* measured response to stimulation. 154

6.1 Tactors for vibrotactile feedback and illusory motion generation 163
6.2 Example motor positioning in the arm sling. 164
6.3 Tendon vibration motors and outline system designs. 166
6.4 Proprioceptive feedback pattern calculation. 168
6.5 Example outputs of the two proprioceptive feedback patterns 168

6.6 Trial 1: (a) visual feedback and (b)symbols used. 170
6.7 Trial 2 task. 170
6.8 Results of trials of vibration frequency control. 173

List of Tables

2.1 Key mechano-receptors involved in proprioception and some of the receptors key parameters 34
2.2 Table of muscles in the upper limb, the actions they contribute to and the nerves that innervate them 40
2.3 Commonly quoted figures for proprioceptive acuity 46
2.4 Comparison of previous human and animal experiments using neural stimulation to induce proprioceptive sensation 51

3.1 Implant site comparison 62
3.2 A subjective review of our understanding of proprioceptors 64

4.1 Spindle models in the literature 101
4.2 GTO models in the literature 103
4.3 Comparison of a selection of ARM microprocessors 118

5.1 Multi-level integrated SC DC converter comparison 134
5.2 Comparison of available CMOS technology processes 139
5.3 Controller state descriptions. 140
5.4 Comparison with other low-power neural stimulator designs. 155

6.1 Vibration sensitivity of skin receptors 162

Publications

Parts of this thesis were previously published as journal or conference papers for which I was the lead or 2nd author.

Chapter 3 contains content from:

- S. Luan, I. Williams, T. G. Constandinou, and K. Nikolic. "Neuromodulation: present and emerging methods". *Frontiers in Neuroengineering* 7 (2014), p. 27

Chapter 4 contains content from:

- I. Williams and T. G. Constandinou. "Computationally Efficient Modelling of Proprioceptive Signals in the Upper Limb for Prostheses: a Simulation Study". *Frontiers in Neuroscience* 8 (2014), p. 181
- I. Williams and T. G. Constandinou. "Modelling muscle spindle dynamics for a proprioceptive prosthesis". *Engineering in Medicine and Biology Society (EMBC), 2013 35th Annual International Conference of the IEEE*. IEEE. 2013, pp. 1923–1926

Chapter 5 contains content from:

- I. Williams and T. G. Constandinou. "An energy-efficient, dynamic voltage scaling neural stimulator for a proprioceptive prosthesis". *IEEE Trans. BioCAS* 7 (2013)
- I. Williams and T. Constandinou. "An energy-efficient, dynamic voltage scaling neural stimulator for a proprioceptive prosthesis". *Circuits and Systems (ISCAS), 2012 IEEE International Symposium on*. IEEE. 2012, pp. 1091–1094

1 Introduction

A prosthetic arm that feels as it was a part of your body and that can be controlled like a normal arm, has been a research goal for many years. 2013 saw a convincing demonstration of stable tactile feedback [1] (and its benefits for hand control) as well as the publication of a series of concept review papers for introducing proprioceptive feedback (the sensations of position, movement and effort) into prosthetic limbs [2–5]. 2014 in turn looks set to build on this momentum with the launch of the DARPA HAnd Proprioception and Touch Interfaces (HAPTIX) programme, which aims to turn this common staple of science fiction into a reality for the millions of amputees worldwide.

1.1 What is proprioception

Sensation accompanies all motions of the body that occur above a certain speed and over distances beyond a certain amount. These perceptions of the body's position, passive motion, active motion and resistance to motion are known as proprioception – a description coined by Charles Scott Sherrington [6] in 1906. Unlike the well known five exteroceptive senses that we are always conscious of, it is a sense that unobtrusively aids us in pose maintenance and skilled motion and is most noticeable in its absence.

1.2 Inspiration

Ironically it was this lack of awareness that inspired this research. The vital feedback role proprioception plays in human motor control appeared to be in stark contrast to the lack of provision made for it in prosthetic limbs and in the multitude of prosthetic limb control systems currently being researched.

To a certain extent this enthusiasm for feedforward approaches is understandable, as recent years have showcased exciting developments in the field: enabling quadriplegics to reliably move a prosthetic limb with just their thoughts [7] or novel use of reinnervated muscles as biological signal amplifiers [8].

However, the use of feedforward motor control in the human body is believed to be largely limited to certain ballistic motions (e.g. throwing a punch); smooth, coordinated motion on the other hand relies on sensory feedback and closed loop control [9]. Prosthesis users compensate for the lack of feedback by constantly visually monitoring their prosthetic limb when in use. This is an approach that: results in a high cognitive load; is unsuitable for many everyday tasks; and that is among prosthesis users' top complaints [10].

It seems evident [5, 11, 12]that a device capable of providing high quality feedback could greatly improve prosthetic users limb control and their associated quality of life, however,

a mechanism of providing this feedback is lacking.

Graded sensory feedback of almost any sort could feasibly provide the user with proprioceptive information about their prosthesis and haptic, visual, auditory, vibratory and electrocutaneous feedback have all been explored (see Chapter 2 for further information) [13, 14]. However, sensory substitution methods such as these, partially deprive the user of another of their senses and suffer from long training periods and high cognitive load as they require the user to learn and interpret the information encoded by the feedback stimuli. Despite decades of experimentation, sensory substitution has not seen significant clinical application [14] and it is an approach that is likely to be increasingly difficult to implement in future – as prosthesis complexity increases and the quantity of feedback increases correspondingly.

Direct neural feedback in the form of a neural prosthesis has the potential to provide high quality and intuitive feedback. The incredible capability of neural prostheses to transform lives has already been vividly demonstrated in recent years by the rise of cochlear implants for the deaf[15] and the tantalising progress in retinal implants for the blind [16]. A proprioceptive prosthesis on the other hand could in theory provide a user with intuitive feedback of their limb's position, motion and the forces it is exerting, as well as potentially providing therapeutic benefit for phantom limb issues [11].

1.2.1 History of proprioceptive neural prostheses

It has long been recognised that amputees would greatly benefit from having sensation in their prosthetic limbs and devices providing proprioceptive neural feedback have been investigated since at least 1974 [13] when Clippinger et al implanted electrodes in several amputees' median nerves. This early work suffered from a number of limitations such as only having a single stimulation channel, level and waveform. However, it did manage to elicit a vibratory sensation in the user's phantom limb at low pulse repetition rates and the sensation of their phantom hand clenching at higher rates. Little functional benefit was demonstrated, but experiments connecting the implant to a strain gauge on a prosthesis showed the ability of some users to discriminate the resilience of objects being gripped.

The following few decades were quiet in terms of proprioceptive neural prosthesis development, however, this was an active time for developments in microelectronics, neural stimulation and proprioception research. In particular 2004 and 2005 saw the publication of key papers by Dhillon et al [11, 12, 17] that reignited research interest in implanted proprioceptive neural prostheses and demonstrated that realistic artificial sensations of limb position could be generated by implanted electrodes even in long term amputees. These papers identified an experimental setup that elicited stable proprioceptive (and tactile) percepts and helped demonstrate the effects of training with feedback in improving amputees ability to conduct experimental tasks. Then 2006 saw the launch of the "Revolutionizing Prosthetics" programme by DARPA which in its first phase developed a highly capable prosthetic with weight and capability approaching that of the human upper limb and which utilised the improvements in feedforward control offered by Targeted Muscle Reinnervation to really capture the interest of the world's press in prosthetics development.

The combination of these developments in the latter part of the noughties almost certainly contributed to a spate of conceptual publications on sensory feedback for prostheses in the last few years – providing feedback either in the brain, Dorsal Root Ganglion (see Chapter 2), or in the Peripheral Nervous System (PNS) [2, 4, 18–20]. Practical systems have also been demonstrated in humans [21, 22] with initially limited success, but recent months have seen 2 independent groups report functional benefit with neural (mostly tactile but some proprioceptive) feedback from a prosthesis [1, 23] which bodes well for the future.

1.3 Motivation

1.3.1 Target group

Amputees are not the only potential users of a proprioceptive neural prosthesis – theoretically anyone with volitional movement capability (but impaired proprioception) in a part of their body could benefit, i.e. people suffering from a wide range of neuropathies and traumatic nerve damage. However, the work presented here focuses on amputee prosthetic limb users because they represent a far more homogenous target group with a clearer future progression of neural changes.

Extrapolating from United States (US) survey figures [24, 25] there are around 5 million people in the US and European Union who have had major amputations. Typically for these amputees the treatment option of choice is to be provided with a prosthetic limb, and in the UK alone there are on average about 15 new referrals to prosthetics services each day [26].

Prosthetics for upper and lower limbs present very different challenges. The lower limb is primarily involved in support, balance and propulsion whereas the upper limb is crucial for interaction with tools and the physical world around us (as well as playing a major role in body language and gesturing). Requirements for prosthetics are consequently very different for these two areas – simple or static prosthetics provide lower limb users with substantial amounts of functionality as ably demonstrated by many paralympians, but much more capable myoelectric prostheses are required for dexterous upper limb function.

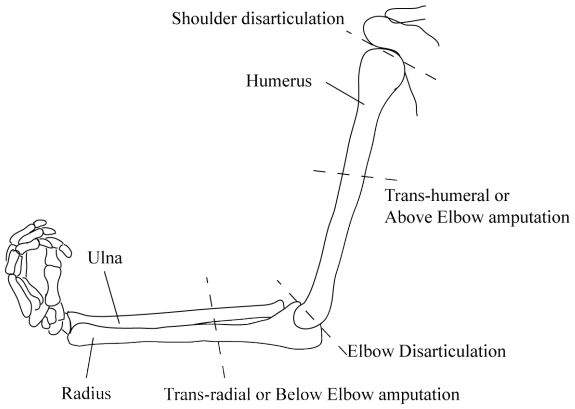
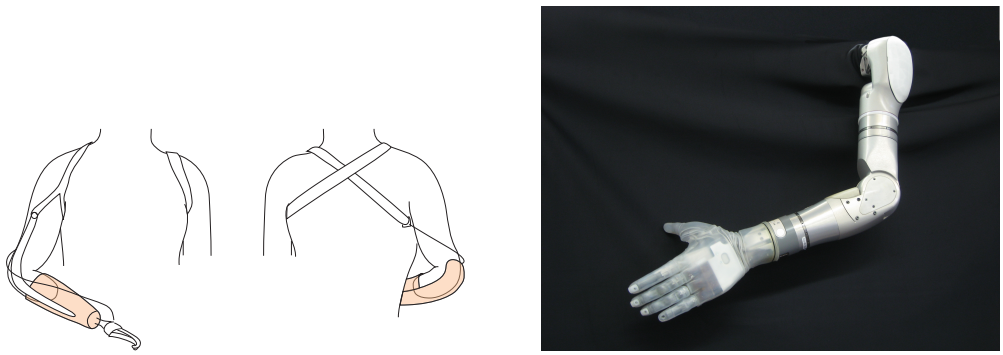


Figure 1.1: Some of the possible levels of amputation for the upper limb.

The level of capability obtained by a patient using a prosthesis is linked with the type of amputation they have undergone [10, 27]. Amputations may occur at any level of the limb and are described in terms of the bone or joint that is transected (see Fig. 1.1). The more proximal the amputation, the more degrees of freedom that are lost and the greater the functionality deficit to the user (and the greater the requirements placed on the prosthetic).

High level upper limb amputees (e.g. trans-humeral or shoulder disarticulation) are the most challenging for prosthetic development. Although this user group represents a small percentage of amputees (approximately 1–2% of all amputees – the majority of which are at the trans-humeral level [26]), they are likely to be the ones that would benefit most from the feedback from a proprioceptive prosthesis. The work presented here therefore focuses on providing proprioceptive feedback to trans-humeral amputees, with the goal of developing systems and techniques that are also applicable to other amputee groups and potentially people with other proprioceptive impairments.

1.3.2 Prosthetic limbs



(a) A body powered prosthesis

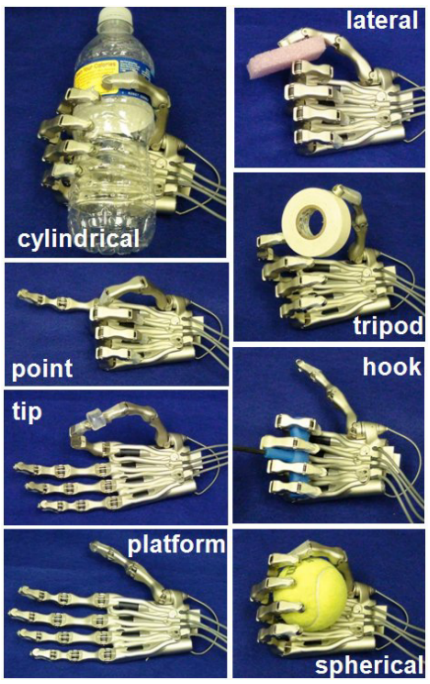
(b) The DEKA arm (reproduced from dekaresearch.com)

Figure 1.2: (a)Body powered prostheses are controlled by cables connected to a harness around the user's shoulders. Gross shoulder movements operate the terminal device. (b) The myoelectrically controlled DARPA funded "DEKA Arm" is controlled by sensing muscle contractions.

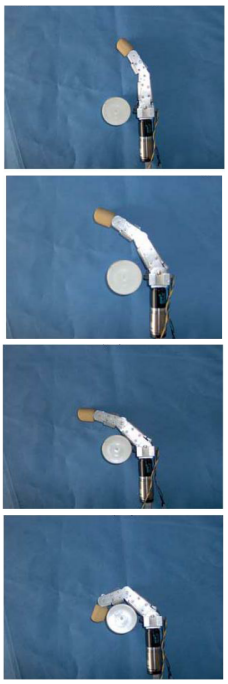
In the 20th century the most popular upper limb prosthtics were either non-functional cosmetic prostheses or functional body powered hook prostheses (see Fig. 1.2(a) that lacked any cosmesis.

Myoelectric prostheses (see Fig. 1.2(b) are motor powered prostheses controlled by sensing electrical signals produced by muscle contractions. They were first developed in the 1950s and 1960s [28] and could bridge this divide between functionality and cosmetics. However, early devices were heavy, provided little or no feedback, were difficult to control and only provided a single powered degree of freedom – with commensurately poor functionality. As a result of this and their relatively high cost, myoelectric prostheses remained relatively unpopular for many years. Research rapidly demonstrated new devices with multiple motors driving additional degrees of freedom, but while this improved the capability it came at the expense of increased weight and control complexity (providing little extra

benefit to the user).



(a) High functionality grips and hand positions targeted in prosthesis development. Reprinted from [29]



(b) An underactuated finger naturally conforming to a cylinder. Reprinted from [30]

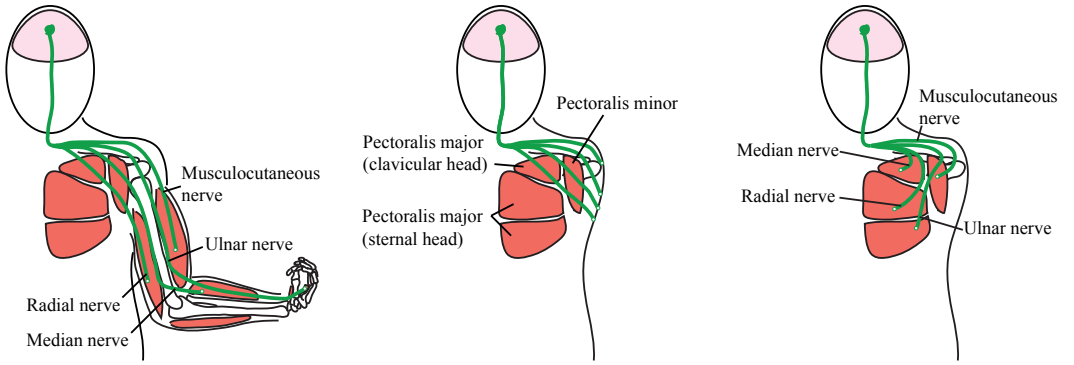
Figure 1.3: Key prosthetic developments.

The following decades in prosthesis development can be characterised as a quest to do more with less. Key developments were: a focus on a subset of hand positions that are most useful in everyday life (see Fig. 1.3(a); automation of grip force to prevent slippage and crushing; and the introduction of under-actuation (having fewer actuators than degrees of freedom). Under-actuation is the technique of using linkages and coupling between joints to enable coordinated and conformal motion (especially of finger joints as depicted in 1.3(b) and has been revolutionary in prosthetic design and weight reduction.

Today myoelectric prostheses have made great strides in capability, market share and user acceptance. Research arms (such as the DARPA funded DEKA arm shown in Fig. 1.2(b) have demonstrated mechanical capability approaching that of the human limb. Commercially available prostheses have also progressed rapidly, although functionality, durability and the quality of the user experience takes precedence over pure limb capability.

This discrepancy between limb capability and user functionality is in part due to the increase in control complexity and it is a gap that is growing. Developments in electromyography (EMG), such as implanted electrodes and advanced multi-electrode pattern recognition, have sometimes struggled to make it out of the laboratory, but one technique which is gaining rapid momentum is Targeted Muscle Reinnervation (TMR) as shown in Figure 1.4.

The fundamental problem that TMR sets out to solve is that with standard EMG control the user must learn to make unintuitive muscle contractions in their remaining muscles to



(a) Diagrammatic representation of normal arm innervation

(b) Amputated arm with truncated nerves

(c) Surgery redirects the truncated nerves to unused muscles

Figure 1.4: Targeted Muscle Reinnervation involves deinnervating unused muscles and surgical redirection of nerves from the amputated limb to reinnervate these muscles.

control the prosthesis. TMR involves redirecting the nerves that would have supplied amputated muscles to innervate muscles that remain (ones with little or no function due to the amputation). This redirection of neural signals means that when the user attempts to move part of their amputated limb, it is expressed as contraction of these reinnervated muscles which then function as amplifiers for the neural signals, allowing standard EMG techniques to detect the movement intent outside the body.

Feedforward control techniques such as TMR have shown major functional benefit for some amputees, but they do little to address a major complaint of amputees – that the user must visually monitor the limb to control it, making many daily tasks such as driving or brushing your teeth a challenge. This is an issue that is unlikely to be addressed by any improvements in feedforward control (at the peripheral level) as the human body's natural system of motor control involves a process of feedback and correction that is absent in a feedforward system. Some progress can be made by automation (e.g. of grip strength to prevent slippage, or of certain grasps and hand positions), however, there are limits to what this can achieve and it is important that the user retain volitional control of the limb lest it start to feel out of control (e.g. Alien Hand Syndrome [31]).

1.3.3 Benefit provided by proprioceptive feedback

Feedback is a crucial element of learning new skills and for controlling our limbs in a smooth and coordinated way. The absence of it in myoelectric prostheses has been repeatedly cited as a significant factor in their abandonment, while even the small quantity of feedback provided by body powered prostheses has been speculated as being key to their enduring success [32, 33].

Research on able-bodied people has indicated that without their normal proprioceptive feedback, their ability to control their body is severely deteriorated and this leads to jerky, poorly coordinated motion. Figure 1.5 shows the results of a simple movement task and gives a flavour of the impact that loss of feedback has on our motor control. A further

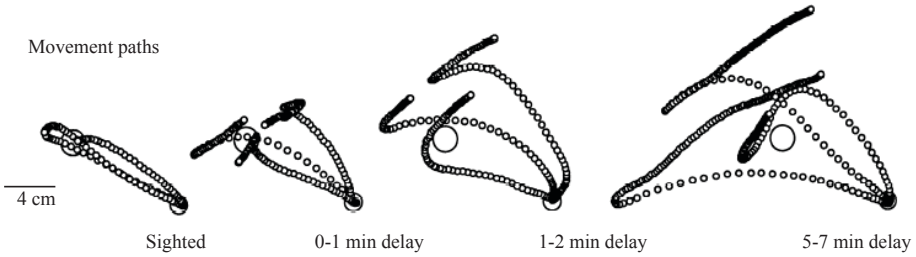


Figure 1.5: Results from a movement task in a patient with no proprioception and with varying delays on visual feedback (reproduced from [34])

example can be seen by considering those people who (due to rare sensory neuropathies) have fully functional motor control of their body but suffer from a lack of proprioception. A lack of this key sense initially leaves them almost completely unable to control their body:

> *"Thus at the time of her catastrophe, and for about a month afterwards, Christina remained as floppy as a ragdoll, unable even to sit up ... She had, at first, to monitor herself by vision, looking carefully at each part of her body as it moved, using an almost painful conscientiousness and care ... Christina learned to walk, to take public transport, to conduct the usual business of life – but only with the exercise of great vigilance ... thus if she was eating while she was talking, or if her attention was elsewhere, she would grip the knife and fork with painful force – her nails and fingertips would go bloodless with pressure; but if there was any lessening of the painful pressure, she might nervelessly drop them straightaway – there was no in-between, no modulation ... She continues to feel, with the continuing loss of proprioception, that her body is dead, not-real, not-hers – she cannot appropriate it to herself."* [35]

It has long been believed that providing artificial proprioceptive feedback would improve the quality of users control; would help them learn to use their prosthesis more quickly; and may even have psychological benefits (such as ameliorating phantom limb issues) by helping the user integrate the prosthesis into their body image [11, 13, 36].

Dhillon et al. [12] in 2005, Kuchenbecker, Gurari, and Okamura [37] in 2007 and Blank, Okamura, and Kuchenbecker [38] in 2008 have explored the potential benefits of providing proprioceptive information to a user in controlling position, movement and grip strength. The results from these studies show that even for subjects using visual feedback, the addition of proprioceptive feedback provided a significant improvement in the ability to carry out the assigned tasks. The research also showed that for subjects deprived of visual feedback, the improvements provided by proprioceptive feedback were much greater, and it is therefore expected a proprioceptive prosthesis could provide the greatest benefits in scenarios where a patient with impaired proprioception cannot visually monitor their affected limb (e.g. driving, brushing teeth, playing sports or if the patient also suffers from visual impairment).

1.4 Research approach

This thesis focuses on providing proprioceptive feedback for a trans-humeral upper limb amputee. Three top level aspirations were identified for guiding the research:

1. That the feedback should be intuitive.
2. That the system should aim for high performance – with the ultimate ideal of one day being capable of providing performance similar to the normal human proprioceptive system.
3. That the system should be designed to deliver initial capability in the near term.

Each of these 3 aspiration presents unique challenges. It was realised early on that achieving high performance and intuitive feedback requires the system to talk directly to the neurons that carry proprioceptive information in the body and to talk to them in the neural language they understand (see Chapter 2 for more information). However, the aim of delivering capability in the near future also puts the focus on targeting neurons that are well understood and can be safely interfaced with (both from a surgical and neural stimulation perspective).

At the outset of this PhD in 2010, there had only been one review (by Riso [39] in the late 1990s) targeted at neural proprioceptive feedback. A review of the feasibility and design of a proprioceptive neural prosthesis was carried out to refresh this and it identified a number of enduring challenges. The research presented here was therefore targeted at addressing those key challenges identified that – as an engineer – I was best placed to address. These areas (see Fig. 1.6) were: 1) the real time generation of neural feedback patterns; 2) development of a safe, low power neural stimulator; and 3) development of a non-invasive test platform for vibration induced proprioceptive feedback.

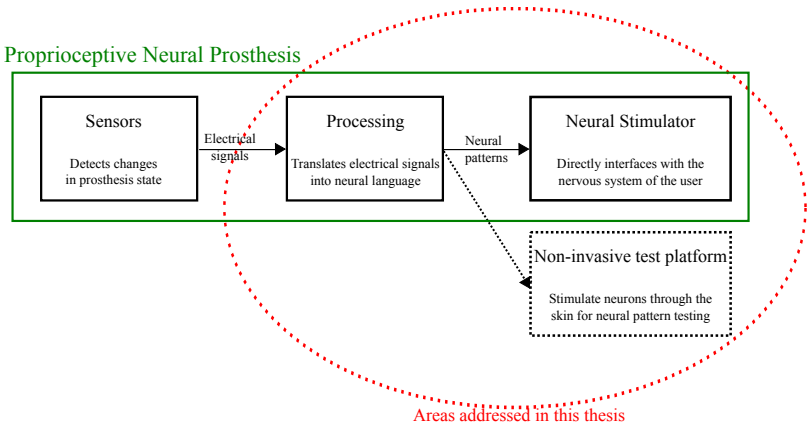


Figure 1.6: Outline of a proprioceptive neural prosthesis, with the areas addressed in this thesis highlighted.

1.4.1 Document structure

This thesis is structured as follows:

Chapter 2, Proprioception: Physiology, Pathophysiology and Functional Replacement, provides an overview of – proprioceptive function in the human upper limb; how the neural signals are conveyed to their endpoints in the spine and brain; how these processes are disrupted following amputation; and the various methods people have explored to restore proprioceptive function in amputees.

Chapter 3, Design of a Proprioceptive Neural Prosthesis – provides a new perspective on the process of designing a proprioceptive prosthesis as well as the requirements and operation of its constituent parts; and identifies challenges and areas of further development required.

Chapter 4, Computationally Efficient Modelling of Proprioceptive Signals in the Upper Limb – explains the creation of a real time model of the upper limb that efficiently combines biomechanical and proprioceptor sub-models to generate estimates of muscular proprioceptive signals.

Chapter 5, Energy efficient neural stimulation for proprioceptive feedback – details the design and performance of a current controlled neural stimulator with a novel charge balancing approach and a fully integrated DC-DC converter for low power operation.

Chapter 6, Vibratory proprioceptive feedback – details efforts to create a non-invasive proprioceptive feedback test platform based on the vibration induced proprioceptive illusion.

Chapter 7, Conclusion – summarises the content of this thesis and looks at future prospects and technologies for a proprioceptive prosthesis.

Bibliography

[1] S. Raspopovic, M. Capogrosso, F. M. Petrini, M. Bonizzato, J. Rigosa, G. Di Pino, J. Carpaneto, M. Controzzi, T. Boretius, E. Fernandez, et al. "Restoring natural sensory feedback in real-time bidirectional hand prostheses". *Science translational medicine* 6 (2014), 222ra19–222ra19.

[2] C. Antfolk, M. D'Alonzo, B. Rosen, G. Lundborg, F. Sebelius, and C. Cipriani. "Sensory feedback in upper limb prosthetics" (2013).

[3] P. Zhang, Q. Xu, and J. P. He. "Review and Perspective: Sensory Feedback in Upper Limb Prosthesis". *Applied Mechanics and Materials* 303 (2013), pp. 261–265.

[4] R. Kwok. "Neuroprosthetics: Once more, with feeling". *Nature* 497 (2013), pp. 176–178.

[5] D. J. Weber, R. Friesen, and L. E. Miller. "Interfacing the Somatosensory System to Restore Touch and Proprioception: Essential Considerations". *Journal of Motor Behavior* 44 (2012), pp. 403–418.

[6] C. Sherrington. *The Integrative Action of the Nervous System*. Yale University Press, 1966.

[7] J. L. Collinger, B. Wodlinger, J. E. Downey, W. Wang, E. C. Tyler-Kabara, D. J. Weber, A. J. McMorland, M. Velliste, M. L. Boninger, and A. B. Schwartz. "High-performance neuroprosthetic control by an individual with tetraplegia". *The Lancet* 381 (2013), pp. 557–564.

[8] T. A. Kuiken, G. Dumanian, R. Lipschutz, L. Miller, and K. Stubblefield. "The use of targeted muscle reinnervation for improved myoelectric prosthesis control in a bilateral shoulder disarticulation amputee". *Prosthetics and Orthotics International* 28 (2004), pp. 245–253.

[9] J. Bossom. "Movement without proprioception". *Brain Research* 71.2 (1974), pp. 285–296.

[10] D. J. A. D. C. Heard and W. H. Donovan. "Epidemiologic overview of individuals with upper-limb loss and their reported research priorities". *J. Prosthetics Orthotics* 8 (1996), pp. 2–11.

[11] G. S. Dhillon and K. W. Horch. "Direct Neural Sensory Feedback and Control of a Prosthetic Arm". *IEEE Transactions on neural systems and rehabilitation engineering* 13 (2005).

[12] G. Dhillon, T. Kruger, J. Sandhu, and K. Horch. “Effects of short-term training on sensory and motor function in severed nerves of long-term human amputees”. *Journal of neurophysiology* 93.5 (2005), pp. 2625–2633.

[13] F. W. Clippinger, R. Avery, and B. R. Titus. “A sensory feedback system for an upper-limb amputation prosthesis.” *Bulletin of prosthetics research* (1973), pp. 247–258.

[14] K. Ohnishi, R. F. Weir, and T. A. Kuiken. “Neural machine interfaces for controlling multifunctional powered upper-limb prostheses”. *Expert Reviews of Medical Devices* 4 (2007), pp. 43–53.

[15] A. A. Eshraghi, R. Nazarian, F. F. Telischi, S. M. Rajguru, E. Truy, and C. Gupta. “The cochlear implant: historical aspects and future prospects”. *The Anatomical Record* 295.11 (2012), pp. 1967–1980.

[16] J. D. Weiland, A. K. Cho, and M. S. Humayun. “Retinal prostheses: current clinical results and future needs”. *Ophthalmology* 118.11 (2011), pp. 2227–2237.

[17] G. S. Dhillon, S. M. Lawrence, D. T. Hutchinson, and K. W. Horch. “Residual Function in Peripheral Nerve Stumps of Amputees: Implications for Neural Control of Artificial Limbs”. *The Journal of Hand Surgery* 29A (2004), pp. 605–615.

[18] D. J. Weber, B. M. London, J. A. Hokanson, C. A. Ayers, R. A. Gaunt, R. R. Torres, B. Zaaimi, and L. E. Miller. “Limb-state information encoded by peripheral and central somatosensory neurons: implications for an afferent interface”. *Neural Systems and Rehabilitation Engineering, IEEE Transactions on* 19 (2011), pp. 501–513.

[19] D. J. Weber, R. Friesen, and L. E. Miller. “Interfacing the Somatosensory System to Restore Touch and Proprioception: Essential Considerations”. *Journal of Motor Behavior* 44 (2012), pp. 403–418.

[20] S. S. Hsiao, M. Fettiplace, and B. Darbandi. “Sensory feedback for upper limb prostheses.” *Progress in brain research* 192 (2011), p. 69.

[21] K. Warwick, M. Gasson, B. Hutt, I. Goodhew, P. Kyberd, B. Andrews, P. Teddy, and A. Shad. “The application of implant technology for cybernetic systems”. *Archives of Neurology* 60 (2003), pp. 1369–1373.

[22] P. M. Rossini, S. Micera, A. Benvenuto, J. Carpaneto, G. Cavallo, L. Citi, C. Cipriani, L. Denaro, V. Denaro, G. Di Pino, et al. “Double nerve intraneural interface implant on a human amputee for robotic hand control”. *Clinical neurophysiology* 121 (2010), pp. 777–783.

[23] M. Schiefer, M. Freeberg, G. Pinault, J. Anderson, H. Hoyen, D. Tyler, and R. Triolo. “Selective activation of the human tibial and common peroneal nerves with a flat interface nerve electrode”. *Journal of neural engineering* 10 (2013), p. 056006.

[24] K. Ziegler-Graham, E. J. MacKenzie, P. L. Ephraim, T. G. Travison, and R. Brookmeyer. “Estimating the prevalence of limb loss in the United States: 2005 to 2050”. *Archives of Physical Medicine and Rehabilitation* 89 (2008), pp. 422–429.

[25] S. L. H. Winkler. *Upper limb amputation and prosthetics epidemiology, evidence and outcomes*. `http://www.bordeninstitute.army.mil/published_volumes/amputee/CCAchapter22.pdf`.

[26] N. S. I. S. Division. *The Amputee Statistical Database for the United Kingdom 2006/07*. Information Services Publications, `http://www.limbless-statistics.org/documents/Report2006-07.pdf`. 2009.

[27] J. Davidson. "A survey of the satisfaction of upper limb amputees with their prostheses, their lifestyles, and their abilities". *Journal of Hand Therapy* 15.1 (2002), pp. 62–70.

[28] A. Muzumdar. *Powered Upper Limb Prostheses: Control, Implementation and Clinical Application ; 11 Tables*. Springer, 2004.

[29] S. A. Dalley, T. E. Wiste, H. A. Varol, and M. Goldfarb. "A multigrasp hand prosthesis for transradial amputees". 2010, pp. 5062–5065.

[30] H. Huang, L. Jiang, D. Zhao, J. Zhao, H. Cai, H. Liu, P. Meusel, and W. Hirzinger. "The development on a new biomechatronic prosthetic hand based on under-actuated mechanism". *Intelligent Robots and Systems, 2006 IEEE/RSJ International Conference on*. IEEE. 2006, pp. 3791–3796.

[31] I. Biran and A. Chatterjee. "Alien hand syndrome". *Archives of Neurology* 61.2 (2004), pp. 292–294.

[32] E. A. Biddiss and T. T. Chau. "Upper limb prosthesis use and abandonment: A survey of the last 25 years". *Prosthetics and Orthotics International* 31 (2007), pp. 236–257.

[33] M. D. O'Riain and D. T. Gibbons. "Position proprioception in a microcomputer controlled prosthesis". *Medical & Biological Engineering & Computing* 25 (1987), pp. 294–298.

[34] C. Ghez, J. Gordon, and M. F. Ghilardi. "Impairments of reaching movements in patients without proprioception II. Effects of visual information on accuracy". *Journal of Neurophysiology* 73.1 (1995), pp. 361–372.

[35] O. Sacks. *The man who mistook his wife for a hat and other clinical tales*. Simon & Schuster, 1998.

[36] K. Horch, S. Meek, T. G. Taylor, and D. T. Hutchinson. "Object discrimination with an artificial hand using electrical stimulation of peripheral tactile and proprioceptive pathways with intrafascicular electrodes". *Neural Systems and Rehabilitation Engineering, IEEE Transactions on* 19.5 (2011), pp. 483–489.

[37] K. J. Kuchenbecker, N. Gurari, and A. M. Okamura. "Effects of Visual and Proprioceptive Motion Feedback on Human Control of Targeted Movement". *Proceedings of the 2007 IEEE 10th International Conference on Rehabilitation Robotics* (2007), pp. 513–524.

[38] A. Blank, A. M. Okamura, and K. J. Kuchenbecker. "Identifying the role of proprioception in upper-limb prosthesis control: Studies on targeted motion". *ACM Trans. Appl. Percept.* 7 (2008), p. 23.

[39] R. R. Riso. “Strategies for providing upper extremity amputees with tactile and hand position feedback–moving closer to the bionic arm”. *Technology and Health Care* 7.6 (1999), pp. 401–409.

2 Proprioception: Physiology, Pathophysiology and Functional Replacement

Feedback is a crucial element for controlling dynamic system behaviours in the presence of system variations, noise and other perturbations. In our bodies, proprioception provides this feedback for movement control and adaptation, allowing us to learn new motor skills and perform smooth coordinated motions despite the complexity and variability of muscle dynamics [1–3].

Chapter 1 looked at some of the impairments resulting specifically from the *absence* of proprioception, but *inappropriate* feedback can be just as detrimental to control. In basic systems this can manifest as issues such as overshoot and oscillation, however, for a neural prosthesis it can also mean distraction, discomfort and frustration.

Intuitive feedback that is natural and transparent to the remaining proprioceptive system (and therefore to the user) is the ultimate goal. However, creating a neural prosthetic capable of mimicking sections of the proprioceptive system requires detailed knowledge of proprioceptors and the pathways that convey their signals through the body.

This chapter reviews the published literature on: the main proprioceptive receptors; the neural pathways carrying the signals from the upper limb to the Central Nervous System (CNS); the specific pathophysiology of an amputated upper limb's proprioceptive pathway; briefly looks at the integration and performance of human proprioception at the system level; and reviews previous efforts at providing artificial proprioceptive feedback.

2.1 Proprioceptors

Proprioceptive sensation is derived principally from specialised nerve receptors (listed in Table 2.1) in four areas – muscles, the musculo-tendinous boundary, joints and the skin [2]. The deformation of these tissues is dependent on posture, limb movement and muscle forces, and the sensitive receptors they contain encode these structural changes as neural signals.

2.1.1 Muscle spindles

Specialised receptors lie embedded in spindle shaped bundles of intra-fusal muscle fibres (as shown in Fig. 2.3). These receptors are sensitive to the tension that occurs due to elongation of elastic tissue when the fibres are stretched [3, 8]. A primary (type Ia – see Fig. 2.1) and a secondary (type II) afferent axon innervate these receptors and convey combined receptor signals to the CNS (see Fig 2.3) [3, 9].

Table 2.1: Key mechano-receptors involved in proprioception and some of the receptors key parameters [4–6].

Location	Receptor	Axon group	Adaptation	Sensation
Cutaneous	Ruffini corpuscle	II	Slow	Skin tension
Muscle	Spindle dynamic	Ia	Rapid	Muscle stretch
Muscle	Spindle static	II	Slow	Muscle stretch
Musculo-tendinous	Golgi Tendon Organ	Ib	Slow	Muscle tension
Articular	Pacinian corpuscle	II	Rapid	Joint movement
Articular	Ruffini ending	II	Slow	Joint pressure
Articular	Golgi Organ	II	Slow	Joint torque

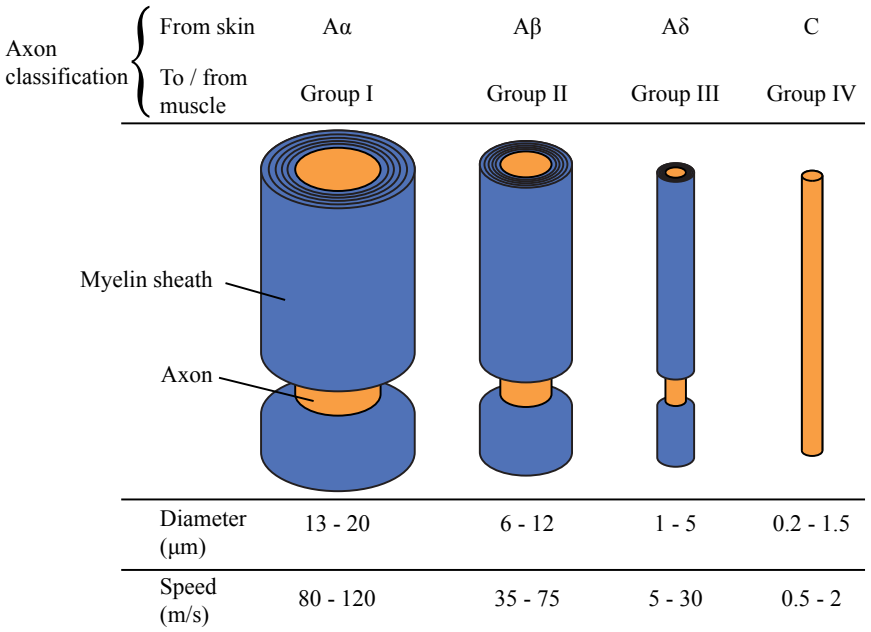


Figure 2.1: Axon types and diameters (adapted from [7]).

Recordings from primary afferents carrying spindle signals show fast adaptation and high dynamic sensitivity [3, 8, 10]. For ramp and hold type muscle stretches their discharge rate has been shown to be related to both the magnitude and the rate of the movement and as such are believed to signal changes in muscle length, velocity and potentially acceleration [2, 8]. In contrast secondary afferents are slow-adapting and have low dynamic sensitivity [2, 10] – ideal for conveying information about static muscle length and pose.

Each spindle is composed of a fibrous capsule containing three types of muscle fibre – short chain fibres and smaller numbers of longer nuclear bag_1 and bag_2 fibres [8, 9]. These fibres are innervated by γ efferent neurons carrying dynamic (for bag_1) and static (for bag_2 and chain) fusimotor signals from the CNS (see Fig. 2.3) [2, 8, 9]. This fusimotor control allows these intra-fusal fibres to contract independently of the extra-fusal muscle fibres (which make up the bulk of the muscle and act to provide motive force).

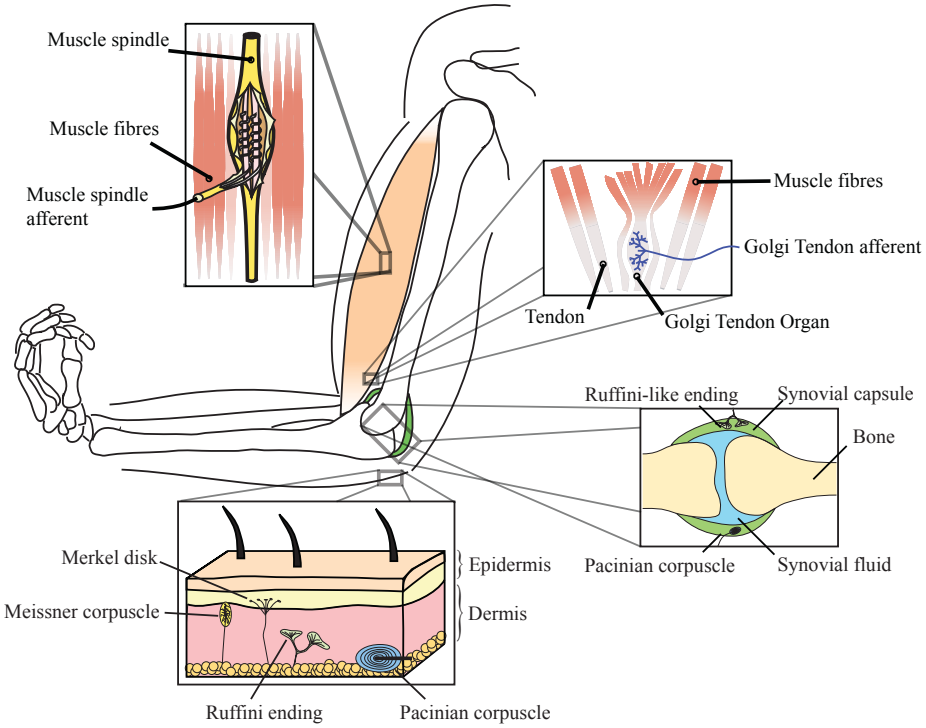


Figure 2.2: The main proprioceptive receptors and their locations in skin, muscles and joints.

Fusimotor control acts to modulate the tension in the intra-fusal fibres and hence the primary and secondary firing rates (see an example in Fig. 2.4). However, despite significant amounts of research the basis for fusimotor modulation is still unclear. One important theory for explaining this modulation, proposes that fusimotor signals encode a temporal template of a planned movement such that if the movement was performed without disturbance the spindle signals should ideally remain constant throughout [11]. However, studies performed under various conditions and types of movements have given varied and conflicting results. It seems likely that the principles governing fusimotor control are significantly more complex and may vary depending on the nature of the motion being undertaken [11].

The interpretation by the CNS of muscle spindle signals into limb position and motion is a demanding problem. The signals from spindles are non-linearly related to intrafusal fibre length and these fibres are contracted independently of the extrafusal muscle fibres that determine limb position. Muscles fibres (both intra- and extrafusal) also display complex thixotropic effects [2, 9] – their recent history of contraction or extension affects their response to stimulation – complicating the relationship between the efferent neural signals and the resulting fibre length. This is even further complicated by the biomechanics of the human musculoskeletal system involving multi-articular muscles (i.e. spanning multiple joints) and multiple degree of freedom joint complexes (e.g. the shoulder).

2.1.2 Golgi Tendon Organs

Golgi Tendon Organs (GTOs) are found at the boundary between muscle and tendon throughout skeletal muscle [12]. Numbers can vary widely from muscle to muscle and

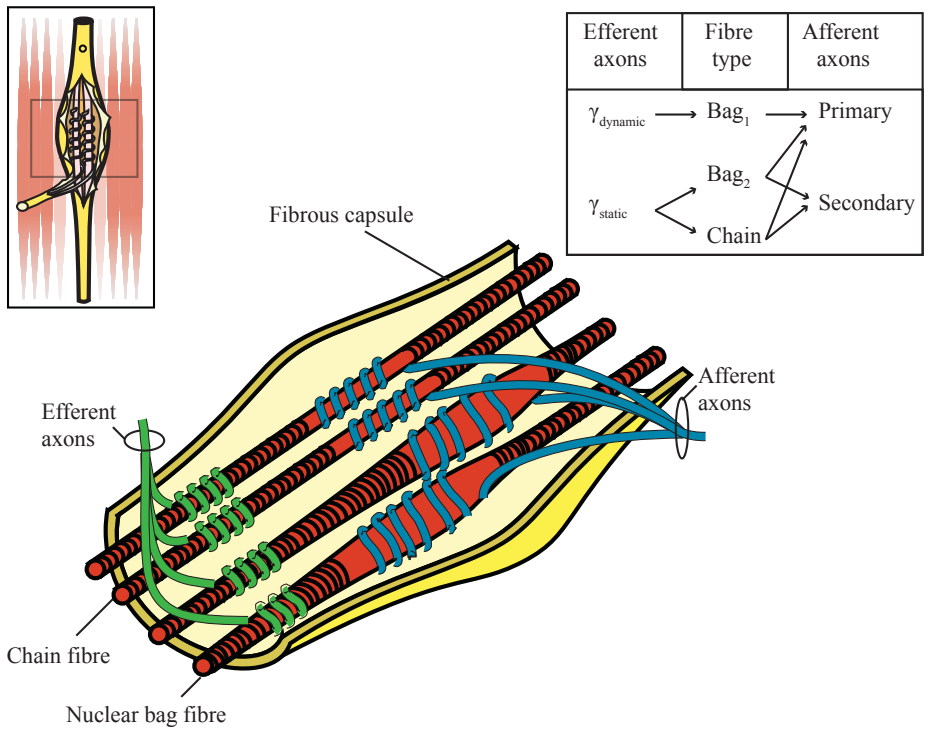
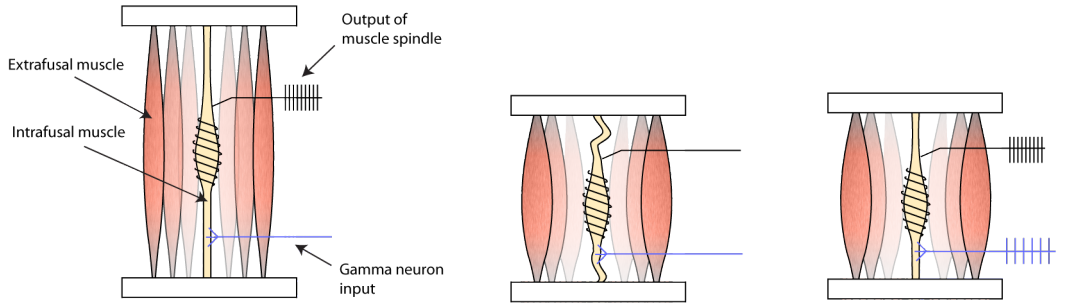


Figure 2.3: Cross section of a muscle spindle and its innervation by fusimotor and afferent axons.



(a) An intrafusal muscle spindle under tension fires off action potentials

(b) The muscle contracts, the slack spindle ceases to fire & is length insensitive.

(c) Fusimotor signals contract the intrafusal fibres increasing spindle sensitivity.

Figure 2.4: Gamma motor neuron action (adapted from [7]).

person to person and there appears to be no clear correlation between their prevalence and muscular function [12]. They consist of an elongated capsule of collagen bundles that at one end merges with the rest of the muscle tendon and at the other end binds with the tendinous endings of a small fascicle of muscle fibres [2, 12]. Interspersed with these collagen bundles is a spray-like receptor ending which is sensitive to deformation (and hence tension) in the bundles. Type Ib fibres innervate and amalgamate the signals from one or more GTOs and convey these signals to the brain [2, 12, 13].

The series connection of GTOs between muscle fibres and the tendon, makes them highly sensitive to active muscle forces developed by the in-series fibres (which may belong to

several different motor units) [12, 13]. In contrast GTOs are largely insensitive to passive stretch of the muscle, as this primarily stretches the connective tissue around the muscle fibres and the tendon around the GTOs [12].

2.1.3 Cutaneous receptors

Ruffini corpuscles are spindle shaped receptor endings found throughout glabrous and hairy skin in the limbs [10]. These receptors are believed to be slow-adapting and sensitive to the deformation and stretch that occurs in the skin around joints [10, 14, 15] – making them well suited for encoding limb position and movement information. However, skin stretch is not uniquely affected by movement at a single joint and may also be readily caused by external stimuli.

It has been speculated that the body may make use of signals from fast adapting skin receptors – believed to be Meissner corpuscles – to resolve this ambiguity [10, 16]. Meissner corpuscles fire phasically in response to shear forces in the skin; they have been observed to mainly occur around joint capsules and have shown sensitivity to motion at only their nearest joint [10, 16]. Pacinian corpusles and Merkel nerve endings are also found throughout the skin of the limb and may also contribute to cutaneous proprioception, however, it is unclear how their sensitivity to transient and sustained pressure are integrated.

2.1.4 Articular receptors

Slow-adapting Ruffini-like endings and fast-adapting Pacinian corpuscles are found in joint capsules and ligaments throughout the body [2, 5]. At first glance their location suggests that they would be ideally suited to providing information about joint deformation and therefore limb movement. However, recordings from Ruffini-like endings typically show that the receptors only fire at both extremes of joint motion [2, 10] – providing neither position feedback over the mid range of joint motion nor clear information on which extreme of motion the joint has reached. Farrell and Smith concluded that they were best described as limit detectors that warn of imminent noxious movements [17]. Pacinian corpuscles on the other hand, respond briefly to joint movement but are again directionally insensitive, suggesting they may be limited to providing feedback on which joint has moved [2, 5].

2.2 Neural pathways

The mechanoreceptors described above are all types of unipolar neuron, with their cell bodies lying in nodules called Dorsal Root Ganglions (DRGs) near each spinal root (see Fig. 2.5). In these neurons the single axon bifurcates shortly after leaving the soma, with one end projecting into the periphery and the other into the spine. This section traces the pathway of these axons from the cell bodies both to the receptor endings and to their synaptic terminii in the CNS, as well as looking at what is known about the post synaptic flow of proprioceptive information in the CNS.

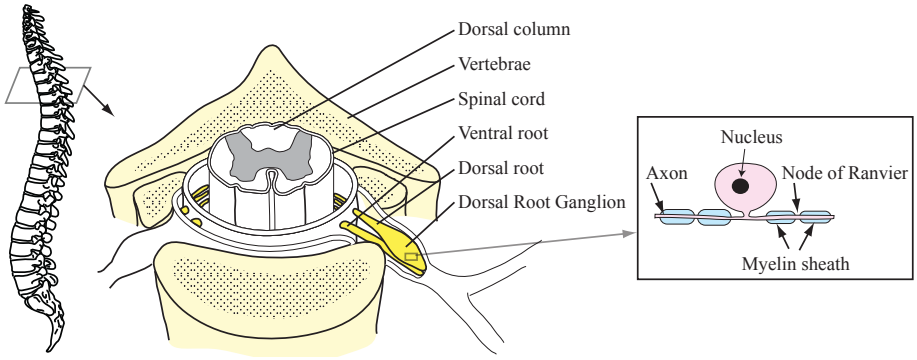


Figure 2.5: The location of a Dorsal Root Ganglion and an example of the unipolar cell bodies found within it.

2.2.1 The peripheral pathway

Afferent (sensory) axons emerging from a DRG into the periphery, merge with efferent (motor) axons from the nearby ventral root (see Fig. 2.5), together forming the spinal roots.

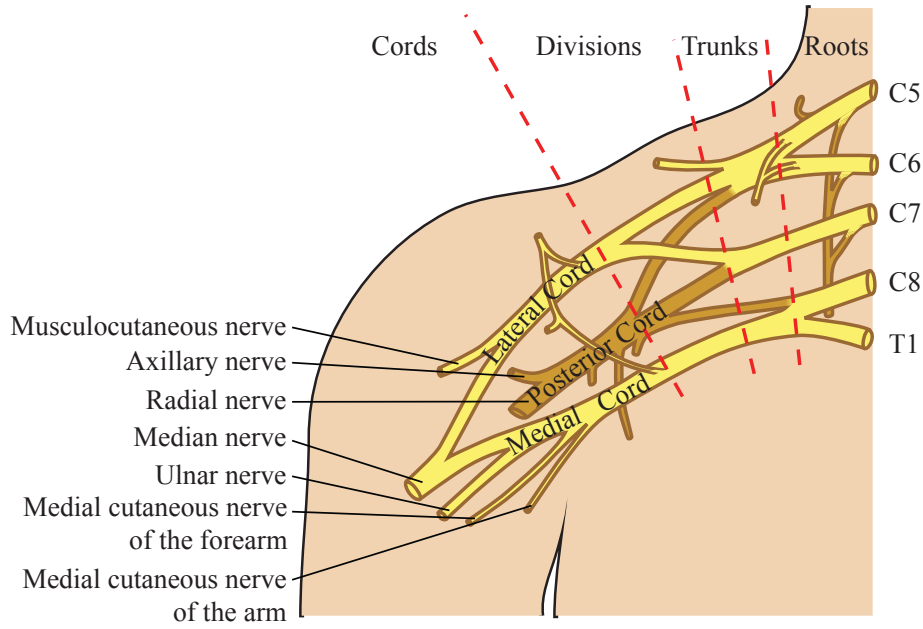


Figure 2.6: The brachial plexus – showing the formation of the major nerves from the spinal roots (adapted from wikipedia.org).

Nearby roots merge and separate in the brachial plexus, resulting in the formation of the major nerves of the upper limb (see Fig. 2.6). Each of these nerves consists of an epineurium sheath wrapped around perineurium, blood vessels and bundles of axons surrounded by endoneurium (called fascicles – see Fig. 2.7).

This fascicular organisation has a somatotopic basis – many of the axons in a particular fascicle innervate a single region of tissue [18]. Moving distally along the nerve, fascicles merge and separate and this somatotopic arrangement becomes more pronounced [18]. Parts of the nerve branch off and then further subdivide in a tree-like fashion to innervate various receptors as well as carrying efferent signals to the muscles [18]. The typical map-

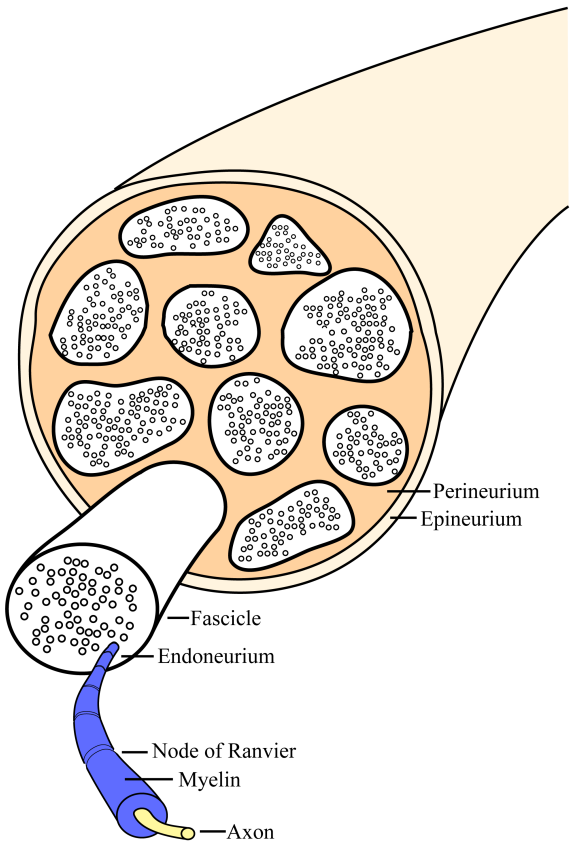


Figure 2.7: Cross-section of a peripheral nerve showing the layers and fascicular arrangement.

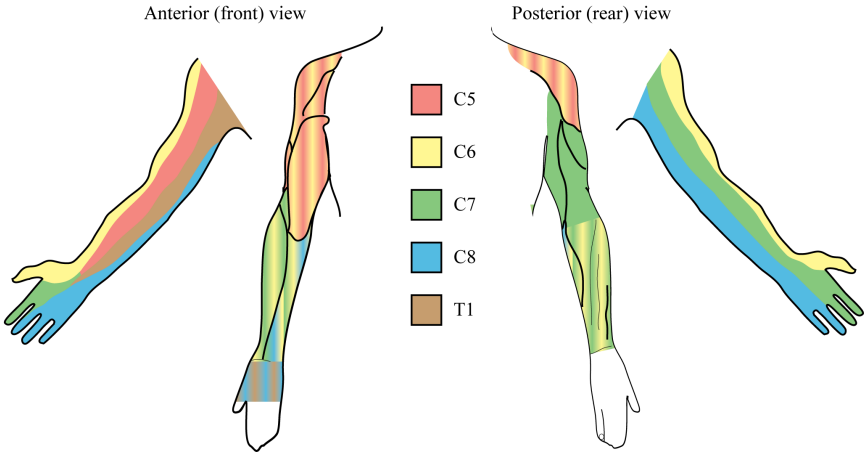


Figure 2.8: Innervation from the spinal roots: outer pictures are maps of skin innervation (dermatome) and inner are maps of muscle innervation (myotome).

ping of nerves to muscles and skin is shown in Figures. 2.8 and 2.9 for spinal roots and major arm nerves respectively; Table 2.2 lists the nerve to muscle mapping and the action of major upper limb muscles.

Table 2.2: Table of muscles in the upper limb, the actions they contribute to and the nerves that innervate them

Joint location	**Motion**	**Muscle**	**Nerve**
Wrist	extensors	extensor digitorum	Radial Nerve
		extensor carpi radialis longus	Radial Nerve
		extensor carpi radialis brevis	Radial Nerve
	flexors	flexor digitorum superficialis	Median Nerve
		flexor digitorum profundus	Median Nerve & Ulnar Nerve
		flexor carpi ulnaris	Ulnar Nerve
	abductors	extensor carpi radialis longus	Radial Nerve
		abductor pollicis longus	Radial Nerve
		extensor pollicis longus	Radial Nerve
	adductors	extensor carpi ulnaris	Radial Nerve
		flexor carpi ulnaris	Ulnar Nerve
		extensor digitorum	Radial Nerve
Elbow	extension	Triceps Long	Axillary Nerve
		Triceps Lateral	Radial Nerve
		Triceps Medial	Radial Nerve
		Anconaeus	Radial Nerve
	Flexion	Biceps Brachii Long	Musculocutaneous nerve
		Biceps Brachii Short	Musculocutaneous nerve
		Brachioradialis	Radial Nerve
		Brachialis	Musculocutaneous Nerve
	Supinators	Biceps Brachii Long	Musculocutaneous nerve
		Biceps Brachii Short	Musculocutaneous nerve
		Supinator	Radial Nerve
		Brachioradialis	Radial Nerve
	Pronators	Pronator teres humeral	Median Nerve
		Pronator teres ulnar	Median Nerve
		Pronator quadratus	Median Nerve
		Brachioradialis	Radial Nerve

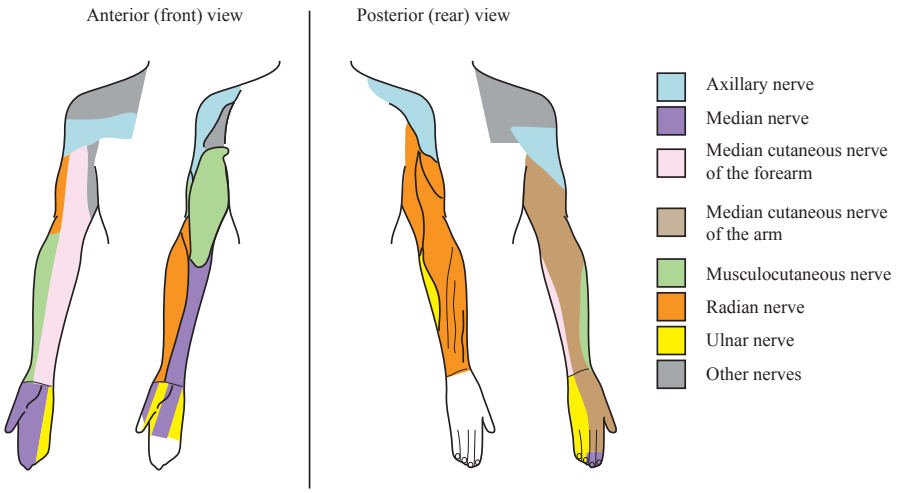


Figure 2.9: Innervation from the major nerves: outer pictures are maps of skin innervation (dermatome) and inner are maps of muscle innervation (myotome).

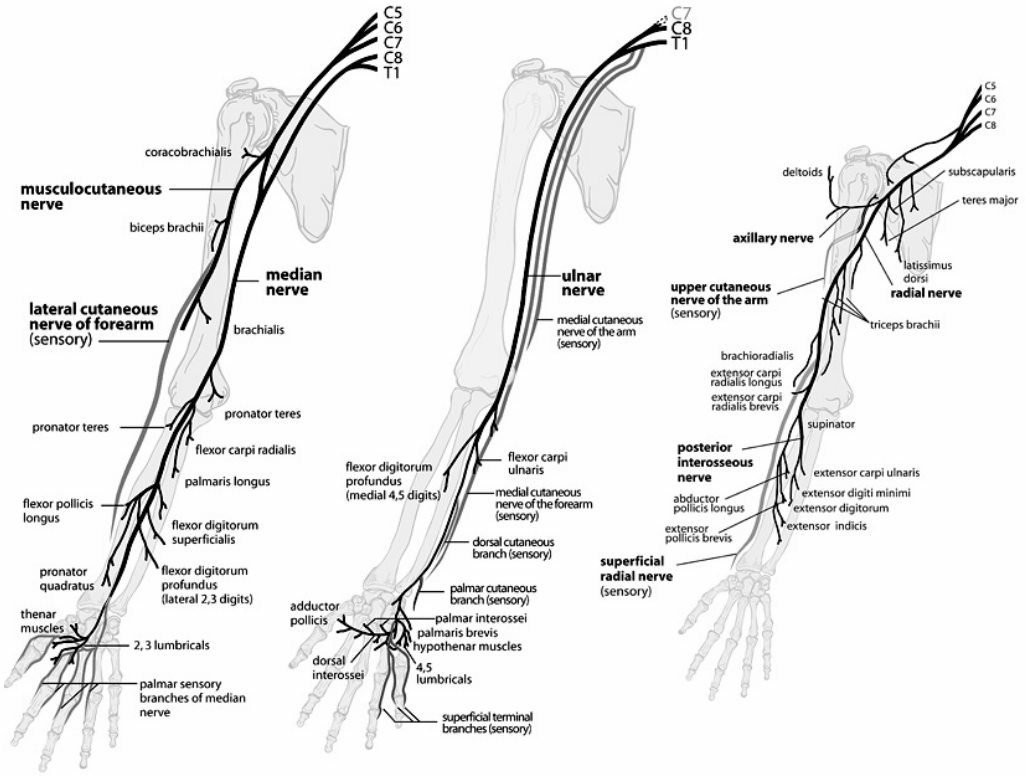


Figure 2.10: Muscle innervations of the major arm nerves (reproduced from orthopaedicsone.com).

2.2.2 Central pathway

The other bifurcation from the cell bodies in the DRG, projects into the spinal grey matter through the dorsal horn. Some axons terminate almost immediately – synapsing on alpha motoneurons and giving rise to mono-synaptic reflexes (like the tendon tap reflex), or synapsing on interneurons which integrate ascending proprioceptive afferent signals and descending efferent signals, in order to modulate motor and fusimotor activity [11]. Other

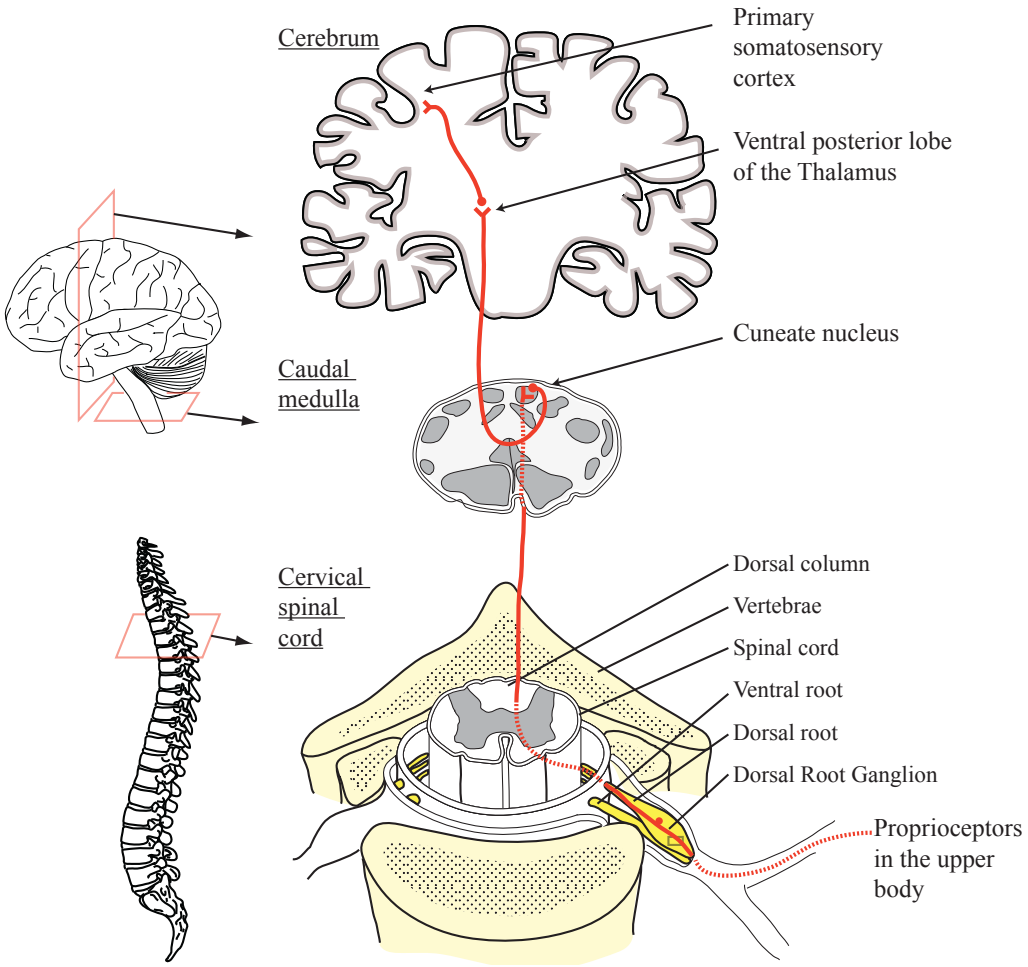


Figure 2.11: The proprioceptive neural pathway in the CNS.

axons ascend through the cuneate fasciculus of the dorsal column in the spine, before separating to either terminate in the cuneate nucleus (for conscious cerebral proprioception) or the accessory cuneate nucleus (for unconscious cerebellar proprioception) [19, 20]. Leaving the cuneate nucleus, second order neurons carrying conscious proprioceptive signals then decussate (switch sides) and travel up to terminate in the Ventral Posterior Lobe (VPL) of the thalamus [19, 20]. Third order neurons then relay the information to the primary somatosensory cortex (S1) – in particular areas 3a and 2 for signals from muscle receptors and 3b, 1 and 2 for cutaneous receptors [19, 20]. Signals are processed in S1 and transmitted elsewhere throughout the brain, of note are pathways to the primary motor cortex (M1) and the cerebellum.

From the accessory cuneate nucleus, second order neurons carrying unconscious proprioceptive signals travel through the cuneocerebellar tract to both the anterior and paramedian lobes of the cerebellum where they terminate in 2 topographic maps of the body [19, 20].

2.3 Proprioception pathophysiology following amputation

2.3.1 Neural changes

In the immediate moments after a nerve is transected during limb amputation there is a significant loss of axoplasmic fluid (of which approximately 90 % lies in the axons) [21]. This fluid is vital for the structure and function of the neurons – containing ions for neural signal generation as well as transporting proteins and neurotransmitters from the cell body to the axonal terminii [21].

The transection divides the nerve into 2 pieces, a distal part disconnected from the cell body that will degenerate, and a proximal part which will undergo a period of degeneration before attempting to regenerate. The removal of receptor endings and subsequent lack of signals from the periphery also has an immediate effect in the CNS. Synaptic connections that were previously functionally silent due to inhibition from peripheral input are unmasked, and this has the effect in the brain of increasing the size of the receptive fields of the areas surrounding the orphaned cortex [22]. This is likely to be the neuroanatomical basis of the phantom limb sensations which are experienced by nearly all amputees [22].

Over the next few weeks the cell bodies of the truncated axons will swell up and the cell nuclei will be displaced peripherally while the cells switch from manufacturing neurotransmitter molecules to manufacturing structural materials to repair and regrow the damaged axons [21]. While the cell is ramping up for regeneration, the distal axon tip dies back to the next node of Ranvier before sprouting an axonal growth cone in an attempt to reconnect with the amputated nerve and nerve ending [21].

In the months that follow, these axonal tips can grow at about 1-3 mm a day [21]. However, without target tissue to innervate or a supporting structure to grow into, they may grow in an unregulated and ineffective manner. Some will form traumatic neuromas – enlarged disorganised clusters of nerve fibres (including the nociceptive fibres that transmit pain signals) – that spontaneously fire and may produce significant pain and discomfort [21, 22]. Other axons will degenerate, demyelinate and atrophy. It is unknown what percentage of fibres are likely to survive long-term after amputation, estimates of axonal death in previous studies have ranged from 17 % to 94 % [23]. Over time, changes also take place in the orphaned cortical areas. Hebbian learning and long-term potentiation occur and new cortico-cortico projections are formed, rewiring the way the brain perceives signals from the damaged part of the body [22].

2.3.2 Phantom limb pain

Pain (or other unpleasant sensations such as itching or cramping) that is felt in the amputated part of the body is a frequent consequence of amputation. An estimated 50 - 90 % of amputees suffer at some point from this phantom limb pain and for some it may last for years [24, 25].The causes of phantom limb pain are likely to be multi-factorial. Memories of pre-amputation pain, pain from neuromas, CNS reorganisation (spinal, deep brain and cortical) and psychological factors have all been implicated [24, 25].

2.3.3 Viability for neural stimulation

Despite the high estimates of axonal death & degeneration and major plastic cortical reorganisation, neural stimulation of transected peripheral nerves has been shown to elicit the same percepts in the phantom limb as they would in intact nerves and limbs [23]. Indicating that the redundancy in the periphery is sufficient to support signal transmission and that the body map in the cortex persists.

2.4 Proprioception integration

The debate about the relative importance of the different mechanoreceptors has been rumbling on for much of the last century [1–3]. Large swings in the general consensus have occurred in that time; the current thinking is that muscle spindles are the main proprioceptor for position and motion, and that GTOs are key muscle force receptors [2, 19]. However, issues with this consensus remain, for example cutaneous proprioception has been shown to have great importance for detecting finger position and for dextrous control of the hand [26]. It has been suggested that this is a result of the long compliant tendons of the muscles controlling the fingers, or the high density of cutaneous receptors found in the hand. However, regardless of the basis, it suggests that the question of importance may not be a simple one to answer and even that the question may be largely limited to academic interest. It seems clear that the CNS is capable of integrating feedback from numerous sources (including visual) and for position much of this information comes from spindle and cutaneous receptors. Synergistic benefit arising from this integration process has also been shown [26, 27].

Integration in the CNS is believed to mainly occur in the thalamus and S1 of the cortex for conscious proprioception, and in the spinal interneurons and 2 lobes of the cerebellum for reflex and unconscious proprioception [11, 19, 20].

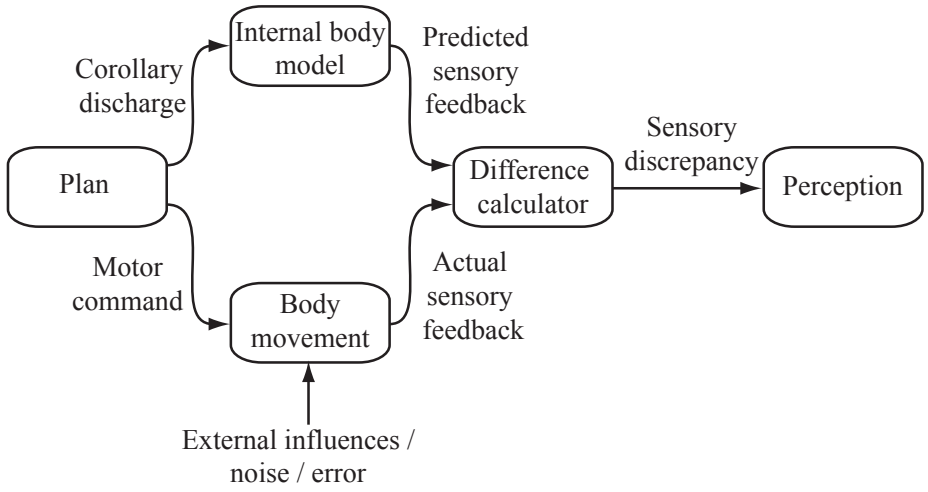


Figure 2.12: A proposed role for the descending corollary discharge is that it is used to highlight differences between expected and actual motion.

It has been suggested that it is not just the ascending feedback that these areas integrate,

but also that there is a descending "corollary discharge" that is also incorporated [2, 11]. The exact nature of this descending signal is unknown (linkages to descending motor, fusimotor or expected afferent signals have been proposed), however, the purpose of this "reafferent" signal is believed to be to highlight the differences between planned and actual motions (as indicated in Fig. 2.12) [2, 11].

The perception of force is an important example of this reafference. Despite force feedback from GTOs and cutaneous receptors, our perception of force is easily manipulated (increased) by muscle fatigue or neuromuscular neurotransmitter blocking [2]. In both these cases it is believed to be the increase in the descending motor signal required for movement that alters our perception. The rationale being that the integration of this increased descending signal (analogous to effort) with the conflicting force receptor signals gives us a combined percept somewhere between the two. Recent studies have cast some doubt on this explanation, indicating that a difference in how intrafusal and extrafusal muscle respond to neuromuscular blocking may play a significant role [2]. However, the concept of a descending corollary discharge remains an accepted part of the consensus on proprioception.

2.5 Proprioceptive performance

Several methods and measures have been proposed for quantifying human proprioceptive performance, but variation and challenges in the experimental procedure and inter-subject variation make this an elusive goal.

Experiments have shown that proprioceptive acuity and sensitivity varies significantly from subject to subject, joint to joint and across the range of motion of a joint. It has also been shown to be affected by the rate of change and differs depending on whether the limb is actively moved or passively manipulated [2, 28, 29].

Despite these challenges, numerous experiments have successfully been conducted and methods for describing performance have been identified. One common measure is known as the 'just noticeable difference' (*jnd*) – the smallest change in a parameter that is consciously perceivable. This can either be measured in absolute terms or as a fractional (or percentage) difference. The basis for this latter approach is the observation that the *jnd* between two stimuli is typically dependent on the magnitude of the stimuli, codified as 'Weber's law':

$$\frac{\Delta S}{S} = K_w$$

where S is the stimulus, ΔS is the just noticeable change in the stimulus and K_w is a constant for the stimulus type known as Weber's fraction.

For illustrative purposes, some commonly quoted figures for proprioceptive performance are shown in Table 2.3, however, as a result of the aforementioned multifactorial variation, these should be treated as approximations only. These results and others have indicated a couple of main trends: 1) that joint angle discrimination accuracy diminishes as you move from proximal to distal joints (where the impact of angular error on the endpoint location of the limb is smaller) [28]; and 2) a Weber fraction of approximately 10% for force

discrimination [29–31].

Table 2.3: Commonly quoted figures for proprioceptive acuity [29, 32].

Joint	**Position *jnd*** *	**Force *jnd*** **
Shoulder	$< 1°$	8 %
Elbow	$2°$	13 %
Wrist	$2°$	11 %

* Figures are highly dependent on angular velocity of movement
** Forces are quoted in terms of their Weber fraction .

2.6 Key unknowns

The latter third of the 20th century saw large gains in our understanding of proprioception, and this has been further built on in the intervening time. However, gaps in the detail of our understanding remain. For our purposes 4 major unknowns are: (1) the role of unconscious proprioception; (2) cerebellar and deep brain changes following amputation; (3) efferent fusimotor and corollary discharges from the brain; (4) human neural firing patterns.

2.6.1 Unconscious proprioception

The extent to which proprioception is a part of our conscious experience has been long debated. One facet of this issue is that the sensations we can consciously perceive are most conspicuous in their absence. Perhaps more important is the suspicion that unconscious proprioception may be as (or more) significant than our conscious sensations for controlling limb motion and learning new skills. Indeed it has been noted that movements by patients lacking proprioceptive feedback mimic those of patients with cerebellar damage. This debate has relevance to the field of proprioceptive prostheses because it is unclear what effect providing proprioceptive feedback to just the cortex will have, or whether the pathways between cortex and cerebellum are sufficient to overcome any problems this may introduce.

2.6.2 Cerebellar and deep brain changes post-amputation

Section 2.3.1 discussed changes in the cortex post-amputation. Less is known about how deeper brain structures and the cerebellum are affected by major limb amputation. Speculation suggests that these structures will undergo a similar process of unmasking and long term plastic change, however, the details of how this affects the various neural pathways is unknown.

2.6.3 Descending proprioceptive signals

Fusimotor signals are challenging to identify and record and much of our knowledge comes from recordings in reduced animal models. These experiments have painted a complex and

sometimes seemingly contradictory picture of how fusimotor signals are modulated during different types of motion. Even less is known about corollary discharges and together these descending signals potentially present a significant unknown for modelling muscle spindle signals and reflex proprioceptive action.

2.6.4 Human neural firing patterns

Recordings from animals are the source of much of our knowledge of receptor firing patterns. Human receptors are structurally the same and appear to fire in a qualitatively similar manner, however, little work has looked at quantitatively modelling human receptors.

2.7 Artificial Proprioceptive Feedback

"The insensate hand is blind" – a phrase coined by eminent hand surgeon Dr Erik Moberg, that neatly conveys the issues facing upper limb prosthesis users. Providing them with proprioceptive feedback is a challenge that has been under active research for at least 50 years, but a commercially viable system remains some way off.

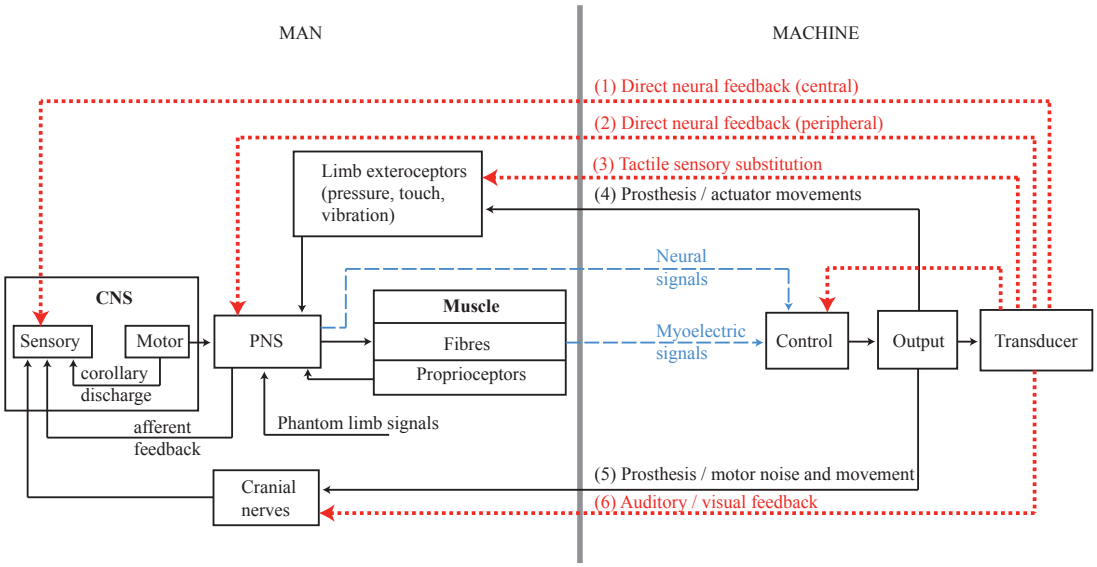


Figure 2.13: An overview of 6 possible feedback paths for prosthetic limb users (adapted from [33]). Red dotted lines indicate artificially introduced feedback, black dotted lines indicate naturally occurring feedback.

Numerous feedback modalities are possible (see Fig. 2.13 for an overview) and these fall into 3 broad categories depending on whether the feedback they provide: stimulates an unrelated sense (sensory substitution); stimulates the same sense but on a different part of the body (modality matched feedback); or stimulates the nerves (direct neural stimulation).

This section reviews the performance of previous work and looks at the opportunities and challenges each of these approaches offers.

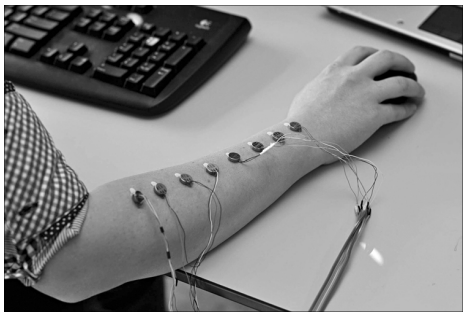
2.7.1 Sensory substitution

The provision of artificial feedback via another sensory channel (e.g. conveying limb position via auditory or visual stimulation) is commonly referred to as sensory substitution. This feedback approach has been a very active and accessible area of research and a huge range of mechanisms and modulation methods have been proposed.

The various devices and implementations created to provide sensory substitution feedback are too numerous to list, however, the two most popular mechanisms are vibrotactile and electrocutaneous stimulation.

Vibrotactile feedback

Modulating the vibration of tactors (see Fig. 2.14(a) applied to the user's skin (typically close to the point of amputation) enables information to be encoded in the vibration pattern. Receptors in the skin detect these vibrations and the pattern can be interpreted by the user to determine the state of the prosthetic limb. These days tactors are small, lightweight, non-invasive, cheap and compatible with myoelectric control systems – making them highly acceptable to users.



(a) Pancake vibration motors for vibrotactile feedback (reproduced from [34])



(b) Electrodes for applying electrocutaneous feedback (reproduced from [35])

Figure 2.14: Devices for vibrotactile and electrocutaneous feedback.

Electrocutaneous feedback

This technique works by attaching electrodes to the user's skin (see Fig. 2.14b) and passing small electric currents through them to stimulate sensory receptors or neurons near the surface. Modulation of the amplitude, frequency, pulse width and on-off keying of pulse bursts, have all been used to convey information. The user experiences it as a tactile sensation (e.g. tingle, itch, vibration, pressure, pain, etc) depending on the stimulation, electrode and skin parameters and the electrode location. Shifts in sensation are possible with small changes in these parameters which can have negative impacts for testing and user training. Electrocutaneous feedback has lower user acceptability than vibrotactile, may interfere with EMG signals, and efficacy may reduce with time due to user adaptation, however, it consumes substantially less power than vibrotactile making it more suitable for portable use.

Sensory substitution overview

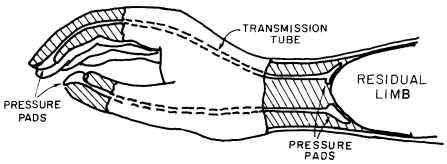
Many devices for substitutive feedback have been tried and published papers generally report some form of functional benefit in laboratory testing (typically in grasping or positioning tasks). However, none of these devices have made the leap to commercial success.

All sensory substitution provides an unnatural form of feedback that the user must consciously interpret. Use and training should improve a user's speed and accuracy at interpreting the feedback, but it remains a non-intuitive task with an associated cognitive load. As the quantity of feedback increases (e.g. due to increased degrees of freedom), so too does the load on the user who must attempt to distinguish between more variations in feedback.

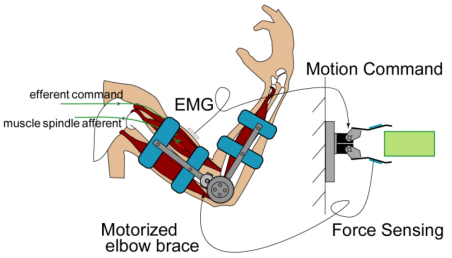
It has been speculated by several authors that the lack of commercial success is a result of this additional cognitive load these devices place on the user, especially in unconstrained real-world use.

2.7.2 Modality matched feedback

Artificial feedback that is of the same modality as the initial stimulus (e.g. pressure on the prosthesis is experienced as pressure on the user's skin) is referred to as being modality matched. This form of feedback may actually predate sensory substitution – drawings and designs from 1916 show the use of pneumatic tubes connecting prosthesis finger tips to pressure pads placed on the limb residuum (see Fig 2.15(a).



(a) A passive fingertip pressure feedback system (reproduced from [36])



(b) Feedback system applying elbow torque proportional to prosthesis grip force(reproduced from [37]

Figure 2.15: Modality matched sensory feedback systems.

Several designs for tactile systems have been proposed, but modality matched proprioceptive systems are challenging – generally requiring the displacement and disturbance of an intact joint. One such system is shown in Figure 2.15(b), linking grasp force to elbow torque. Antfolk et al. [38] also suggested the use of tendon vibration (which generates a proprioceptive illusion – see Chapter 6 for further information) as a mechanism; the absence or truncation of relevant muscles is an obstacle to this approach, but combination with Targeted Muscle Reinnervation may make this feasible.

The idea of feeding back the prosthetic limb motion and forces to intact parts of the body has previously been extensively explored for Extended Physiologic Proprioception (EPP). EPP refers to a user's ability to achieve proprioceptive knowledge of objects mechanically

linked to their body (e.g. a body powered cable and hook prosthesis). This automatically provides the user with proprioceptive feedback and has been cited as a major reason for the enduring success of body powered prostheses. Unfortunately application of this technique to modern electric prostheses that have multiple degrees of freedom and myoelectric control appears to be impractical, due to the number of joints and the method of actuation involved.

2.7.3 Direct neural stimulation

Using implanted electrodes to directly stimulate the neurons carrying sensory information, has the potential to provide modality matched and somatotopically appropriate feedback (i.e. the right sensation is felt in the appropriate part of the amputated limb) that the user can intuitively interpret.

A safe, stable, highly selective neural interface capable of selectively targeting the desired neurons remains the major challenge with this approach. However, a few groups have demonstrated the core feasibility (see Table 2.4) and one group has demonstrated functional benefit in humans [42] with as little as 2 stimulating electrodes.

The studies by Dhillon et al. [40], Horch et al. [42] and a number of other human tactile sensory feedback experiments [46, 47] share a common heritage that is clear in the similarity of their approach – which focuses on grasping in the hand, implantation in the median nerve, and use of similar electrodes & stimulation patterns. However, the approach converged on in these studies is not the only possible one and the field may benefit from a re-evaluation of the underpinning choices and assumptions.

Animal experiments targeting proprioceptive feedback have also been attempted (see latter half of Table 2.4) with some apparent success, although significant uncertainty about the sensations elicited remains.

2.8 Summary

This chapter has provided an overview of proprioceptive function for the human upper limb. Neural signals from receptors have been traced back from their origins in skin, muscle and joints back to primary areas for proprioceptive processing in the spine, cortex and cerebellum.

Understanding the receptor function and the pathways is a crucial element for the design and planning of a high performing proprioceptive prosthesis. Several significant unknowns persist and any proprioceptive prosthesis will need to work around the limitations these present.

Previous attempts at providing proprioceptive feedback were identified along with the limitations and challenges each presents. Of these, direct neural feedback presents the greatest opportunities and as such is the preferred technique for the remainder of this thesis. However, this is an area that has been relatively little studied, likely as a result of the difficulties interpreting the results of animal testing as well as the safety, ethics and relative paucity of suitable subjects for human testing.

The next chapter will look at how the physiology presented here and the aforementioned

Table 2.4: Comparison of previous human and animal experiments using neural stimulation to induce proprioceptive sensation

	Year	Implant site(s)	Electrode type(s)	Channels implanted	Channels used	Subjects	Comment
Clippinger et Al[39]	1973	Median	Cuff	1	1	15 amputees	Some proprioceptive sensations of hand (especially finger) movement elicited. Strong parasthesia present
Dhillon et al. [40]	2005	Median	LIFE	8	4 – 8	8 amputees	Consistent, graded finger flexion position and motion sensations reported. Sensation of thumb and finger moving in pincer grip motion also noted.
Gasson et al. [41]	2005	Median	Micro-electrode array	20	Unknown	1 healthy	Control of grasp force improved with time
Horch et al. [42]	2011	Median, ulnar	LIFE	Unknown	2	2 amputees	Subject 1 had 2 tactile channels. Subject 2 had 1 tactile and 1 proprioceptive. In object discrimination tests, subject 1 performed no better than chance, while subject 2 performed significantly better (pj0.0005)
Tan et al. [43]	2013	Medial	FINE and cuff	20	19	1 amputee	No information other than proprioceptive sensations elicited.
London et al. [44]	2008	Cortex (S1 area 3a)	Tungsten or Pt-Ir micro-electrodes	Unknown	Unknown	1 monkey	Animal was able to distinguish between 2 stimulation frequencies (and absence of stimulation) applied in the cortex.
Weber et al. [45]	2011	DRG	Micro-electrode array	16 – 50	16 – 50	4 cats	Artificial stimulation patterns created cortical neural patterns strongly correlated with movements.
Weber et al. [45]	2011	Cortex	Micro-electrode array	96	96	1 monkey	Animal was able to recognise the onset of stimulation and associate it with a movement task

limitations shape proprioceptive prosthesis design decisions. A target top level system design will be proposed and this will help identify areas where improvements are required and effort should be focused.

Bibliography

[1] S. C. Gandevia and D. Burke. "Does the nervous system depend on kinesthetic information to control natural limb movements?" *Behavioral and Brain Sciences* 15 (1992), p. 19.

[2] U. Proske and S. C. Gandevia. "The Proprioceptive Senses: Their Roles in Signaling Body Shape, Body Position and Movement, and Muscle Force". *Physiological Reviews* 92 (2012), pp. 1651–1697.

[3] P. B. C. Matthews. "Evolving views on the internal operation and functional role of the muscle spindle." *The Journal of physiology* 320 (1981), p. 1.

[4] J. H. B. (ed.) *Neuroscience Online: An Electronic Textbook for the Neurosciences.* 1997.

[5] E. Hagert. "Proprioception of the Wrist Joint: A Review of Current Concepts and Possible Implications on the Rehabilitation of the Wrist". *Journal of Hand Therapy* 23 (2010), pp. 2–17.

[6] A. Siegel and H. N. Sapru. *Essential neuroscience.* 2nd ed. Lippincott Williams and Wilkins, 2010.

[7] M. Bear, B. Connors, and M. Paradiso. *Neuroscience:* Neuroscience: Exploring the Brain. Lippincott Williams & Wilkins. ISBN: 9780781760034.

[8] M. P. Mileusnic, I. E. Brown, N. Lan, and G. E. Loeb. "Mathematical Models of Proprioceptors. I. Control and Transduction in the Muscle Spindle". *Journal of Neurophysiology* 96 (2006), pp. 1772–1788.

[9] U. Proske. "The mammalian muscle spindle". *Physiology* 12 (1997), pp. 37–42.

[10] V. G. Macefield. "Physiological characteristics of low-threshold mechanoreceptors in joints, muscle and skin in human subjects". *Clinical and Experimental Pharmacology and Physiology* 32 (2005), pp. 135–144.

[11] U. Windhorst. "Muscle proprioceptive feedback and spinal networks". *Brain research bulletin* 73 (2007), pp. 155–202.

[12] L. Jami. "Golgi Tendon Organs in Mammalian Skeletal Muscle: Functional Properties and Central Actions". *Physiological Reviews* 72 (1992), pp. 623–666.

[13] M. P. Mileusnic, I. E. Brown, N. Lan, and G. E. Loeb. "Mathematical Models of Proprioceptors. II. Structure and Function of the Golgi Tendon Organ". *Journal of Neurophysiology* 96 (2006), pp. 1789–1802.

[14] B. B. Edin. "Quantitative Analyses of Dynamic Strain Sensitivity in Human Skin Mechanoreceptors". *Journal of Neurophysiology* 92 (2004), pp. 3233–3243.

[15] B. B. Edin. “Cutaneous afferents provide information about knee joint movements in humans”. *The Journal of physiology* 531 (2001), pp. 289–297.

[16] B. B. Edin and J. H. Abbs. “Finger Movement Responses of Cutaneous Mechanoreceptors in the Dorsal Skin of the Human Hand”. *Journal of Neurophysiology* 65 (1991), pp. 657–670.

[17] W. R. Ferrell and A. Smith. “The effect of digital nerve block on position sense at the proximal interphalangeal joint of the human index finger”. *Brain research* 425 (1987), pp. 369–371.

[18] J. D. Stewart. “Peripheral nerve fascicles: anatomy and clinical relevance”. *Muscle & nerve* 28 (2003), pp. 525–541.

[19] D. J. Weber, R. Friesen, and L. E. Miller. “Interfacing the Somatosensory System to Restore Touch and Proprioception: Essential Considerations”. *Journal of Motor Behavior* 44 (2012), pp. 403–418.

[20] O. Arslan. *Neuroanatomical Basis of Clinical Neurology*. Taylor & Francis, 2001.

[21] C. Cooper. *Fundamentals of Hand Therapy: Clinical Reasoning and Treatment Guidelines for Common Diagnoses of the Upper Extremity*. Mosby Elsevier, 2007.

[22] G. Di Pino, E. Guglielmelli, and P. Rossini. “Neuroplasticity in amputees: main implications on bidirectional interfacing of cybernetic hand prostheses”. *Progress in neurobiology* 88 (2009), pp. 114–126.

[23] G. S. Dhillon, S. M. Lawrence, D. T. Hutchinson, and K. W. Horch. “Residual Function in Peripheral Nerve Stumps of Amputees: Implications for Neural Control of Artificial Limbs”. *The Journal of Hand Surgery* 29A (2004), pp. 605–615.

[24] S. Bach, M. F. Noreng, and N. U. Tjellden. “Phantom limb pain in amputees during the first 12 months following limb amputation, after preoperative lumbar epidural blockade”. *Pain* 33 (1988), pp. 297–301.

[25] H. Flor. “Phantom-limb pain: characteristics, causes, and treatment”. *The Lancet Neurology* 1 (2002), pp. 182–189.

[26] D. F. Collins, K. M. Refshauge, G. Todd, and S. C. Gandevia. “Cutaneous receptors contribute to kinesthesia at the index finger, elbow, and knee”. *Journal of Neurophysiology* 94 (2005), pp. 1699–1706.

[27] J.-M. Aimonetti, V. Hospod, J.-P. Roll, and E. Ribot-Ciscar. “Cutaneous afferents provide a neuronal population vector that encodes the orientation of human ankle movements”. *The Journal of physiology* 580 (2007), pp. 649–658.

[28] L. A. Hall and D. McCloskey. “Detections of movements imposed on finger, elbow and shoulder joints.” *The journal of physiology* 335.1 (1983), pp. 519–533.

[29] H. Z. Tan, M. A. Srinivasan, B. Eberman, and B. Cheng. “Human factors for the design of force-reflecting haptic interfaces”. *Dynamic Systems and Control* 55 (1994), pp. 353–359.

[30] H. Z. Tan, X. D. Pang, and N. I. Durlach. “Manual resolution of length, force, and compliance”. *Advances in Robotics* 42 (1992), pp. 13–18.

[31] L. A. Jones et al. “Matching forces: constant errors and differential thresholds”. *Perception* 18.5 (1989), pp. 681–687.

[32] S. Feyzabadi, S. Straube, M. Folgheraiter, E. Kirchner, S. Kim, and J. Albiez. “Human Force Discrimination During Active Arm Motion for Force Feedback Design” (2013).

[33] P. Herberts and L. Korner. “Ideas on sensory feedback in hand prostheses”. *Prosthetics and orthotics international* 3.3 (1979), pp. 157–162.

[34] H. J. Witteveen, L. de Rond, J. S. Rietman, and P. H. Veltink. “Hand-opening feedback for myoelectric forearm prostheses: Performance in virtual grasping tasks influenced by different levels of distraction”. *Journal of rehabilitation research and development* 49.10 (2012), pp. 1517–1526.

[35] P. Steenbergen, J. R. Buitenweg, J. Trojan, B. Klaassen, and P. H. Veltink. “Subject-level differences in reported locations of cutaneous tactile and nociceptive stimuli”. *Frontiers in Human Neuroscience* 6.325 (2012). ISSN: 1662-5161.

[36] D. S. Childress. “Closed-loop control in prosthetic systems: Historical perspective”. *Annals of biomedical engineering* 8.4 (1980), pp. 293–303.

[37] R. B. Gillespie, J. L. Contreras-Vidal, P. A. Shewokis, M. K. O’Malley, J. D. Brown, H. Agashe, R. Gentili, and A. Davis. “Toward improved sensorimotor integration and learning using upper-limb prosthetic devices”. *Engineering in Medicine and Biology Society (EMBC), 2010 Annual International Conference of the IEEE*. IEEE. 2010, pp. 5077–5080.

[38] C. Antfolk, M. D’Alonzo, B. Rosen, G. Lundborg, F. Sebelius, and C. Cipriani. “Sensory feedback in upper limb prosthetics” (2013).

[39] F. W. Clippinger, R. Avery, and B. R. Titus. “A sensory feedback system for an upper-limb amputation prosthesis.” *Bulletin of prosthetics research* (1973), pp. 247–258.

[40] G. Dhillon, T. Kruger, J. Sandhu, and K. Horch. “Effects of short-term training on sensory and motor function in severed nerves of long-term human amputees”. *Journal of neurophysiology* 93.5 (2005), pp. 2625–2633.

[41] M. Gasson, B. Hutt, I. Goodhew, P. Kyberd, and K. Warwick. “Invasive neural prosthesis for neural signal detection and nerve stimulation”. *International Journal Of Adaptive Control And Signal Processing* 19 (2005), pp. 365–375.

[42] K. Horch, S. Meek, T. G. Taylor, and D. T. Hutchinson. “Object discrimination with an artificial hand using electrical stimulation of peripheral tactile and proprioceptive pathways with intrafascicular electrodes”. *Neural Systems and Rehabilitation Engineering, IEEE Transactions on* 19.5 (2011), pp. 483–489.

[43] D. Tan, M. Schiefer, M. W. Keith, R. Anderson, and D. J. Tyler. “Stability and selectivity of a chronic, multi-contact cuff electrode for sensory stimulation in a human amputee”. *Neural Engineering (NER), 2013 6th International IEEE/EMBS Conference on*. IEEE. 2013, pp. 859–862.

[44] B. M. London, L. R. Jordan, C. R. Jackson, and L. E. Miller. “Electrical stimulation of the proprioceptive cortex (area 3a) used to instruct a behaving monkey”. *Neural Systems and Rehabilitation Engineering, IEEE Transactions on* 16 (2008), pp. 32–36.

[45] D. J. Weber, B. M. London, J. A. Hokanson, C. A. Ayers, R. A. Gaunt, R. R. Torres, B. Zaaimi, and L. E. Miller. “Limb-state information encoded by peripheral and central somatosensory neurons: implications for an afferent interface”. *Neural Systems and Rehabilitation Engineering, IEEE Transactions on* 19 (2011), pp. 501–513.

[46] P. M. Rossini, S. Micera, A. Benvenuto, J. Carpaneto, G. Cavallo, L. Citi, C. Cipriani, L. Denaro, V. Denaro, G. Di Pino, et al. “Double nerve intraneural interface implant on a human amputee for robotic hand control”. *Clinical neurophysiology* 121 (2010), pp. 777–783.

[47] S. Raspopovic, M. Capogrosso, F. M. Petrini, M. Bonizzato, J. Rigosa, G. Di Pino, J. Carpaneto, M. Controzzi, T. Boretius, E. Fernandez, et al. “Restoring natural sensory feedback in real-time bidirectional hand prostheses”. *Science translational medicine* 6 (2014), 222ra19–222ra19.

3 Design of a Proprioceptive Neural Prosthesis

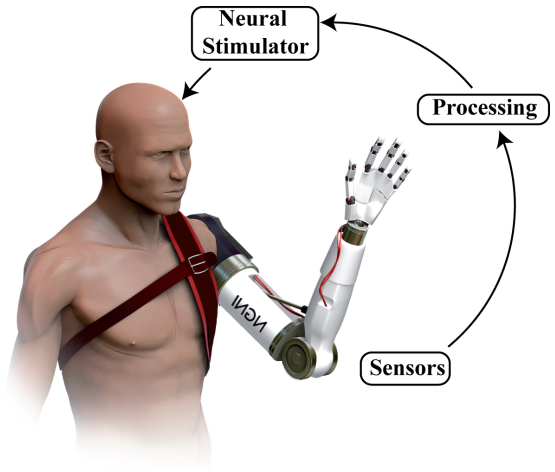


Figure 3.1: Generic concept of a proprioceptive prosthesis.

Figure 3.1 shows a generic breakdown of a proprioceptive neural prosthesis into sensors, processing and neural stimulation. These can be further subdivided and numerous options exist for each aspect of the system. Chapter 2 identified a strong commonality in previous human proprioceptive neural prosthesis research. However, other approaches are possible and a number of concept review papers have been published suggesting alternatives.

3.0.1 Previous reviews

A search of the literature identified 3 publications that reviewed previous work in the design of a proprioceptive neural prosthesis, made recommendations and proposed directions for future research [1–3]. A further 9 reviews of artificial sensory feedback were identified that considered neural interfaces in passing but that did not provide significant recommendations specific to this topic [4–12]. It is perhaps interesting to note that although these papers cover a span of 35 years, the majority (2 of 3 and 5 of 9 respectively) were published within the last 3 years – possibly indicative of a significant increase in research interest in this area.

Parts of this chapter have been previously published in:

- S. Luan, I. Williams, T. G. Constandinou, and K. Nikolic. "Neuromodulation: present and emerging methods". *Frontiers in Neuroengineering* 7 (2014), p. 27

All of the papers focused on sensory feedback for the upper limb and considered electrical stimulation in the PNS as an option for providing this feedback (with nearly all identifying electrodes and the neural interface as a key issue). Stimulation in the brain as a feedback path does not appear in the reviews (even speculatively) prior to 2007, but is often a feature of later reviews – likely as a result of animal experimentation demonstrating the concept feasibility in the 2000s [13, 14].

In 1999, Riso [1] published the first of the focused neural prosthesis papers identified here. This paper proposes muscle spindles as the target receptor for proprioceptive feedback, identifies candidate electrodes and that research is required to develop interfaces for single neuron activation. It also proposes a prototype system for a prosthetic hand with: Hall-effect / fibre-optic sensors in the finger joints to determine finger angles, an external microprocessor for signal encoding, a transcutaneous wireless link for power and data, and an electronic micro-electrode interface with a sensory nerve.

Over a decade went by before the next focused review was published. However, it was a decade in which important feasibility work was carried out both in animals and in humans [15–18]. In 2011, Hsiao, Fettiplace, and Darbandi [2] published their review, which drew substantially different conclusions to Riso's. The review identifies SA2 cutaneous afferents as being the key receptor to convey joint angle (although it notes that muscle spindle afferents must also be stimulated with the SA2 afferents in a coordinated fashion). The review suggests that there is currently insufficient understanding of joint angle coding in the PNS and therefore proposes that stimulation in the brain is a more reasonable candidate. Hsiao, Fettiplace, and Darbandi [2] go on to consider the pathway the proprioceptive feedback takes through the CNS and identify area 3a of primary somatosensory cortex as the prime candidate for a neural interface. Finally the review addresses the issue of feedback encoding and suggests that mimicking the natural neural code should be the preferred approach – on the basis of its success in cochlear implants.

Then in 2012, Weber, Friesen, and Miller [3] published the most recent of the focused reviews identified. The review considers various possible stimulation sites in the PNS and CNS (identifying the PNS as the low risk approach and muscle spindles as the primary receptor for position and motion) and looks at electrode technology for these sites. It then goes on to look at lessons from the development of other neural prostheses and concludes that peripheral interfaces offer a higher chance of success in the near time noting that it is possible that "the central representation is simply too complex and high order to be evoked by electrical stimulation". The review identifies a number of knowledge gaps (1 – 3 below) and technology gaps (4 – 6) that should be addressed to help create a proprioceptive prosthesis, including: 1) greater understanding of the higher order neural representation of proprioception; 2) understanding the impact of feedback loops on prosthetic limb control; 3) understanding the role of proprioceptive feedback in motor learning and modulating motor cortical neuron output; 4) developing neural interface technology for selective activation of homogenous nerve fibres; 5) determining the number of stimulation channels necessary for sufficient feedback; and 6) developing low power implants with wireless transcutaneous links. Finally the review identifies the impracticality of evaluating sensory feedback inter-

faces in humans (due to surgical issues and the non-availability of suitable patients), while also discussing the many challenges faced in performing animal experimentation for this purpose.

There are common themes running through the focused reviews – such as a need for an improved neural interface and neural stimulation patterns – however, there were fundamental disagreements about whether the CNS or PNS represented the best candidate for implantation and which the best receptors to target are. There was also an unstated assumption that electrical neural stimulation would be used (although the potential of optogenetics to replace this in the near [2] or long [3] term was raised). The requirements and feasibility of the sensors, processing and stimulator design also were largely unaddressed.

3.0.2 Chapter content

This chapter takes a fresh look at the options and assumptions underpinning the design of a proprioceptive prosthesis – addressing areas not covered in previous reviews and providing new perspective on areas of disagreement. It aims to provide a structured approach to making more detailed system design choices, reviews the decisions of previous relevant work, and ultimately proposes a prototype system in order to identify areas requiring further development work.

Underlying these design choices are a number of assumed constraints and guiding principles, including that:

- safe operation is the number one priority;
- a low risk design that is achievable in the near term is preferable;
- the feedback should be as intuitive as possible;
- the feedback should cover all aspects of human limb proprioception – position, motion and force;
- the assumed target system performance is normal human proprioceptive capability;
- the system should be suitable for portable, chronic use.

The proposed process for addressing the system design choices is shown in Fig. 3.2; it is designed as a logical progression based on the dependencies of each stage, however, it is only one of the many possible ways of approaching the design challenge. The remainder of the chapter is structured along the lines of this diagram and presents a range of options for each stage. Where necessary preferred approaches or technologies are chosen to limit the range of options that must be considered by later dependent sections (e.g. an implant site is chosen and so only neuromodulation methods and stimulation patterns suitable for that site are considered).

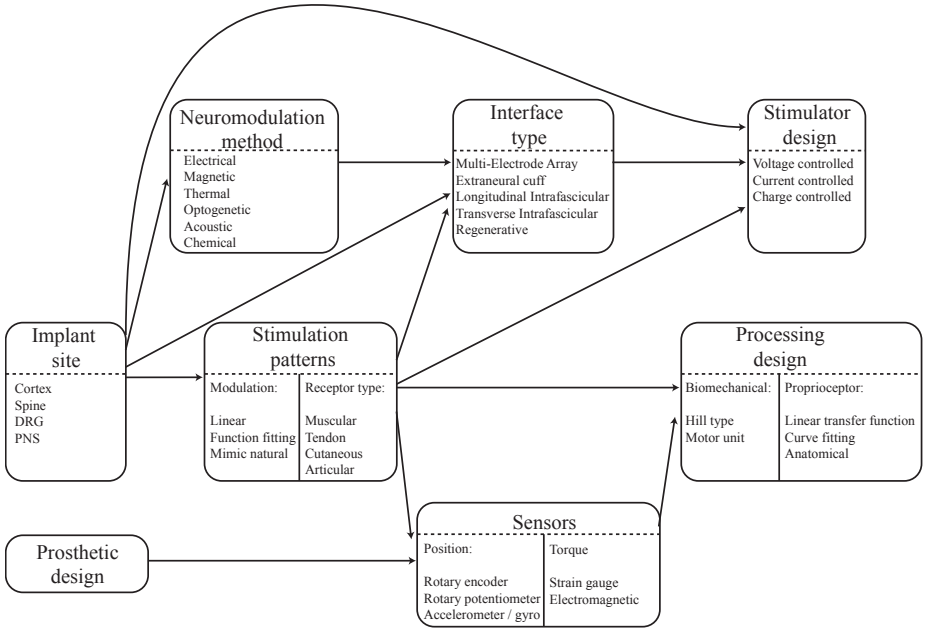


Figure 3.2: The proposed system design process with arrows showing dependencies. Below each headline is an overview of the choices discussed in this chapter.

3.1 Implant Site

Choice of stimulation site has major implications for just about every aspect of the design. It determines the types and numbers of neurons present, the characteristics of the surrounding tissue and the nature of the neural signals present. There are a continuous range of possible sites following the neural pathway from near the point of amputation to the terminii in the Central Nervous System (CNS), however, in previous proprioceptive feedback work and animal studies the stimulation site has fallen into 4 discrete categories: (1) the cortex, (2) the spine, (3) the Dorsal Root Ganglion (DRG), and (4) the Peripheral Nervous System (PNS) [15–17, 19–21]. There are numerous considerations for assessing each of these sections; only the key advantages and disadvantages will be presented below, along with a brief discussion of previously proposed systems for each site.

3.1.1 The brain

Deep brain structures and the cerebellar lobes associated with proprioception have seen little interest as targets for proprioceptive implants, likely as a result of surgical risk in accessing them and because of the difficulty of achieving effects with unconscious proprioception (where the patient cannot provide information on what sensations any stimulation are evoking). However, the primary somatosensory cortex (S1) has been investigated for proprioceptive feedback in several animal experiments [19, 22, 23].

Previously proposed approaches for a cortical proprioceptive prosthesis have suggested implantation of a Micro-Electrode Array (MEA) with a large number of electrodes in Brodmann area 3a of S1 [2, 21]. This approach has been preliminarily demonstrated in a monkey and indicated that variable sensation could be evoked that the monkey could

interpret. The requirements for achieving effect in this part of the body include the need for neuromodulation at various depths, as this area of the cortex is layered – i.e. the perceived location and type of percept evoked, changes with depth. There is a separation in S1 of cutaneous feedback from muscular which is potentially a major benefit and this area brings together proprioception from all four limbs in a relatively small region – enabling a low number of implanted neural stimulators to feasibly generate all the necessary percepts for a prosthetic limb. The other implication of this is that the neuromodulation will need to be highly selective and stable otherwise unwanted percepts will be evoked in intact parts of the body.

Experiments have shown that electrodes implanted in this region can generate the desired sensations of position, motion and effort. However, the somatotopic map (i.e. how sensation in the body maps to the cortical surface) in this area is poorly understood and little is known about how to modulate the stimulation patterns to provide graded sensations. In addition, the location of area 3a, at the bottom of the central sulcus of the brain, makes it a challenging implant location from a surgical perspective.

3.1.2 The spine

Intraspinal microstimulation has been proposed for functional neural prostheses (i.e. stimulating muscles), but stimulation of the dorsal spinocerebellar tract has received relatively little attention as a site for a proprioceptive implant. Similarities with the cortex (e.g. the high density of neurons present, the depth organisation of the axons, the isolation of muscular feedback and the potential for serious complications) means that it shares many of the advantages and disadvantages of a cortical implant. However, there are 2 main advantages over a cortical implant: firstly that a significant number of the axons are first order neurons (i.e. they are the axons of the receptors that initiated the action potentials) carrying well understood signals from proprioceptive receptors; and secondly that stimulation in the spine would potentially be received in the cerebellum for use in unconscious proprioception. In contrast a major challenge will be electrode stability, which is exacerbated (compared to the cortex) by the mobile nature of the spine.

3.1.3 The DRG

At the crux between the PNS and the CNS, Dorsal Root Ganglions (DRGs) possess some of the attractive qualities of both domains from a stimulation perspective. They offer an almost optimal concentration of neurons from a single limb, however, there is no separation of proprioceptive feedback from exteroceptive which means that an implant at this site may need to be more selective than cortical or spinal implants (although the risk of stimulating undesirable areas and the risk of implantation damage should be lower). Given their location next to the spine, they may also represent a lower surgical risk than a cortical or spinal implant. However, a review of the literature did not identify any instances of neural implants being inserted in human DRGs and as such the best surgical approachand the implant stability remain major unknowns. There is also no clear organisation and the fact

that cell bodies (rather than axons) will be stimulated may require slightly different design choices.

3.1.4 The PNS

Stimulating in the PNS has been demonstrated providing proprioceptive feedback in amputees in several separate studies and due to the low surgical risk has also been attempted in healthy volunteers [15–17, 24, 25]. These studies have shown that the full range of proprioceptive percepts can be stably elicited in the periphery. Numerous experiments have also demonstrated the chronic stability and effectiveness of extraneural cuff-type electrodes, although electrodes that penetrate the epineurium are often preferred for acute studies due to the greater selectivity possible [15, 16, 26].

There are however, a couple of disadvantages to a PNS implant: firstly the intermingling of exteroceptive sensory, proprioceptive sensory and motor nerves makes stimulating one type without the other a major challenge; and secondly the more diffuse nature of the sensory neurons – which means that multiple discrete sets of electrodes would need to be implanted to provide feedback from a prosthesis. Despite these disadvantages, previous successful work with implants in the PNS mean that they are considered the most mature and lowest risk approach [18, 20, 26, 27].

3.1.5 Overview

Table 3.1 shows a subjective assessment of the advantages and disadvantages of the various implant sites considered here. It indicates a preference for an interface in the PNS or DRG (in agreement with Weber, Friesen, and Miller [3]) and a PNS implant fits well with the design guidelines emphasising low risk and safety. In subsequent analysis it will therefore be assumed that the neural interface is in the PNS.

Table 3.1: Implant site comparison

	PNS	**DRGs**	**Spine**	**Cortex**
Modulation*	++	++	+	- -
Specificity**	+	-	-	- -
Surgical risk	++	-	- -	- -
Spatial distribution***	-	++	++	+
Key challenges	High number of tactile and motor neurons present. Multiple implants required	Surgical risk & number of neurons present	Surgical risk, safety & modulation of signal by spinal interneurons	Surgical risk, limb representation & somatotopic map poorly understood.

* Modulation – represents whether the relationship between limb state and neural signals is clear.
** Specificity – represents how difficult it is to modulate a specific sensation.
*** Spatial distribution – a measure of how physically diffuse the target neurons are, with implications for how many implants will be required.

3.2 Neural feedback

> *Intuitive – using or based on what one feels to be true even without conscious reasoning; instinctive.*

Providing intuitive feedback which is familiar or trivially easy to interpret is the ultimate goal for any neural prosthesis. Previous research stimulating proprioceptive neurons has focused on simple graded modulation of the stimulation frequency (and hence action potential firing rate), e.g. a simple relationship between a joint angle and the rate of stimulation [15–17, 25]. More recently Weber et al. [22] recorded a set of proprioceptive neural firing patterns, fitted functions linking limb movement to these patterns (using regression) and then used these functions to create artificial patterns that when stimulated appeared to generate the appropriate percepts of motion (based on recordings of cortical neural patterns).

Although intended as an experimental investigation (and indicative of the challenges faced when conducting sensory research on animals), the approach of Weber et al. [22] has potential wider application for providing feedback and the advantage that it is indifferent to the type of receptors that have been interfaced with. However, it has limitations as well: for many amputees it may well be impossible to obtain recordings of their limb functioning normally prior to amputation; and the receptor recordings are only valid for the range of positions, rates of movement and forces exerted during the training phase, (extrapolation outside these ranges may not be appropriate to producing intuitive feedback) and the appropriateness of the feedback is dependent on high electrode stability.

This progression, from simple graded stimulation to systems of modulation that mimic natural patterns, is one that has also been evident in the development of cochlear and retinal prostheses. The brain's ability to adapt and learn is impressive, but it seems that fitting in with its pre-existing neural processing offers the best performance.

An alternative approach is preferred here – one that takes this progression to its logical conclusion and aims to mimic as closely as possible the neural firing patterns of certain receptors in select muscles / segments of the body. If the correct neurons can then be interfaced with, then the feedback provided should be as intuitive as possible. However, to achieve this, it is necessary to map the position, motion and forces experienced by the prosthesis onto a model of the human limb, and this must be combined with high quality models of tissue deformation and receptor firing patterns. It is an approach that potentially requires modelling of all factors that significantly affect the receptor firing patterns and this may make the system computationally demanding – an issue that requires further investigation.

3.2.1 Mapping prosthetic state to a human model

Prosthetic limb properties can differ substantially from those of a human limb. For the purposes of this mapping the differences between the human and prosthesis can be grouped into 3 main categories: 1) physical properties – weight, moments of inertia, size and shape (including for instance the number of digits); 2) actuation properties – strength, speed, joint

coupling and actuator non-linearities; 3) kinematic properties – degrees of freedom, range of motion, axis of rotation and joint structure (including for instance joint complexes).

These differences were most evident in the days when cable and hook prostheses dominated the market. However, under the twin pressures of prosthesis users' desire for cosmesis and functionality (in a world of tools and equipment designed to be operated by the human hand), there has been a strong trend towards anthropomorphic convergence. Commercially available prostheses such as the i-Limb (or soon to be available DEKA arm), clearly demonstrate the progress that has been made towards approximating the human upper limb. Even the rise in underactuation for finger joints – which was largely driven by actuator weight considerations – moves prosthetics closer to the human form and with anthropomorphic design as a guiding principle, it is a trend that looks set to continue.

This has important implications because the closer the match between prosthetic limbs and human limbs, the easier the process of mapping the state of one to the other becomes. However, a perfect match is both an unlikely aspiration and a potentially unnecessary target. Around 0.1 - 0.2% of people are born with some form of upper limb dysmorphism and for these people functional usefulness and treatment aims are not dependent on mimicking normal upper limb characteristics [28, 29]. While minimising prosthetic dysmorphism is desirable, it seems reasonable to accept that some will exist for the foreseeable future and should not be an insurmountable obstacle for the user.

3.2.2 Nerve receptor selection

Proprioceptive receptors (as discussed in Chapter 2) vary in how much proprioceptive information they provide to the CNS, how well the receptor firing patterns are understood and how well the underlying tissue deformation can be modelled.

Table 3.2: A subjective review of our understanding of proprioceptors

	Type	**Importance**	**Tissue model**	**Receptor model**
Articular	Ruffini like ending	- -	- -	- -
	Pacinian corpuscle	- -	- -	- -
Cutaneous	Ruffiini corpuscle	+ +	-	-
	Meissner corpuscle	+	-	-
	Pacinian corpuscle	- -	-	- -
	Merkel nerve ending	- -	-	- -
Muscular	Spindle Primary	+ +	+	+ +
	Spindle Secondary	+ +	+	+ +
	Golgi Tendon Organ	+	+	+

Ideally we would be able to model the output of any of the receptors in Table 3.2 so that appropriate stimulation could be applied to any receptors that are interfaced with. However, in a system constrained by power, portability and (as a result) complexity, it is necessary to prioritise. Table 3.2 gives an overview with a qualitative and relative assessment of how useful each of the receptors is and how well we are currently able to model them. From this table it is evident that muscle spindles and GTOs stand out as the best candidates for modelling and feedback. Together these receptors also provide feedback on

all aspects of limb proprioception – position, motion and force.

3.2.3 Neural Signal Modelling

In the human body the generation of proprioceptive neural signals is implicitly linked with musculoskeletal biomechanics as well as muscle and proprioceptor dynamics [30]. It is therefore likely that a model for generating these signals should also be based on these three factors and indeed such an approach has already been demonstrated in the field of neuro-musculoskeletal models of human motor control [31–35]. However, neuro-musculoskeletal modelling is a relatively new field and the extant models are unsuitable for this application – either due to limb coverage, computational complexity, the quality of the proprioceptor models used, or a requirement for input that is not available in this application. This is therefore an area that requires further investigation both to demonstrate feasibility and that the problem is computationally tractable in portable hardware.

3.2.4 Portable Processing

Today "portable" processing brings an implicit focus on low-power computation. Mobile power generation (e.g. solar) still yields very low power and although battery energy density is constantly improving it is still a limiting factor in device design. The meteoric rise in powerful mobile devices (smartphones and tablets) and related rise of the ARM core processor has seen processor development change from a raw speed race to focus more on performance per watt.

Improving performance and power efficiency can in part be achieved by moving to a CMOS technology with a smaller feature size, however, this approach no longer provides the improvements once associated with Dennard scaling [36]. Thermal factors, physical limits and device leakage have all contributed to this demise. These days techniques like parallel multi-core processing provide much of the speed progress and the desire for low power has driven interest in techniques like Dynamic Voltage Frequency Scaling (where power supply voltage and clock frequency are varied to trade speed against power consumption) and gating of clock and power to unused cores of the processor to reduce dynamic and static power consumption.

All of this development has resulted in microcontrollers such as the the Arm Cortex M0+ which is capable of in the order of 10,000 dMIPS/W (Dhrystone Million Instructions per Second per Watt). While impressive, these low power devices fall well short of the raw performance of desktop processors and are further limited by the resources (e.g. RAM, storage and data links) available to them, which may present significant challenges to computationally demanding biomechanical and receptor modelling.

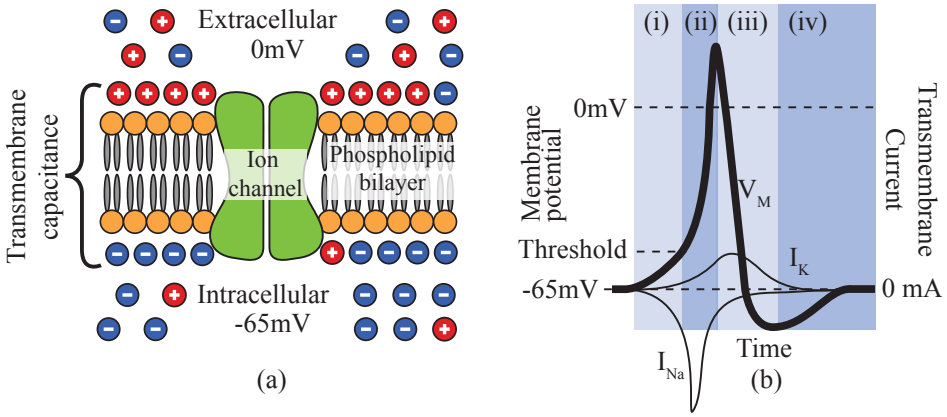


Figure 3.3: (a) – The phospholipid cell membrane, ionic charges and an ion channel. (b) – A typical action potential (i) stimulation causing depolarisation to above threshold, (ii) Na^+ channels open and Na^+ enters cell, (iii) K^+ channels are open and K^+ leaves cell, (iv) ion pumps restore resting potential.

3.3 Neuromodulation

3.3.1 Action potential generation

Neuronal cell membranes consist mainly of a phospholipid bilayer across which selective ion pumps work to create a separation of charge – ultimately resulting in a resting cell membrane polarisation where the intracellular potential is between 60–80 mV below the extracellular fluid and where the bilayer acts as the dielectric of a capacitor (Fig. 3.3).

Neural stimulation works by causing a transmembrane or axial current that depolarises part of the cell membrane. If this depolarisation reduces the transmembrane potential to a critical level (threshold), voltage gated sodium ion channels open and a positive feedback loop is created that amplifies a small depolarisation (∼15 mV) into a full reverse polarisation of the membrane (Fig. 3.3(b) and an action potential is created.

The states and dynamics of voltage gated sodium and potassium channels play major roles in neuromodulation. Each channel can be considered to have two voltage sensitive gates – an activation gate (normally closed) and an inactivation gate (normally open) – each with different opening and closing time constants and different threshold voltages triggering a change of state (as shown by the transmembrane currents (I_{Na} and I_K in Fig. 3.3(b).

3.3.2 Modulation methods

Creating an influx of current to initiate depolarisation can be achieved in a number of ways. Electrical, thermal, chemical, optogenetic and acoustic methods have all been demonstrated, This subsection (summarised from [37]) gives a brief overview of the fundamental mechanism by which they each operate, as well as key advantages and disadvantages.

Electrical stimulation

Electrical stimulation is the most mature and widely used method of stimulation and is applicable in both the CNS and PNS. It uses electrodes to apply a potential gradient across a neuron causing intracellular ionic current flow and localised depolarisation and hyperpolarisation of the cell membrane that results in neural stimulation. Applying a different potential gradient can be used to create a region of cell membrane hyperpolarisation sufficient to block action potential propagation, thereby achieving neural inhibition. More complex stimulation, inhibition and selectivity mechanisms are also possible by applying waveforms that exploit the differing time constants of the ion channels – for example anode break stimulation occurs when a long hyperpolarising (inhibitory) pulse is suddenly ceased and results from differences in the rate that the sodium activation and inactivation gates change state [38]. The use of implanted electrodes which are electrochemically active is a key disadvantage as it requires surgical implantation and leads to chronic biocompatibility concerns.

Magnetic

The mechanism for magnetic stimulation is similar to that of direct electrical stimulation, except that the potential gradients are induced in the tissue by a rapidly changing strong magnetic field (>1 T) – typically generated by discharging large capacitors through an electromagnet or via kilowatt amplifier. It is usually implemented transcutaneously (e.g. Transcranial Magnetic Stimulation (TMS)) and hence non-invasively. The removal of the biochemical issues associated with the electrode, potentially offers a major advantage over electrical stimulation, however, these devices currently offer very poor spatial selectivity, very high peak power consumption and miniaturisation of the electromagnets is only just beginning to be addressed [39]. Hand-held TMS devices have been used for neuroscience purposes and clinically for stroke and depression treatment [25].

Optogenetic

Optogenetics is a new neuromodulation technology in which light-sensitive proteins ('opsins') are genetically inserted into cell membranes or cells [40, 42]. These proteins act as light-activated ion pumps, channels or enzymes to achieve fast and precise optical manipulation of electrical and biochemical processes in cells as well as modulation of signalling cascades [43]. Optogenetics has numerous applications which are only beginning to be explored – hence its choice as "Method of the Year 2010" by Nature Methods [44]. The first and most famous of these opsins were channelrhodopsin for neural stimulation [42] and halorhodopsin for neural inhibition [41] (see Fig. 3.4). Since then a wide range of opsins with varying temporal, ionic and spectral properties have been discovered. This has combined with parallel developments in techniques for genetic manipulation and improvements in our understanding of gene expression; ultimately resulting in a tool with peerless precision for neural manipulation.

However, creating a chronic, portable implant capable of exploiting even a fraction of

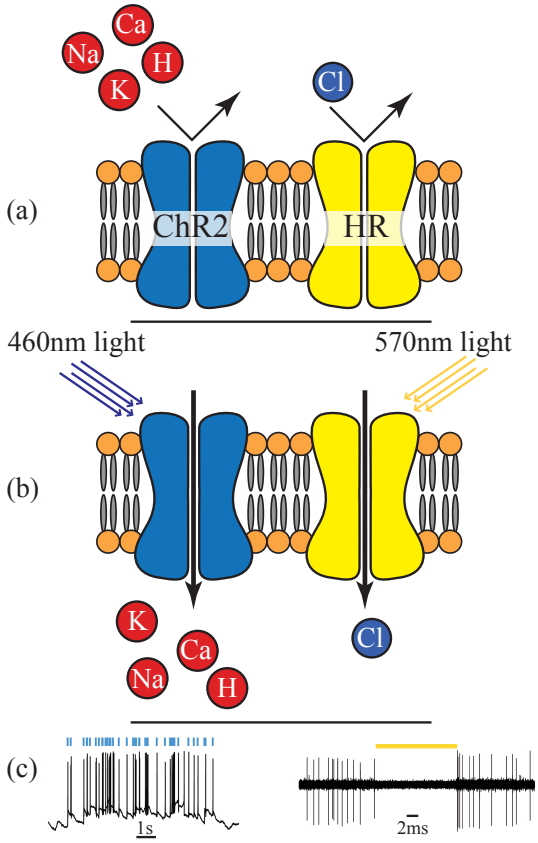


Figure 3.4: (a) – An unilluminated Channelrhodopsin-2 (ChR2) ion channel and Halorhodopsin (HR) ion pump are closed and inactive. (b) – Once exposed to specific frequencies of light, ChR2 allows certain positive ions into the cell, and HR begins to pump chloride ions in. (c) – Activation of ChR2 initiates individual action potentials, in contrast HR activation suppresses action potentials, from [40] and [41].

the potential of this technique remains an open challenge. In-vivo experimental setups to date have previously involved either benchtop lasers (coupled with fibre-optics) or transcutaneous illumination, (although McCall et al [45] recently demonstrated a promising fully wireless LED system with 25 channels). The need to genetically modify the neurons being modulated is also a major drawback both from an ethical & safety perspective and because it may prevent clinical applications in the PNS (it is unclear how quickly new ion channels would be expressed along the long axons that exist in the periphery). In summary the high precision and ability to selectively express the opsins in target neuron types makes this a highly attractive tool, but sadly one which isn't likely to be suitable for human PNS stimulation in the near term.

Thermal

Thermal modulation of neural activity is believed to result from a combination of the temperature induced changes in the transmembrane capacitance and non-uniform changes in the conductance dynamics of the various ionic channels [46].

During rapid localised heating, the capacitive effect dominates and the reduced trans-

membrane capacitance leads to ionic current flow, depolarisation and action potential initiation [46, 47]. Conversely during slow heating the changes to ionic channels dominate and in particular changes to Na^+ and K^+ activation/deactivation dynamics prevent action potential initiation and propagation [46, 48]. Thermal damage to tissue is a major issue with this method of neuromodulation, especially for suppression due to the higher temperatures and slower, more diffuse heating necessary [49].

Acoustic/Mechanical

Experiments have indicated that ultrasound waves can elicit action potentials from retinal and brain cells [50, 51]. However, very little is understood about how mechanical deformations (typically in the cell membrane) affect ion channels, membrane capacitances and neurons – although proposed mechanisms have included cavitation and thermal effects. Despite a lack of clarity on the actual mechanism, potential applications for non-invasive Deep Brain Stimulation and retinal prostheses are being investigated.

Chemical

Microfluidics can be used to control the chemical environment around a neuron, potentially changing its transmembrane or post-synaptic potential and inducing or suppressing action potential generation. Implants releasing or sequestering neurotransmitter molecules or certain ions have been demonstrated providing neuromodulatory effects [52, 53] however, achieving high temporal or spatial resolution with such systems may be challenging – depending on concentrations required to elicit effects and the dynamics of the chemical diffusion, breakdown or uptake in the tissue. It is an approach that may be suited to applications requiring a longer term effect with a wider area of effect, e.g. Deep Brain Stimulation, but is unlikely to be of use in a system where rapid modulation of action potential generation is required. Major challenges with this approach include safe chemical storage, modulation efficacy and economic manufacture.

Stimulation method choice

Due to its maturity, suitability for the PNS and proven ability to excite proprioceptive neurons, electrical neural stimulation is the preferred stimulation method and is examined in greater depth below.

3.3.3 Electrical Neural Stimulation

ENS uses electrodes to apply a potential gradient across a neuron (e.g. differing voltages at nodes V_{e1},V_{e2} and V_{e3} in Fig. 3.5(a) and (b) resulting in intracellular ionic current flow and localised depolarisation and hyperpolarisation of the cell membrane (V_{i1},V_{i2} and V_{i3} in Fig. 3.5(b) to trigger the action potential. Stimulation can be modelled using the cable model as described below.

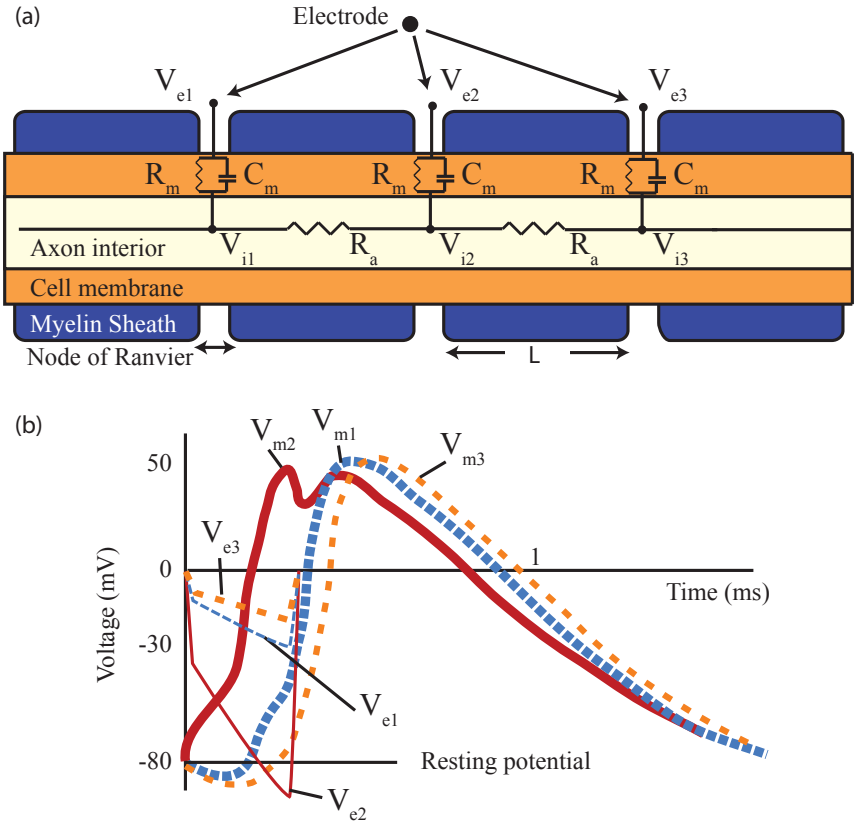


Figure 3.5: (a) – A cross-section of a myelinated nerve axon stimulated using an external electrode and an equivalent circuit model. (b) – An AP generation in the nerve: simulation on the Neuron platform for AP generation with axon diameter of 15 μm, L=1.5 mm, T=23 °C, stimulus=300 μs, stimulus current of 147 μA. Lines show the extracellular (V_m) and membrane voltage ($V_m = V_i - V_e$, V_i is intracellular voltage) at the nodes 1, 2 and 3 shown in (a) [48].

Cable model

The following cable model derivation is summarised from [54]. In the simplified cable model the cell membrane impedances are modelled as a parallel resistor (R_m) and capacitor (C_m) combination and the impedance between each two Nodes of Ranvier as a resistor (R_a). In Figure 3.5(a) $V_e(n,t)$ represents the external voltage at the nth node of Ranvier and $V_i(n,t)$ represents the external voltage at the n^{th} node at time t.

Using Kirchoff's current law at the n^{th} node [54]:

$$\frac{V_i(n-1,t)-V_i(n,t)}{R_a} + \frac{V_i(n+1,t)-V_i(n,t)}{R_a} + \frac{V_e(n,t)-V_i(n,t)}{R_m} + C_m\frac{d[V_e(n,t)-V_i(n,t)]}{dt} = 0 \qquad (3.1)$$

If we define V_m as the voltage across the membrane, i.e. $V_m = V_i - V_e$ and substitute it into Equation 3.1 we can obtain an equation solely in terms of V_m and V_e and can group the V_m and V_e terms separately:

$$\frac{V_m(n-1,t)-2V_m(n,t)+V_m(n+1,t)}{R_a} - \frac{V_m(n,t)}{R_m} - C_m\frac{d[V_m(n,t)]}{dt} + \frac{V_e(n-1,t)-V_e(n,t)+V_e(n+1,t)}{R_a} = 0 \qquad (3.2)$$

Separating the external voltages from the transmembrane voltages the equation becomes:

$$\frac{V_m(n,t)}{R_m} + C_m \frac{d[V_m(n,t)]}{dt} - \frac{V_m(n-1,t)-2V_m(n,t)+V_m(n+1,t)}{R_a} = \frac{V_e(n-1,t)-V_e(n,t)+V_e(n+1,t)}{R_a} \quad (3.3)$$

Equation 3.3 is known as the cable equation and describes the relationship between the extracellular voltages and the transmembrane voltages induced. The second derivative of the extracellular voltage w.r.t. distance along the axon has been shown to be the key factor determining whether a myelinated axon generates an action potential or not and is sometimes referred to as the "Activating Function". The difference between the extracellular voltages at nodes $n-1$, n, and $n+1$ at time t is key to determining whether stimulation occurs and so axons with large inter-node spacings (and therefore large diameter axons) or axons that are closer to the electrode are typically stimulated at lower amplitudes.

3.3.4 Electrode physics

Electrodes are the interface between electrical circuits (where electrons are the majority charge carriers) and the electrolyte environment of biological tissue (where ions convey charge). At the interface between a charged electrode and the electrolyte an electrical double layer forms – a narrow region of trapped charge with a more diffuse region of mobile ions, as depicted in Fig. 3.6. The capacity of the electrode to store charge in this double layer is referred to as the Helmholtz capacitance. Charging of this capacitance and electrochemical reactions at the phase boundary are the two mechanisms by which charge is "injected" into the tissue, and the quantity of charge injected into the tissue is a key determinant of neural stimulation success.

Ideally all induced current in the tissue would be through charging and discharging the Helmholtz capacitance. Electrodes that are purely capacitive have been demonstrated by coating the surface with a thin dielectric. This prevents chemical reactions (meaning that the applied voltage can be significantly higher), however, it drastically reduces the capacitance (for a given surface area). Overall this reduces the amount of charge that can be injected and capacitive electrodes have suffered from low stimulation efficacy. In practice therefore, the vast majority of electrodes in practical use allow some Faradaic current to flow across the phase boundary and as a result undergo reversible and irreversible redox chemical reactions at the Electrode-Electrolyte Interface (EEI) [54]. These reactions may lead to electrode degradation and products that are toxic to the surrounding tissue. Minimising the impact of these redox processes can be achieved by: 1) reducing the amount of electrochemical reactions occurring; 2) controlling the nature of the products; or 3) reversing any reversible reactions is therefore highly desirable.

The rate and nature of the reactions (and therefore products) is dependent on the reactants available (determined by the electrode material and the chemical make-up of the electrolyte) and the potential difference across the EEI. Some reactions are reversible provided the products are still within close proximity of the electrodes and the polarity of the electrode is reversed. As a result, carefully chosen electrode materials that produce

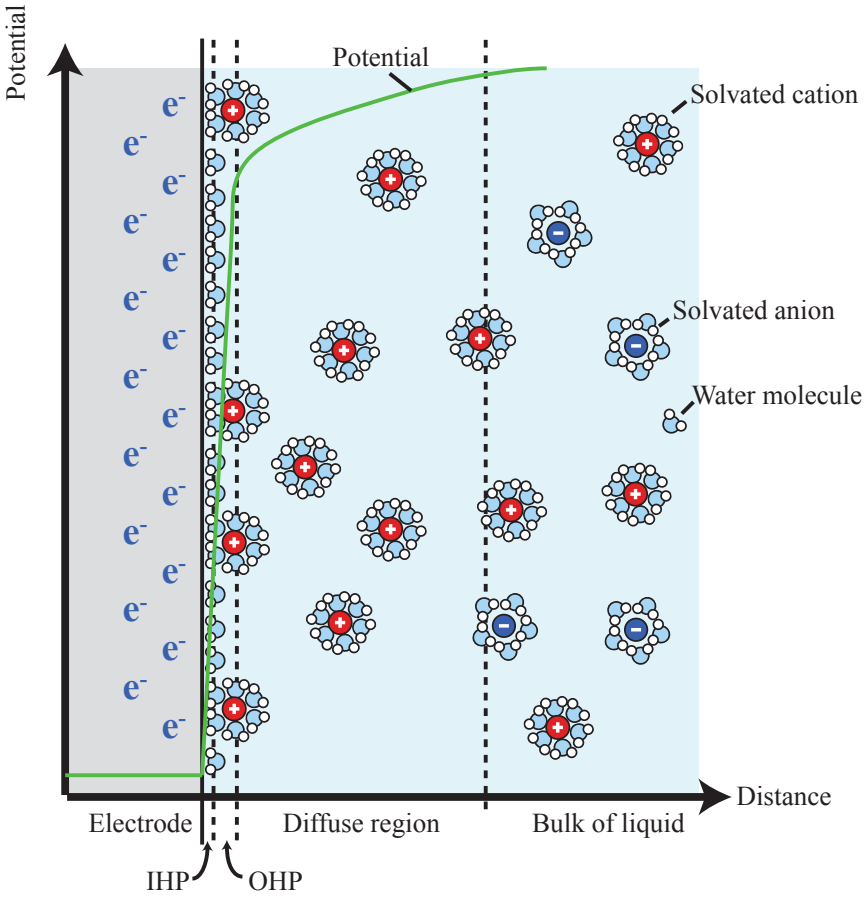


Figure 3.6: Solvated ions forming an electrical double layer at the electrode-electrolyte boundary and the electrical potential across the boundary (adapted from wikipedia.org). Shown are: the Inner Helmholtz Plane (IHP) – a layer of adsorped molecules bound to the electrode surface; the Outer Helmholtz Plane (OHP) – the closest approach of solvated ions in the electrolyte attracted to the electrode; the diffuse region – where ion concentrations are significantly affected by the electrode potential; and the bulk of the liquid where the electrode potential has negligible effect.

reversible reactions and act to reduce the diffusion of products have been combined with rapidly cycled charge balanced biphasic waveforms (as shown in Fig. 3.7) to greatly reduce electrode and tissue damage [56].

The voltage across the EEI is difficult to measure and therefore to control, however, controlling the charge flow into an electrode is much easier to achieve. Electrodes are therefore often classified by their reversible charge injection limit – the amount of charge that can flow into the electrode without causing irreversible reactions – this is a function of the material and the electrode surface area.

3.3.5 Electrode types

There are five main types of electrode that have been demonstrated for peripheral nerve stimulation (as depicted in Fig.s 3.8 and 3.9) these are: extraneural, longitudinal intrafascicular (LIFE), penetrating Micro-Electrode Arrays (MEAs), regenerative and transverse

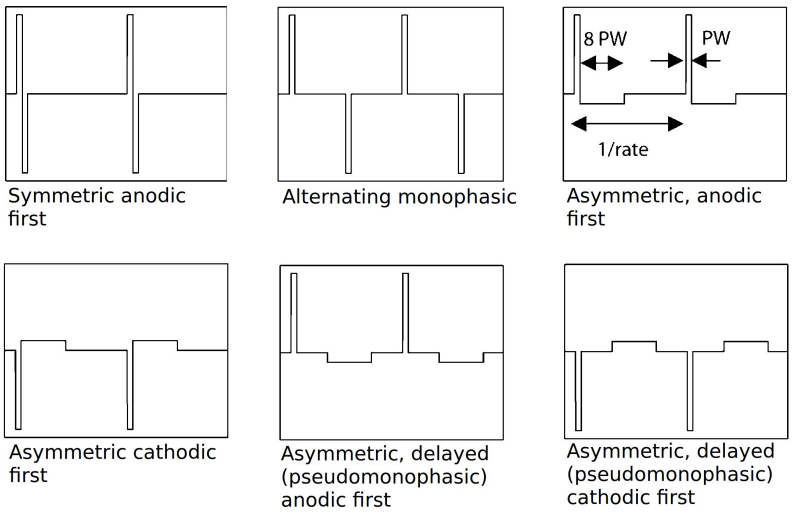


Figure 3.7: Examples of charge balanced waveforms (reproduced from [55]).

intrafascicular (LIFE) electrodes. The choice of electrode type is a multi-dimensional trade-off of factors such as: how small an area it can effectively stimulate (i.e. its selectivity), how many electrodes it can contain, its chronic stability and its chronic biocompatibility .

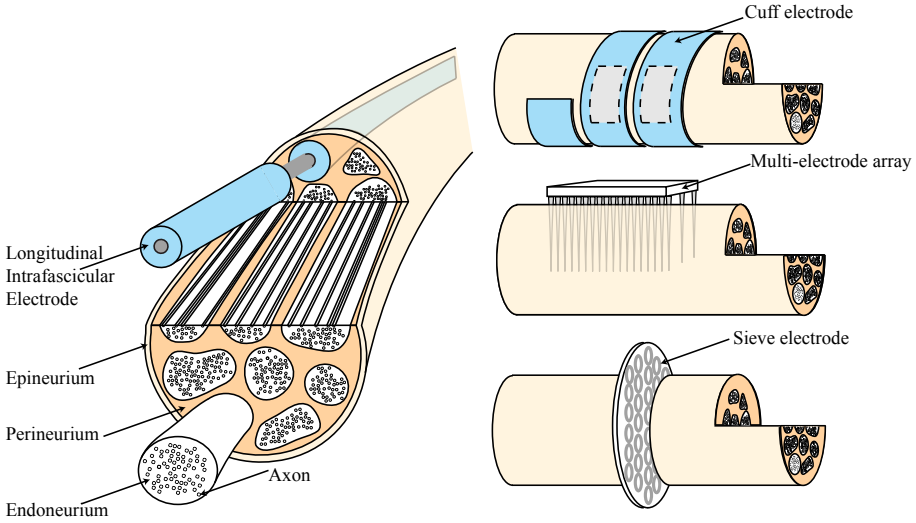
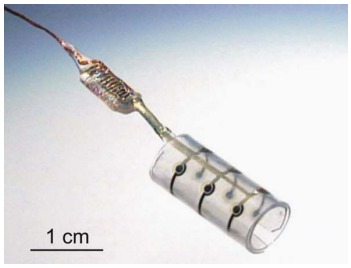


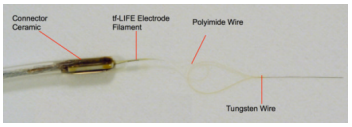
Figure 3.8: Cross sections through a nerve bundle indicating the interfaces provided by some common electrode types.

Extraneural (cuff-type) electrodes have been widely used for acute and chronic experiments for many years [62]. Their location outside the epineurium of the nerve means that they have excellent biocompatibility, cause minimal damage to the nerve and have good long-term stability. However, it also means that they have relatively poor selectivity. Progress has been made to address this – cuff designs with up to 32 electrodes integrated and novel shapes & structures to alter the nerve layout have all been demonstrated (as shown in Figure 3.10), but selectivity remains the weak point of this electrode type [63, 64].

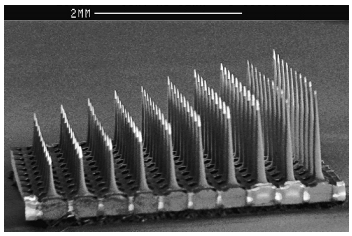
At the other end of the scale, penetrating MEAs offer excellent selectivity and a high



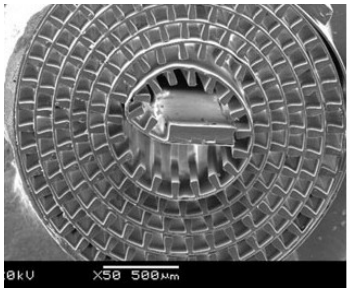
(a) Cuff electrode [57]

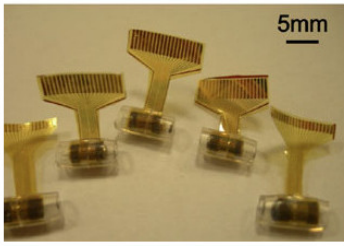


(b) LIFE electrode[58]

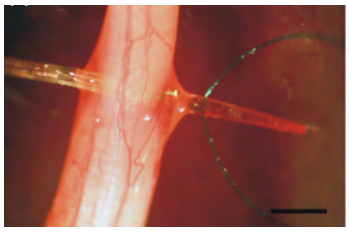


(c) Multi-electrode array [59]





(d) Regenerative electrode array [60]



(e) Transverse intrafascicular electrode [61]

Figure 3.9: Pictures of the 5 main types of electrodes.

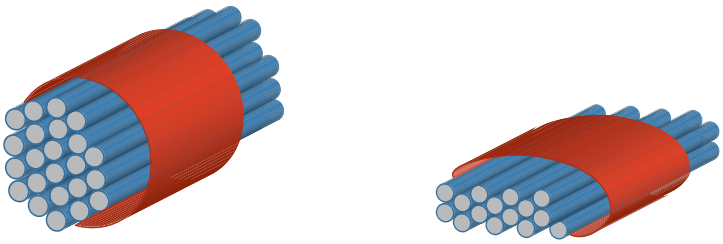
electrode count, but their penetration through the perineurium introduces a break in the blood-nerve barrier and has been observed to cause endoneural accumulation of fluid that may lead to neural damage. Tissue rejection in the form of fibrous build up has also been observed as well as neural damage caused by relative motion (boring at the electrode tip) [65, 66]. Designs with flexible polymer substrates & electrodes have been shown to reduce this latter effect, however, attempts to use biocompatible coatings to reduce rejection are still in their infancy [67, 68]. Overall penetrating MEAs have been used in chronic trials with mixed success.

Transverse and longitudinal intrafascicular electrodes have generally been used in acute experiments (their chronic safety is less well known) and in terms of selectivity and biocompatibility offer a halfway point between the two aforementioned electrode types.

Regenerative electrodes are a deviation from typical electrode design, requiring that the nerve be severed and directed to regrow through the electrode array. This gives excellent selectivity and stability, however, the percentage of neurons that have been observed to successfully regrow following implantation has been low, implying that significant damage to the nerve occurs [69, 70]. This latter point has implications if distal parts of the nerve previously provided functional benefit or if motor neurons distal to the transection could have been used for prosthesis control. Nerve transection is also linked to formation of neuromas that may cause discomfort.

3.3.6 Influencing neuron recruitment

The insertion of electrodes for stimulation is performed without *a priori* knowledge of the distribution of target neurons in the nerve and without fine control of the position of the

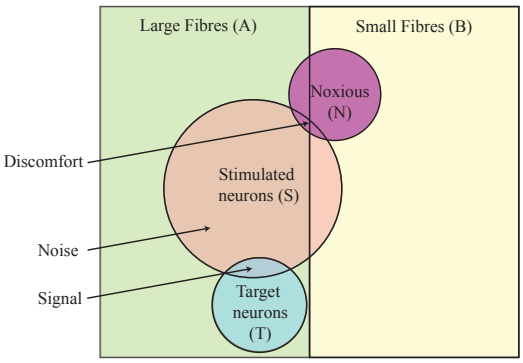


(a) A cuff electrode wrapped around a nerve

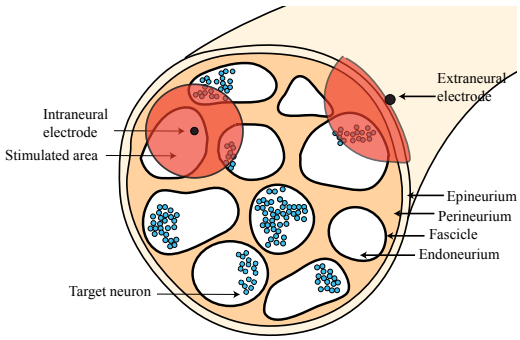
(b) A Flat Interface Nerve Electrode wrapped around a nerve

Figure 3.10: A comparison between a standard cuff electrode and a Flat Interface Nerve Electrode (FINE) shows how the FINE has deformed the nerve to increase the surface area and bring deep fascicles closer to the surface (adapted from newscientist.com)

electrode stimulation sites relative to these neurons. The ability to selectively stimulate only target neurons or neuron types is also currently not possible with electrical neural stimulation and as a result whether the actual neurons interfaced with are useful is something of a lottery as illustrated in Figure 3.11(a) and (b).



(a) Venn representation of the electrical stimulation from a single electrode in a peripheral nerve. As described by the cable equation, the set S is slightly skewed in favour of stimulating larger diameter axons (which is favourable for this application especially for spindle primary and GTO afferents).



(b) Physical representation of intraneural and extraneural stimulation

Figure 3.11: Alternative representations of the challenge of stimulating target neurons.

Whether a stimulation elicits a useful sensation can to a certain extent be considered a matter of signal to noise ratio (SNR), where signal here is represented as the intersection between the stimulated neurons (S) and the target neurons (T) i.e. $S \cap T$, while noise is the remainder i.e. $S \cap T'$. Similarly the level of discomfort experienced from the stimulation is depicted as $S \cap N$, where N represents the neurons conveying noxious sensation (e.g. nociceptors and Golgi type joint receptors).

An examination of the cable equation (Eqn. 3.3) suggests a few ways of influencing which neurons are stimulated by an implanted electrode – namely increasing the field strength,

altering the field shape and altering the distance between the electrode and the neurons. There are also a number of other techniques (of varying maturity) that have been proposed that can be used to influence recruitment – improving SNR and reducing noxious sensation. For the purposes of analysis here, all these techniques will be grouped into three categories: 1) inhibition of non-target or promotion of target neurons; 2) electric field modulation; and 3) proximity modulation.

Inhibition or promotion of neurons

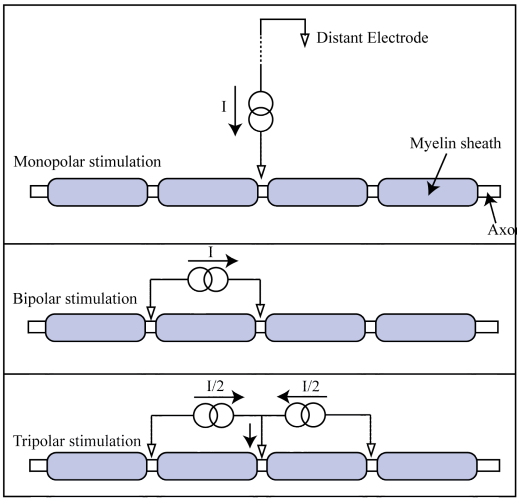
The cable equation identified the preferential recruitment of large neurons. In general this is beneficial for this application as spindle and GTO afferents are all relatively large myelinated fibres, however, in some cases benefit may be gained by either reversing or further strengthening this order of recruitment.

- Pre-pulses: long duration sub-threshold depolarising pre-pulses have been applied in order to alter the state of the sodium and potassium ion channels in nearby axons, thereby increasing stimulation thresholds. This has a disproportionate effect on large diameter axons and those close to the electrodes – increasing their stimulation threshold and enabling smaller and further axons to be stimulated preferentially. Long hyperpolarising pre-pulses have also been used to lower the stimulus threshold and strengthen the preferential recruitment of large and near fibres [71].
- Anodic blocking: neural inhibition can be used to prevent unwanted action potentials from propagating. Hyperpolarising the axons distal or proximal to the stimulation site can prevent action potentials from propagating in an unwanted direction (e.g. preventing muscular activation during sensory stimulation or vice-versa). This idea can be refined using a form of speed gating – creating a window of time post-stimulation in which action potentials can propagate – to selectively allow only fast conducting (large) or slow (small) neurons to propagate the stimulation [72].
- Waveform modulation: stimulus duration (pulse width) has been shown to affect the threshold difference between large and small axons, with shorter pulses generally increasing the threshold difference [73].

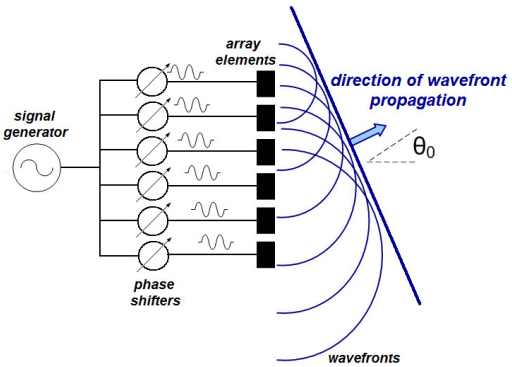
Electric field modulation

Modulation of the size and shape of the electric field is a relatively mature method of influencing recruitment. At its most basic, simply changing the amplitude of stimulation will alter the SNR and level of noxious sensation. More complex methods of field shaping have been proposed using multiple electrodes:

- Multipolar configurations: electrical stimulation typically occurs between two electrodes, however, more electrodes can be used and there are a variety of options regarding the electrode spacing. Some common electrode configurations (monopolar, bipolar and tripolar) are depicted in Figure 3.12(a). Bipolar and tripolar configurations enable greater control over the flow of current in the tissue [54] and this may



(a) Monopolar, bipolar and tripolar stimulation arrangements. Alignment of electrodes with Nodes of Ranvier is purely for illustrative purposes



(b) Phased array electronic stimulation concept, reproduced from [74]

Figure 3.12: Electric field shaping.

enable a stimulator to more accurately control which of the fascicles in its vicinity that it stimulates. Unfortunately, this selectivity comes at a price and multipolar configurations have been shown to be less power efficient than the normal monopolar approach. Accurate charge balancing on more than two electrodes is also significantly more challenging.

- Phased array: a more ambitious approach to field shaping was proposed in Valente, Demosthenous, and Bayford [74], it used a phased electrode array and beamforming techniques to more precisely target neurons for Deep Brain Stimulation. Unfortunately this approach required operation at GHz frequencies and as a result suffers from significant safety and practicality concerns.

Proximity

The inability to identify target neurons and finely aim the insertion of electrodes is a major limitation for neural prosthetics. A few possible methods for reducing the distance between electrodes and target neurons have been proposed, these include:

- Moving the electrode until a good interface is established. This is a simple solution and one that is similar to the technique used in microneurography [75], but for a system with multiple electrodes it is generally impractical. Issues include: tissue damage; a requirement for multiple surgical or transcutaneous manipulations; and for high effectiveness would require the user to be conscious and have sensation at the implant site while the manipulation is being carried out.

- Micro-Electro-Mechanical Systems (MEMS) technology has been proposed as an alternative means of adjusting electrode position [76]. This offers a potential method

of altering neural recruitment post-insertion, but increases the size of the implant, reduces the number of electrodes possible and is currently limited to penetrating electrode designs.

- Bringing the neurons to the electrode is another potential approach. Preliminary experiments indicate that neurotrophic factors can be used to influence neural growth through microchannel arrays, potentially providing the ability to selectively attract target neuron types to an electrode [77]. However, this approach is currently in early development and only applicable to regenerative electrodes.

3.3.7 Electrode choice

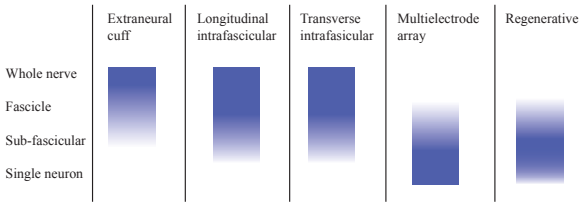


Figure 3.13: Diagrammatic representation of electrode type selectivity.

If chronic safety is the overriding requirement for implanted electrodes then ensuring that the implantation is effective is a close second. Stimulating sufficient desired neurons without stimulating undesired neighbouring neurons is a function of the number of electrodes and their selectivity.

Levels of electrode selectivity can be grouped into 4 categories as depicted in Fig. 3.13. Previous proprioceptive experiments with longitudinal and extraneural electrode arrays indicated that selectivity at approximately the sub-fascicular – fascicular level is capable of inducing well defined percepts – although results from microneurography suggest that most of the sensations elicited will be cutaneous in nature.

Interfacing selectively with a target neuron population is a major unsolved challenge in neural prostheses. At present the simplest and most effective solutions for electronic stimulation are: careful choice of the nerve (and ideally nerve branch) to interface with; implanting many more electrodes than are strictly required; and employing a variety of spatial and fibre diameter selection techniques (as described in Section 3.3.6) to alter the population of neurons that are stimulated.

Given the desire for chronic safety, extraneural electrodes are preferred. Therefore in order to increase efficacy, it is proposed that a multi-contact nerve shaping design is utilised.

3.3.8 Neural stimulator design

Electrical neural stimulation began all the way back in the 18th century when Galvani first began experimenting on frogs with a simple voltage controlled stimulator. Since then advances in biology, electrochemistry, and electronics has led to 2 other classes of neural

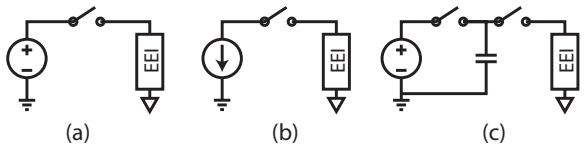


Figure 3.14: (a) Current-Controlled Stimulation (b) Voltage-Controlled Stimulation (c) Charge-Controlled Stimulation (d) Electrode-Electrolyte Interface model. Rs is solution spreading resistance, C_{dl} is double layer capacitance, R_t is charge transfer resistance. (Reproduced from [78]).

stimulator – current controlled and charge controlled (as depicted in Fig. 3.14) – as well as numerous innovations for all three classes.

Key considerations for electrical neural stimulation are power consumption (see Section 3.4) and methods for enhancing the chronic biocompatibility of the electrode-tissue interface – in particular charge balanced biphasic waveforms and limiting charge injection.

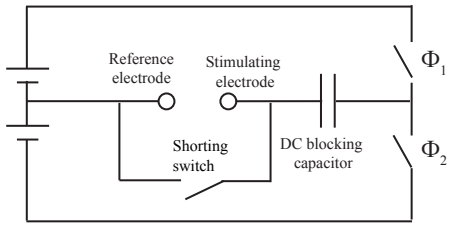
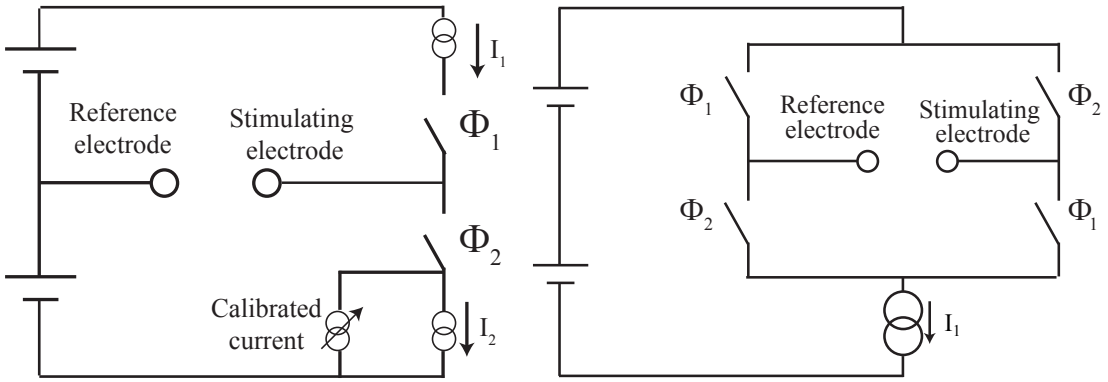


Figure 3.15: Conceptual diagram of a Voltage Controlled Stimulator with DC blocking capacitors and electrode shorting. Φ_1 is closed during anodic stimulation and Φ_2 during cathodic. Shorting switch is closed between stimulation cycles.

Voltage Controlled Stimulation (VCS)

Voltage controlled stimulators were initially monophasic, leading to significant electrode and biocompatibility problems. Biphasic stimulators were developed but because the EEI impedance is not purely resistive this did not lead to equal charge being delivered and removed from the electrodes. An early approach to address this charge imbalance was to follow stimulation by shorting the stimulation electrode to a large reference electrode to leave it electrically neutral with the tissue (see Fig. 3.15). However, the time constants for the electrode capacitance to discharge mean that this technique is poorly suited to devices with high numbers of channels. Another technique is to use DC-blocking capacitors in series with the stimulation electrode, this prevents long term DC currents through the electrode and the associated problems. Unfortunately the size of the capacitors means that they need to be implemented off-chip and this become increasingly undesirable as the number of stimulation channels increases. None of these solutions address the other key problem with voltage controlled stimulation, namely that the total charge injected is not controlled.



(a) Conceptual diagram of an a calibrated CCS

(b) An H-bridge style CCS

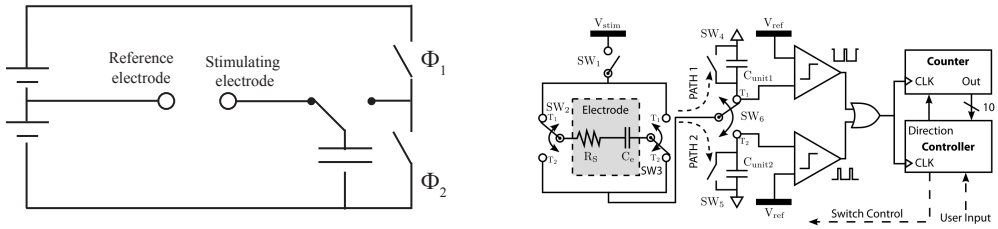
Figure 3.16: Current Controlled Stimulators. Φ_1 switches are closed during anodic stimulation and Φ_2 during cathodic.

Current Controlled Stimulation (CCS)

Current controlled stimulators were developed to address all these problems, providing close control of the charge delivered and removed from the tissue and enabling fully integrated on-chip solutions. Experiments in the 1990s identified minimum levels of DC current flow (100 nA) across electrodes that were correlated with tissue damage [79] and hence (depending on on the stimulation pulse rate) the level of charge mismatch for the anodic and cathodic phases of the biphasic waveform. This target led to the development of two main approaches of matching current in the two phases (see Fig. 3.16): 1) automated calibration of the current sources and sinks, and 2) an H-bridge configuration to allow the same current controller to act as either a source or sink. One downside of both these approaches is that it constrains the waveform in both phases to be identical rather than just charge balanced – this is unfortunate as asymmetric waveforms have been shown to stimulate at lower (safer and more efficient) thresholds. However, the main issue with current controlled stimulation is that of high power consumption due to power waste in the transistors that are typically used to control the current in the front-end of the stimulator. An attempt to address this has been made by integrating a switched mode converter to replace the current controlling transistors [80], however, this approach led to inaccurate current control and required off-chip components – undermining two of the key advantages of current controlled stimulation.

Charge Controlled Stimulation (QCS)

Charge controlled stimulators were proposed as something of halfway house between voltage and current control – limiting the total charge delivered to the tissue and offering lower power consumption, but not offering as good charge control as current controlled stimulators. The first proposed design in some ways resembled a voltage controlled stimulator with DC blocking capacitors built in (see Fig. 3.17(a). These large (off-chip) capacitors were charged to a voltage and then discharged through the electrodes (thereby limiting the total charge delivered). However, although these early designs showed reduced power



(a) Conceptual diagram of an early Charge Controlled Stimulator

(b) Fully integrated Charge Controlled Stimulator proposed in [81] with good charge balance

Figure 3.17: Charge Controlled Stimulators. Φ_1 is closed during anodic stimulation and Φ_2 during cathodic.

consumption (compared to current control) the requirement for off-chip capacitors and the poor charge balancing (assuming the EEI is not purely resistive) were undesirable. A more recently proposed system addresses these problems by repeatedly charging and discharging small on-chip capacitors (see Fig. 3.17(b). This offered improved charge control and is fully integrated, but comes at the expense of low limits of total charge that can be delivered [81].

3.4 Implant

To achieve selective stimulation it is currently necessary to implant parts of the system inside the user's body – at a minimum the electrodes near the nerve. Minimising the amount of hardware implanted is desirable because these parts of the system become inaccessible for modification or repair and may damage surrounding tissue either mechanically, chemically or thermally.

Mechanical and chemical damage can be reduced by miniaturisation and biocompatible coating of the hermetically sealed implant [82]. Thermal tissue damage is directly related to the power dissipated per unit surface area and as such energy intensive components (e.g. computational processing) should be kept outside the body and the power efficiency of the implanted hardware should be optimised. Heating of tissue 1^oC above normal body temperature has been correlated with tissue damage and research into the body's ability to conduct heat has indicated that the power density of an implant should therefore be strictly controlled [83].

The fundamental obstacle for this reduction in implanted hardware is the transcutaneous (through skin) link. Transcutaneous wires are acceptable for short term implants, but are discomforting and greatly increase the risk of infection. Wireless links are therefore favoured [84–86], requiring only an implanted wireless receiver and neural stimulator be implanted.

Proposed sources of power for a biomedical implant include: transcutaneous power transmission, implanted primary or secondary batteries, and kinetic or thermal energy harvesting. Of the three, energy harvesting is currently the least viable as existing systems are only able to provide very low levels of power [86]. Primary batteries are used in applications where uninterrupted power is crucial (e.g. pacemakers), but the unfortunately require

surgery to replace them when exhausted. Wireless transcutaneous power transmission is fairly inefficient – due to: the limited space for the receiving coil, issues with coil alignment and the limitations imposed by the tissue environment – but when used in conjunction with an implanted secondary battery is a commonly proposed method of powering neural implants. The rechargeable battery implanted has limited recharge cycles and therefore will still require replacement; maximising battery lifetime by reducing power consumption is therefore highly desirable. Devices supporting power transfer in the order of 10 mW and a downlink data transfer rate in the order of 2 Mbps have been demonstrated [87], although few (if any) of these have been demonstrated in-vivo.

3.5 Sensors

Achieving the desired level of proprioceptive capability requires monitoring of the pose, motion and forces exerted on the prosthetic limb with as good or better acuity as in the human body. However, defining this performance and translating it into a sensor specification is challenging, as human proprioceptive acuity is highly variable from joint to joint, muscle to muscle and person to person.

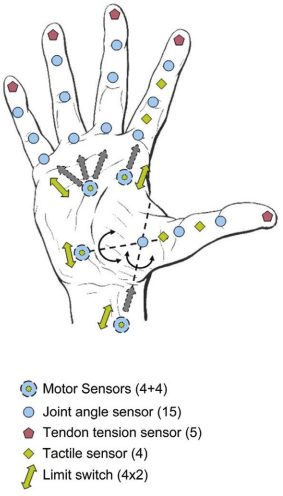
Approximate trends in acuity were identified in Chapter 2. They showed human joint position estimates are generally in the order of 1° with decreasing accuracy as you move from proximal joints to distal. Force proprioception is more difficult to quantify – depending on: fatigue, the CNS interpretation of perceived effort, and related to the strength and leverage of the muscles involved – with changes in the order of 10% eliciting noticeable sensation.

Numerous solutions exist for measuring these quantities in the field of robotics and, on the face of it, the requirements imposed by achieving human level performance are not particularly demanding; however, size, weight and cosmetic constraints may make integration in the prosthetic more challenging.



Key	Sensor	Number
	Absolute Position Sensor	21
	Contact Sensor	10
	Torque Sensor	14
	Joint Temperature Sensor	17
	3-Axis Acclerometer	3
	3-Axis Force Sensor	3
	Additional Sensors ▪ Incremental rotor position (x17) ▪ Drive voltage (x17) ▪ Upperarm drive current (x7)	41

(a) The John Hopkins Modular Prosthetic Limb [88].



(b) The Smarthand prosthesis [89]

Figure 3.18: The sensor fit for two research prostheses

3.5.1 Position and motion sensors

The assumed output from this stage (to the biomechanical modelling) is the joint angles, i.e. the **relative** position of each limb segment. Absolute sensors (e.g. accelerometers and gyroscopes), while still a possibility, are therefore at a disadvantage in this application and introduce significantly higher levels of complexity.

Analogue (e.g. rotary potentiometers) and digital angle sensors (e.g. rotary encoders) are simple, mature and high performance solutions and have been used in numerous prosthetic arms such as the John Hopkins arm and Smarthand prosthesis (see Fig. 3.18). Both these sensors types are only able to measure a single axis, however, this matches with the typical design of prosthetic limbs. If a joint with more than one degree of freedom needs to be measured then the sensors could be put in a type of gimbal apparatus (such as those used in joysticks) to monitor multiple degrees of freedom, however, this may have mechanical implications for the joint and may cause integration challenges. Hall effect sensors have previously been used when mechanical integration would be challenging [90] or when a simple limit switch is required [89].

Another approach to measuring body position is to measure the output of the actuators (or for cable or linearly actuated devices the length of components they extend or contract) and use a model of the prosthesis articulation in order to infer the limb position [91].

Alternatively the inputs to the actuators can be monitored and, providing the output of the actuator is sufficiently deterministic (as in the case of a stepper motor), then an estimate of the pose of the prosthesis can again be calculated. However, an input monitoring approach suffers from error propagation and accumulation; and as such in practice output monitoring sensors are usually used to establish ground truth and provide pose maintenance [91].

3.5.2 Force measurement

Measuring how much force or effort is being applied is likely to be the most challenging aspect of monitoring the status of a limb. The most straightforward approach is the use of cable tension sensors or strain gauges to estimate the forces applied to material in series with the actuators being monitored [90, 91]. However, accurate force measurement by strain gauges is expensive and may feasibly affect the limb's mechanical performance [92].

An alternative approach to measuring forces, would be to estimate them based on the power applied to the actuators. Electromagnetic torque is often calculated based on the current applied to a DC motor, however, this calculation is most accurate in a steady state where the motor is continuously rotating (and average current can be measured) and it should be noted that electromagnetic torque is not the same as the final torque delivered at the output (e.g. due to losses and gearing). In general for the transient motor operations used in a prosthesis an approach based on input power is likely to be complex and potentially involve a high degree of error.

3.5.3 Practical implementation

Reviewing the literature and the publicly available information on commercial prostheses, there is a large divide between the sensor fits of research and commercial arms.

Research arms such as the Modular Prosthetic Limb [93] (see Fig. 3.18) and the Smarthand [89] have upwards of 40 sensors in the hand alone and are capable of measuring every joint angle, motor torque and also the tactile grasp forces.

Meanwhile commercial products – with no means of providing feedback to the user – take a more pragmatic approach and appear to be adverse to additional wiring (especially into the fingers) or adding components that could affect the reliability, durability or maintainability of the device. Instrumentation of the motors (limit switches, integrated hall sensors and current monitoring) seem to be the preferred approach and are mainly beneficial for the automated control of grip force.

In the end the preferred sensor fit for this application will depend largely on the detailed mechanical design and actuation of the prosthesis as well as the numerous other factors identified in this section. However, it seems likely that a practical proprioceptive prosthesis will need to fall somewhere between the extremes of the current ambitious research arms and the minimalist commercial arms – with careful system integration to minimise the impact on system reliability, durability and maintainability.

3.6 Discussion

This chapter has reviewed the options, assumptions and state of the art solutions to many of the problems and challenges involved in the design of a proprioceptive neural prosthesis. Putting it all together gives an outline proposed system (pictured in Fig. 3.19) for a transhumeral amputee consisting of:

- Rotary encoders and strain gauge sensors at all the actuated joints, providing prosthesis position, motion and joint torques.
- Biomechanical musculotendon models combined with spindle and GTO proprioceptor models running on a portable device to generate estimates of neural signals to stimulate.
- A wireless link transmitting power and data to an implanted low power wireless receiver.
- A current controlled low power neural stimulator connected to 3 sets of FINE electrodes (each with on the order of 10 stimulation sites), that are wrapped around the radial, musculocutaneous and median nerves in the arm (based on the myotome maps provided in Chapter 2).

3.6.1 Gaps and areas of further work

Previous proprioceptive neural experiments in humans have demonstrated impressive performance with only one or two channels of feedback. However, it is clear that improved

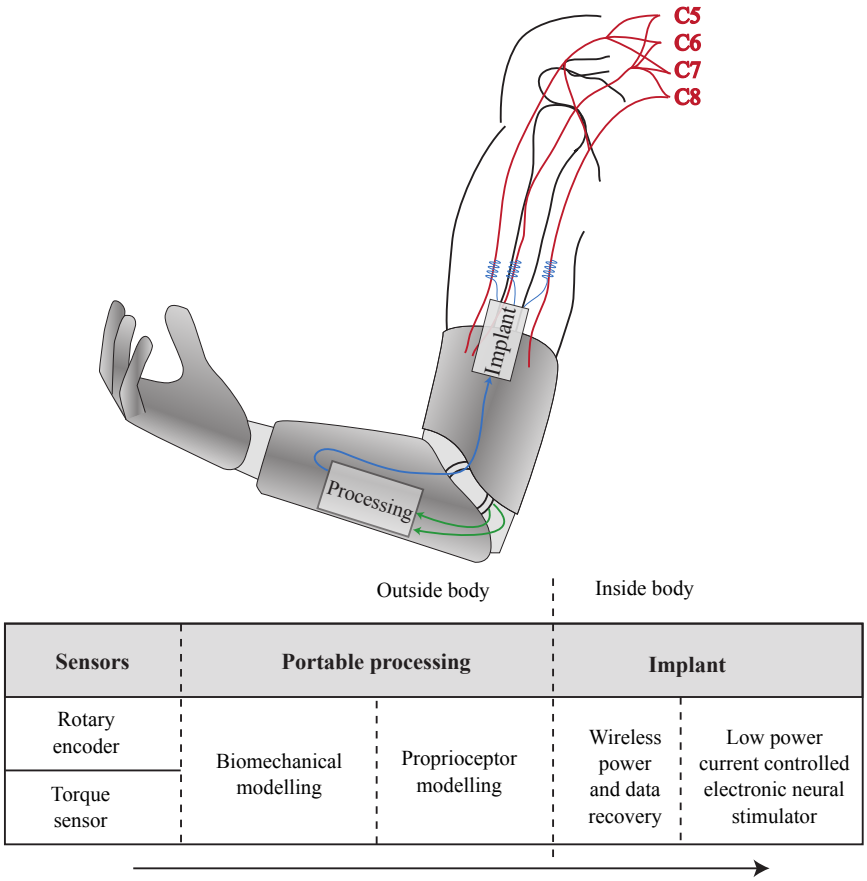


Figure 3.19: Outline proposed system design

performance requires innovations in the neural interface and the neural signals that are applied.

This work has identified a need for:

- Research into methods of improving selectivity – ideally developing tools and techniques to either: enable the identification and targeting of desired neurons during electrode implantation; or to enable the manipulation of neurons post-implantation.
- A low power current controlled stimulator, capable of stimulating tens of cuff electrode sites while running within the tight thermal and wireless power budgets.
- Research into the feasibility of mimicking neural proprioceptive patterns and to develop an efficient method of implementing these models on low power hardware. Plus a safe and ethical method of evaluating the performance of different patterns of modulation, e.g. either a non-invasive test in humans or more useful testing in animal models.
- Further psychophysical research into human proprioceptive acuity (especially force) to refine the requirements of prosthetic sensors.

Bibliography

[1] R. R. Riso. "Strategies for providing upper extremity amputees with tactile and hand position feedback–moving closer to the bionic arm". *Technology and Health Care* 7.6 (1999), pp. 401–409.

[2] S. S. Hsiao, M. Fettiplace, and B. Darbandi. "Sensory feedback for upper limb prostheses." *Progress in brain research* 192 (2011), p. 69.

[3] D. J. Weber, R. Friesen, and L. E. Miller. "Interfacing the Somatosensory System to Restore Touch and Proprioception: Essential Considerations". *Journal of Motor Behavior* 44 (2012), pp. 403–418.

[4] P. Herberts and L. Korner. "Ideas on sensory feedback in hand prostheses". *Prosthetics and orthotics international* 3.3 (1979), pp. 157–162.

[5] D. S. Childress. "Closed-loop control in prosthetic systems: Historical perspective". *Annals of biomedical engineering* 8.4 (1980), pp. 293–303.

[6] C. Phillips. "Sensory feedback control of upper-and lower-extremity motor prostheses." *Critical reviews in biomedical engineering* 16.2 (1987), pp. 105–140.

[7] K. Ohnishi, R. F. Weir, and T. A. Kuiken. "Neural machine interfaces for controlling multifunctional powered upper-limb prostheses" (2007).

[8] A. E. Schultz and T. A. Kuiken. "Neural interfaces for control of upper limb prostheses: the state of the art and future possibilities". *PM&R* 3.1 (2011), pp. 55–67.

[9] C. Antfolk, M. D'Alonzo, B. Rosen, G. Lundborg, F. Sebelius, and C. Cipriani. "Sensory feedback in upper limb prosthetics" (2013).

[10] P. Zhang, Q. Xu, and J. P. He. "Review and Perspective: Sensory Feedback in Upper Limb Prosthesis". *Applied Mechanics and Materials* 303 (2013), pp. 261–265.

[11] D. Farina, W. Jensen, and M. Akay. *Introduction to Neural Engineering for Motor Rehabilitation*. IEEE Press Series on Biomedical Engineering. Wiley, 2013, pp. 311–326. ISBN: 9781118628492.

[12] J. S. Schofield, K. R. Evans, J. P. Carey, and J. S. Hebert. "Applications of sensory feedback in motorized upper extremity prosthesis: a review". *Expert Review of Medical Devices* (2014), pp. 1–13.

[13] R. Romo, A. Hernandez, A. Zainos, C. D. Brody, and L. Lemus. "Sensing without touching: psychophysical performance based on cortical microstimulation". *Neuron* 26.1 (2000), pp. 273–278.

[14] B. M. London, L. R. Jordan, C. R. Jackson, and L. E. Miller. "Electrical Stimulation of the Proprioceptive Cortex (Area 3a) Used to Instruct a Behaving Monkey". *IEEE Transactions On Neural Systems And Rehabilitation Engineering* 16 (2008).

[15] G. S. Dhillon, S. M. Lawrence, D. T. Hutchinson, and K. W. Horch. "Residual Function in Peripheral Nerve Stumps of Amputees: Implications for Neural Control of Artificial Limbs". *The Journal of Hand Surgery* 29A (2004), pp. 605–615.

[16] G. S. Dhillon and K. W. Horch. "Direct Neural Sensory Feedback and Control of a Prosthetic Arm". *IEEE Transactions on neural systems and rehabilitation engineering* 13 (2005).

[17] G. Dhillon, T. Kruger, J. Sandhu, and K. Horch. "Effects of short-term training on sensory and motor function in severed nerves of long-term human amputees". *Journal of neurophysiology* 93.5 (2005), pp. 2625–2633.

[18] K. Horch, S. Meek, T. G. Taylor, and D. T. Hutchinson. "Object discrimination with an artificial hand using electrical stimulation of peripheral tactile and proprioceptive pathways with intrafascicular electrodes". *Neural Systems and Rehabilitation Engineering, IEEE Transactions on* 19.5 (2011), pp. 483–489.

[19] B. M. London, L. R. Jordan, C. R. Jackson, and L. E. Miller. "Electrical stimulation of the proprioceptive cortex (area 3a) used to instruct a behaving monkey". *Neural Systems and Rehabilitation Engineering, IEEE Transactions on* 16 (2008), pp. 32–36.

[20] D. J. Weber, R. Friesen, and L. E. Miller. "Interfacing the Somatosensory System to Restore Touch and Proprioception: Essential Considerations". *Journal of Motor Behavior* 44 (2012), pp. 403–418.

[21] B. Nashold, G. Somjen, and H. Friedman. "Paresthesias and EEG potentials evoked by stimulation of the dorsal funiculi in man". *Experimental neurology* 36 (1972), pp. 273–287.

[22] D. J. Weber, B. M. London, J. A. Hokanson, C. A. Ayers, R. A. Gaunt, R. R. Torres, B. Zaaimi, and L. E. Miller. "Limb-state information encoded by peripheral and central somatosensory neurons: implications for an afferent interface". *Neural Systems and Rehabilitation Engineering, IEEE Transactions on* 19 (2011), pp. 501–513.

[23] N. Fitzsimmons, W. Drake, T. Hanson, M. Lebedev, and M. Nicolelis. "Primate reaching cued by multichannel spatiotemporal cortical microstimulation". *The Journal of neuroscience* 27 (2007), pp. 5593–5602.

[24] K. Warwick, M. Gasson, B. Hutt, I. Goodhew, P. Kyberd, B. Andrews, P. Teddy, and A. Shad. "The application of implant technology for cybernetic systems". *Archives of Neurology* 60 (2003), pp. 1369–1373.

[25] P. M. Rossini, S. Micera, A. Benvenuto, J. Carpaneto, G. Cavallo, L. Citi, C. Cipriani, L. Denaro, V. Denaro, G. Di Pino, et al. "Double nerve intraneural interface implant on a human amputee for robotic hand control". *Clinical neurophysiology* 121 (2010), pp. 777–783.

[26] S. Raspopovic, M. Capogrosso, F. M. Petrini, M. Bonizzato, J. Rigosa, G. Di Pino, J. Carpaneto, M. Controzzi, T. Boretius, E. Fernandez, et al. "Restoring natural sensory feedback in real-time bidirectional hand prostheses". *Science translational medicine* 6 (2014), 222ra19–222ra19.

[27] G. S. Dhillon and K. W. Horch. "Direct neural sensory feedback and control of a prosthetic arm." *IEEE Trans. TNSRE* 13 (2005), pp. 468–72.

[28] S. Watson. "The principles of management of congenital anomalies of the upper limb". *Archives of disease in childhood* 83.1 (2000), pp. 10–17.

[29] M. S. Chung. "Congenital differences of the upper extremity: classification and treatment principles". *Clinics in orthopedic surgery* 3.3 (2011), pp. 172–177.

[30] U. Proske and S. C. Gandevia. "The Proprioceptive Senses: Their Roles in Signaling Body Shape, Body Position and Movement, and Muscle Force". *Physiological Reviews* 92 (2012), pp. 1651–1697.

[31] D. Song, N. Lan, G. E. Loeb, and J. Gordon. "Model-Based Sensorimotor Integration for Multi-Joint Control: Development of a Virtual Arm Model". *Annals of Biomedical Engineering* 36 (2008), pp. 1033–1048.

[32] A. Frigon and S. Rossignol. "Experiments and models of sensorimotor interactions during locomotion". *Biological cybernetics* 95 (2006), pp. 607–627.

[33] F. M. Colacino, E. Rustighi, and B. R. Mace. "An EMG-driven musculoskeletal model for the estimation of biomechanical parameters of wrist flexors". 2010, pp. 4870–4873.

[34] N. Lan, Y. Li, Y. Sun, and F. Yang. "Reflex regulation of antagonist muscles for control of joint equilibrium position". *Neural Systems and Rehabilitation Engineering, IEEE Transactions on* 13 (2005), pp. 60–71.

[35] T. K. Koo and A. F. Mak. "A neuromusculoskeletal model to simulate the constant angular velocity elbow extension test of spasticity". *Medical engineering & physics* 28 (2006), pp. 60–69.

[36] R. H. Dennard, F. H. Gaensslen, V. L. Rideout, E. Bassous, and A. R. LeBlanc. "Design of ion-implanted MOSFET's with very small physical dimensions". *Solid-State Circuits, IEEE Journal of* 9 (1974), pp. 256–268.

[37] S. Luan, I. Williams, T. G. Constandinou, and K. Nikolic. "Neuromodulation: present and emerging methods". *Frontiers in Neuroengineering* 7 (2014), p. 27.

[38] D. Zhou and E. Greenbaum. *Implantable Neural Prostheses 2: Techniques and Engineering Approaches*. Springer, 2010.

[39] G. Bonmassar, S. W. Lee, D. K. Freeman, M. Polasek, S. I. Fried, and J. T. Gale. "Microscopic magnetic stimulation of neural tissue." *Nature communications* 3 (2012), p. 921.

[40] E. S. Boyden, F. Zhang, E. Bamberg, G. Nagel, and K. Deisseroth. "Millisecond-timescale, genetically targeted optical control of neural activity". *Nature Neuroscience* 8 (2005), pp. 1263–8.

[41] B. Y. Chow, X. Han, A. S. Dobry, X. Qian, A. S. Chuong, M. Li, M. A. Henninger, G. M. Belfort, Y. Lin, P. E. Monahan, and E. S. Boyden. "High-performance genetically targetable optical neural silencing by light-driven proton pumps". *Nature* 463 (2010), pp. 98–102.

[42] G. Nagel, T. Szellas, W. Huhn, S. Kateriya, N. Adeishvili, P. Berthold, D. Ollig, P. Hegemann, and E. Bamberg. "Channelrhodopsin-2, a directly light-gated cation-selective membrane channel". *Proceedings of the National Academy of Sciences of the United States of America* 100 (2003), pp. 13940–5.

[43] O. Yizhar, L. E. Fenno, T. J. Davidson, M. Mogri, and K. Deisseroth. "Optogenetics in Neural Systems". *Neuron* 71 (2011), pp. 9–34.

[44] K. Deisseroth. "Optogenetics". *Nature* 8 (2011), pp. 26–29.

[45] J. G. McCall, T.-i. Kim, G. Shin, X. Huang, Y. H. Jung, R. Al-Hasani, F. G. Omenetto, M. R. Bruchas, and J. A. Rogers. "Fabrication and application of flexible, multimodal light-emitting devices for wireless optogenetics". *Nature protocols* 8 (2013), pp. 2413–2428.

[46] A. R. Duke, M. W. Jenkins, H. Lu, J. M. McManus, H. J. Chiel, and E. D. Jansen. "Transient and selective suppression of neural activity with infrared light". *Scientific reports* 3 (2013).

[47] M. G. Shapiro, K. Homma, S. Villarreal, C.-P. Richter, and F. Bezanilla. "Infrared light excites cells by changing their electrical capacitance". *Nature communications* 3 (2012), p. 736.

[48] Z. Mou, I. F. Triantis, V. M. Woods, C. Toumazou, and K. Nikolic. "A Simulation Study of the Combined Thermoelectric Extracellular Stimulation of the Sciatic Nerve of the Xenopus Laevis: The Localized Transient Heat Block". *Biomedical Engineering, IEEE Transactions on* 59 (2012), pp. 1758–1769.

[49] J. Wells, C. Kao, P. Konrad, T. Milner, J. Kim, A. Mahadevan-Jansen, and E. D. Jansen. "Biophysical Mechanisms of Transient Optical Stimulation of Peripheral Nerve". *Biophysical Journal* 93 (2007), pp. 2567–2580.

[50] Y. Tufail, A. Matyushov, N. Baldwin, M. L. Tauchmann, J. Georges, A. Yoshihiro, S. I. H. Tillery, and W. J. Tyler. "Transcranial pulsed ultrasound stimulates intact brain circuits." *Neuron* 66 (2010), pp. 681–94.

[51] O. Naor, Y. Hertzberg, E. Zemel, E. Kimmel, and S. Shoham. "Towards multifocal ultrasonic neural stimulation II: design considerations for an acoustic retinal prosthesis." *Journal of neural engineering* 9 (2012), p. 026006.

[52] L. Theogarajan. "Strategies for restoring vision to the blind: current and emerging technologies." *Neuroscience letters* 519 (2012), pp. 129–33.

[53] Y.-A. Song, R. Melik, A. N. Rabie, A. M. S. Ibrahim, D. Moses, A. Tan, J. Han, and S. J. Lin. "Electrochemical activation and inhibition of neuromuscular systems through modulation of ion concentrations with ion-selective membranes." *Nature materials* 10 (2011), pp. 980–6.

[54] K. Horch and G. Dhillon. *Neuroprosthetics: Theory and Practice*. Series on bioengineering and biomedical engineering. World Scientific, 2004. ISBN: 9789812380227.

[55] O. Macherey, A. van Wieringen, R. P. Carlyon, J. M. Deeks, and J. Wouters. "Asymmetric pulses in cochlear implants: effects of pulse shape, polarity, and rate." *Journal of the Association for Research in Otolaryngology : JARO* 7 (2006), pp. 253–66.

[56] J. C. Lilly, J. R. Hughes, E. C. Alvord, and T. W. Galkin. "Brief, Noninjurious Electric Waveform for Stimulation of the Brain". *Science* 121 (1955), pp. 468–469.

[57] M. Schuttler. "Dreidimensionale Formgebung von planaren Mikroelektroden zur Optimierung der Signalableitung und Stimulation am peripheren Nerven". PhD thesis. 2002.

[58] S. Micera, P. M. Rossini, J. Rigosa, L. Citi, J. Carpaneto, S. Raspopovic, M. Tombini, C. Cipriani, G. Assenza, M. C. Carrozza, et al. "Decoding of grasping information from neural signals recorded using peripheral intrafascicular interfaces". *J Neuroeng Rehabil* 8 (2011), p. 53.

[59] A. Branner, R. B. Stein, and R. A. Normann. "Selective stimulation of cat sciatic nerve using an array of varying-length microelectrodes". *Journal of Neurophysiology* 85.4 (2001), pp. 1585–1594.

[60] S. P. Lacour, S. Benmerah, E. Tarte, J. FitzGerald, J. Serra, S. McMahon, J. Fawcett, O. Graudejus, Z. Yu, and B. Morrison III. "Flexible and stretchable micro-electrodes for in vitro and in vivo neural interfaces". *Medical & biological engineering & computing* 48.10 (2010), pp. 945–954.

[61] T. Boretius, J. Badia, A. Pascual-Font, M. Schuettler, X. Navarro, K. Yoshida, and T. Stieglitz. "A transverse intrafascicular multichannel electrode (TIME) to interface with the peripheral nerve". *Biosensors and Bioelectronics* 26.1 (2010), pp. 62–69.

[62] W. M. Grill, S. E. Norman, and R. V. Bellamkonda. "Implanted neural interfaces: biochallenges and engineered solutions". *Annual Review of Biomedical Engineering* 11 (2009), pp. 1–24.

[63] D. J. Tyler and D. M. Durand. "Functionally selective peripheral nerve stimulation with a flat interface nerve electrode". *Neural Systems and Rehabilitation Engineering, IEEE Transactions on* 10 (2002), pp. 294–303.

[64] K. H. Polasek, H. A. Hoyen, M. W. Keith, and D. J. Tyler. "Human nerve stimulation thresholds and selectivity using a multi-contact nerve cuff electrode". *Neural Systems and Rehabilitation Engineering, IEEE Transactions on* 15 (2007), pp. 76–82.

[65] V. S. Polikov, P. A. Tresco, and W. M. Reichert. "Response of brain tissue to chronically implanted neural electrodes". *Journal of neuroscience methods* 148 (2005), pp. 1–18.

[66] R. Biran, D. C. Martin, and P. A. Tresco. "Neuronal cell loss accompanies the brain tissue response to chronically implanted silicon microelectrode arrays". *Experimental neurology* 195.1 (2005), pp. 115–126.

[67] J. B. Leach, A. K. H. Achyuta, and S. K. Murthy. "Bridging the divide between neuroprosthetic design, tissue engineering and neurobiology". *Frontiers in neuroengineering* 2 (2009).

[68] D. F. Williams. "On the mechanisms of biocompatibility". *Biomaterials* 29 (2008), pp. 2941–2953.

[69] N. Lago, D. Ceballos, F. J Rodriguez, T. Stieglitz, and X. Navarro. "Long term assessment of axonal regeneration through polyimide regenerative electrodes to interface the peripheral nerve". *Biomaterials* 26 (2005), pp. 2021–2031.

[70] P. M. Klinge, M. A. Vafa, T. Brinker, A. Brandis, G. F. Walter, T. Stieglitz, M. Samii, and K. Wewetzer. "Immunohistochemical characterization of axonal sprouting and reactive tissue changes after long-term implantation of a polyimide sieve electrode to the transected adult rat sciatic nerve". *Biomaterials* 22 (2001), pp. 2333–2343.

[71] W. M. Grill and J. T. Mortimer. "Stimulus waveforms for selective neural stimulation". *Engineering in Medicine and Biology Magazine, IEEE* 14 (1995), pp. 375–385.

[72] N. J. Rijkhoff, J. Holsheimer, E. Koldewijn, J. J. Struijk, P. Van Kerrebroeck, F. Debruyne, and H. Wijkstra. "Selective stimulation of sacral nerve roots for bladder control: a study by computer modeling". *Biomedical Engineering, IEEE Transactions on* 41.5 (1994), pp. 413–424.

[73] M. Schiefer, M. Freeberg, G. Pinault, J. Anderson, H. Hoyen, D. Tyler, and R. Triolo. "Selective activation of the human tibial and common peroneal nerves with a flat interface nerve electrode". *Journal of neural engineering* 10 (2013), p. 056006.

[74] V. Valente, A. Demosthenous, and R. Bayford. "Application of phased array systems to deep brain stimulation". *Electronics, Circuits, and Systems, 2009. ICECS 2009. 16th IEEE International Conference on*. IEEE. 2009, pp. 643–646.

[75] M. Bergenheim, J.-P. Roll, and E. Ribot-Ciscar. "Microneurography in humans". *Modern techniques in neuroscience Research*. Springer, 1999, pp. 803–819.

[76] N. Jackson, A. Sridharan, S. Anand, M. Baker, M. Okandan, and J. Muthuswamy. "Long-term neural recordings using MEMS based movable microelectrodes in the brain". *Frontiers in neuroengineering* 3 (2010).

[77] P. Lotfi, K. Garde, A. K. Chouhan, E. Bengali, and M. I. Romero-Ortega. "Modality-specific axonal regeneration: toward selective regenerative neural interfaces". *Frontiers in neuroengineering* 4 (2011).

[78] S. Luan and T. G. Constandinou. "A novel charge-metering method for voltage mode neural stimulation". IEEE, 2012, pp. 2239–2242.

[79] R. K. Shepherd, J. Matsushima, R. E. Millard, and G. M. Clark. "Cochlear pathology following chronic electrical stimulation using non charge balanced stimuli." *Acta Otolaryngol* 111 (1991), pp. 848–60.

[80] J.-J. Sit and R. Sarpeshkar. “A Low-Power Blocking-Capacitor-Free Charge-Balanced Electrode-Stimulator Chip With Less Than 6 nA DC Error for 1-mA Full-Scale Stimulation”. *Biomedical Circuits and Systems, IEEE Transactions on* 1 (2007), pp. 172–183.

[81] S. Luan and T. G. Constandinou. “A charge-metering method for voltage-mode neural stimulation”. *Journal of neuroscience methods* 224 (2014), pp. 39–47.

[82] T. Stieglitz. “Manufacturing, assembling and packaging of miniaturized neural implants”. *Microsystem Technologies* 16 (5 2010). 10.1007/s00542-009-0988-x, pp. 723–734. ISSN: 0946-7076.

[83] J. C. LaManna, K. A. McCracken, M. Patil, and O. J. Prohaska. “Stimulus-activated changes in brain tissue temperature in the anesthetized rat”. *Metabolic brain disease* 4.4 (1989), pp. 225–237.

[84] M. Ghovanloo. “An overview of the recent wideband transcutaneous wireless communication techniques”. Vol. 2011. 2011, p. 5864.

[85] R. Bashirullah. “Wireless implants”. *Microwave Magazine, IEEE* 11 (2010), S14–S23.

[86] M. R. Mhetre, N. S. Nagdeo, and H. Abhyankar. “Micro energy harvesting for biomedical applications: A review”. Vol. 3. 2011, pp. 1–5.

[87] M. Kiani and M. Ghovanloo. “A 13.56-Mbps Pulse Delay Modulation Based Transceiver for Simultaneous Near-Field Data and Power Transmission” (2014).

[88] *The Modular Prosthetic Limb*. `http://www.jhuapl.edu/prosthetics/scientists/mpl.asp`. 2014.

[89] C. Cipriani, M. Controzzi, and M. C. Carrozza. “The SmartHand transradial prosthesis”. *Journal of neuroengineering and rehabilitation* 8 (2011), p. 29.

[90] M. C. Carrozza, F. Vecchi, F. Sebastiani, G. Cappiello, S. Roccella, M. Zecca, R. Lazzarini, and P. Dario. “Experimental analysis of an innovative prosthetic hand with proprioceptive sensors”. 2003, pp. 2230–2235.

[91] B. Siciliano and O. Khatib. *Springer Handbook of Robotics*. Springer-Verlag Berlin Heidelberg, 2008.

[92] R. K. Mittal and I. J. Nagrath. *Robotics and Control*. Tata McGraw-Hill, 2003.

[93] M. Gonzalez-Fernandez. “Development of Upper Limb Prostheses: Current Progress and Areas for Growth”. *Archives of physical medicine and rehabilitation* 95.6 (2014), pp. 1013–1014.

4 Computationally Efficient Modelling of Proprioceptive Signals in the Upper Limb

4.1 Introduction

Ultimately the ideal for a sensory neural prosthesis would be to mimic all naturally occurring afferent neural patterns and stimulate the appropriate neurons with those patterns – providing the user with comprehensive feedback that is as intuitive as possible. However, major obstacles remain to be overcome, and it seems likely that neural prostheses will rely on the brain's ability to interpret limited and abnormal feedback for some time yet.

The best near-term solution for providing proprioceptive feedback to prosthesis users is an active area of research and there are numerous challenges both in implementing and in comparing alternative methods. At a top level the two main approaches can be summarised as sensory substitution feedback and neural feedback.

As discussed in Chapter 2, sensory substitution methods provide limited and unnatural feedback and despite numerous sensory modalities being researched over the decades, this approach has so far achieved little clinical success. Neural feedback offers an alternative approach, albeit one that is significantly less mature. Early efforts have focused on stimulation that is linearly or logarithmically correlated with either force or joint angle – a relatively simple approach that has been shown to be interpretable by a human user [1, 2]. However, in these experiments, targeting proprioceptive neurons was a lower priority and the stimulation patterns were unrepresentative of recorded patterns from proprioceptors (due to non-linearities in limb biomechanics and receptor firing patterns). As a result the functional benefit to the user is strongly dependent on the user's ability to learn and interpret these unnatural sensations. This is similar in many ways to the situation with sensory substitution, however, the ability to stimulate nerves and neural pathways that may otherwise be silent and which would have carried information from similar parts of the body prior to amputation, may offer some advantages.

Our concept for a proprioceptive prosthesis (as discussed in Chapter 3) also uses neu-

Parts of this chapter have been previously published in:

- I. Williams and T. G. Constandinou. "Computationally Efficient Modelling of Proprioceptive Signals in the Upper Limb for Prostheses: a Simulation Study". *Frontiers in Neuroscience* 8 (2014), p. 181
- I. Williams and T. G. Constandinou. "Modelling muscle spindle dynamics for a proprioceptive prosthesis". *Engineering in Medicine and Biology Society (EMBC), 2013 35th Annual International Conference of the IEEE*. IEEE. 2013, pp. 1923–1926

ral feedback, however, it instead aims to mimic the function and signals of the body's proprioceptors. This is an approach that is inspired by research into cochlear and retinal prostheses where efforts to mimic the function and signals of specialised neurons is an active area of focus. This mimicking of natural neural function and signals is aimed at enhancing the user's ability to interpret the feedback – the brain's ability to adapt and learn is impressive, but fitting in with its pre-existing neural processing is expected to offer better performance. This progression, (from simple graded stimulation to systems of modulation that mimic natural patterns) has not yet been addressed for proprioception, despite tantalising indications that limited but appropriate neural stimulation can generate limb state representations in the brain [3].

The work presented in this chapter focuses on the processing element of our proposed sensory neural prosthesis – translating the input of electrical signals from man-made sensors into the output of neural signal patterns that will be stimulated in the user's body. The aim being to create a real time model of proprioceptive signals from these receptors to demonstrate its feasibility and to support future work investigating the possible benefits of mimicking natural signals. Our proposed implementation involves mapping the motion of a prosthetic onto a model of the human arm so that estimations of tissue deformation and receptor modulation can be calculated. This mimics the process in the human body where generation of proprioceptive neural signals is implicitly linked with musculoskeletal biomechanics as well as muscle and proprioceptor dynamics [4] and is an approach that shares much in common with neuro-musculoskeletal models developed for research in the field of human motor control [5–9].

The integration of sensory feedback models with representations of musculoskeletal components is still a relatively new field and most publications have focused on the lower limb and locomotion. Upper limb models considering only 1 degree of freedom have previously been proposed [7–9] and a more complex three degree of freedom, 15 muscle "Virtual Arm" model covering shoulder and elbow joints was proposed by Song et al. [5]. These studies focus on understanding limb motion and control and therefore simplifications and qualitative representations of proprioceptive signals are used which are unlikely to be suitable for implementation in a proprioceptive prosthesis due to limitations that include: using models fitted to feline firing patterns despite much lower observed firing rates in humans; using individual receptor or ensemble firing patterns interchangeably even though there may be multiple orders of magnitude difference between the two; and using simple piecewise linear approximations to population firing rates that do not capture the observed dynamics or non-linearities of proprioceptive receptors. These models also have muscle activation or excitation as inputs, and limb movement as the output. However, in a proprioceptive prosthesis the situation is reversed with limb movement as an input and muscle activation an unknown. The addition of static optimisation (an inverse dynamics tool) is proposed here to estimate muscle forces & activations. However, inverse dynamics problems are computationally demanding – even systems operating many times slower than real time on desktop computers are considered efficient [10] – making them unsuited to the real-time, portable and low-power nature of a proprioceptive prosthesis and as such approximations

are proposed to address this.

This chapter will first look at the field of neuro-musculoskeletal modelling, discussing the top level design and choice of component biomechanical and receptor models; then the actual system proposed here is presented along with model results and finally these results are examined along with a discussion of remaining issues, limitations and areas of further work.

4.2 Neuro-musculoskeletal modelling

The outline of the proposed processing model is shown in Figure 4.1. It consists of 2 biomechanical and 2 receptor sub-models, the purpose of which are described below.

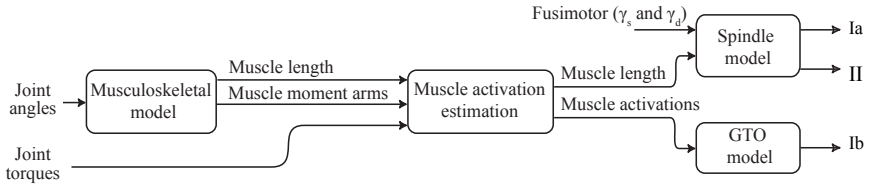


Figure 4.1: Outline of the modelling presented here, showing inputs from sensors (left) being translated into predictions of neural firing patterns (right).

4.2.1 Musculoskeletal modelling

The musculoskeletal model describes the physical structure and characteristics of the modelled arm, allowing estimation of internal forces, torques and tissue deformation. They typically consist of a mathematical description of a system with stiff segments (representing bone) connected by mechanisms that impose kinematic constraints (representing joints) and actuated by contractile elements (representing muscles and tendons).

There are a wide range of musculoskeletal models in the literature as necessitated by the wide range of problems the models are used to address. Typically for studies of gross limb movement the models assume the segments are rigid and describe them in terms of a wrapping surface (so that physiologically impossible overlaps of bones and muscles do not occur), combined with a mass and a moment of inertia matrix (to model the mass distribution). Joints are generally assumed to be composed of one or more uni-axial pin joints with orthogonal axes of rotation [11] (although some models also consider non-rotational translation at the joints such as rolling or sliding) and are often described in terms of the location and axis of their centre of rotation along with a set of kinematic constraints. Meanwhile muscles are treated as massless, frictionless connectors of variable length which run between the muscles origin and insertion points, while wrapping round simple geometric shapes, running via specified points or within specified constraints.

Once the system has been described, the system mechanics are typically modelled in a matrix and polar form of Newton's law of motion ($F = ma$):

$$\mathbf{T}(\mathbf{q}) = \mathbf{M}(\mathbf{q}) \cdot \ddot{\mathbf{q}} + \mathbf{C}(\mathbf{q}, \dot{\mathbf{q}}) + \mathbf{G}(\mathbf{q}) + \mathbf{E} \tag{4.1}$$

where $\mathbf{q}, \dot{\mathbf{q}}, \ddot{\mathbf{q}}$ are the joint angles, velocities and accelerations; $\mathbf{T}(\mathbf{q})$ is the vector of joint torques; $\mathbf{M}(\mathbf{q})$ is the mass matrix;$\mathbf{C}((\mathbf{q}, \dot{\mathbf{q}})$ represents the centrifugal and coriolis forces; $\mathbf{G}(\mathbf{q})$ the gravitational forces; and $\mathbf{E}$ represents any external forces [12].

However, for a proprioceptive prosthesis $\mathbf{q}, \dot{\mathbf{q}}, \ddot{\mathbf{q}}$ and $\mathbf{T}(\mathbf{q})$ will be directly measured and calculation of the centrifugal, coriolis, gravitational and external forces is unnecessary. Instead the focus of the biomechanical modelling is on calculating the muscle fibre lengths (for spindle modelling) and resolving the joint torques into a muscle forces vector ($\mathbf{F_{MT}}$) and muscle moment arms matrix ($\mathbf{R}(\mathbf{q})$) where:

$$\mathbf{T}(\mathbf{q}) = \mathbf{F_{MT}} \cdot \mathbf{R}(\mathbf{q}) \tag{4.2}$$

The moment arm of a muscle around a joint it actuates is defined as the distance between the muscle's line of action and the joint's centre of rotation. The moment arm matrix is a representation of each muscle's ability to actuate each joint and can be directly calculated from the pose of the musculoskeletal model, however, the selection of a force vector that satisfies the equality (in Eqn. 4.2) for calculating the joint torques is a non-deterministic problem (with infinite solutions) and is discussed further in section 4.2.2

Several musculoskeletal models of the upper limb have been proposed and parameterised [13–19]. Many of these focused on the complex shoulder joint and included some of the muscles spanning the elbow joint, however, a few also (or exclusively) cover the elbow, wrist and some of the hand joints along with the actuating muscles [16, 17, 19].

Muscle model

Muscles are intricate and complex, and as such biomechanical models need to greatly simplify them to make them computationally tractable. In addition to the simplifications at the musculoskeletal model level (massless and frictionless), it is also generally assumed that all fibres are straight, parallel, of equal length and coplanar. The variation in muscle shapes (and the changes in muscle shape during contraction) are typically covered by considering the angle the fibres make with the tendon (pennation angle – see Fig. 4.2) and altering this according to the muscle state [20]. Muscle models also assume all muscles can be represented as scaled versions of a single representative fibre, allowing models to describe any muscle using a relatively short set of parameters.

The purpose of the muscle model is to describe the force production capability of the various muscles in any given state. Two main classes of models have been implemented in the literature – an empirically derived phenomenological (Hill) type and a physical (cross-bridge) type [20, 22]. To understand the basis for each it is helpful to look at the composition and function of a muscle.

The structure of a muscle is shown in Figure 4.3, at a top level it is composed of muscle

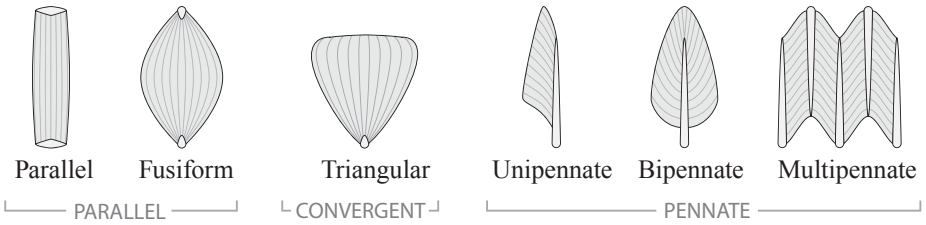


Figure 4.2: A selection of muscle architectures illustrating how pennation angles vary (reproduced from [21]).

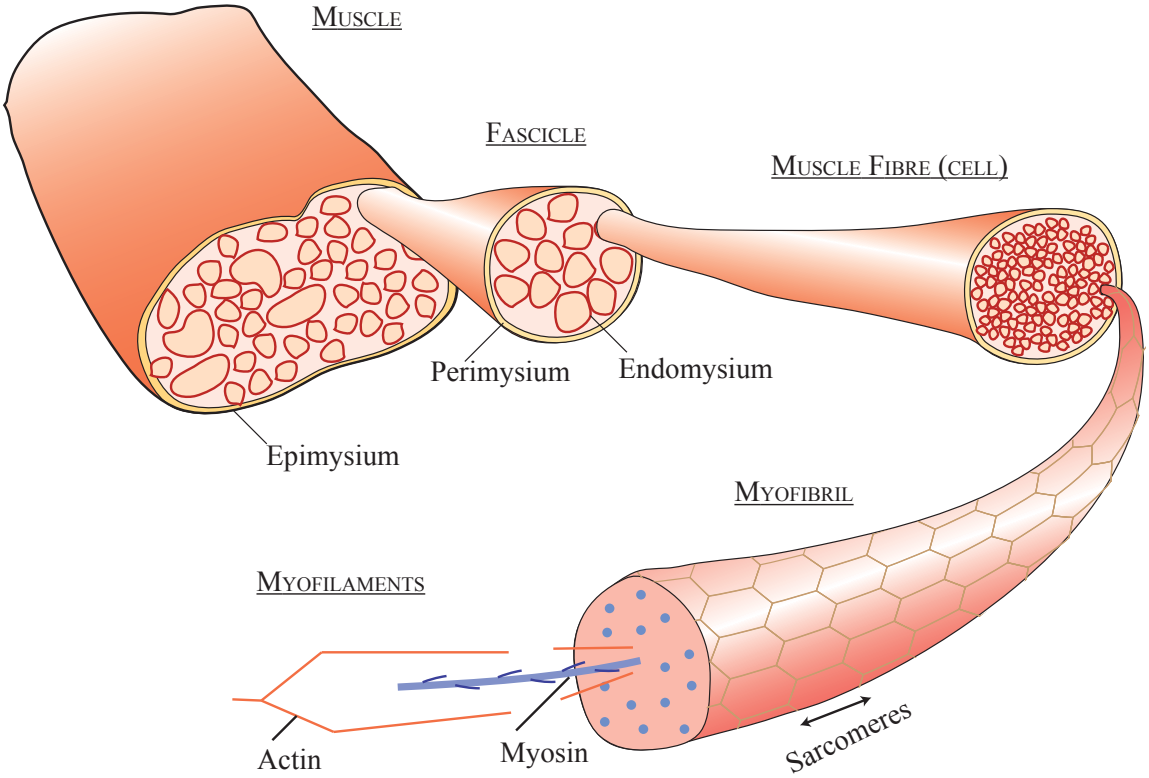


Figure 4.3: The structure of a muscle (adapted from [23]).

fibres wrapped in three layers of connective tissue. The endomysium wraps around individual muscle fibres, the perimysium groups these encapsulated fibres into fascicles and finally the epimysium bundles these fascicles together – forming the exterior of a muscle. However, the muscle fibre is not the fundamental component of a muscle contraction; instead each individual fibre is composed of groups of myofibrils which are in turn made of smaller sub-units called sarcomeres. These sarcomeres are the fundamental blocks of force generation, with each containing thick filaments of myosin and thin filaments of actin.

In 1957, A. F. Huxley proposed that the underlying process in muscle contraction is the formation and movement of cross-bridges between the myosin heads of thick filaments and the actin thin filaments. The presence of Adenosine Tri-Phosphate (ATP) then enables a process whereby the myosin heads walk along an actin filament in a sliding motion, allowing the sarcomeres to be shortened by up to 70% without the filaments themselves actually changing length.

In looking at muscle composition it is also important to consider tendons – which connect

muscle and bone. These elastic tissues are composed of dense fibrous connective tissue largely consisting of collagen and are generally considered in models as an elastic element with a non-linear stress-strain relationship.

Ultimately as gross simplifications, all muscle models fall short of representing observed muscle behaviour [11]. The aim in choosing a model for a particular implementation is rather finding one that is sufficiently accurate and useful. The empirical Hill-type model approach is often preferred for macroscopic modelling in systems with multiple muscles due to the low computational requirements [24]. Whereas the biochemically based cross-bridge approach is more often used for understanding the properties of microscopic contractile elements in a single muscle [21]. For a proprioceptive prosthesis, the focus is on large scale movement in a complex system of muscles, as such the Hill-type model is preferred.

The empirical Hill-type model considers any muscle as a scaled version of a template "normalised" muscle with 3 components: a series elastic element (the tendon), a parallel elastic (the epimysium) and a contractile element (see Fig. 4.4(a). The tension produced by the contractile element and parallel elastic element are modelled in terms of the muscle activation (a); three non-linearities ($f_l(\bar{L^M})$, $f_{pe}(\bar{L^M})$ and $f_v(\bar{v^M})$ – see Fig. 4.4(d) and (e) describing how the muscle force varies with the normalised muscle length ($\bar{L^M}$) and rate of contraction ($\bar{v^M}$) respectively; and F_o the maximum isometric force produced by the muscle:

$$F = \Big[a \cdot f_l(\bar{L^M}) \cdot f_v(\bar{v^M}) + f_{pe}(\bar{L^M})\Big] F_o \tag{4.3}$$

The muscle activation (a) is a normalised value between 0 and 1 representing how strongly the muscle is contracting. The rate at which this activation varies can be accounted for using a method proposed by Thelen [25]. In that paper an idealised neural excitation signal to the muscle (u) was used as an input and the muscle activation (a) was modelled by a non-linear first order differential equation:

$$\frac{da}{dt} = \frac{u - a}{\tau_a(a, u)} \tag{4.4}$$

where τ_a is a time constant that varies depending on the muscle activation level and on whether the activation level is increasing or decreasing:

$$\tau_a = \begin{cases} \tau_{act}(0.5 + 1.5a) & u > a \\ \tau_{deact}/(0.5 + 1.5a) & u \leq a \end{cases} \tag{4.5}$$

where τ_{act} is 15 ms and τ_{deact} is 50 ms.

4.2.2 Muscle activation estimation

It has been widely noted that there is redundancy in the human musculoskeletal system and hence there is typically not a unique combination of muscle forces to generate any particular motion or set of joint torques. The situation is further complicated by the fact that muscles are often multi-articular and produce moments around each of the joints they span. Methodologies such as static or dynamic optimisation (which rely on minimising

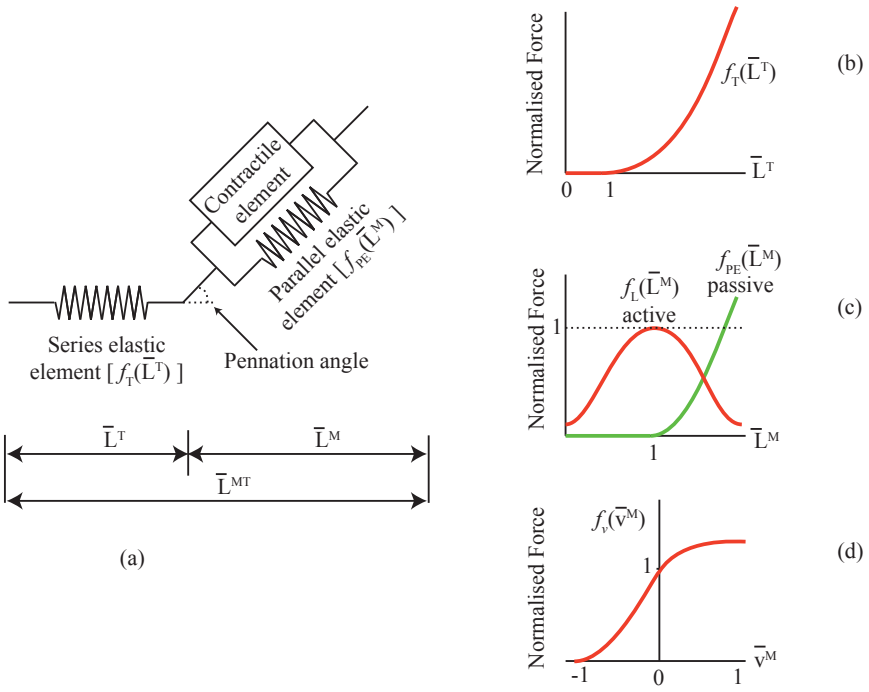


Figure 4.4: (a) 3 component Hill-type model standard configuration (b) The tendon force-length relationship. (c) The muscle active (contractile element) and passive (parallel elastic element) force-length relationship. (d) The force-velocity relationship.

or maximising some optimisation criteria [12]) are used to address this redundancy and complexity problem.

Static optimisation involves formulating the set of simultaneous equations:

$$\mathbf{T}(\mathbf{q}) = \mathbf{F_{MT}} \cdot \mathbf{R}(\mathbf{q}) \tag{4.6}$$

for a single instant in time and finding a solution which minimises or maximises the optimisation criteria. Both static and dynamic optimisation have been shown to be robust methods for estimating muscle activations [26, 27], however, static optimisation is computationally more tractable than dynamic optimisation, and also better suited to a real time system like a proprioceptive prosthesis.

4.2.3 Receptor modelling

As noted in Chapter 3, proprioceptor models have been under development since at least the 1960s and over the years many variations have been proposed. Two possible problems with all the models identified are that: 1) the models have focused on modelling the observed neural response of average responses of individual receptors to imposed movements; 2) the models have been fitted to data obtained from experiments on specific muscles in cats.

The response of individual receptors are often qualitatively similar but quantitatively vary widely. This has led to the theory that accurate feedback of limb movement to the CNS is encoded in the neuronal population response rather than any individual receptor signal and that integration in the CNS averages out this variation (and possibly even derives

benefit from it) [28, 29]. The system concept proposed in Chapter 3, aims to achieve neural selectivity at the fascicular level (i.e. will stimulate the collection of neurons in a fascicle with the same pattern). We propose that the stimulation pattern applied should be based on the ensemble average (equivalent to the average individual response) on the assumption that integration in the CNS would interpret this similarly to the variable population signal. However, this remains an area requiring further experimental investigation as only a small subset of the population of proprioceptive neurons will be carrying this feedback and it is unclear how the synchronously generated action potentials will be interpreted in the CNS.

Feline muscle spindle & GTO morphology and function is very similar in humans and felines. Observed firing patterns are also qualitatively similar, however, the actual neuronal firing rates in cats appear to be significantly higher than have been observed in humans. It is therefore likely that modifications will need to be made to proposed models to fit them to human data and to generalise them to a range of muscles.

Muscle spindle model

Models linking muscle stretch to spindle firing rates go back to at least the 1960's [30]. Initial attempts tended to focus only on spindle response to a single set of motions e.g. small/large, fast/slow sinusoidal or ramp and hold stretch. As time passed more complex models appeared that were designed to fit data from a variety of imposed stretches and naturally occurring motions. Numerous models have been proposed (see Table 4.1) and these fall into three broad categories: nonlinear curve fitting, transfer functions, and anatomically derived models. The advantage of the curve fitting and transfer function models is their computational simplicity and many have shown good fits in third party validation, however, all of these models have been fitted to spindle recordings from specific feline muscles and it is not clear how to adapt them to fit data from other muscles or animals. The advantage of an anatomically derived model is it's potential predictive power for other muscles and species. Varying the model's parameters according to anatomical and fundamental spindle characteristics potentially allows the model to be adapted to different species – e.g. human. An anatomical approach does however, generally involve high computational complexity which may be an issue. Another advantage of certain recent anatomic models is their ability to model the influence of fusimotor activity, although the value of this depends on developments in fusimotor modelling.

Fusimotor activity has an important modulating effect on spindle firing rates, however, our understanding of how fusimotor signals vary during motion is limited. Several papers have been published with details of recordings of fusimotor activity from decerebrate cats during walking [41, 42]. A simplistic model of this observed activity has been proposed [43], however, this is based on a very limited data set and fusimotor signals are believed to vary significantly from task to task. Alternatively fusimotor models based on modulating spindle output to track an objective (a linear correlation with joint angle) were examined in [44]. However, there is not a strong case for the proposed objective and the published evaluation did not substantially distinguish between the preferred method of fusimotor modulation and a lack of fusimotor modulation.

Table 4.1: Spindle models in the literature

Paper	Type	Fusimotor	Comment
Matthews & Stein, 1969 [30]	LTF	✗	Small sinusoid fitted
Rudjord, 1970 [31]	Anat.	✗	Secondary afferent only
Chen & Poppele, 1978 [32]	LTF	✗	Small sinusoid fitted
Houk et al, 1981 [33]	NLC	✗	Large ramp fitted
Hasan, 1983 [34]	NLC	✗	
Schaafsma, 1991 [35]	Anat.	✓	Primary afferent only
Otten et al, 1995 [36]	Anat.	✗	
Prochazka, 1998 [37]	NLC	✗	Primary afferent only
Lin & Crago, 2002 [38]	Anat.	✓	Complex to implement
Maltenfort & Burke, 2003 [39]	NLC	✓	
Mileusnic, 2006 [40]	Anat.	✓	Complex to implement, extensive validation in paper

LTF = Linear Transfer Function, Anat. = Anatomical, NLC = Non-Linear Curve fitting

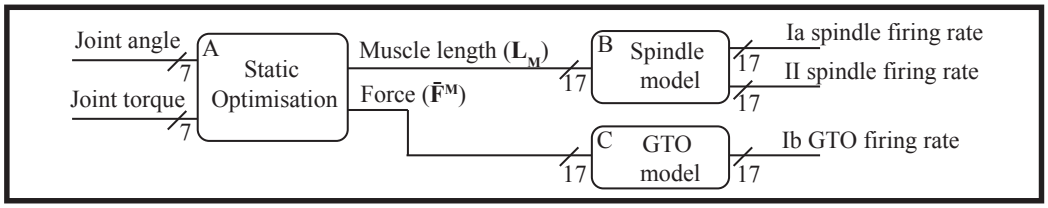
To date there are no convincing models of fusimotor activity and this is probably a result of the paucity of available data recordings. Despite the suspected significant role of the fusimotor system, the omission of this input may not be overly detrimental to a proprioceptive prosthesis as feedback without fusimotor input is analogous to passive motion of a limb. However, as models of fusimotor activity improve it would be desirable to (in future) be able to integrate a model of fusimotor activity.

GTO model

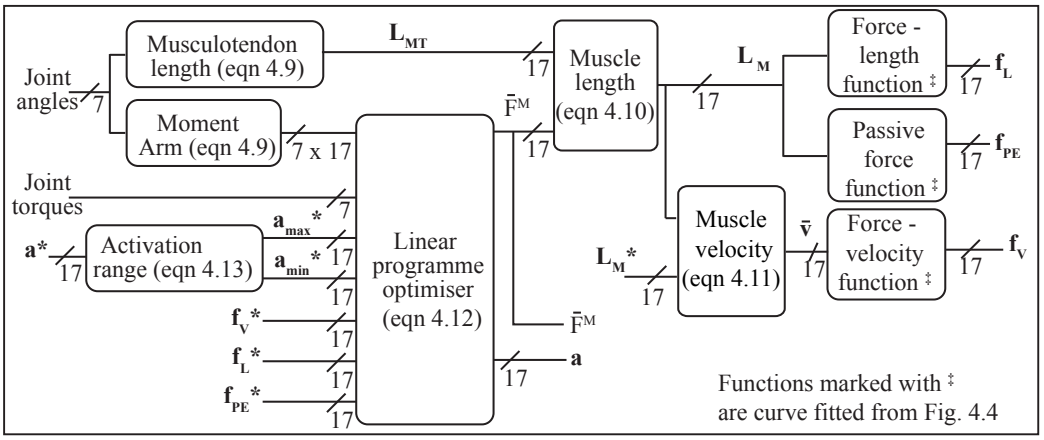
The progress in GTO modelling since the 1960's parallels that of muscle spindle models – starting with simple models fitted to a limited set of motions and gradually becoming more complex and generically applicable. However, there are relatively fewer GTO models in the literature (see Table 4.2) and most are based on a transfer function approach (combined with a non-linear step). A key difference compared to the muscle spindle models is the higher level of complexity involved in the anatomic models. It should be noted that as with the spindle modelling all the models have been parameterised based on recordings from feline receptors in specific muscles and work is required to extrapolate this to other muscles in other species.

4.3 Models and Methods

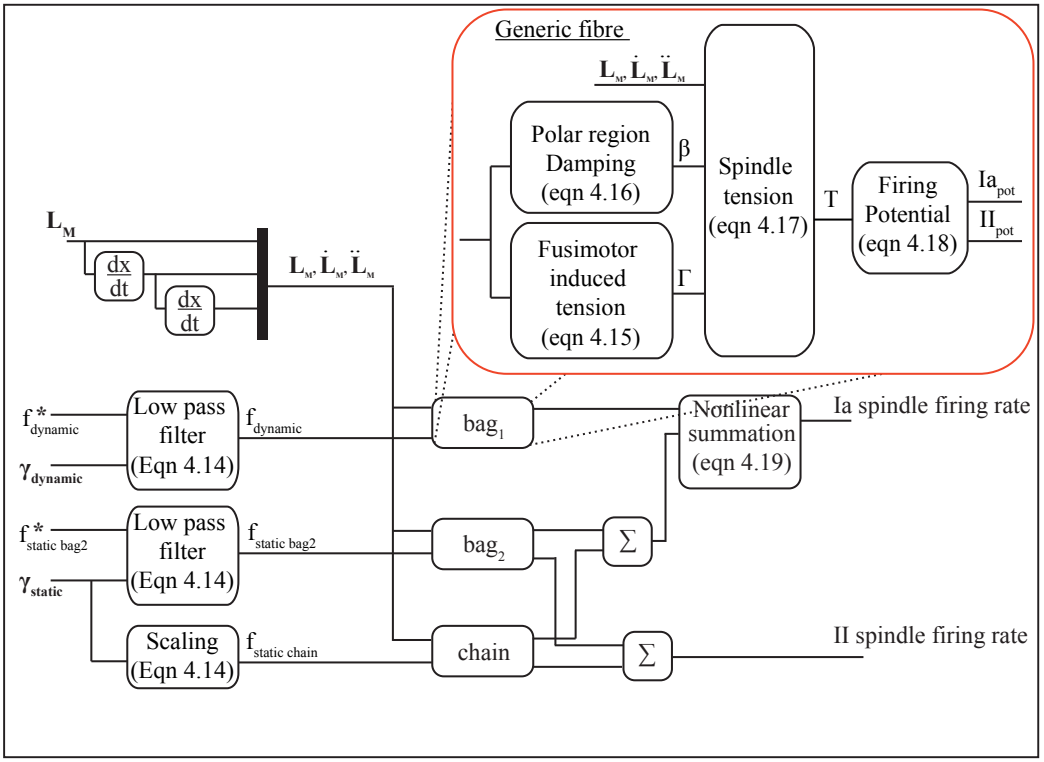
The system described here is shown in Fig. 4.5 and broadly consists of biomechanical modelling combined with 2 previously described proprioceptor models. The sensor data from the prosthetic limb consists of joint angles and torques mapped onto the joints of the modelled human limb; the role of the biomechanical modelling is to convert this data into estimates of muscle length & force. These parameters are in turn converted by the receptor models into estimates of neural firing patterns.



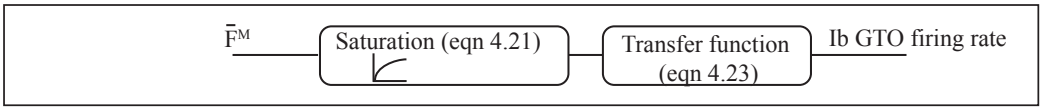
(a) Top Level



(b) Static Optimisation



(c) Spindle model



(d) GTO model

Figure 4.5: The models presented here: (a) System model; (b) Static optimisation model - starred parameters indicate state variable values from previous iteration; (c) Muscle spindle model; (d) Golgi Tendon Organ model. Variable labels are explained in Section 4.3.1.

Table 4.2: GTO models in the literature

Paper	Type	Ensemble / Individual	Comment
Houk & Simon, 1967 [45]	LTF	Individual	Ramp and hold fitted
Anderson, 1974 [46]	LTF	Individual	Single frequency sine wave fitted
Gregory & Proske, 1981 [47]	Anat.	Individual	Limited detail in paper
Lin & Crago, 2002 [38]	LTF	Ensemble	Based on Houk & Simon 1967
Mileusnic, 2006 [48]	Anat.	Individual	Complex to implement
Song, 2008 [5]	LTF	Ensemble	Basic piecewise-linear approximation

LTF = Linear Transfer Function, Anat. = Anatomical

4.3.1 Musculoskeletal model

Skeletal structure

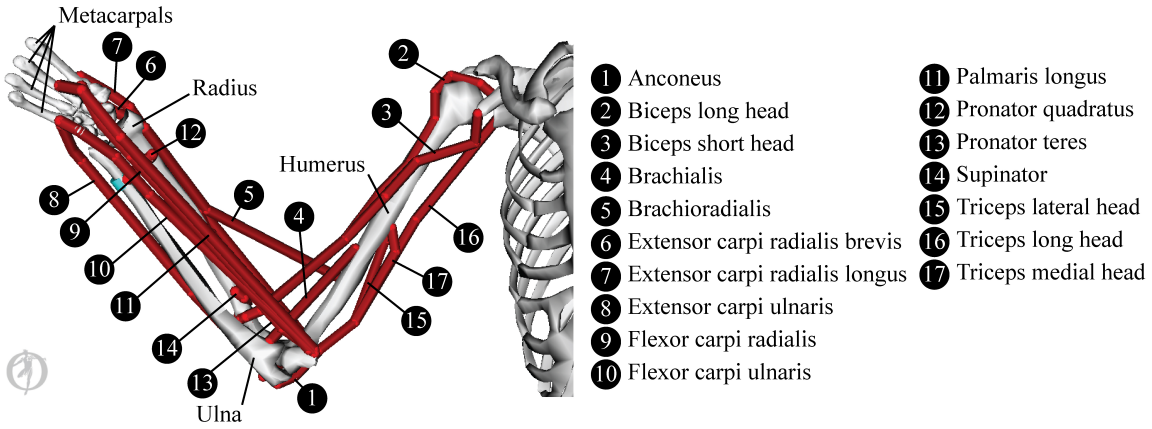


Figure 4.6: The musculoskeletal model

The biomechanical modelling is underpinned by data from a 3D musculoskeletal model of the upper limb in OpenSim [49]. The OpenSim model used here is a reduced form of the Stanford VA Upper Limb model which is based on the measurements and proposals in Holzbaur, Murray, and Delp [50]. This model was preferred because it is based on a wide range of experimental data, has been independently validated, and is compatible with the OpenSim software enabling simple setup, validation and modification. The reduced form of the Holzbaur model is shown in Figure 4.6 and consists of the following skeletal elements: thorax, sternum, scapula, clavicle, humerus, radius, ulna, wrist bones and 2nd to 5th metacarpals; muscles are as indicated in the diagram; and muscle spans are indicated in Figure 4.7. Mass and inertial properties were obtained from [51, 52] and the mass and inertia of the not-included finger and thumb segments were approximated as a lumped mass at the centre of gravity of the hand.

Joints and degrees of freedom

The model covers 7 degrees of freedom in the upper limb: 3 at the shoulder (describing elevation angle, shoulder elevation and shoulder rotation), 2 at the elbow (covering elbow

flexion and forearm pronation) and 2 at the wrist (covering flexion and deviation). Joint kinematics and ranges of motion were unchanged from the original model.

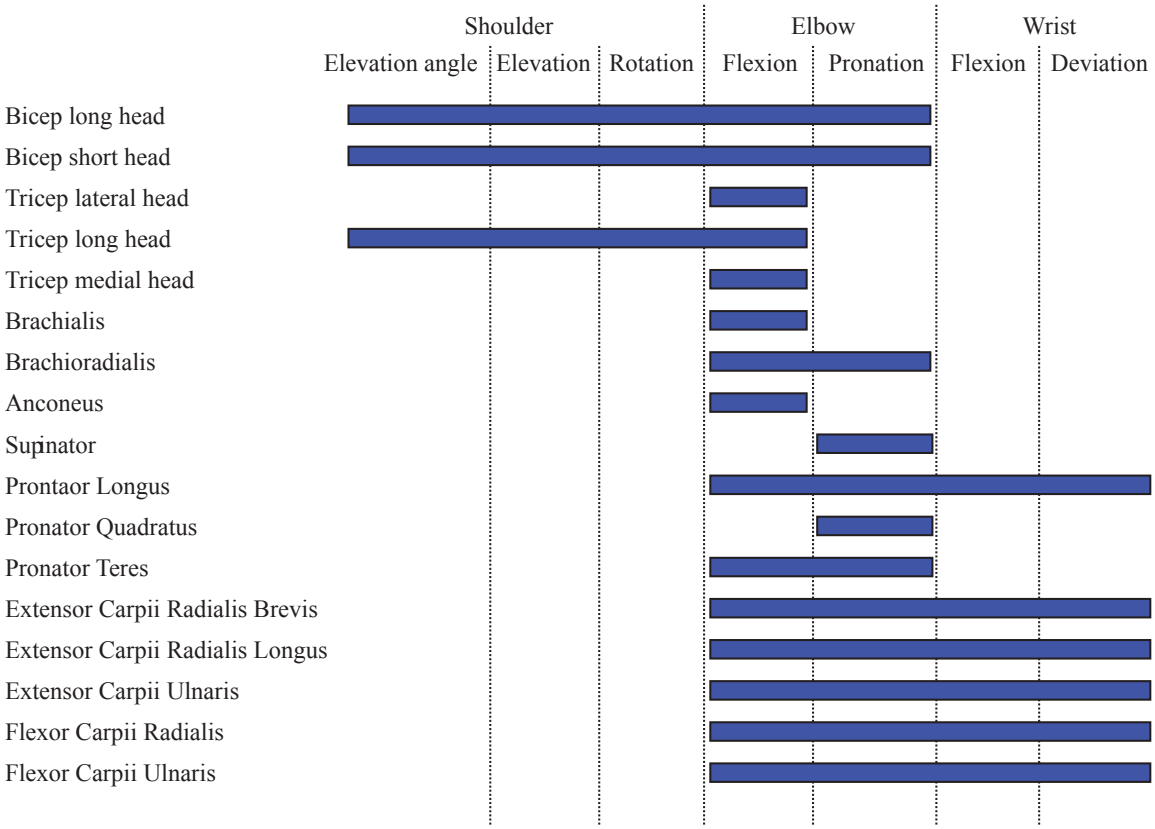


Figure 4.7: The articular span of the muscles in this model.

Muscle model

A standard 3 component dimensionless Hill type muscle model was used and scaled to fit individual muscles as proposed by Zajac [53]. This approach allows all muscles to be modelled by the same functions with the differences between each muscle described by only a few variables. A 0° pennation angle was assumed as measured pennation angles are typically less than 15° for the muscles under consideration and previous analysis has indicated that for angles under 20° the effects of pennation are generally negligible [53, 54]. Normalised muscle length ($\bar{L^M}$), tendon length ($\bar{L^T}$), muscle force ($\bar{F^M}$) and muscle velocity ($\bar{v^M}$), were respectively calculated using:

$$\bar{L^M} = \frac{L^M}{L_o^M}, \quad \bar{L^T} = \frac{L^T}{L_s^T}, \quad \bar{F^M} = \frac{F^M}{F_o^M}, \quad \bar{v^M} = \frac{v^M}{v_{max}^M} \tag{4.7}$$

where L_o^M is the optimal muscle length, L_s^T is the tendon slack length, F_o^M is the muscle's maximum isometric force and v_{max}^M is the muscle's maximum shortening velocity. All muscle paths and muscle insertion points are as specified in the Holzbaur model. Parameters for the muscles were obtained from the Holzbaur model and v_{max}^M was assumed to be 7 times the optimal fibre length (a figure approximately midway between that recorded for slow

and fast twitch fibres [25, 55]).

The torque (T) produced by the 17 muscles (m) around joint (j) is modelled as:

$$T_j = \sum_{m=1}^{17} \left(\left[a_m \,.\, f_l(\bar{L_m^M}) \,.\, f_v(\bar{v_m^M}) + f_p(\bar{L_m^M}) \right] R_{m,j} \,.\, F_{o,m}^M \right) \tag{4.8}$$

where f_l, f_v and f_p are functions describing the muscle's force-length, force-velocity and passive force-length relationships; a_m is the level of muscle activation (between 0 and 1); $R_{m,j}$ is the muscle's moment arm around joint j; and $F_{o,m}^M$ is muscle m's maximum isometric force. Equations for calculating force-velocity, force-length and passive force are as described by Thelen [25].

4.3.2 Biomechanical modelling

Musculotendon length and muscle moment arms

In OpenSim the musculotendon length and muscle moment arms are calculated based on the muscle's origin & insertion points as well as anatomical wrapping points and constraints. However, running a 3D model is computationally intensive. A more efficient approximation, based on fitting a polynomial surface to the length-joint angles relationship, and another for the moment arm-joint angles relationship was described in [56].

In order to determine the polynomial coefficients for this relationship, the OpenSim musculoskeletal model was swept through the full range of possible poses of all the various joints and at each pose the lengths and moment arms of all the muscles were recorded. This data was then processed in Matlab with the polyfitn function to generate polynomial surfaces fitted to this data. The polyfitn function outputs the polynomial surface coefficients (c_i^L for length and c_i^{MA} for moment arm) relating the musculotendon lengths (L^{MT}) and muscle moment arms ($R_{m,j}$) to the joint angles (q_j) for muscle m such that:

$$L_m^{MT} = \sum_{i=1}^{N^L} c_i^L \prod_{j=1}^{7} q_j^{e_\theta^L} \quad , \quad R_{m,j} = \sum_{i=1}^{N^{MA}} c_i^{MA} \prod_{j=1}^{7} q_j^{e_\theta^{MA}} \tag{4.9}$$

where N^L and N^{MA} are the number of polynomial terms for length and moment arm respectively, while e_θ^L and e_θ^{MA} are the integer exponents for length and moment arm respectively. A cubic polynomial fit was used, therefore giving e_θ^L and e_θ^{MA} values between 0 and 3.

In order to obtain a good fit with these curves, a high number of data points (model poses) is required. However, the number of data points increases exponentially with the number of joints causing the computation time to become impractical. To circumvent this, the model poses were considered in two halves, the first half covering the three shoulder joints and two elbow joints and the second half overlapping by covering the two elbow joints and two wrist joints. The basis for this split is that a muscle's length and moment arm are only affected if a joint spanned by that muscle is rotated. As can be seen in Figure 4.7, this allows muscle length and moment arm curves for eleven muscles to be calculated in the first sweep and fourteen muscles in the second (eight of the muscle curves are fitted

twice and produced identical fitting equations).

The length of the muscle (L^M) was calculated from the musculotendon length, by subtracting an estimate of the tendon length under tension. This estimate of tendon length was based on the recorded strain curve of normalised tendons as described in [25]. For efficient modelling this force strain relationship was approximated by computing the equilibrium position (removing differential equations) using a cubic polynomial fitted to the strain curve:

$$\bar{L^T} = 0.04879\bar{F^M}^3 - 0.1009\bar{F^M}^2 + 0.1003\bar{F^M} + 1 \tag{4.10}$$

Normalised muscle velocity was calculated using the equation:

$$\bar{v} = \frac{\bar{L^M} - \bar{L^M}^*}{\delta t} \tag{4.11}$$

where δt is the timestep between iterations of the model.

Muscle activations and forces

As discussed in Section 4.2.2, due to the real time nature of this system, the static optimisation technique will be used to address the redundancy in the simultaneous equations governing muscle activation. A key factor in determining the accuracy and speed of this technique is the choice of optimisation function. Probably the simplest proposed optimisation criteria is to try to minimise the total amount of muscle activation ($\sum_{m=1}^{17} a_m$). This approach has the advantage of being linear and hence solvable by fast linear programme solvers, however, this optimisation approach does not produce results that are representative of observed patterns of muscle activation [57]. There is still no clear agreement on the best optimisation criteria for all joints, motions and loads, however, representative muscle activations have been produced by systems minimising sum of activation squared, cubed or to a higher order polynomial ($\sum_{m=1}^{17} a_m^n$ where n is an integer greater than 1). However, solving these criteria requires significantly higher computational power than the linear criteria. In [57], Rasmussen proposed using a min-max optimisation criteria which approximates the high order polynomial, but which can be solved using efficient linear techniques. This optimisation criteria can be formulated by introducing an artificial criterion variable(γ):
Minimise γ subject to:

$$\begin{aligned}
&a_m \leq \gamma, \quad \forall m \in \{1, 2, ...17\} \\
&0 \leq a_m \leq 1 \\
&T_j^* = \sum_{m=1}^{17} \left(\left[a_m \,.\, f_l(\bar{L}_m^M) \,.\, f_v(\bar{v}_m^M) + f_p(\bar{L}_m^M) \right] R_{m,j} \,.\, F_{o,m}^M \right), \\
&\forall j \in \{4, 5, 6, 7\}
\end{aligned} \tag{4.12}$$

where, T_j^* is the measured torque around joint j and the muscle activations (a_m) are the variables for the algorithm.

A weakness of this optimisation criteria is that once a minimum γ value has been calcu-

lated, the optimisation process does not try to reduce muscle activations below this value, e.g. if muscle i needs to be fully activated ($a_i = 1, \gamma = 1$) there is no optimisation penalty for setting other muscles to be fully activated. To address this the optimisation criteria was modified, with the new aim being to minimise $\gamma + 0.01 \sum_{m=1}^{17} a_m$.

The open source simplex package lp_solve was used to solve this linear programme around the 4 joints in the elbow and wrist. Given the limited subset of shoulder spanning muscles being modelled (and the target application being a transhumeral amputee with extant shoulder musculature), it was not possible to resolve the torques at the three shoulder joints ($j = 1, 2, 3$). These joints were however included in the system because their configuration influences the lengths of and moments developed by the bicep and tricep muscle groups around the elbow and hence have an impact on all distal muscle activations.

Activation dynamics

In a proprioceptive prosthesis the neural excitation signal (u) is not available, but the muscle activation dynamics are an important constraint in the static optimisation. This problem was resolved by determining the the feasible range of activation levels ($a_{min} \rightarrow a_{max}$) for each muscle after a time dt. This was approximated from the differential equation describing the muscle activation by setting $u = 0$ to determine a_{min} and $u = 1$ to determine a_{max}, giving:

$$\begin{aligned} a_{min} &= a - \frac{dt \cdot a \cdot (0.5 + 1.5a)}{\tau_{deact}} \\ a_{max} &= a + \frac{dt(1-a)}{\tau_{act}(0.5 + 1.5a)} \end{aligned} \tag{4.13}$$

The feasible activation range was calculated for each muscle and included as constraints in the linear programme solver.

4.3.3 Proprioceptor modelling

Muscle spindles

The muscle spindle outputs were simulated using a model based on that proposed by Mileusnic et al [40]. This model was preferred on the basis of its extensive validation, the ability to in future incorporate fusimotor input, and the ability to fit the model to multiple muscles. The model inputs are muscle length (L^M) & fusimotor activation levels (γ_{static} and $\gamma_{dynamic}$).

The conversion of instantaneous fusimotor neural activity into levels of fusimotor activation ($f_{dynamic}$ and f_{static}) is achieved using low pass filters for bag_1 and bag_2 and by direct

scaling for the *chain* fibre:

$$\begin{aligned}
\frac{d(f_{dynamic})}{dt} &= \frac{\frac{\gamma_{dynamic}}{\gamma_{dynamic}+freq_{bag1}} - f_{dynamic}}{\tau_{bag1}} && \text{for } bag_1 \text{ fibre} \\
\frac{d(f_{static})}{dt} &= \frac{\frac{\gamma_{static}}{\gamma_{static}+freq_{bag2}} - f_{static}}{\tau_{bag2}} && \text{for } bag_2 \text{ fibre} \\
f_{static} &= \frac{\gamma_{static}}{\gamma_{static}+freq_{chain}} && \text{for } chain \text{ fibre}
\end{aligned} \tag{4.14}$$

Where $freq$ represents the fusimotor saturation frequency for a particular fibre type and τ represents the time constant of the low pass filtering for a particular fibre.

These calculated levels of activation are then used to estimate the spindle tension due to fusimotor input (Γ) and the damping that occurs in the polar region of the spindle (β):

$$\Gamma = \Gamma_1 \cdot f_{dynamic} + \Gamma_2 \cdot f_{static} \tag{4.15}$$

$$\beta = \beta_0 + \beta_1 \cdot f_{dynamic} + \beta_2 \cdot f_{static} \tag{4.16}$$

Where Γ_1, Γ_2, β_0, β_1 and β_2 are all constants for a particular fibre type.

The model then calculates the tension in the transduction zone of each fibre-type by modelling each of the fibres as a spring-mass system and solving a second order differential equation (equation (6) in [40]). However, euler integration of this differential equation requires a small time step size and therefore a high number of calculations. We propose that the tension in the system can be approximated by assuming that all the stretch happens in the polar regions of the fibre (which have a much lower spring constant) and then calculating the equilibrium tension in the fibres by modifying equation (3) in [40] to:

$$T = M \cdot \ddot{L^M} + \beta \cdot C \cdot (L^M - R - L_o^{sr}) \cdot |\dot{L^M}|^{0.3} \cdot sgn(\dot{L^M}) + K^{pr} \cdot (L^M - L_o^{pr} - L_o^{sr}) + \Gamma \tag{4.17}$$

where T and L^M are variables representing the fibre tension and muscle length respectively and the remaining terms are constants given in the original paper – C is the coefficient of asymmetry in the muscle force-velocity curve, R is the muscle length below which force production is zero, L_o^{pr} and L_o^{sr} are the rest lengths of the polar and sensory parts of the fibre, and K^{pr} is the polar region spring constant). The proposed modification means that there are no differential equations to solve, so the time step for calculating the spindle output can be increased by orders of magnitude and the computational efficiency is likewise improved.

Once the tension has been calculated the model computes the contribution of each fibre-

type to the primary and secondary afferent firing potential using the following equations:

$$\begin{aligned} Ia_{pot} &= G \cdot [\quad \frac{T}{K^{SR}} - (L_N^{SR} - L_0^{SR}] \\ II_{pot} &= G \cdot \Big\{ \quad X \cdot \frac{L_{secondary}}{L_0^{SR}} \cdot [\frac{T}{K^{SR}} - (L_N^{SR} - L_0^{SR}] \\ &\qquad +(1-X) \cdot \frac{L_{secondary}}{L_0^{PR}} \cdot \big[L - \frac{T}{K^{SR}} - L_0^{SR} - L_N^{PR}\big] \Big\} \end{aligned} \tag{4.18}$$

Where G is a scaling term relating a fibre-types transduction zone stretch to the spindle firing rate and X represents the proportion of the secondary afferent on the transduction zone. The secondary (II) firing rate is simply calculated by summing the potential of the bag2 and chain fibres, however, the primary (Ia) firing rate is calculated using a non-linearly summation of the potential from each fibre-type (as indicated in Fig. 4.5(c)) according to:

$$Ia_{rate} = \begin{cases} Ia_{pot(bag1)} + S \cdot (Ia_{pot(bag2)} + Ia_{pot(chain)}) & \text{if } Ia_{pot(bag1)} > (Ia_{pot(bag2)} + Ia_{pot(chain)}) \\ (Ia_{pot(bag2)} + Ia_{pot(chain)}) + S \cdot Ia_{pot(bag1)} & \text{if } Ia_{pot(bag1)} < (Ia_{pot(bag2)} + Ia_{pot(chain)}) \end{cases} \tag{4.19}$$

Where S represents the proportion of the smaller potential that contributes to the firing rate.

The scaling parameter 'G' in the Mileusnic model – maps normalised spindle firing rates to feline data in the paper – and was estimated based on changes in spindle firing rates of up to 150 pulses per second (pps), that occur due to fusimotor stimulation in a feline muscle. There is limited data about the fusimotor sensitivity of human muscle spindle, but the maximum observed change in spindle output due to fusimotor signals has been observed to be < 30 pps [37] and as such we scaled the Mileusnic et al [40] derived values of 'G' by a factor of $\frac{1}{5}$ to better fit human spindle firing rates.

Golgi Tendon Organs

The GTO model used here is based on the model described by Lin and Crago in [38], which in turn is based on work by Houk and Simon [45] studying the feline soleus muscle. The model consists of 2 stages.

Firstly a non-linearity:

$$R^{NL} = k_1.ln(\frac{F^M}{k_2} + 1) \tag{4.20}$$

where R^{NL} is the output of this stage, while k_1 (60 impulses per second) and k_2 (4 Newtons) are constants scaling the GTO firing rate to the force applied. However, these parameters are based on data from the feline soleus muscle, and given the limited amount of data from human recordings it is difficult to determine human appropriate values for these parameters. We propose to modify this non-linearity to use normalised muscle force:

$$R^{NL} = k_1.ln(\bar{F^M}.\frac{F_{o,s}^M}{k_2} + 1) = k_1.ln(\bar{F^M} \cdot k_3 + 1) \tag{4.21}$$

where $F_{o,s}^M$ is the maximum isometric muscle force of the feline soleus (measured as 25.8N [58]), giving k_3 a value of 6.45. In addition we propose to adjust k_1 to reflect the lower observed

firing rates in human GTOs compared to feline GTOs [59]. Feline GTOs have been observed firing at rates of up to 300 pps, but in normal motion don't significantly exceed 120 pps [59]. A review of the literature did not find any examples of human GTOs being subject to tests that would produce maximal firing rates, however, a review of microneurographic recordings showed firing patterns that rarely exceed 50pps in normal motions [59, 60]. We therefore propose a k_1 figure scaled accordingly of 25 pps.

Secondly, the output of the non-linearity is then fed into a linear dynamics transfer function:

$$H(s) = \frac{1.7s^2 + 2.58s + 0.4}{s^2 + 2.2s + 0.4}. \tag{4.22}$$

For efficient implementation this transfer function was transformed into the z-domain in Matlab using a bilinear approximation with a sample frequency of 1 kHz and warped to fit at 6 Hz giving a z-domain transfer function of:

$$H(z) = \frac{1.69942 - 3.39626z^{-1} + 1.69684z^{-2}}{1 - 1.99780z^{-1} + 0.99780z^{-2}}. \tag{4.23}$$

4.4 Results

4.4.1 Model validation

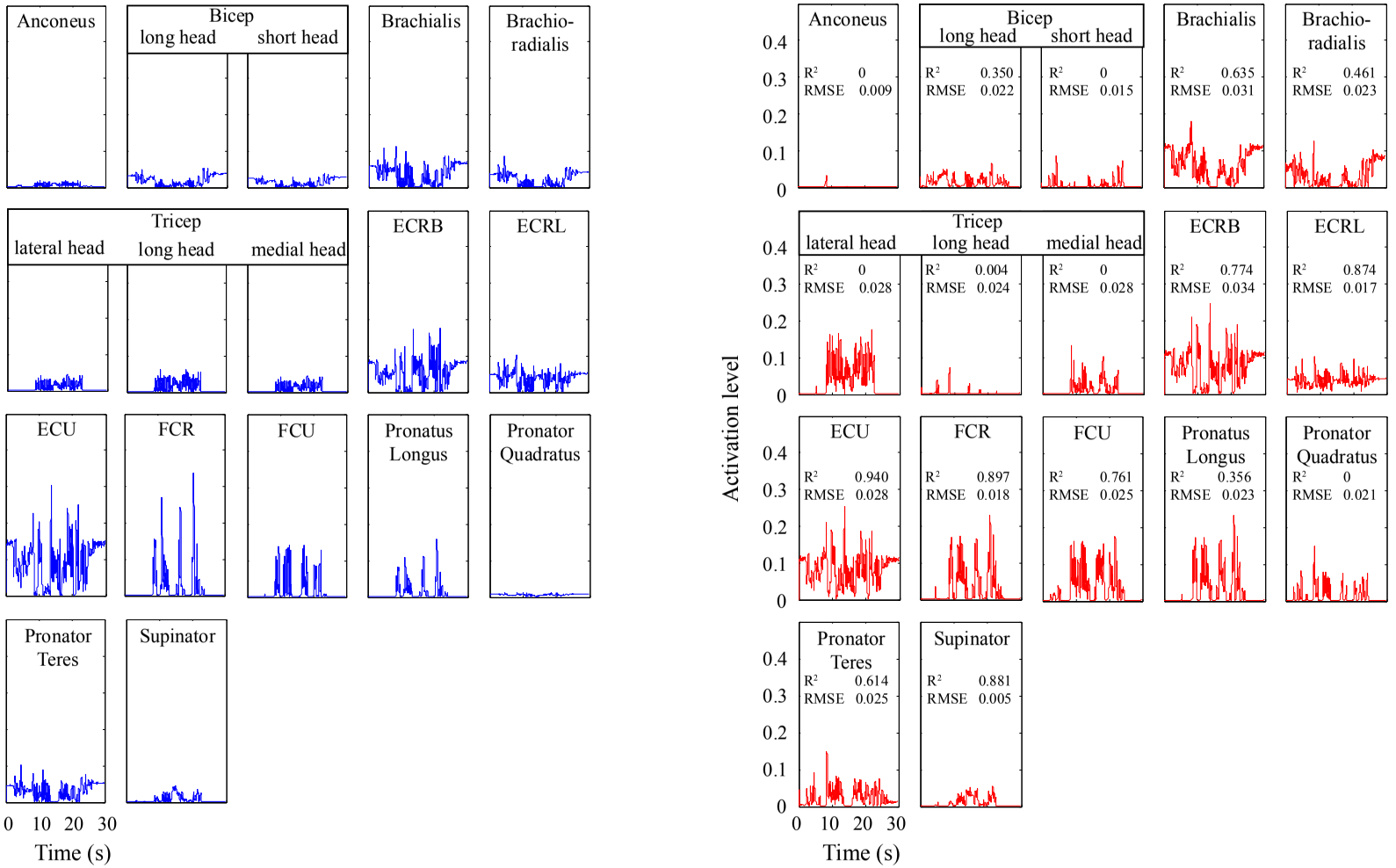
The focus of the work presented here is on choosing and modifying existing validated models to create a real time system. As such the approximations will be validated against the original models and the computational efficiency compared. To generate a dataset for realistic comparison, 30 seconds (at 120 Hz) of motion capture data from the mocapdata.com website (product_id=15044 showing an actor swinging his arms while walking across a room, then brushing his teeth before walking back to the original spot) was scaled, fed into OpenSim and the resulting joint angles for the upper limb were used for all simulations. This data set was chosen because it has a range of fast and slow upper limb motions and because tooth brushing represents an example of where a prosthesis user would not be able to visually monitor their limb and so feedback could provide significant benefit.

Length and moment arm validation

The polynomial approximation for estimating length showed close conformance with the values generated by OpenSim's 3D model throughout the dataset; giving a coefficient of determination (R^2) of in excess of 0.99 for all muscles. The fit of the moment arm approximation was slightly worse with R^2 values of in excess of 0.9 for the two bicep muscles and above 0.98 for all other muscles for the 4 joints of interest.

Static optimisation validation

Fig. 4.8 shows a comparison between a baseline static optimisation tool and results obtained from the model proposed here. The baseline results were obtained by running the built-in OpenSim static optimisation tool using a sum of activation squared optimisation criteria. Muscle forces and moment arms from OpenSim were used to estimate the joint torques at



(a) Standard OpenSim output

(b) Proposed system output

Figure 4.8: Predicted muscle activations for an actor brushing his teeth.

each point in time and these torques were used as the inputs to the model described here. The results indicate the proposed system can produce results qualitatively very similar to existing standard techniques, however, they also show an issue in the load sharing between the tricep muscles (see Discussion).

Spindle model validation

To test how well the equilibrium spindle approximation corresponded to the original Mileusnic et al model, a number of the validation runs from the original paper were repeated and the results are shown in Fig. 4.9 and Fig. 4.10. Differences are generally small and this is consistent with the observed performance for more complex data (as shown in Fig. 4.11), although the proposed spindle model is stiffer and as a result rapid movements do give rise to minor discrepancies - the most notable of which is shown in Fig. 4.9F.

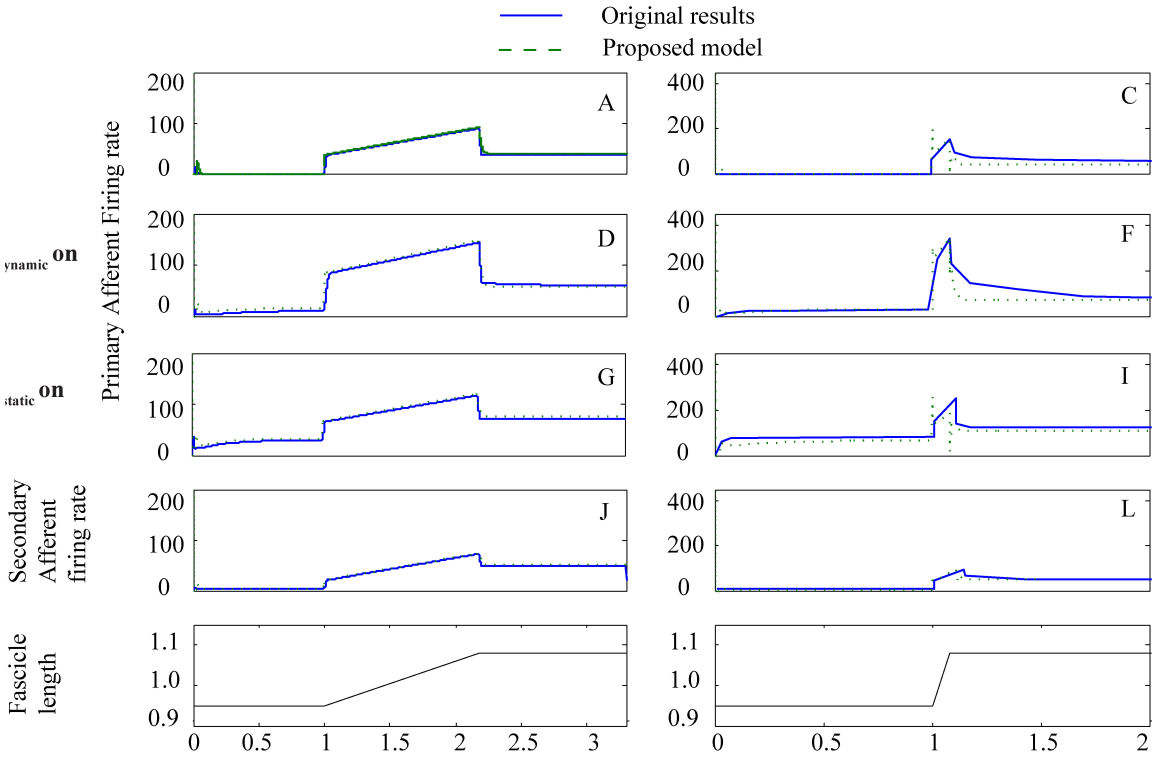


Figure 4.9: Proposed spindle model compared to original results from paper [40] for 2 triangular stretches with different levels of fusimotor activity. Results are from Fig. 3: A, C, D and F showing primary and secondary afferent firing in the presence or absence of static or dynamic fusimotor activation at 70pps.

There is little data available to assess the models performance for human spindles, however, the limited validation possible did highlight a potential limitation of the Mileusnic model which is discussed below. Fig. 4.12 shows a comparison with the recordings, from 2 sets of 9 primary afferents and 2 sets of 7 secondary afferents, published in [62]. The recordings are from the radial nerve during imposed motions about the metacarpophalangeal (MCP) joint. Predicted firing patterns were generated by using the original Holzbaur et al model in OpenSim to estimate the lengths of the two extensor muscles innervated by the radial nerve (extensor digitorum communis interossei (EDCI) and extensor indicis proprius

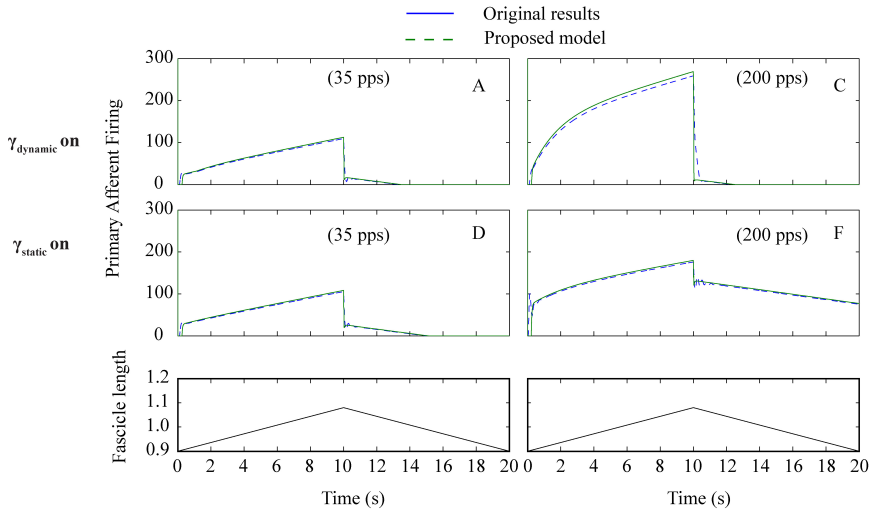


Figure 4.10: Proposed spindle model compared to original results (Fig. 4) from paper [40] for primary afferent undergoing triangular stretches with different levels of fusimotor activity. Labels are as in original paper

(EIP)) during MCP joint motions as described in the paper.

Spindle lengths vary significantly less from muscle to muscle than muscle fascicle lengths do. This discrepancy is possible because the spindle attachment to muscle endpoints or perimysium is varied to provide consistent proprioceptive acuity across a range of joints and muscles [63]. The Mileusnic et al model was optimised for muscles whose fibre length varies above and below the optimal fibre length, whereas both the EDCI and EIP muscles are physiologically constrained to be longer than their optimal lengths. As such the unmodified model overestimates spindle firing rates throughout the range of motion (even in the absence of fusimotor input). Spindle rest and threshold lengths in the model were therefore adjusted to correspond to the fibre length when the MCP joint is in a physiologically neutral position (0° flexion) rather than the optimal muscle length. This approach gives the results shown in Fig. 4.12.

Full system output

The system was run to generate primary afferent and GTO neural signals to enable 3rd party validation of this work, and the neural firing patterns are shown in Figure 4.13(a) and (b). It is intended that in the final system each of these neural firing patterns would be mapped to a set of electrodes (that have been identified as interfacing with the relevant neurons) and commands would be sent to the neural stimulator to generate action potentials at the appropriate frequencies on those electrodes. Update rates for each electrode set are expected to be similar to the maximum stimulation frequency (equivalent to the maximum observed receptor firing rate), i.e. approximately 100 Hz.

Model stability and sensitivity

System stability and sensitivity was tested using an artificially generated motion consisting of a static pose with the elbow at 65° and all other joints at 0° followed by increasing

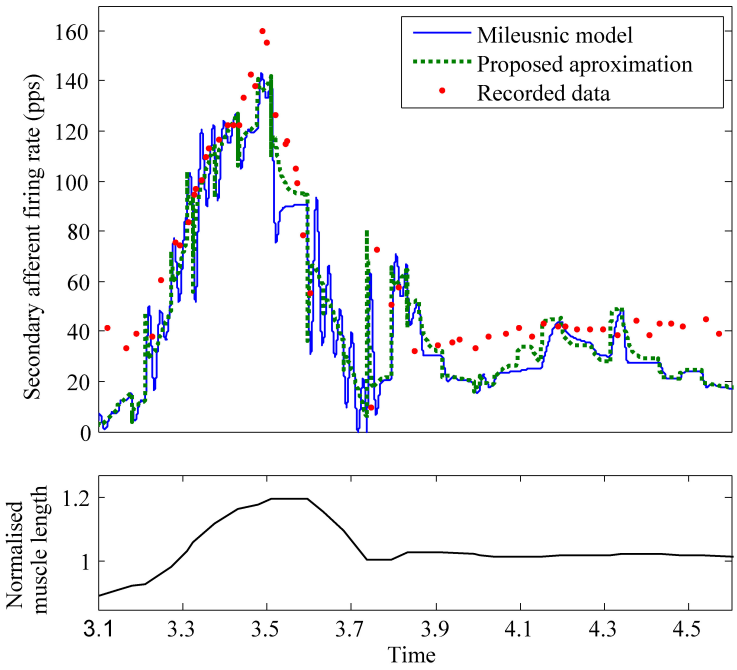


Figure 4.11: Comparison of Mileusnic modelled data and proposed approximation against recorded data from a cat (Fig. 4A of [61]). Fusimotor activity was assumed to be absent.

oscillation of the elbow joint (up to 20° peak to peak) around this set point at a frequency of 6 Hz (chosen to be near the limits of controlled human motion). In order to investigate the impact of sampling frequency on the model, the motion was sampled at 4 different timesteps – 1 kHz, 200 Hz, 100 Hz and 20 Hz – and passed into the model. The results are shown in Figure 4.14 and indicate that the model is stable under all these conditions. Some differences are noticeable at the 20 Hz sampling frequency, however, these appear to result from distortion of the input signal due to the low sampling rate, rather than errors in the model. Conversely at the highest sampling rate, a significant amount of jitter appears on the spindle output and indicates a need for low pass filtering if this output is to be conveyed to the nervous system as an action potential pulse train.

4.4.2 Computational efficiency

Ultimately this modelling will need to be performed on a portable processing platform, and this section looks at the feasibility of implementing it on currently available hardware.

For the purposes of this analysis the code was broken down into 2 parts - a deterministic part and a non-deterministic part. The deterministic part consisting of the newly written code (calculating muscle lengths, moment arms, force-velocity / length relationships, muscle spindle output, etc), while the non-deterministic part of the code (formulating and solving the optimisation linear programme) used an open source library.

The 30 second 120Hz dataset (consisting of 3600 samples) was processed by a 2.1 GHz laptop in under 1.09 seconds (i.e. 27.5 times faster than real time). Profiling showed that 15 % of that time was spent in the deterministic part of the code and 85 % in the non-deterministic optimisation code. A manual estimate of the number of instructions required

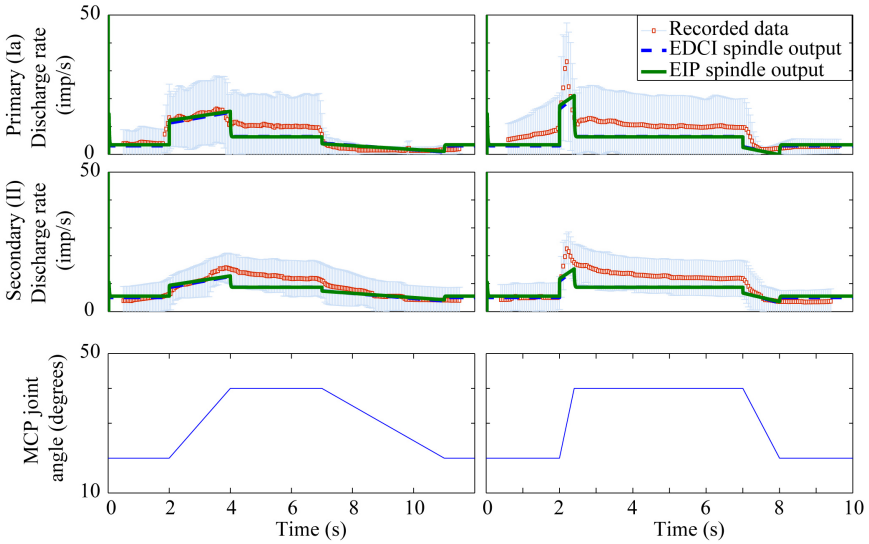
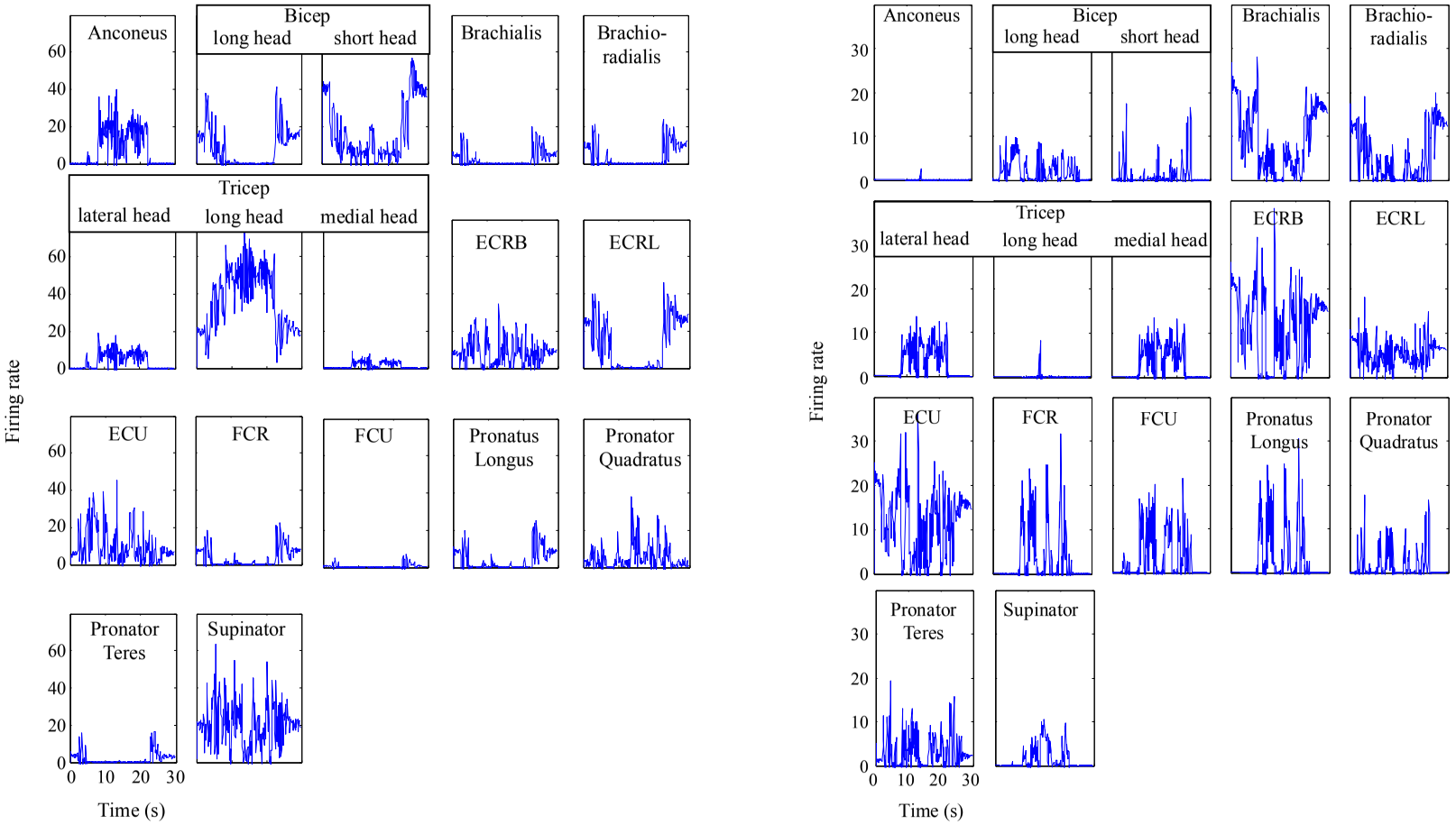


Figure 4.12: Human muscle spindle firing patterns for imposed motions. Mean values and 1 standard deviation error bars are shown for recorded data from [62] and contrasted with modelled primary and secondary spindle firing patterns for the EDCI and EIP muscles. Firing patterns for EDCI and EIP muscles are almost identical. Fusimotor input was assumed to be absent.

to process each time sample (based on the source code) was conducted for the deterministic part of the code – yielding a value of approximately 77000 instructions. A conservative estimate of the total number of instructions (deterministic and non-deterministic) necessary for processing each sample was made based on scaling the estimated number of instructions by the relative processing duration of the deterministic and non-deterministic parts and then multiplying by a factor of 2 – this provided an estimate of 1.03 million instructions per sample. In the final system the sample rate is assumed to be $\leq$100 Hz (on the basis that human voluntary motion occurs at <10hz and this is the maximum update rate to the stimulator so higher rates are unlikely to increase the information provided to the user) giving an estimate of 103 Million Instructions Per Second (MIPS).

Executable size (on a linux desktop) was 645kB when statically linked – an estimated 10% of which was for the bespoke code and 90% for the simplex solver library (based on executable sizes for a dynamically linked version). While peak heap and stack combined memory usage was measured at 576 kB.

The outline minimum requirements for the processing platform are therefore assumed to be a processing rate of 103 MIPS, flash memory of 645 kB and RAM of 576 kB. The relatively high processing rate and memory requirements, rule out a number of 8 & 16 bit low power microcontroller platforms (e.g. the MSP430), but fall within the range of ARM based microprocessors (see Table 4.3) many of which have built in Flexible Static Memory Controllers to support the addition of external flash and RAM. Perhaps unsurprisingly, it is the Cortex M3 and M4 processors (which are targeted at low cost, low power, but relatively high performance embedded applications) that appear to be the most suitable, and the task appears to be well within their capabilities, with an estimated power consumption of 2.2mW.



(a) Predicted primary afferent firing patterns

(b) Predicted GTO firing patterns

Figure 4.13: Predicted proprioceptor firing patterns for the actor brushing his teeth.

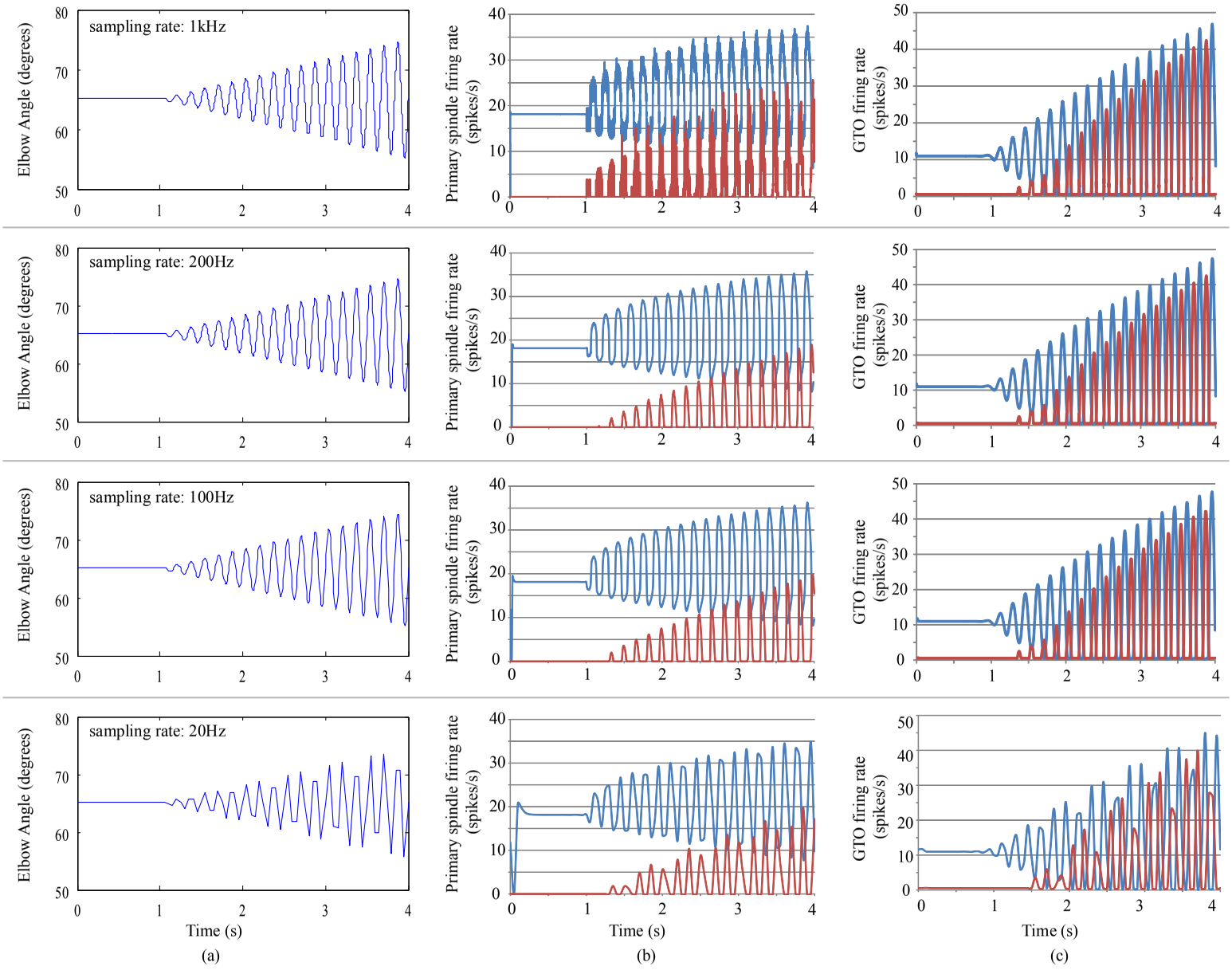


Figure 4.14: The impact of rapid sinusoidal elbow flexion and extension on the model outputs at four different sampling rates (1kHz, 200Hz, 100Hz, 20Hz). (a). Shows the input elbow angle, while (b) and (c) are the spindle and GTO firing rates respectively for the brachialis and extensor carpii ulnaris muscles during this elbow oscillation.

Table 4.3: Comparison of a selection of ARM microprocessors

ARM core	$\mu W/_{Mhz}$*	$DMIPS/_{MHz}$*,**	Max frequency (MHz)***		
			STMicroelectronics	NXP	Freescale
Cortex M0	12.5	0.87	48	50	-
Cortex M0+	9.8	0.95	32	50	75
Cortex M3	32	1.25	120	180	-
Cortex M4	33	1.25	180	204	167
Cortex A5	-	1.57	-	-	500
Cortex A7	-	1.9	-	84	1000
Cortex A9	-	2.5	-	270	1200

* From the ARM product specifications.
** DMIPS – Dhrystone Million Instructions Per Second, where Dhrystone is a synthetic benchmark programme.
*** All figures are from manufacturer websites.

Comparison with standard implementations

Comparisons between the proposed spindle model and a C-code implementation of the standard Mileusnic model (using a standard euler method solver) showed that the majority of the improvement in processing speed was due to differences in the time steps that can be used (rather than reduction in the number of calculations per time step). The standard Mileusnic model can become unstable if too large a time step is chosen (experimentation showed that a maximum timestep in the order of 0.1 - 1ms is required, depending on the dataset), whereas the proposed solution is stable regardless of the timestep. As such it was necessary to upsample the 120Hz dataset used here, by a factor of 8, to obtain results with the standard model but not for the proposed model. However, the maximum timestep for the proposed model will be upper bounded by the limb position update frequency and the maximum firing frequency of the spindle – meaning that the efficiency improvement is data dependent – but in this situation was in the region of an 8 fold improvement.

The fitting of cubic polynomials to calculate length and moment arm make these elements of the processing almost negligible and appears to represent a reduction in required calculations by multiple orders of magnitude compared to 3D modelling.

4.5 Discussion

4.5.1 Generating proprioceptive feedback for a prosthesis

Providing intuitive and comprehensive feedback which is familiar or trivially easy to interpret is the ultimate goal for any neural prosthesis. However, it is unknown what the most effective and achievable format for providing proprioceptive neural feedback to prosthesis users is in the near term and there are numerous challenges in implementing, comparing and optimising competing methods.

Feedback that approximates all the naturally occurring neural patterns in the human limb, seems a logical, albeit distant, ideal to aim for. There is uncertainty about how

close to this ideal the feedback needs to be in order to demonstrate benefits compared to simpler forms of modulation, and there are major obstacles – such as limitations in our understanding of proprioceptors and modulating signals from the brain, as well as our limited ability to interface with and selectively modulate large numbers of neurons.

4.5.2 Approximations

The system presented here is focused on real time prediction of neural stimulation patterns and firing rates that would be suitable for human nerve stimulation and which only uses data available from a prosthetic limb. A number of models and approximations were used to achieve this aim and their limitations will be discussed here.

The cubic polynomial approximations for muscle length curves fitted the OpenSim data closely, however, the equivalent moment arm approximations showed substantially worse correlation. It was observed that the quality of a muscle's moment arm approximation decreased as the number of joints the muscle spanned increased and that the surface fit for moment arms about the shoulder joints were particularly poor (although that did not matter for this application). Considering these differences in input data and the difference in optimisation criteria employed, the output of the static optimisation stage showed a reasonably good match with the standard OpenSim tool. However, substantial differences were visually evident in the distribution of load between the three tricep muscle branches and this is reflected in the very low R^2 values for these branches. This was likely due to the linear nature of the optimisation, which becomes increasingly poor at load sharing as the number of joints and muscles increases. Examination of the results showed that simply averaging the modelled activations of the three tricep branches would have closely fitted the OpenSim results (R^2 values of 0.912, 0.970 and 0.906 for the lateral, long and medial heads respectively). In more complex systems (with greater numbers of joints and muscles) it may be necessary to compartmentalise the optimisation process and run multiple iterations or implement some alternative method of sharing load. Results for bicep long and short head activation were also well below average and may be a result of the poorer moment arm fit observed for these muscle branches.

The simplified version of the spindle model closely matched the outputs of the original model for the validations proposed in the original paper as well as for some real movement data. Discrepancies were visible during rapid movements, however, given the duration of these transient differences and peak firing rates in humans of approximately 100 Hz, these discrepancies represent only a low number of missed action potentials. As mentioned in the results, the efficiency improvement provided by the proposed model appears to be largely data dependent and related to the sample frequency of the system, the maximum spindle output frequency and the maximum step size for stable solving of the differential equations in the standard model. It should be noted that the analysis here assumed a standard euler method for solving these equations, but that many alternative numerical methods exist and could improve or guarantee stability.

The proposed parameter change and adjustment to rest & threshold lengths allowed the model to estimate human spindle recordings to within a standard deviation, but without

a significantly greater quantity of human data it is unclear how widely applicable these adjustments are.

4.5.3 Issues and areas for further work

- The inaccuracy of the polynomial fitting of moment arms for shoulder and highly multi-articular muscles indicates that alternative fitting models may need to be investigated to achieve good fits.

- The scaling of animal spindle and GTO models to fit human data is an area requiring further investigation. Here we have proposed simple modifications to better align the models with human firing rates, however, further data, validation and modification is required. The shape of the modelled human firing patterns was qualitatively different from the recorded data – most notably in that it lacked an initial burst or peak. Further analysis of recorded human spindle data from [64] (not shown), has supported this observation and indicates that the Mileusnic spindle model does not accurately represent the human spindle firing profile observed. Initial peaks are generated with the Mileusnic spindle model, but only at significantly faster movements – potentially indicating greater acceleration or velocity sensitivity in human spindles compared to feline or an area requiring further investigation and potentially model modification.

- In addition the Mileusnic spindle model is formulated on a limited subset of muscles and may need modification for wider applicability. In this work we noted a need for further research on how well the model copes with muscles whose optimal length is above or below the range of lengths the muscle is physiologically limited to. In our work looking at the recordings in [62], we made the assumption that the muscle physiological rest length should be used to calculate spindle rest and threshold parameters, this was based on the assumption that spindles firing rates should be at their lowest when the muscle is in a relaxed and neutral position.

- The work presented here assumed zero fusimotor activity, producing signals that are analogous to those experienced during passive motion of the limb. However, if the user is able to control their prosthesis naturally (i.e. the prosthesis responds to physiologically appropriate neural commands – e.g. following Targeted Muscle Reinnervation), then there will be a descending fusimotor signal that will act in the CNS on the pathways carrying the stimulated proprioceptive feedback, potentially interfering with it and reducing effectiveness. Ultimately it would be preferential to integrate fusimotor behaviour and the Mileusnic spindle model was in part chosen to enable future implementations to easily introduce this. However, current proposed models of fusimotor action are in their infancy and largely based on recordings performed on decerebrate cats or surrogate outcomes like obtaining a linear relationship between joint angle and spindle firing [42, 43, 65].

- The integration of motion capture, a musculoskeletal model, static optimisation and proprioceptor models enables some proprioceptive signals to be non-invasively mod-

elled for real movements. Further integration of inverse dynamic modelling to estimate joint torques, as well as a suitable musculoskeletal model of the feline hind limb (a preferred experimentation model), would enhance this system, allowing novel experimentation and extensive validation.

- Between first submission and final publication of this work, an alternative approach for optimising the static optimisation stage was proposed by Bogert et al. [66]. Their approach was based on a quadratic optimisation criteria and achieved better than real time operation on a desktop computer using an iterative approach on a neural network approach and accepting up to $\pm 5\,\%$ error. This alternative approach appears to offer better performance for scaling up to systems with high degrees of freedom and should be considered in future work.

4.5.4 Conclusion

Realistic models that link human motion to proprioceptor signals could one day form the basis for a proprioceptive neural prosthesis in much the same way retinal and cochlear implants aim to mimic auditory and retinal cells. In contrast to previous neuro-musculoskeletal models, this work has proposed: the integration of static optimisation; modifications to approximate human proprioceptors; and a variety of approximations & optimisations to reduce computational complexity without substantial degradation of the output. A key uncertainty in aiming to provide natural feeling proprioceptive feedback to a prosthesis user is how close to normal it needs to be in order to provide benefit over simpler forms of feedback modulation. This work aims to build capability to explore this question.

The model presented here is able to simulate muscle lengths, moment arms and activations as well as the corresponding muscle spindle and GTO neural signals in real time on low power hardware – potentially enabling novel proprioceptive and motor control experimentation, and perhaps someday forming the basis for a highly intuitive proprioceptive prosthesis, provided the right neurons can be targeted in the PNS.

Bibliography

[1] G. S. Dhillon and K. W. Horch. "Direct Neural Sensory Feedback and Control of a Prosthetic Arm". *IEEE Transactions on neural systems and rehabilitation engineering* 13 (2005).

[2] G. Dhillon, T. Kruger, J. Sandhu, and K. Horch. "Effects of short-term training on sensory and motor function in severed nerves of long-term human amputees". *Journal of neurophysiology* 93.5 (2005), pp. 2625–2633.

[3] D. J. Weber, B. M. London, J. A. Hokanson, C. A. Ayers, R. A. Gaunt, R. R. Torres, B. Zaaimi, and L. E. Miller. "Limb-state information encoded by peripheral and central somatosensory neurons: implications for an afferent interface". *Neural Systems and Rehabilitation Engineering, IEEE Transactions on* 19 (2011), pp. 501–513.

[4] U. Proske and S. C. Gandevia. "The Proprioceptive Senses: Their Roles in Signaling Body Shape, Body Position and Movement, and Muscle Force". *Physiological Reviews* 92 (2012), pp. 1651–1697.

[5] D. Song, N. Lan, G. E. Loeb, and J. Gordon. "Model-Based Sensorimotor Integration for Multi-Joint Control: Development of a Virtual Arm Model". *Annals of Biomedical Engineering* 36 (2008), pp. 1033–1048.

[6] A. Frigon and S. Rossignol. "Experiments and models of sensorimotor interactions during locomotion". *Biological cybernetics* 95 (2006), pp. 607–627.

[7] F. M. Colacino, E. Rustighi, and B. R. Mace. "An EMG-driven musculoskeletal model for the estimation of biomechanical parameters of wrist flexors". 2010, pp. 4870–4873.

[8] N. Lan, Y. Li, Y. Sun, and F. Yang. "Reflex regulation of antagonist muscles for control of joint equilibrium position". *Neural Systems and Rehabilitation Engineering, IEEE Transactions on* 13 (2005), pp. 60–71.

[9] T. K. Koo and A. F. Mak. "A neuromusculoskeletal model to simulate the constant angular velocity elbow extension test of spasticity". *Medical engineering & physics* 28 (2006), pp. 60–69.

[10] D. G. Thelen, F. C. Anderson, and S. L. Delp. "Generating dynamic simulations of movement using computed muscle control". *Journal of biomechanics* 36.3 (2003), pp. 321–328.

[11] F. Valero-Cuevas, H. Hoffmann, M. Kurse, J. Kutch, and E. Theodorou. "Computational Models for Neuromuscular Function". *Biomedical Engineering, IEEE Reviews in* 2 (2009), pp. 110–135.

[12] A. Erdemir, S. McLean, W. Herzog, and A. J. van den Bogert. "Model-based estimation of muscle forces exerted during movements". *Clinical Biomechanics* 22 (2007), pp. 131–154.

[13] D. Karlsson and B. Peterson. "Towards a model for force predictions in the human shoulder". *Journal of biomechanics* 25.2 (1992), pp. 189–199.

[14] I. W. Charlton and G. Johnson. "A model for the prediction of the forces at the glenohumeral joint". *Proceedings of the Institution of Mechanical Engineers, Part H: Journal of Engineering in Medicine* 220.8 (2006), pp. 801–812.

[15] M. Damsgaard, J. Rasmussen, S. T. Christensen, E. Surma, and M. de Zee. "Analysis of musculoskeletal systems in the AnyBody Modeling System". *Simulation Modelling Practice and Theory* 14.8 (2006), pp. 1100–1111.

[16] M. A. Lemay and P. E. Crago. "A dynamic model for simulating movements of the elbow, forearm, and wrist". *Journal of biomechanics* 29.10 (1996), pp. 1319–1330.

[17] F. C. Van der Helm. "Analysis of the kinematic and dynamic behavior of the shoulder mechanism". *Journal of Biomechanics* 27.5 (1994), pp. 527–550.

[18] B. A. Garner and M. G. Pandy. "Musculoskeletal model of the upper limb based on the visible human male dataset". *Computer methods in biomechanics and biomedical engineering* 4.2 (2001), pp. 93–126.

[19] K. R. S. Holzbaur, S. L. Delpa, G. E. Gold, and W. M. Murray. "Moment-generating capacity of upper limb muscles in healthy adults". *Journal of Biomechanics* 40 (2007), p. 2007.

[20] M. Millard, T. Uchida, A. Seth, and S. L. Delp. "Flexing computational muscle: Modeling and simulation of musculotendon dynamics". *Journal of biomechanical engineering* 135 (2013), p. 021005.

[21] D. Lee, M. Glueck, A. Khan, E. Fiume, and K. Jackson. "A survey of modeling and simulation of skeletal muscle". *ACM Transactions on Graphics* 28.4 (2010), p. 162.

[22] E. Eisenberg, T. L. Hill, and Y.-d. Chen. "Cross-bridge model of muscle contraction. Quantitative analysis". *Biophysical Journal* 29.2 (1980), pp. 195–227.

[23] J. Clay, D. Pounds, and V. Overman. *Basic Clinical Massage Therapy: Integrating Anatomy and Treatment*. LWW massage therapy & bodywork educational series. Lippincott Williams and Wilkins, 2008. ISBN: 9780781756778.

[24] T. Siebert, C. Rode, W. Herzog, O. Till, and R. Blickhan. "Nonlinearities make a difference: comparison of two common Hill-type models with real muscle". *Biological cybernetics* 98.2 (2008), pp. 133–143.

[25] D. Thelen. "Adjustment of muscle mechanics model parameters to simulate dynamic contractions in older adults." *Journal of biomechanical engineering* 125 (2003), pp. 70–77.

[26] F. C. Anderson and M. G. Pandy. "Static and dynamic optimization solutions for gait are practically equivalent". *Journal of biomechanics* 34.2 (2001), pp. 153–161.

[27] Y.-C. Lin, T. W. Dorn, A. G. Schache, and M. G. Pandy. "Comparison of different methods for estimating muscle forces in human movement". *Proceedings of the Institution of Mechanical Engineers, Part H: Journal of Engineering in Medicine* (2011), p. 0954411911429401.

[28] M. Bergenheim, E. Ribot-Ciscar, and J.-P. Roll. "Proprioceptive population coding of two-dimensional limb movements in humans: I. Muscle spindle feedback during spatially oriented movements". *Experimental Brain Research* 134 (2000), pp. 301–310.

[29] R. H. Ray and G. S. Doetsch. "Coding of stimulus location and intensity in populations of mechanosensitive nerve fibers of the raccoon: II. Across-fiber response patterns". *Brain research bulletin* 25.4 (1990), pp. 533–550.

[30] P. B. C. Matthews and R. Stein. "The sensitivity of muscle spindle afferents to small sinusoidal changes of length". *The Journal of Physiology* 200.3 (1969), pp. 723–743.

[31] T. Rudjord. "A mechanical model of the secondary endings of mammalian muscle spindles". *Kybernetik* 7 (1970), pp. 122–128.

[32] W. Chen and R. Poppele. "Small-signal analysis of response of mammalian muscle spindles with fusimotor stimulation and a comparison with large-signal responses". *Journal of neurophysiology* 41 (1978), pp. 15–27.

[33] J. Houk, W. Rymer, and P. Crago. "Dependence of dynamic response of spindle receptors on muscle length and velocity." *Journal of neurophysiology* 46 (1981), p. 143.

[34] Z. Hasan. "A model of spindle afferent response to muscle stretch". *Journal of neurophysiology* 49 (1983), pp. 989–1006.

[35] A. Schaafsma, E. Otten, and J. Van Willigen. "A muscle spindle model for primary afferent firing based on a simulation of intrafusal mechanical events". *Journal of neurophysiology* 65 (1991), pp. 1297–1312.

[36] E. Otten, K. Scheepstra, and M. Hulliger. "An integrated model of the mammalian muscle spindle". Springer, 1995, pp. 294–301.

[37] A. Prochazka and M. Hulliger. "The continuing debate about CNS control of proprioception". *The Journal of Physiology* 513 (1998), p. 315.

[38] C.-C. K. Lin and P. E. Crago. "Neural and mechanical contributions to the stretch reflex: a model synthesis". *Annals of Biomedical Engineering* 30 (2002), pp. 54–67.

[39] M. G. Maltenfort and R. Burke. "Spindle model responsive to mixed fusimotor inputs and testable predictions of β feedback effects". *Journal of neurophysiology* 89 (2003), pp. 2797–2809.

[40] M. P. Mileusnic, I. E. Brown, N. Lan, and G. E. Loeb. "Mathematical Models of Proprioceptors. I. Control and Transduction in the Muscle Spindle". *Journal of Neurophysiology* 96 (2006), pp. 1772–1788.

[41] A. Taylor, P. H. Ellaway, R. Durbaba, and S. Rawlinson. “Distinctive patterns of static and dynamic gamma motor activity during locomotion in the decerebrate cat”. *The Journal of Physiology* 529 (2000), pp. 825–836.

[42] A. Taylor, R. Durbaba, P. H. Ellaway, and S. Rawlinson. “Static and dynamic motor output to ankle flexor muscles during locomotion in the decerebrate cat”. *The Journal of Physiology* 571 (2006), pp. 711–723.

[43] I. Williams and T. G. Constandinou. “Modelling muscle spindle dynamics for a proprioceptive prosthesis”. *Engineering in Medicine and Biology Society (EMBC), 2013 35th Annual International Conference of the IEEE*. IEEE. 2013, pp. 1923–1926.

[44] N. Lan and X. He. “Fusimotor control of spindle sensitivity regulates central and peripheral coding of joint angles”. *Frontiers in computational neuroscience* 6 (2012).

[45] J. Houk and W. Simon. “Responses of Golgi tendon organs to forces applied to muscle tendon.” *Journal of neurophysiology* 30 (1967), pp. 1466–1481.

[46] J. H. Anderson. “Dynamic characteristics of Golgi tendon organs”. *Brain research* 67 (1974), pp. 531–537.

[47] J. Gregory and U. Proske. “Motor unit contractions initiating impulses in a tendon organ in the cat.” *The Journal of physiology* 313 (1981), pp. 251–262.

[48] M. P. Mileusnic, I. E. Brown, N. Lan, and G. E. Loeb. “Mathematical Models of Proprioceptors. II. Structure and Function of the Golgi Tendon Organ”. *Journal of Neurophysiology* 96 (2006), pp. 1789–1802.

[49] S. L. Delp, F. C. Anderson, A. S. Arnold, P. Loan, A. Habib, C. T. John, E. Guendelman, and D. G. Thelen. “OpenSim: open-source software to create and analyze dynamic simulations of movement”. *Biomedical Engineering, IEEE Transactions on* 54 (2007), pp. 1940–1950.

[50] K. R. Holzbaur, W. M. Murray, and S. L. Delp. “A model of the upper extremity for simulating musculoskeletal surgery and analyzing neuromuscular control”. *Annals of biomedical engineering* 33 (2005), pp. 829–840.

[51] D. A. Winter. *Biomechanics and motor control of human movement*. Wiley. com, 2009.

[52] R. Chandler, C. Clauser, J. McConville, H. Reynolds, and J. Young. *Investigation of inertial properties of the human body*. Tech. rep. 1975.

[53] F. E. Zajac. “Muscle and tendon: properties, models, scaling, and application to biomechanics and motor control.” *Critical reviews in biomedical engineering* 17 (1988), pp. 359–411.

[54] H. Veeger, B. Yu, K.-N. An, and R. Rozendal. “Parameters for modeling the upper extremity”. *Journal of biomechanics* 30.6 (1997), pp. 647–652.

[55] S. V. Brooks and J. A. Faulkner. “Contractile properties of skeletal muscles from young, adult and aged mice.” *The Journal of physiology* 404 (1988), pp. 71–82.

[56] A. J. van den Bogert, D. Blana, and D. Heinrich. “Implicit methods for efficient musculoskeletal simulation and optimal control”. *Procedia IUTAM* 2 (2011), pp. 297–316.

[57] J. Rasmussen, M. Damsgaard, and M. Voigt. “Muscle recruitment by the min/max criterion: a comparative numerical study”. *Journal of Biomechanics* 34 (2001), pp. 409–415.

[58] S. H. Scott, I. E. Brown, and G. E. Loeb. “Mechanics of feline soleus: I. Effect of fascicle length and velocity on force output”. *Journal of Muscle Research & Cell Motility* 17 (1996), pp. 207–219.

[59] L. Jami. “Golgi Tendon Organs in Mammalian Skeletal Muscle: Functional Properties and Central Actions”. *Physiological Reviews* 72 (1992), pp. 623–666.

[60] N. al-Falahe, M. Nagaoka, and A. Vallbo. “Response profiles of human muscle afferents during active finger movements.” *Brain: a journal of neurology* 113 (1990), p. 325.

[61] A. Prochazka, J. A. Stephens, and P. Wand. “Muscle spindle discharge in normal and obstructed movements.” *The Journal of Physiology* 287 (1979), pp. 57–66.

[62] B. B. Edin and A. B. Vallbo. “Dynamic Response of Human Muscle Spindle Afferents to Stretch”. *Journal of Neurophysiology* 63 (1990), pp. 1297–1306.

[63] U. Proske, A. Wise, and J. Gregory. “The role of muscle receptors in the detection of movements”. *Progress in Neurobiology* 60 (2000), pp. 85–96.

[64] P. J. Cordo, C. Flores-Vieira, S. M. Verschueren, J. T. Inglis, V. Gurfinkel, et al. “Position sensitivity of human muscle spindles: single afferent and population representations”. *Journal of neurophysiology* 87.3 (2002), pp. 1186–1195.

[65] A. Taylor, R. Durbaba, and P. Ellaway. “Direct and indirect assessment of γ-motor firing patterns”. *Canadian journal of physiology and pharmacology* 82.8-9 (2004), pp. 793–802.

[66] A. J. van den Bogert, T. Geijtenbeek, O. Even-Zohar, F. Steenbrink, and E. C. Hardin. “A real-time system for biomechanical analysis of human movement and muscle function”. *Medical & biological engineering & computing* 51.10 (2013), pp. 1069–1077.

5 Energy efficient neural stimulation for proprioceptive feedback

A neural stimulator forms the link between man-made electronics and the human nervous system and the electrodes represent the crux between these two domains. Chapter 3 identified how careful design of the interaction between the stimulator and the electrodes is crucial for safe and effective neuromodulation.

Ideally an electrical neural stimulator would efficiently deliver charge to a set of electrodes – causing sufficient current to flow through the tissue, but without causing redox reactions at the Electrode Electrolyte Interface (EEI) – and then remove that same quantity of charge (giving a charge balanced stimulation) to leave the electrodes electrochemically neutral with respect to the surrounding tissue. Precise control of the quantity and rate of charge delivery and recovery is most readily achieved using a Current Controlled Stimulator (CCS), but even so obtaining this charge balance remains challenging and precision is often achieved at the expense of strict and undesirable limitations on the stimulation waveform.

The charge and timescale required for effective stimulation as well as the electrode and tissue impedances, mean that significant potential differences can be developed across the output terminals of the stimulator and leads to a requirement for high voltage compliance in the stimulator to accommodate worst case impedances. In a CCS, front end transistors are typically used to limit the current and during stimulation much of this potential difference is across these transistors resulting in significant power waste.

Power consumption can be reduced by careful choice of electrode surface treatment, electrode material, stimulation time and waveform [1]. However, despite this, power dissipation in the front end current controlling transistors remains the major source of power waste. In a system with tightly constrained transcutaneous power supply or implanted energy storage (as neural implants typically are) and with strict thermal constraints (due to the risk of damage to surrounding tissue [2]), this waste consumption is highly undesirable.

This chapter presents the design and demonstration of a low power current controlled stimulator providing accurate charge balancing even with an asymmetric waveform. Section 5.1 analyses the charge balance challenge as well as previously proposed modifications. Section 5.2 looks at CCS power consumption, some possible methods to address this and de-

Parts of this chapter have been previously published in:

- I. Williams and T. G. Constandinou. "An energy-efficient, dynamic voltage scaling neural stimulator for a proprioceptive prosthesis". *IEEE Trans. BioCAS* 7 (2013)
- I. Williams and T. Constandinou. "An energy-efficient, dynamic voltage scaling neural stimulator for a proprioceptive prosthesis". *Circuits and Systems (ISCAS), 2012 IEEE International Symposium on*. IEEE. 2012, pp. 1091–1094

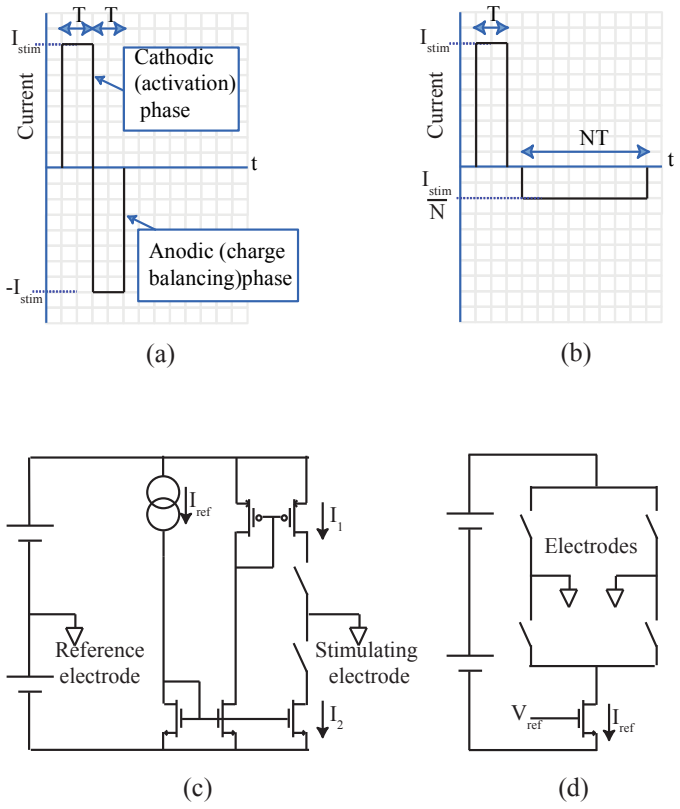


Figure 5.1: (a) A standard symmetrical biphasic waveform, (b) an asymmetric biphasic waveform (NB the area, i.e. charge, in the two phases remains equal), (c) a conventional current stimulator design, (d) an h-bridge stimulator.

scribes the rationale for the solution proposed here. Section 5.3 details the proposed system design, and sections 5.4 and 5.5 present experimental results and conclusions respectively.

5.1 Charge Balanced Stimulation

In a current controlled stimulator, charge neutral stimulation has been treated as fundamentally a challenge of matching the duration and amplitudes of the anodic and cathodic phases of a biphasic waveform (Fig 5.1(a)). This is challenging with a conventional design (as depicted in Fig 5.1(b) most notably because of mismatch between the current mirroring transistors leading to small differences between I_{ref}, I_1 and I_2. These differences can be reduced with careful design and layout, however, residual mismatch will still lead to a small charge imbalance of consistent polarity after each stimulation. This consistent error will therefore tend to accumulate, increasing the voltage across the electrode-electrolyte interface and could eventually lead to DC current flow and irreversible electrochemical reactions. 100 nA of DC current has been shown to cause tissue degradation [3] and as such limiting accumulated charge imbalance per second to less than 25 nA has been targeted as a maximum safe error [4].

As discussed in Chapter 3, several passive solutions have been developed for voltage

controlled stimulation such as DC blocking capacitors (which requires off-chip capacitors that increase system size and are not readily scalable to systems with many stimulation channels) and shorting electrodes together (where the time constant for discharge makes it unsuited to rapid stimulation).

Active solutions have also been proposed, Sit and Sarpeshkar [4] demonstrated an active current calibration approach combined with a electrode shorting to reduce error down to approximately 6nA. However, a calibration system like this limits the system to a very simple constant current waveform (for best performance). An elegant solution that has been in use for over 20 years is to use an H-bridge, enabling just a single set of transistors to control both phases of the current and essentially eliminating mismatch issues. The direction of current flow through the electrode is simply switched / steered as shown in Figure 5.2.

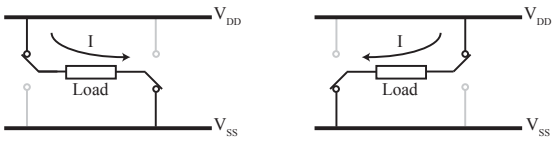


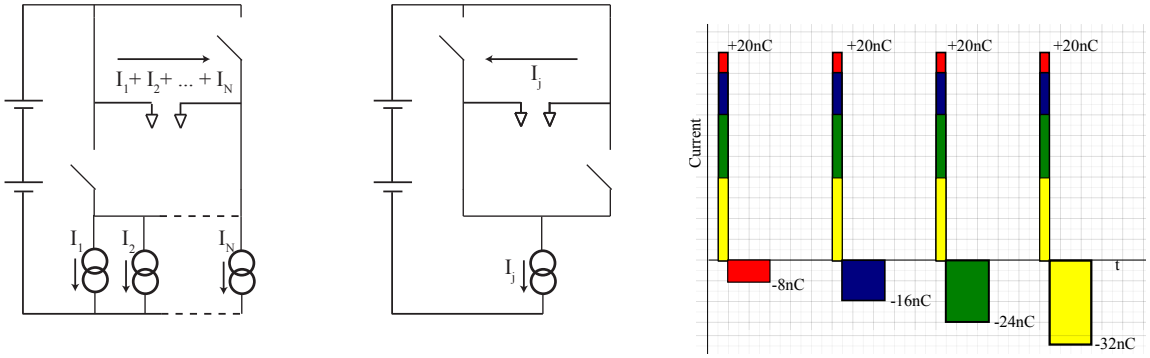
Figure 5.2: H-bridge configuration for biphasic current control. Switches allow bi-directional flow of current through a load.

An H-bridge approach widens the range of stimulation waveforms possible. However, the matching of anodic and cathodic currents still prevents the use of asymmetric waveforms – which have been shown to stimulate neurons at significantly lower thresholds [5], reducing power consumption and increasing stimulation safety.

Here we propose a variant on the H-bridge approach that is compatible with an asymmetric waveform and is based on the assumption that it is acceptable to achieve accurate charge balancing over a series of pulses rather than on a single pulse. The fundamental principle is depicted in Figure 5.3 and shows that during the high amplitude cathodic phase N current sinks are acting in parallel to pull current through the electrodes for a time T. Then during the low amplitude anodic phase 1 current sink is acting to pull current through the electrodes (in the opposite direction) for a time NT. On a single stimulation this will not give accurate charge balancing as the current sinks are not perfectly matched. However, if the current sink that is active in the anodic phase is changed after each stimulation then after N stimulations each sink will have been active for the same amount of time during cathodic and anodic phases giving accurate charge balancing. The value of N can be any real, positive integer and choosing a value for N depends on a tradeoff between the aforementioned benefits of asymmetric pulses versus the increased duration of the anodic phase that occurs as N is increased, as well as increased die area as the number of parallel current sinks increases.

5.2 Power Consumption

Voltage drop across the current controlling transistors is the fundamental driver for front end power waste. Kelly in [6] calculated that, even using a *low power* current source,

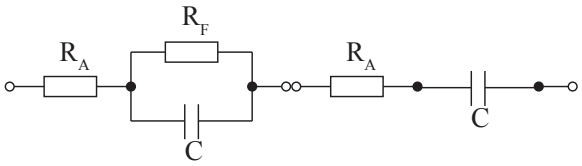


(a) The cathodic phase lasting T seconds with N current sinks active.

(b) An anodic phase lasting NT seconds with only one sink active (where j = 1,2 ... N).

(c) A sequence of stimulations with exaggerated mismatch (colours represent the current drawn by each sink), demonstrating the robust charge balancing.

Figure 5.3: The proposed charge balancing scheme.



(a) Full model

(b) Simplified model for analysis

Figure 5.4: Lumped circuit models of the electrode-tissue interface.

as much as 92% of the front end power is dissipated as heat by the current controlling transistors. The reason for this can be observed by looking at the electrodes, voltages, and currents in the front end of this system.

Electrodes in neural stimulators are usually modelled as a resistor in series with a parallel resistor and capacitor (see Fig. 5.4). This parallel resistance (R_F) corresponds to the Faradaic flow of current into the tissue due to non-reversible redox reactions at the interface. R_F is typically very large and is often assumed to be infinite. Electrode impedances are typically on the order of (1 – 10 kΩ) for R_S and 1-10 nF of capacitance. In practice the impedance of the electrodes and tissue will vary considerably and the impact of this on efficiency will be briefly discussed in Section 5.5).

The voltage developed across these electrodes and the contribution of the two impedances is illustrated in Figure 5.5(a). The maximum potential difference that the front end of the system can accommodate is termed the voltage compliance. For good control of the current waveform the stimulator's voltage compliance needs to exceed the peak voltage developed across the electrodes at the maximum stimulation amplitude (plus a small headroom to keep the current controlling transistors in saturation). However, it should be noted that this peak voltage is only transient and for the vast majority of the time the system does not need to operate at this voltage, either as a result of the voltage waveform (see Fig. 5.5(b)) or because the stimulation amplitude is sub-maximal. Studies stimulating human peripheral nerves

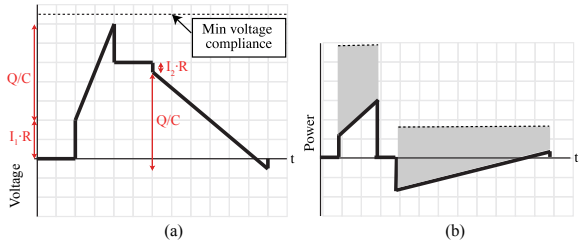


Figure 5.5: Electrical neural stimulation waveforms showing: (a) the voltage across the electrode – where I_1 and I_2 are the cathodic and anodic currents, R is the electrode resistance, C is the electrode capacitance and Q is the total charge injected; (b) the power consumption in a typical (current-mode) stimulator. In (b) the dark line is the theoretical minimum power consumption, dotted line is the actual power consumption and the shaded area is the power wasted.

have quoted stimulation threshold dynamic ranges of 6.9dB [7], 7.8dB [8] and 11.1dB [9], however, looking at the data contained in the graphs of these papers shows dynamic ranges of up to 17dB – indicating that in some stimulations the supply voltage is up to 20 times higher than necessary. A typical neural stimulator, however, has fixed supplies and as such there is no option but to continuously operate at this high voltage. This excess voltage is the basis of the power waste (see shaded area Fig. 5.5(b) in the front end transistors.

In this chapter we propose the use of a fully integrated DC-DC converter that modulates the voltage supplied to the front end in order to achieve high voltage compliance [10], but also reducing the excess voltage across the front end transistors and therefore the power consumption. Figure 5.6 shows the power implications of 3 ways of implementing this as described below.

Discrete interstimulus power supply modulation

Figure 5.6(a) shows a system controlling the supply voltage to the front-end on a stimulation by stimulation basis. This could be achieved either using multiple voltage supplies from off-chip (which would increase the size of the implant and likely the number of fragile bond wires required) or using a fully integrated switched capacitor DC-DC converter. However, this scheme offers the lowest power savings of the three options, and runs the risk that if the electrode impedance is higher than expected then there may not be sufficient headroom and the transistors may drop out of saturation. However, it is likely the simplest to implement and is potentially the easiest with which to achieve good current control.

Continuous intrastimulus power supply modulation

Figure 5.6(b) proposes smoothly modulating the voltage supply to the front-end during each stimulation, potentially approximating the ideal supply shown in Fig 5.6(c) and therefore could offer the greatest energy savings of the three. This modulation could theoretically be achieved using a switching DC-DC converter and an approach along these lines was proposed in [11]. However, switching DC-DC converters require off-chip components – due to the low inductance to resistance ratio (Q-factor) of on-chip inductors and due to the low currents involved – which is undesirable. The current control achieved with this approach

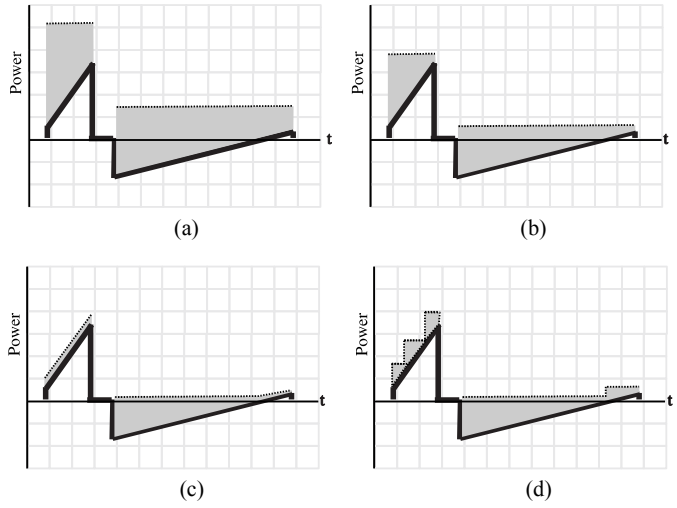


Figure 5.6: Power consumption for a sub-maximal current stimulation for a (a) standard fixed supply (current-mode) stimulator, (b) system with variable supplies that are set on a per stimulation basis (discrete interpulse supply modulation), (c) system with a variable supply that is smoothly modulated during each stimulation (continuous intrapulse supply modulation), and (d) system with multiple discrete supply voltages that are switched between during the stimulation (discrete intrapulse supply modulation). The dark line is the theoretical minimum power consumption, the dotted line is the actual power consumption and the shaded area is the power wasted.

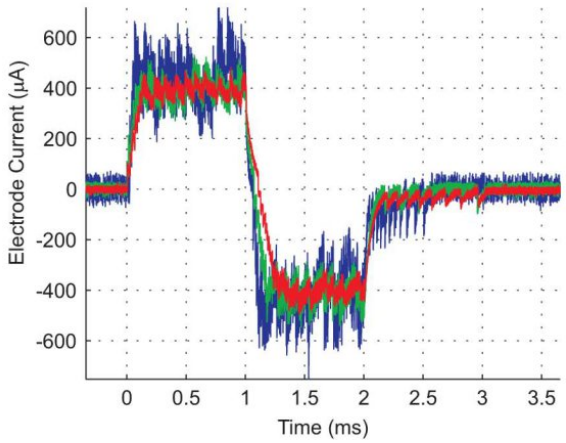
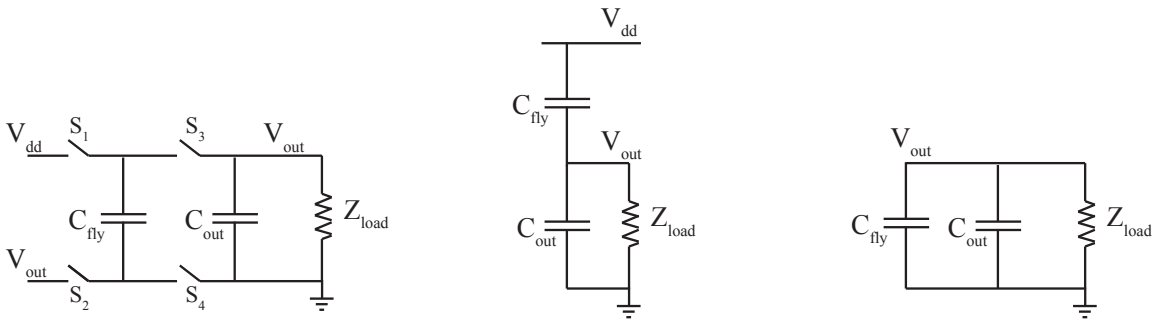


Figure 5.7: Current waveform generated using a switching DC-DC converter with various resistive loads (Blue 500 Ω, Green 1000 Ω, Red 1500 Ω). From [11].



(a) (b) (c)

Figure 5.8: A simplified DC-DC converter - a) Capacitors are charged in a series potential divider, following reconfiguration these capacitors are discharged in parallel with their bottom plate connected to voltage V. b) Capacitors are charged in parallel, following reconfiguration these capacitors are discharged in series with their bottom plate connected to voltage V.

was also incompatible with our desire for precise charge control and good charge balancing (see Fig 5.7).

Discrete intrastimulus power supply modulation

Figure 5.6(c) shows the power consumption for a system with discrete supply voltages that are stepped between during each stimulation. This could be implemented using multiple off-chip voltage supplies or a fully integrated switched capacitor DC-DC converter. Power savings offered by this approach are dependent on the control circuitry and the number of output voltage steps (with more steps more closely approximating the ideal).

This latter approach is the preferred one due to its suitability for on-chip implementation and the substantial potential power savings it offers. It is an approach very similar to one used widely in low power processors and is commonly referred to as Dynamic Voltage Scaling [12].

5.2.1 Switched capacitor DC-DC converter design

A switched capacitor DC-DC converter involves the use of capacitors in a switch matrix that allows reconfiguration of the circuit topology. Their operation usually involves a two phase process (examples of which are illustrated in Fig. 5.8(a) and (b); in the first the switch matrix connects the flying capacitor(s) to a source to charge them to a desired voltage, and in the second the switches are reconfigured to discharge the capacitor(s) into the load. In practice potential division (by charging capacitors in series) or charge pumping effects (by connecting the flying capacitor bottom plate to a raised voltage) are often exploited to achieve desired voltages.

Many different topologies have been proposed each offering a tradeoff in terms of voltage conversions possible, switching complexity, charge transfer capability and efficiency under light and heavy loads. Common topologies typically only efficiently produce a single output voltage. However, the inclusion of additional switches to connect various nodes, enables

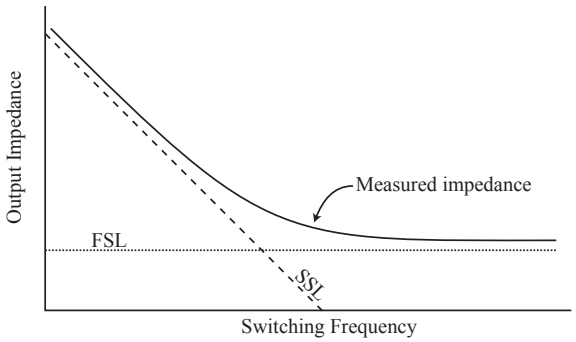


Figure 5.9: Asymptotic limits for switched capacitor performance. FSL – Fast Switching Limit, SSL – Slow Switching Limit

the creation of multi-level converters which can be reconfigured to implement a variety of topologies and efficiently produce a range of output voltages [13]. A comparison of previously published work in switched capacitor integrated multi-level DC-DC converters is shown in Table 5.1.

The performance of switched capacitor converters can be analysed using 2 asymptotic limits (see Fig. 5.9): 1) the Fast Switching Limit (FSL) – where the converter capacitors don't approach equilibrium during the charging phase and which is dependent on the power lost in the switching transistors; 2) the Slow Switching Limit (SSL) – where capacitors are approximated as being fully charged during the charging phase and which is dependent on the power consumed charging and discharging all the capacitances. Under light load and low switching frequency, or in a system where performance is limited by constraints on capacitor size, the performance of the system can approach the SSL, while in a system where the switches become the limiting factor the performance is limited by the FSL.

Table 5.1: Multi-level integrated SC DC converter comparison

	Pique [14]	el-Damak et Al [15]	Le et Al[16]	Salem et Al[17]
Year	2012	2013	2013	2014
Technology (nm)	90	130	65	250
Capacitor type	MOS	Ferroelectric	PMOS	MIM
Capacitance (nF)	1.15	8	3.88	3
Area (mm^2)	0.25	0.37	0.64	4.65
Conversion ratios	⅔, ½	1, ⅔, ½, ⅓	⅖, ⅓	15 levels
Topology	S/P	S/P	S/P	4-bit SAR
V_{in} (V)	1.2 – 2	1.5	3 – 4	2.5
V_{out} (V)	0.7	0.4 – 1.1	1	0.1 – 2.18
Current (mA)	8	1	122	2
Efficiency (%)	81	93	74	85

S/P – Series / parallel topology
SAR – Successive approximation

Efficiency

Converter efficiency is dependent on a number of factors such as topology, load and the conversion ratio – where a ratio between input and output closer to 1:1 offers better ef-

ficiency. However, the fundamental mechanisms determining power waste are generally energy dissipation in switch impedances and charging & discharging various capacitances. Key areas of power waste (in the steady state) include:

1. **Switch loss**

   $P_{res} = I^2R$ power loss due to resistance in the switching transistors

2. **Ripple loss**

   $P_{ripple} = \frac{f_{sw}C_{conv}\Delta V^2}{2}$ loss charging the converter capacitance (C_{conv}) with a voltage ripple of ΔV at switching frequency

3. **Gate capacitance loss**

   $P_{sw} = f_{sw}C_{sw}V_{sw}^2$ loss charging and discharging the gate capacitances (C_{sw}) to the required voltage (V_{sw}).

4. **Bottom plate loss**

   $P_{bottom} = C_{bott}V_{bott}^2 f_{sw}$ loss charging and discharging the bottom plate capacitance (C_{bott}).

Switch on-resistance is ideally minimised and is dependent on the technology, the type of MOSFET, it's $\frac{W}{L}$ and the gate-source voltage (V_{GS}) applied. Node voltages vary widely in a reconfigurable converter, presenting challenges for maximising V_{GS} while managing gate, source & drain potential differences within design tolerances. The use of high voltage (e.g. Shallow Trench Insertion) MOSFETs mitigates some of these challenges but generally reduces transconductance and raises the required gate-source voltage for efficient operation. The choice of transistor $\frac{W}{L}$ is a trade-off between increased switch conductance and increased capacitance. Charging and discharging this capacitance is a direct cause of power waste (especially for large transitions in gate voltage) and also may indirectly affect converter efficiency by slowing switching times.

Improving efficiency by changing flying or smoothing capacitances or switching frequency is a more complex trade-off due to the relationships between switching frequency and capacitor sizes with output ripple and die area. Reducing voltage ripple on the output can alternatively be achieved by interleaving multiple converters together as depicted in Figure 5.10. This is a technique that was initially developed for inductive switching converters but has been employed in switching converters [18].

System efficiency is a combination of efficiency in the converter as well as in the load. As identified earlier the waste power consumption of the load is dependent on the number (and levels) of output voltages provided by the converter. Although standard topologies are in general only capable of efficiently providing 1 output voltage, a multi-level converter could provide a series of output voltage levels. Matlab modelling was conducted to assess how front end efficiency varied with the number of output levels. Figure 5.11(a) shows the significant potential system power savings this approach could offer (with 100% converter efficiency); Figure 5.11(b) translates this into energy savings per stimulation; and Figure 5.11(c) shows the required converter efficiency for the overall system efficiency to

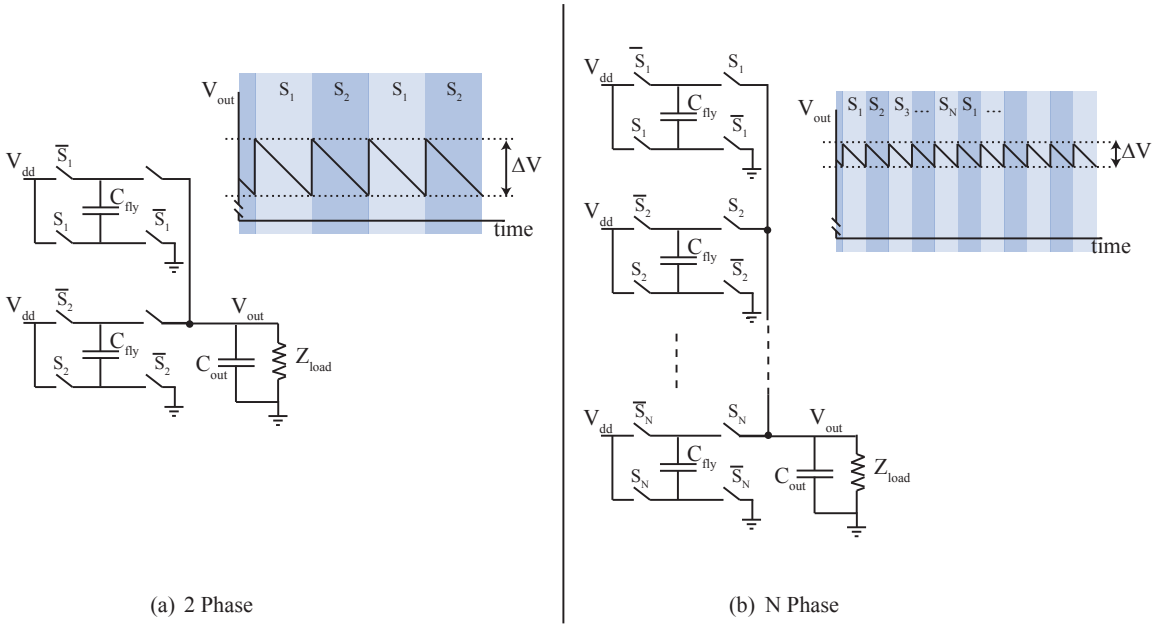


Figure 5.10: Interleaving multiple converters together to reduce ripple. a) A two phase charge pump, switch signals S_1 and S_2 are alternated as indicated in the graph resulting in the shown waveform. b) An N-phase charge pump, switches S_1 to S_N are activated in turn to achieve lower ripple (ΔV).

"break-even" and achieve benefit. Figure 5.11(b) can be interpreted as showing the available margin for generating the various output voltages. This margin is minimal at low stimulation currents indicating that achieving energy savings across the entire stimulation range would be extremely challenging to achieve. All the figures demonstrate the diminishing returns as the number of levels increases, and any benefit of increased levels is further eroded by expected increases in overhead as the number of switches required and system complexity increases.

Based on this initial analysis a 4 level multi-topology converter was targeted (see Fig. 5.12). This was selected on the basis of the potential energy savings possible and the perceived achievability of the required converter efficiency (Fig. 5.11(c). The low level of margin at low stimulus levels is of potential concern, however, the savings possible at higher stimulation levels indicate that overall net benefit should be readily achievable.

5.2.2 DC-DC converter parameters

At the time of conducting this work we believed that sub-fascicular level selectivity will be required and as such we are expecting to use micro-electrode arrays or intra-fascicular devices such as the TIME electrodes [19]. These electrodes are usually modelled as a resistor in series with a parallel resistor and capacitor (see Fig. 5.4). This parallel resistance (R_F) corresponds to the Faradaic flow of current into the tissue due to non-reversible redox reactions at the interface. R_F is typically very large and so for the simplicity of the analysis in this paper it will be assumed to be infinite. Based on TIME electrode impedances we are therefore assuming a resistor (7 kΩ) in series with a capacitor (7 nF) as our electrode model for this analysis. In practice the impedance of the electrodes and tissue will vary

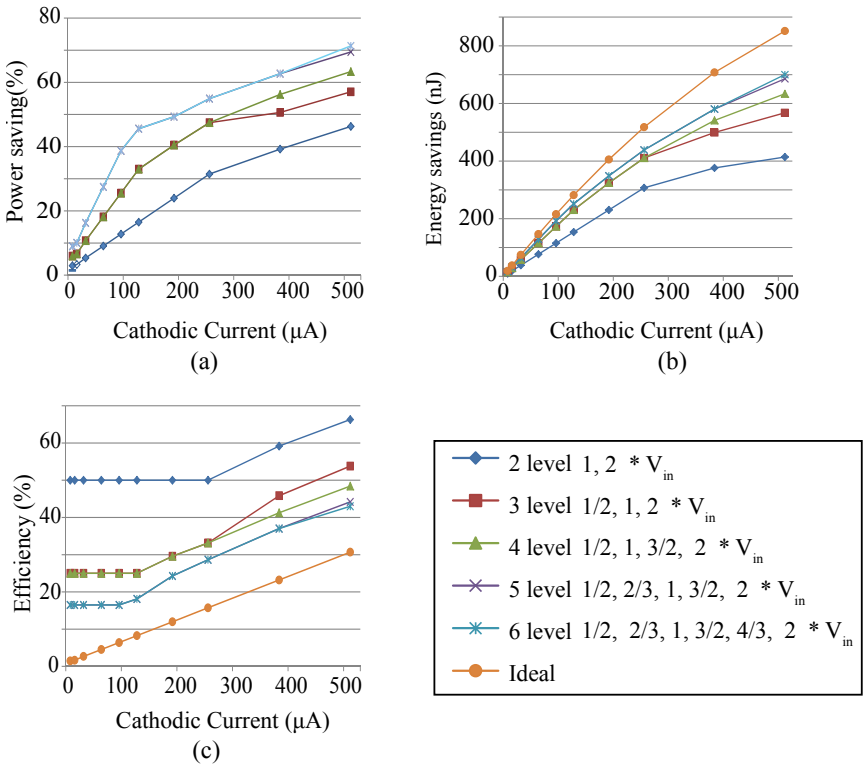


Figure 5.11: Effect of number of converter voltage outputs on a) percentage power saving compared to a baseline system, b) energy saved per stimulation, and c) required converter efficiency for system to provide benefit. 1 level is a standard fixed supply system and Ideal represents infinite output levels. $V_{in} = 6\,V$, $R = 7\,k\Omega$, $C = 7\,nF$, $I_{max} = 500\mu A$ $time = 100\mu s$.

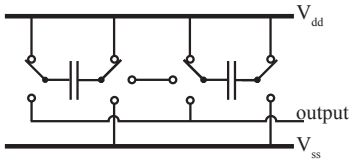


Figure 5.12: A reconfigurable multi-topology switched capacitor DC converter. The switch configuration allows serial or parallel charging and discharging of the capacitors, as well as connecting of the capacitor bottom plates to V_{dd}.

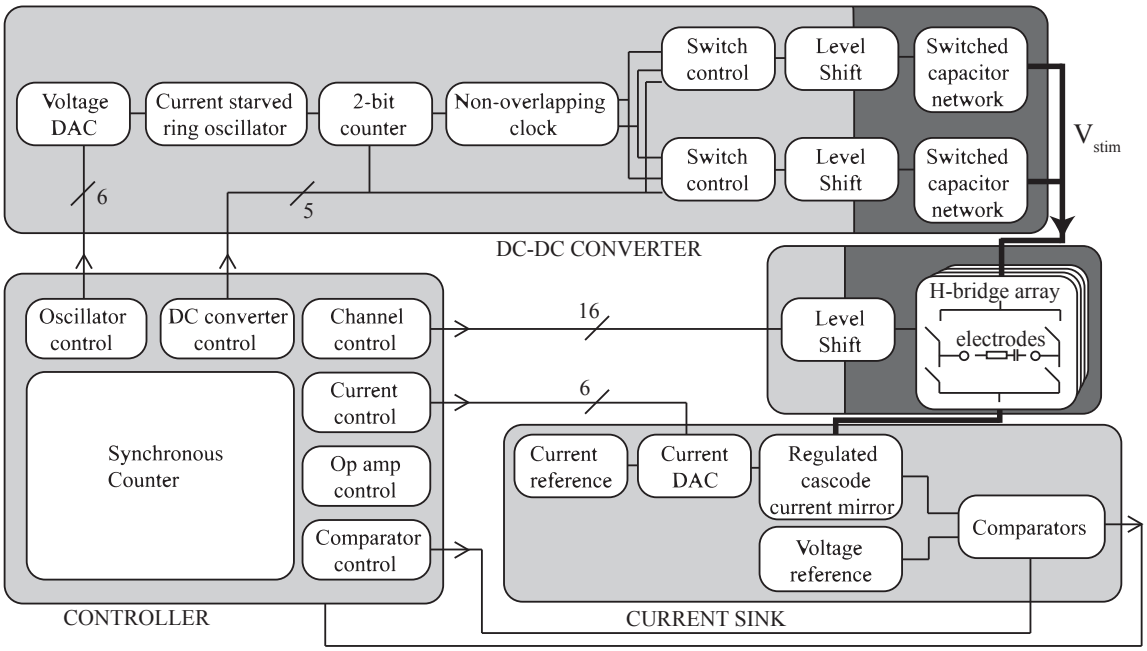


Figure 5.13: Overview of the proposed neural stimulator. Light grey areas are powered from 1.8V supply, dark grey areas from a 6 V supply. Thick black lines indicate the main current path. Not shown are the electrodes connected to their respective nodes inside the H-bridge.

considerably and the impact of this on efficiency will be briefly discussed in Section 5.5.

Selective stimulation of efferent neurons (similar to the afferent Type Ia and Ib neurons we are targeting) in the human PNS has been demonstrated in [20, 21] to occur with charge packets of between 11±5 nC to 29±17 nC. Given these values our stimulator will be designed to deliver up to 50 nC in a 100 μs pulse (a common pulse duration). The voltage compliance of the system needs to be greater than the voltage developed across the electrodes given by:

$$V_e = I_{stim} \times R_{elec} + \frac{Q_{total}}{C} \tag{5.1}$$

where V_e, I_{stim}, R_{elec}, Q_{total} and C are the voltage across the electrodes, stimulation current, electrode resistance, charge stimulus and capacitance respectively. Using our chosen impedance and charge packet values, this means our system requires a voltage compliance of ≥ 10.64 V.

5.3 Circuit Implementation

The main system components are shown in Figure 5.13. At a top level it consists of: a Digital Control block which outputs timing and control signals; a DC-DC converter which provides a variable stimulation voltage; an H-bridge array which selects the electrodes involved in each stimulation; and finally a Current Sink which controls the amount of current that flows through the electrodes during a stimulation. A second DC-DC converter has additionally been included to provide the 1.8 V supply to power the system core.

5.3.1 Technology selection

Switched Capacitor DC-DC converters generally require large capacitances (see Table 5.1) and as such a key requirement when choosing a CMOS process for implementation is the maximum capacitance per unit area. Other key considerations for this application are: the maximum voltage supported (which must be higher than 12V); the integrating density (to minimise the size of the digital); and finally price. Table 5.2 compares the technologies that were available for implementation.

On the basis of the criteria stated above, the AMS H18 High Voltage CMOS technology provided by AMS / IBM (H18A4/7HV) was selected.

Table 5.2: Comparison of available CMOS technology processes

	AMS C18	AMS C35	AMS H18	AMS H35	XFAB XH018	XFAB XT018
Feature size (nm)	180	350	180	350	180	180
MIM Cap density (fF/μm^2)	4.1*	1.25	4.1*	1.25	1*	1*
Integrating density (k gates/mm^2)	118	18	118	18	125	125
Max voltage (V)	5	5	50	50	21	200
Price** (€/mm^2)	1050	580	1100	900	1430	1450

* Higher densities are possible with unavailable add-on process modules
** Discounted research prices from Europractice.

5.3.2 Controller

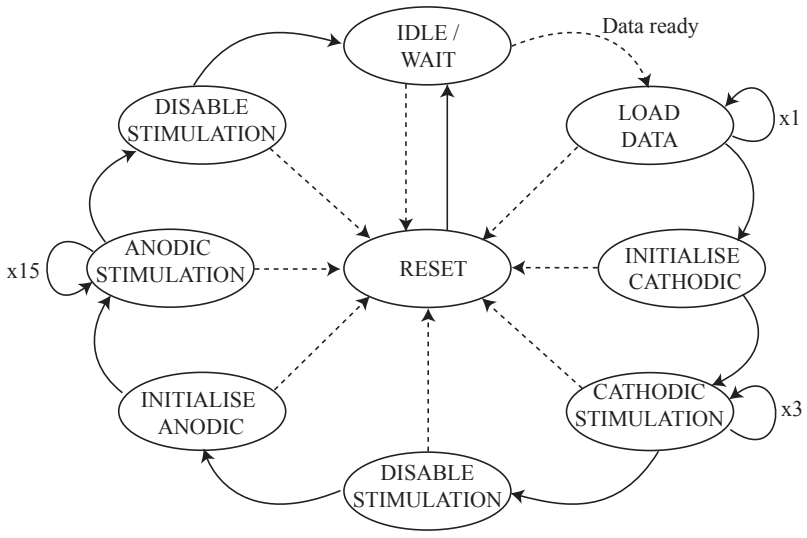


Figure 5.14: State diagram for the neural stimulator controller. The solid lines indicate normal clock cycle based transitions, dotted lines indicate transitions caused by data ready (labelled) or reset signals.

This is essentially a finite state machine made up of a synchronous counter and a series of supporting digital logic blocks for controlling the various sub-systems. The stimulus

is initiated on receipt of a data ready signal which enables the synchronous counter and reads in a 15-bit instruction that controls the stimulus output. This 15 instruction consists of: channel selection (3-bit), stimulation current (6-bit) and oscillator frequency (6-bit) for the DC-DC converter. The counter runs on a fixed 40 kHz clock and steps through the various states indicated in Figure 5.14 to provide the stimulation timing signals and power enable signals to the sub-systems (reducing power consumption) as described in Table 5.3. A single stimulation takes 26 clock cycles (650 μs) and therefore this system is currently capable of in excess of 1500 stimulations per second.

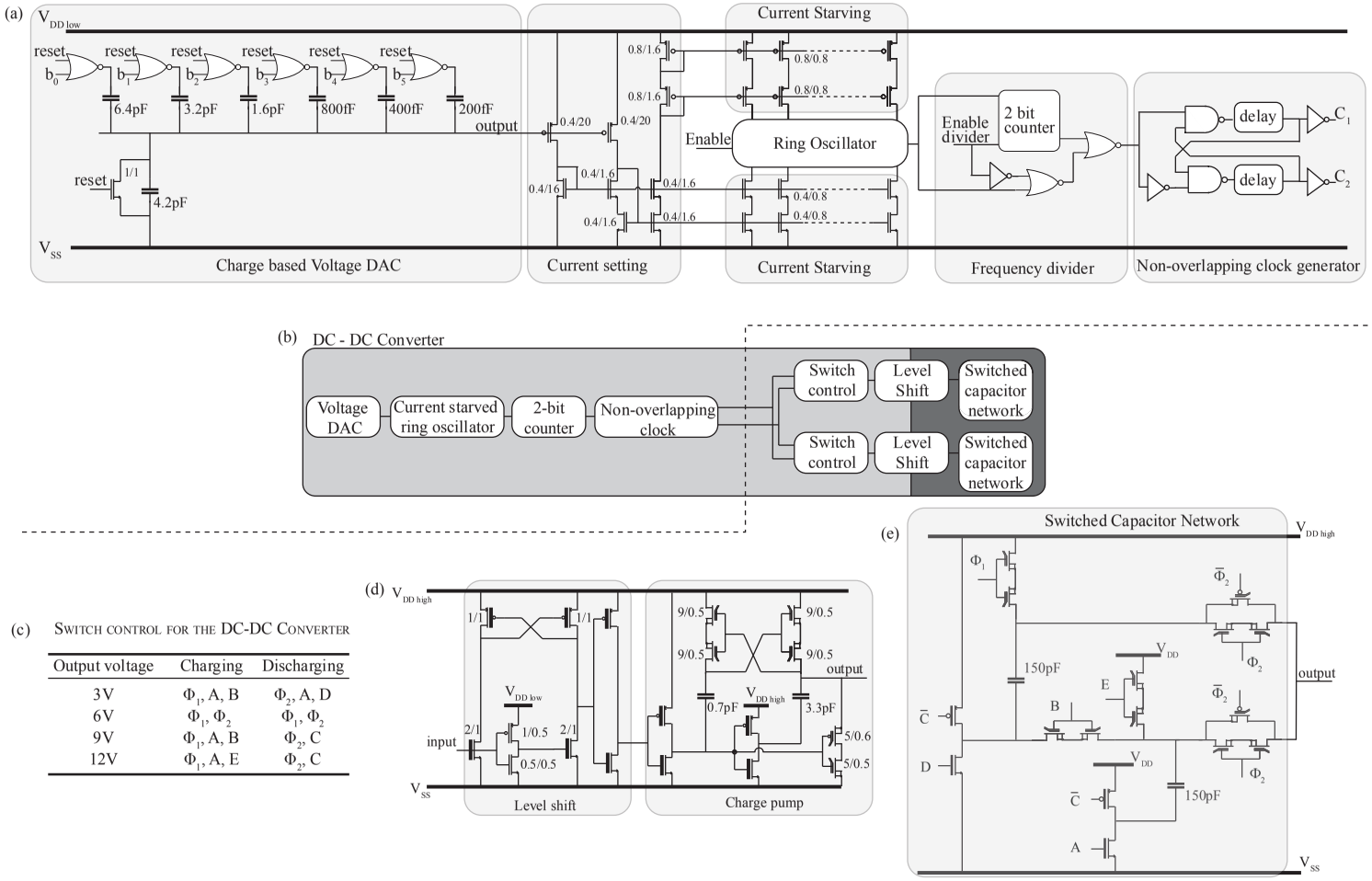
Table 5.3: Controller state descriptions.

State	**Clock Cycles**	**Action**
Idle / wait	N/A	Await data ready signal
Load data	1	Read in 15 bit control instruction
Initialise Cathodic	2	Set & enable oscillator, current sink and comparators.
Cathodic stimulation	4	H-bridge set to chosen channel
Disable stimulation	1	Disable all subsystems
Initialise Anodic	1	Set and enable oscillator, current sink and comparators.
Anodic Stimulation	16	H-bridge set to chosen channel
Disable stimulation	1	Disable all subsystems
Reset	1	Disable all outputs, reset all latches and flip flops

5.3.3 DC-DC converter

At the core of this system is a DC-DC converter to provide V_{stim}. This converter is a rapidly reconfigurable switched-capacitor network capable of generating: 3 V, 9 V and 12 V from an input power supply of 6 V. These outputs are unregulated and thus drop slightly under load. This, however, does not affect the stimulation output as the current is controlled using a floating source voltage that is independent of the DC-DC converter output. The DC-DC converter operates in a free running mode, i.e. it starts outputting at 3 V and asynchronously increases the output voltage during a stimulation. The signal for increasing the output voltage is determined by comparing the gate voltages (V_1 - V_4 in Fig. 5.17) on the high voltage thin oxide cascode transistors with a reference voltage. When this reference voltage is exceeded (indicating that the cascode transistors are close to leaving the saturation region), a feedback signal is sent to the DC-DC converter to increase the output voltage.

The building blocks of the DC-DC converter are shown in Figures 5.15(a)–(e). The first section includes a 6-bit charge scaling DAC which is combined with a current starved ring oscillator to create a digitally controlled oscillator (as shown in Fig. 5.15(a) with an output frequency range of between 50 kHz and 3.3 MHz. This frequency is determined by the time taken for the load to drain the combined flying and output capacitance by the target ripple



Output voltage	Charging	Discharging
3V	Φ_1, A, B	Φ_2, A, D
6V	Φ_1, Φ_2	Φ_1, Φ_2
9V	Φ_1, A, B	Φ_2, C
12V	Φ_1, A, E	Φ_2, C

Figure 5.15: The DC-DC converter. (a) Circuit schematic of the digitally controlled oscillator comprising of a voltage DAC, a current starved ring oscillator, a frequency divider and a non-overlapping clock generator. (b) Block diagram of the DC-DC converter. (c) Switching combinations for the transistors in the Switched Capacitor network. (d) Level shift and charge pump for driving high voltage transistors from low voltage logic. Mid-voltage transistors are shown with thick gates and high voltage transistors are shown with thick asymmetric gates. PMOS dimensions are $2/1\,\mu$m and NMOS dimensions are $1/1\,\mu$m unless otherwise stated. (e) Circuit schematic showing the switched capacitor network as implemented. All transistors are minimum length, wide devices (width $\gg$ length).

amount, and given the constant current nature of the load there is an approximately linearly relationship between this current and the minimum frequency for a given voltage ripple. This frequency is therefore tuned according to the current required during the cathodic (high amplitude) phase and the amount of voltage ripple that is acceptable on the output. To prevent excess power consumption during the lower amplitude anodic phase (i.e. when the stimulation current to be delivered is a quarter of the cathodic level) a frequency divider (based on a 2 bit counter) is used.

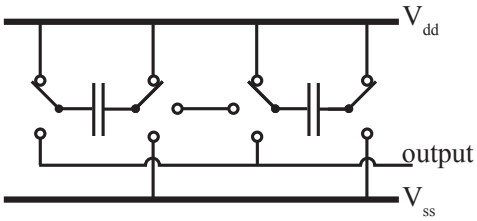
The output of the oscillator is then passed to a non-overlapping clock generator (as described in [22]) which generates 2 complementary and non-overlapping clocks at the oscillator frequency. The separation between the two clock phases (C_1, C_2) has been designed to be approximately 8 ns to ensure that, even with process variation and delay mismatch, the complementary switch groups will never be active at the same time (as verified in Monte Carlo and transient simulations).

At this point the DC-DC converter splits into 2 identical component chains consisting of: a logic block that determines the switches to activate; a level shifting block to enable the 1.8 V logic signals to drive high voltage transistors; and a switched capacitor network which performs the voltage conversion. Each of these component chains is supplied with both C_1 and C_2, but the input pins for the clocks are reversed in one of the chains, causing the two chains to operate in antiphase (i.e. when one chain is charging its switched capacitor network the other is discharging). The level shift circuit used (see Fig. 5.15(d) is a combination between a standard level shift circuit and a clock driver (charge pump) [22], enabling high voltage switches to be driven at approximately twice the supply voltage.

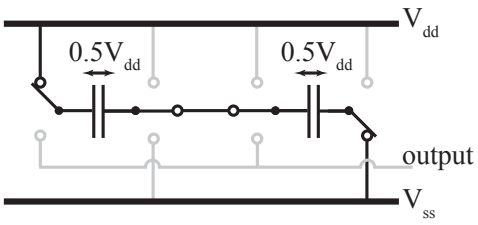
The principle of operation of each of the switched capacitor networks is illustrated in Figure 5.16. This shows how each of the networks charge and discharge to each of the output voltages (i.e. 3 V, 6 V, 9 V, 12 V). During charging, the capacitors can be connected either in series as a potential divider (Figs 5.16(b) and (d)) or in parallel (Fig 5.16(f)) charging the capacitors to 3 V or 6 V respectively. During the discharge phase the bottom plate of the capacitor can either be connected to ground, providing an output of 3 V or to the supply, giving an output of 9 V or 12 V. As 6 V is the supply voltage, it is most efficient to simply connect the output to the supply for this voltage. Again it should be noted that due to the clock arrangement when one switched capacitor network is charging the other is discharging, as this greatly reduces the voltage ripple on the output.

The actual implementation of the switched capacitor network is shown in Figure 5.15(e). Back to back (source to source) high voltage NMOS transistors were used so as to comply with design rules. The operation of the switches (i.e. selection) is shown in Figure 5.15(c).

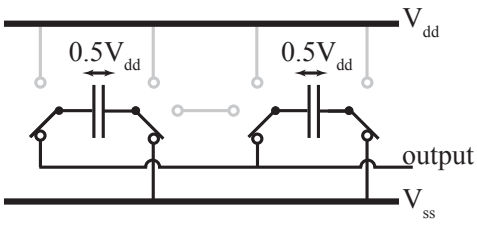
For the complete DC-DC converter, a total on chip capacitance of 900 pF (using Dual Metal Insulator Metal capacitors) is used for the two switched capacitor networks. This consists of 150 pF for each of the 2 capacitors in each network and a 300 pF load capacitance to limit the output ripple.



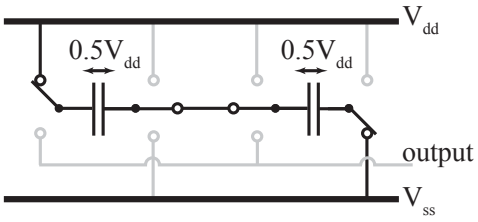
(a) Diagrammatic representation of the switched capacitor network



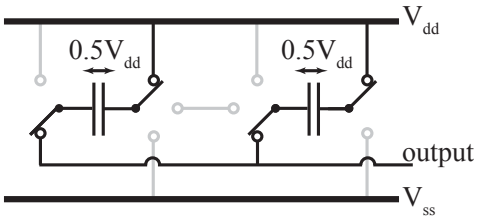
(b) 3 V charging



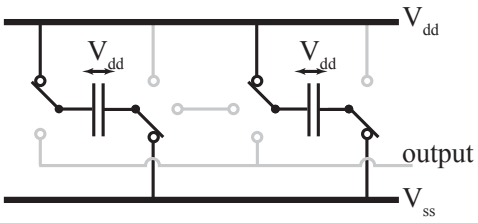
(c) 3 V discharging



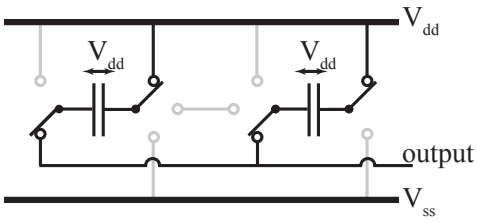
(d) 9 V charging



(e) 9 V discharging



(f) 12 V charging



(g) 12 V discharging

Figure 5.16: Charging and discharging cycles of the DC-DC converter. Not shown is the 6 V output where the supply is shorted to the output.

5.3.4 Current Sink

The design of the current sink is shown in Figure 5.17. The first stage, consisting of a current reference, produces a stable 1.6μA current which is mirrored into a 6-bit binary-weighted current-DAC. PMOS transistors (S_1 - S_6) act as switches controlling which branches of the DAC are active and therefore the output of the DAC stage. Due to the binary weighting the gain of the DAC stage is selectable between 0 and $3\frac{15}{16}$ and as such the output current is controllable in steps of 0.1 μA up to 6.3 μA.

The current generated by the DAC then flows into a regulated cascode current mirror. This mirror is set up with each branch having a W/L ratio 20 times that of the branch being mirrored so that up to 80 times the DAC output current can flow through the combined sink. A folded cascode op-amp driving a high voltage thin-oxide transistor (V_{GS}(max) = 1.8 V) is used to regulate the V_{DS} of each of the mirroring transistors [23, 24]. Op-amps

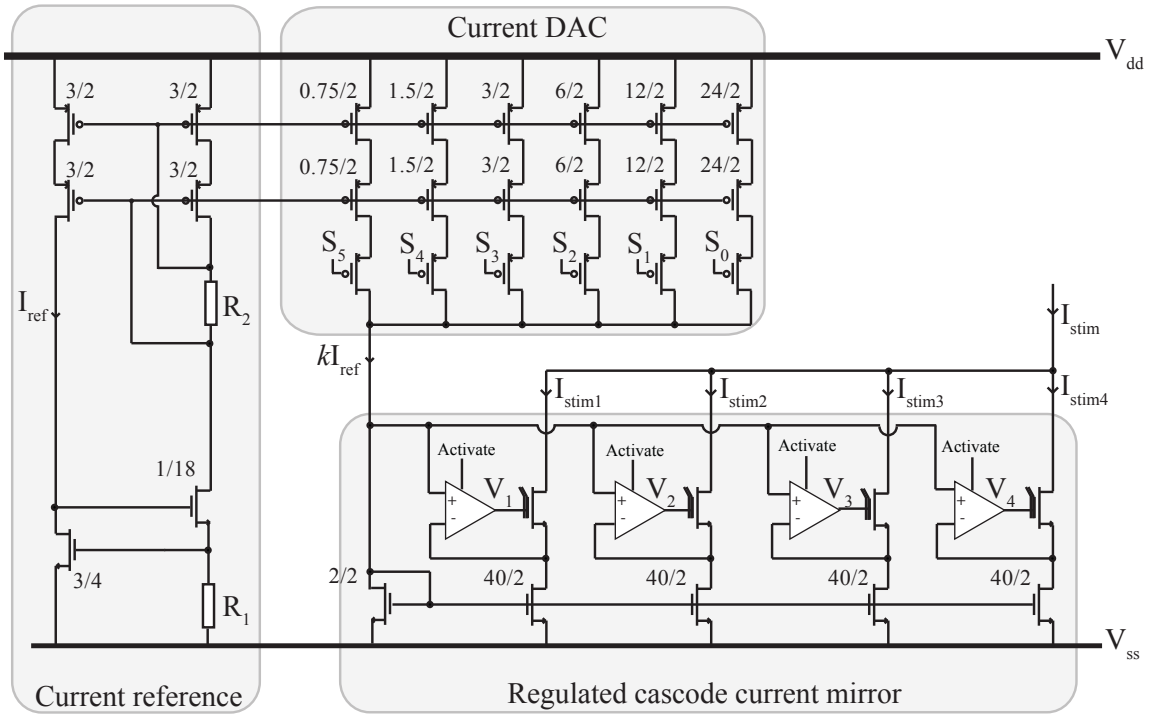


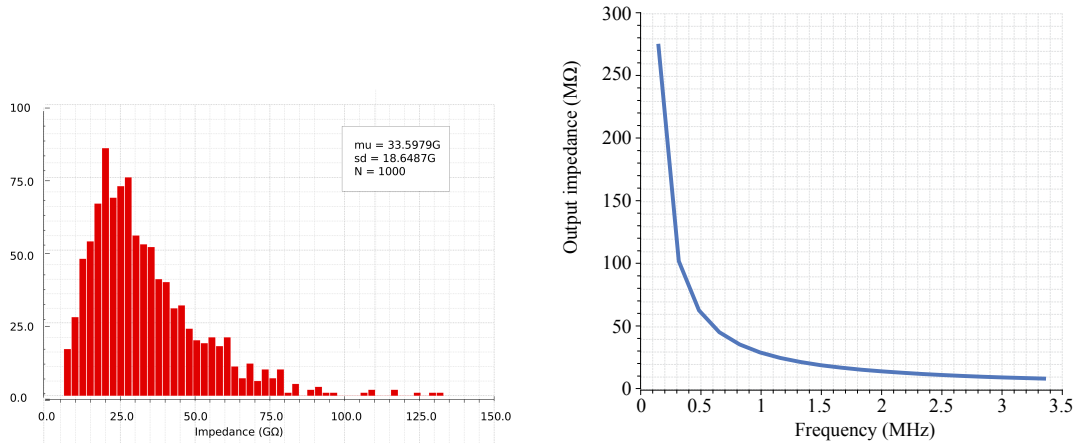
Figure 5.17: Circuit schematic of the current reference, DAC and regulated cascode current mirror.

were chosen to drive the cascoding transistors to minimise the current changes due to the ripple ($\leq$100mV at frequencies $\leq$3.3MHz) and rapid voltage changes introduced by the DC-DC converter. Each op-amp can be individually deactivated, thereby turning off the respective cascode device. During the cathodic stimulation phase all four op-amps are active providing the full factor of 80 gain, however, during the anodic stimulation phase only one of the op-amps is used and as such the gain drops to a factor of 20. This provides the 4:1 ratio between the cathodic and anodic phases. The current sink is capable of sinking between 2μA and 504μA. Monte Carlo (process and mismatch) DC sweep simulations were performed to measure the peak-to-peak change in sunk current (at the maximum stimulation current) while varying the DC voltage applied at the output between 1.5V - 12V, this produced an estimate of the DC output impedance for the current sink of 33GΩ (see Fig. 5.18(a)). Repeating this simulation with a fixed DC voltage combined with a 100mV sinusoidal ripple of varying shows the frequency dependence of the impedance (see Fig. 5.18(b)) and indicates that at the maximum system oscillator frequency of 3.3MHz the impedance is around 8MΩ.

The novel charge balancing approach discussed in Section 5.1 can now be examined with this system. Looking at Figure 5.17, in the cathodic phase the total charge injected (Q_i) into the electrodes will be:

$$Q_i = (I_{stim1} + I_{stim2} + I_{stim3} + I_{stim4}) \times T \tag{5.2}$$

where T is the cathodic phase duration. In the subsequent anodic phase, one of the regulated cascodes will be active for 4 times the duration and the charge removed (Q_r) from



(a) Monte Carlo simulation of DC output impedance

(b) Frequency dependence of the output impedance

Figure 5.18: Simulations of the output impedance.

the electrodes will be (for example):

$$Q_r = I_{stim2} \times 4 \times T \tag{5.3}$$

The 4 cascoded transistors were matched carefully during layout so this will provide a certain level of charge balancing, but accurate charge balancing can be achieved if the op-amp activated in the anodic phase is changed sequentially for each stimulation, i.e. interleaved. This is because over a series of 4 stimulations each of the mirrors will have been active for the same amount of time *anodically* as they were *cathodically* and as such errors due to process variation and mismatch will cancel. The controller has a 2-bit counter for each channel that increments after each anodic stimulation so as to ensure that each op-amp is used in turn.

As mentioned in Section 5.3.3, the outputs from these op-amps are monitored to determine when the cascode transistors are leaving saturation and therefore when to trigger an increase in the DC-DC converter output. The monitoring is achieved using a 2-stage comparator with 100 mV of hysteresis - one terminal is connected to the op-amp output and the other connected to a reference voltage (approximate value 1.4 V).

5.3.5 H-bridge

The H-bridge block consists of an array of 8 H-bridges (one per channel) arranged in parallel and level shifters to drive the high voltage transistors that are used for the switches (in a transmission gate arrangement). The level shift circuit is identical to the one used in the DC-DC converter. The parallel H-bridge arrangement enables a single current sink to selectively pull current through any of the 8 channels, however, this does mean that only a single channel can be active at any moment in time. It is envisaged that the end application will target electrode sites at close proximity and therefore a Continuous Interleave Sampling (CIS) [25, 26] will be used to avoid any cross-stimulation.

5.3.6 Core Supply DC-DC converter

To operate the system from a single 6 V supply, a second, auxiliary DC-DC converter has been included to generate the lower voltage supply to the system core. This has been implemented as a serial-parallel switched capacitor converter [27], but utilises the same 2 phase concept as the core DC-DC converter to reduce voltage ripple. The 6 V (peak to peak) clock for this converter is supplied by an external input and is split into 2 phases using the same non-overlapping clock method as used for the core DC-DC converter.

5.3.7 ESD and pad ring

The combination of high voltage inputs and outputs, and low voltage logic signals requires a split approach to ESD protection and the pad ring. Figure 5.19 shows a photograph of the manufactured chip die. Along the left hand side and partway along the top of the die, the high voltage I/O cells can be seen and these are protected with a 20 V clamp device provided in the foundry models. Along the top-right and right hand side of the die are the low voltage digital and analogue pads for external interfacing and core test. These are standard low voltage I/O cells protected by a 1.8 V clamp.

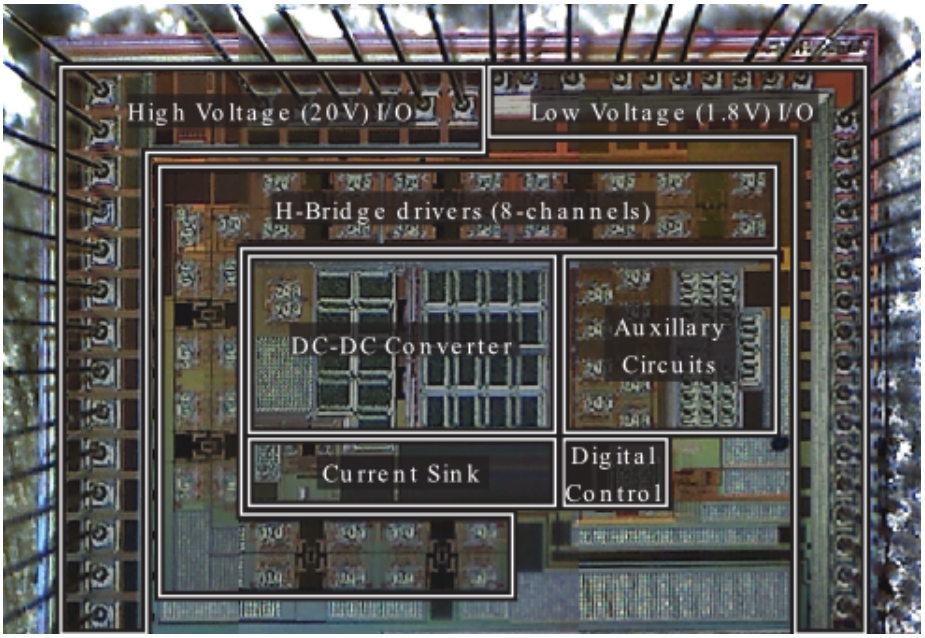


Figure 5.19: Microphotograph of the neural stimulator, measuring 2 mm × 2.7 mm.

5.4 Experimental Results

The system has been validated through a series of tests including design simulation, bench-top chip measurements and *ex-vivo* lab experiments on a peripheral nerve.

5.4.1 Simulated Results

The circuit was initially simulated using foundry-supplied PSP models with the Cadence Ultrasim and Spectre simulators. Transient simulations (shown in Fig. 5.20) for the neural stimulator show that it should be capable of achieving a voltage output of approximately 11.5 V, although between 0.3 V (at minimum current) and 0.7 V (at maximum current) of this is required as voltage headroom to keep the current sink transistors in saturation. The results also show that despite 100 mV ripple on the DC-DC converter output, the resulting current sink ripple was typically $<2\,\mu$A (at the maximum current of 504 μA). Figure 5.20(a) shows the asymmetric current through the electrode with a high-amplitude short-duration cathodic phase lasting for 100 μ s and a low-amplitude, long-duration anodic phase lasting for 400 μ s. Figure 5.20(b) shows the DC-DC converter output changing during the stimulation, as the cascoding transistor approaches the point that it would be pushed out of saturation. Figure 5.20(c) shows the voltage across the electrodes and closely mirrors the theoretical voltage shown in Figure 5.5(a).

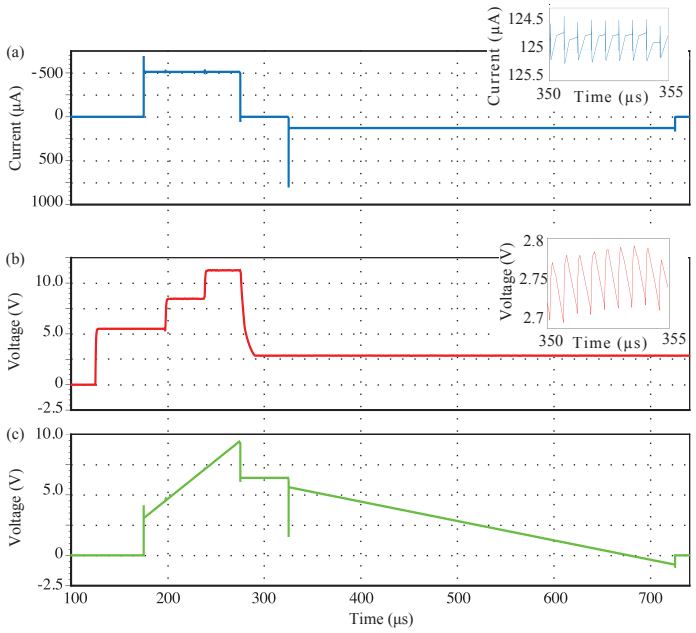


Figure 5.20: Transient analysis of the neural stimulator for a full-scale stimulus (504 μA) showing: (a) stimulation (electrode) current, (b) voltage output of the DC-DC converter, (c) voltage across the electrode model. Insets show close ups of the ripple.

Converter efficiency

The DC-DC converter efficiency was evaluated under a variety of ideal current loads (with switching frequency tuned to the load) and the results are shown in Fig. 5.21. These results show that the conversion efficiency is above 80% for 9 V and 12 V outputs across much of the load range. However, the efficiency is worse for light loads and across the entire range for the 3 V output. This is because the clock, level shift and charge pump overheads make up a significantly higher proportion of the total power consumption at these lower outputs.

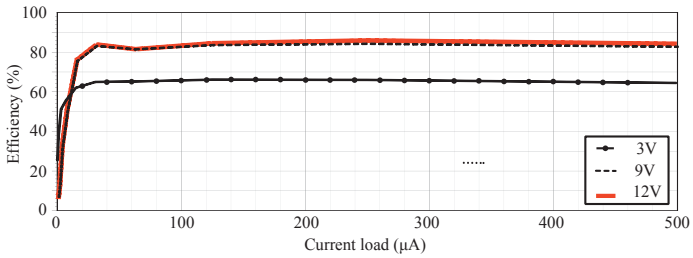


Figure 5.21: Simulated DC converter efficiency for different target stimuli (i.e. output currents) for 3 V, 9 V and 12 V compliances.

Charge balance

Monte-Carlo simulations were performed with a fixed DC voltage source to ensure that the proposed charge balance approach was robust to process variation and mismatch (using foundry supplied models of the process). Figure 5.22 shows simulated charge imbalance after 1 and 4 stimulation cycles at maximum current. The results show that although there is still some error in charge balance, the likely error is reduced from hundreds of pico-coulombs (for a single pulse) to a few tens of pico-coulombs over 4 stimulations. Possible causes of the fixed offset of approximately -26 pC include charge injection and an inaccuracy in the timing of the signals controlling the stimulation.

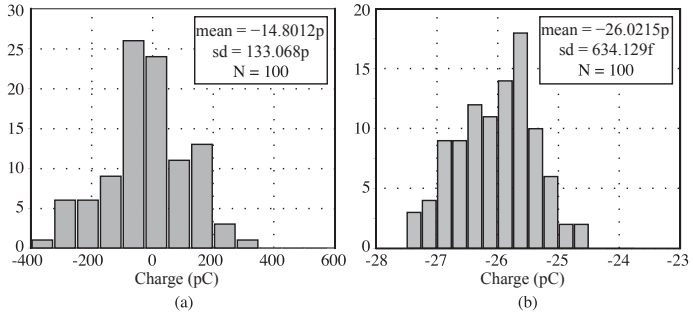


Figure 5.22: Monte Carlo simulations of charge remaining on the electrodes after: (a) single stimulation pulse, and (b) a series of 4 stimulations at maximum stimulation current.

5.4.2 Measured results

The fabricated chips were bonded in a JLCC84 package and mounted on a custom designed PCB test platform. Power was supplied from a Keithley 2602 source meter, the 40kHz clock was supplied from a function generator, and, for testing purposes, the digital inputs were simply controlled from DIL switches. A lumped model for the electrode was used (consisting of a 6.8 kΩ resistor in series with 2 parallel ceramic capacitors totalling 6.9 nF) to approximate our target electrode impedance. Initial investigations focused on verifying that the various subsystems of the chips were working as expected. This was achieved by observing the currents and voltages output by the chip during stimulation cycles. A selection of the measured waveforms are presented in Figure 5.23 and in comparison with those shown in Figure 5.20 show that the chip is operating as expected, in particular that

the maximum voltage output closely matches the 11.5 V expected. Figs. 5.23(a) and (c) involved measuring voltage drops across a resistor and this is likely a major contributor to the noise shown on these signals.

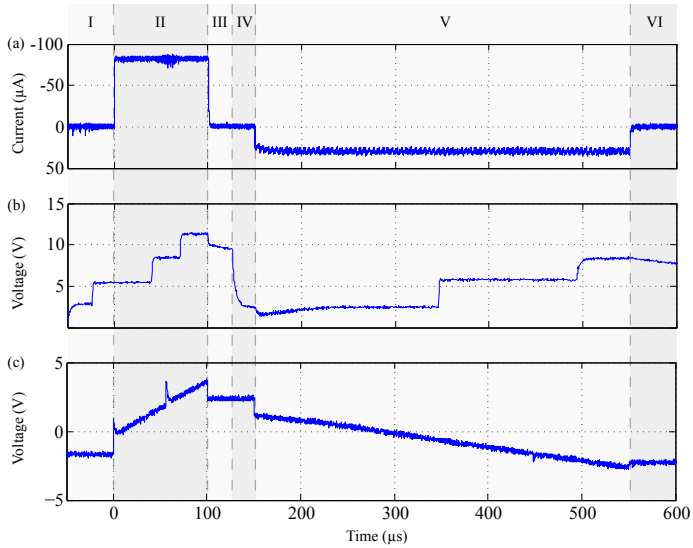


Figure 5.23: Sample results of the neural stimulator. Shown are: (a) the current through the lumped electrode model, (b) the output voltage of the DC-DC converter, (c) the electrode voltage during stimulation. Phases I through to VI match the states listed in Table 5.3 starting with "Initialise Cathodic".

Charge balancing

Once the functional verification had been completed, performance measurements were undertaken. The first to be measured was the charge balancing performance. This was tested by driving the stimulation current into the charge measuring terminals of a Keithley 6517a electrometer, which functionally acts as op-amp based charge integrator. The cumulative charge imbalance over 1000 stimulations was measured for a range of stimulation currents and the average charge imbalance is shown in Figure 5.24(a) and the percentage error is shown in Figure 5.24(b). These results indicate good charge balancing with a charge delivery error of between 0.05% to 0.15% across nearly the entire stimulation range with only the lowest stimulation level deviating from this.

A possible source of this correlation between charge error and stimulation level is the fluctuation in stimulation current during transitions between DC-DC converter output voltages. During these transitions the voltage across the cascoded transistors rises rapidly, with a 10–90% rise time of as little as 0.67μ s (equating to a slew rate of around $3.57 \cdot 10^{-6}$ V/s). Simulations were run to characterise the impact of these fluctuations at the transitions from 3V–6V, 6V–9V and 9V–12V. The results indicated maximum charge imbalances of 7.5 pC per transition for a maximum amplitude stimulus. Some of this charge error is offset by opposite polarity charge errors during the anodic phase, however, the asymmetric waveforms and the charge accumulated in the electrode capacitance mean that fewer transitions occur during this phase, while the lower frequency of operation also reduces the charge

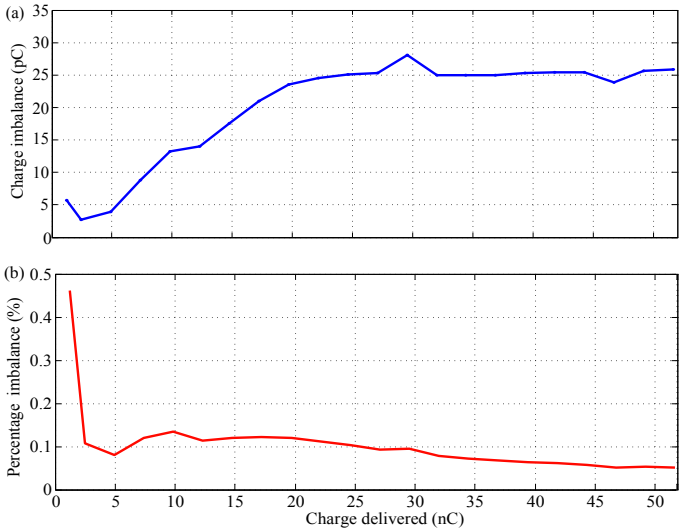


Figure 5.24: Charge imbalance results. Shown are (a) the cumulative charge imbalance averaged over 1000 stimulations vs charge injected per stimulation; (b) the charge imbalance as a percentage of charge injected.

error during the anodic phase.

Power consumption

The quiescent power consumption of the chips was measured as approximately 185 μW using an Agilent 6705b (averaging out as 23.2 μW per channel). The dynamic power consumption (during stimulation) of the fabricated chips was measured by connecting a 1.2 kΩ resistor in series with the 6 V power supply and monitoring the voltage drop across it on an oscilloscope. This allowed the current, and therefore the power consumed, during a stimulation to be estimated. As proposed in [6] and [11], power savings achieved by this proposed system will be evaluated by comparing with power consumption in the front end of a baseline fixed supply current stimulator that has similar voltage compliance (in our case 11 V) and a low voltage headroom. Power consumption measurements for the whole system were gathered for a range of stimulation currents on an electrode (6.8 kΩ and 6.9 nF) and are shown in Figure 5.25(a) alongside simulated and baseline results. The percentage energy reduction that this stimulator provides compared to a standard current mode stimulator is shown in Fig. 5.25(b).

The energy savings (ΔE_{system}) of this proposed system are at a top level given by:

$$\Delta E_{system} = \Delta E_{Front-end} - E_{DC-DC} - E_{Converter-control} \tag{5.4}$$

where $\Delta E_{Front-end}$ is the energy savings in the front end transistors, E_{DC-DC} is the energy wasted in the DC-DC converter and $E_{Converter-control}$ is the additional energy used by the system to control the converter.

The energy savings in the front end result from the reduced voltage across the cascoded current controlling transistors. Using the previously discussed RC series electrode model and noting that the cathodic current (I_{stim}) is 4 times the anodic stimulation current, while

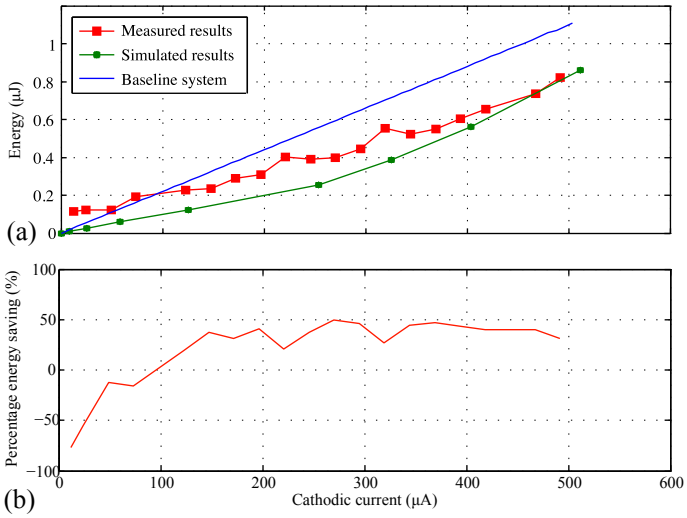


Figure 5.25: Energy per stimulation. Shown are (a) how energy consumption (per stimulation cycle) varies with stimulation current; (b) percentage energy saving by the proposed system.

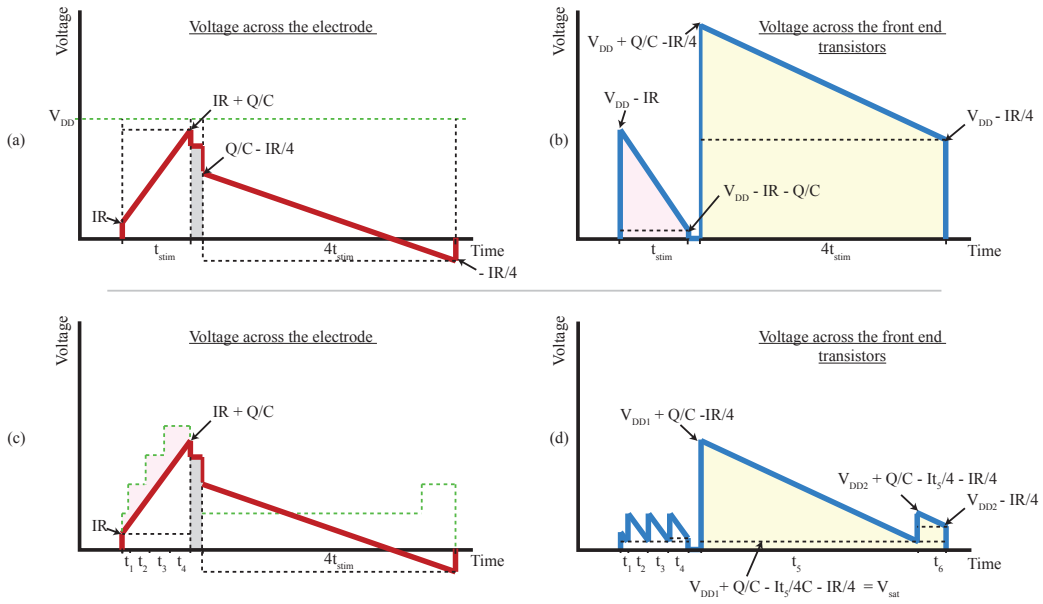


Figure 5.26: n

Voltages across the electrode and the current controlling transistors. During the first (cathodic) phase the voltage across the transistors is equal to the difference between the supplied voltage and the voltage across the electrodes, while in the anodic phase (due to the H-bridge) it is equal to the supply voltage plus the difference between the supplied voltage and the voltage across the electrodes. (a) The voltage across the electrodes for a baseline (fixed voltage) system is shown in red, the supply voltage in green. (b) The voltage across the front end transistors for a baseline (fixed voltage) system is shown in blue. Shaded pink and yellow areas correspond to equation 5.5. (c) The voltage across the electrodes for the proposed system. Shaded pink area corresponds to equation 5.6. (d) The voltage across the front end transistors for the proposed system. Shaded yellow area corresponds to equation 5.7.

the cathodic stimulation time (t_{stim}) is ¼ the anodic stimulation time; we find that in the baseline system with a fixed supply (V_{DD}) the energy dissipated in these transistors (see Fig 5.26(a) and (b)) is:

$$E_{Front-end} = 2 \cdot V_{DD} \cdot I_{stim} \cdot t_{stim} - \frac{5}{4} I_{stim}^2 \cdot R \cdot t_{stim} \tag{5.5}$$

Where $V_{DD} \geq I_{stim} \cdot R + {}^{I_{stim} \cdot t_{stim}}/_{C} + V_{sat}$ and V_{sat} is the voltage overhead required to keep the cascoded transistors in saturation.

Meanwhile the energy dissipated in the cascoded transistors of the proposed system can be analysed in a similar way but in 4 discrete time sections for the cathodic phase and 2 for the anodic phase – each representing a particular output of the DC-DC converter – as can be seen in Figure 5.26 (c) and (d) which show the voltage across the front-end transistors.

For the cathodic phase the energy dissipated in the front-end is:

$$E = I_{stim}(V_{DD1} \cdot t_1 + V_{DD2} \cdot t_2 + V_{DD3} \cdot t_3 + V_{DD4} \cdot t_4) - I_{stim}^2 \cdot R \cdot t_{stim} - \frac{Q_{tot} \cdot t_{stim} \cdot I_{stim}}{2C} \tag{5.6}$$

where Q_{tot} is the total charge injected into the tissue, V_{DD1} – V_{DD4} are the four output voltages of the DC-DC converter and t_1 – t_6 are the time periods that each output voltage is active.

For the anodic phase where the maximum DC-DC converter output should not exceed 6V (due to the asymmetric waveform and the charge stored in the electrode capacitance) the energy consumed (see Fig 5.26(d)) is:

$$E = \frac{I_{stim}}{4} \cdot \left[4 \cdot V_{sat} \cdot t_5 + \frac{t_5}{2} \left(\frac{I_{stim} \cdot t_5}{4C} \right) + \frac{t_6}{2} \left(\frac{I_{stim} \cdot t_6}{4C} \right) + t_6 \cdot \left(V_{DD2} - \frac{I_{stim} \cdot R}{4} \right) \right] \tag{5.7}$$

where:

$$t_1 = \begin{cases} 100\mu s & \text{if } \frac{C(V_{DD1} - V_{sat} - I_{stim} \cdot R)}{I_{stim}} > 100\mu s \\ \frac{C(V_{DD1} - V_{sat} - I_{stim} \cdot R)}{I_{stim}} & \text{else} \end{cases} \tag{5.8}$$

and for t_2, t_3 and t_4:

$$t_n = \begin{cases} 100\mu s - \sum_{i=0}^{n-1} t_i & \text{if } \frac{C(V_{DDn} - V_{sat} - I_{stim} \cdot R)}{I_{stim}} > 100\mu s \\ \frac{C(V_{DDn} - V_{DDn-1})}{I_{stim}} & \text{else if } \frac{C(V_{DDn} - V_{sat} - I_{stim} \cdot R)}{I_{stim}} < 100\mu s \\ 0 & \text{else if } \sum_{i=0}^{n-1} t_i = 100\mu s \end{cases} \tag{5.9}$$

while t_5 and t_6 are determined by:

$$t_5 = \begin{cases} 400\mu s & \text{if } \frac{4 \cdot C(V_{DD1} - \frac{I_{stim} \cdot R}{4} - V_{sat})}{I_{stim}} > 400\mu s \\ \frac{4 \cdot C(V_{DD1} + \frac{Q_{tot}}{C} - \frac{I_{stim} \cdot R}{4} - V_{sat})}{I_{stim}} & \text{else} \end{cases} \tag{5.10}$$

$$t_6 = \begin{cases} 0 & \text{if } t_5 = 400\mu s \\ 400\mu s - t_5 & \text{else} \end{cases} \tag{5.11}$$

The energy wasted ($E_{DC-waste}$)in the DC-DC converter is calculated using the converter

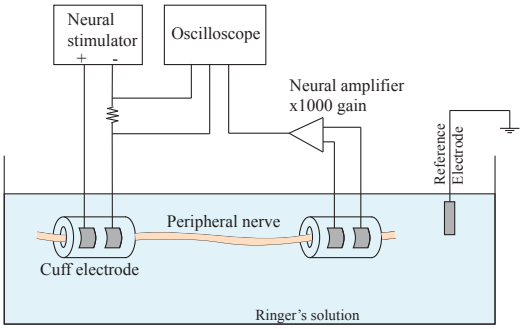
efficiencies at each of the 4 DC-DC converter ouptput voltages (Eff_1, Eff_2, Eff_3 and Eff_4) shown in Figure 5.21 giving:

$$E_{DC-waste} = I_{stim}\left\{\sum_{i=1}^{4}[(1-\text{Eff}_i)t_i \cdot V_{DDi}] + \frac{(1-\text{Eff}_1)t_5 \cdot V_{DD1}}{4} + \frac{(1-\text{Eff}_2)t_6 \cdot V_{DD2}}{4}\right\} \tag{5.12}$$

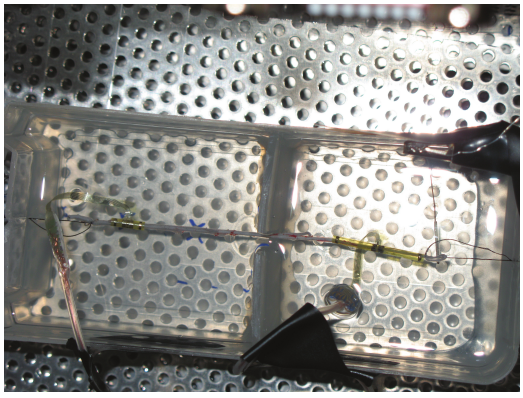
Meanwhile the energy consumed controlling the DC-DC converter ($E_{Converter-control}$) is dominated by the current through the comparators ($2\,\mu$ A each) running at 1.8 V each (approximately 1.6 pJ per stimulation).

Putting all these component parts together results in the performance estimates shown in Figure 5.25(a).

5.4.3 Ex-Vivo Results



(a)



(b) Photo of the experimental setup, stimulation on the left and recording on the right (reproduced from [28]).

Figure 5.27: Experimental setup for the *ex-vivo* test.

Once the various laboratory tests had been performed to characterise the chip's performance, the core system functionality was validated *ex-vivo* by stimulating a peripheral nerve. The experimental setup is outlined in Figure 5.27 and is based closely on the setup proposed in [28]. The peripheral nerve was a carefully extracted sciatic nerve (from a dissected African clawed frog - *Xenopus laevis*) of approximately 10 cm length, that had been tied at both ends and immersed in amphibian Ringer's solution [29]. Self-closing cuff electrodes were placed around both ends of the nerve, one end connected to the stimulator and the other connected to a custom made tripolar amplifier [28] and sampled at 40kHz using a NI DAQPAD 6015 data acquisition system. An Ag|AgCl electrode was used to provide the reference ground.

The measured cuff impedance was 3.01 kΩ and the stimulator was set up to repeatedly deliver and recover 20 nC of charge (200 μA) at a rate of 10 stimulations per second. Induced action potentials were measured at the other end of the nerve fascicle and a sample of the recorded data is shown in Figure 5.28. The results clearly show that the chip successfully stimulated the nerve fascicle, and an enlarged action potential shows: the stimulation

artefacts (I), the cumulative action potential of the fast conducting (A-α) fibres (II), and the cumulative action potential of the slower conducting (A-β) fibres (III) [28].

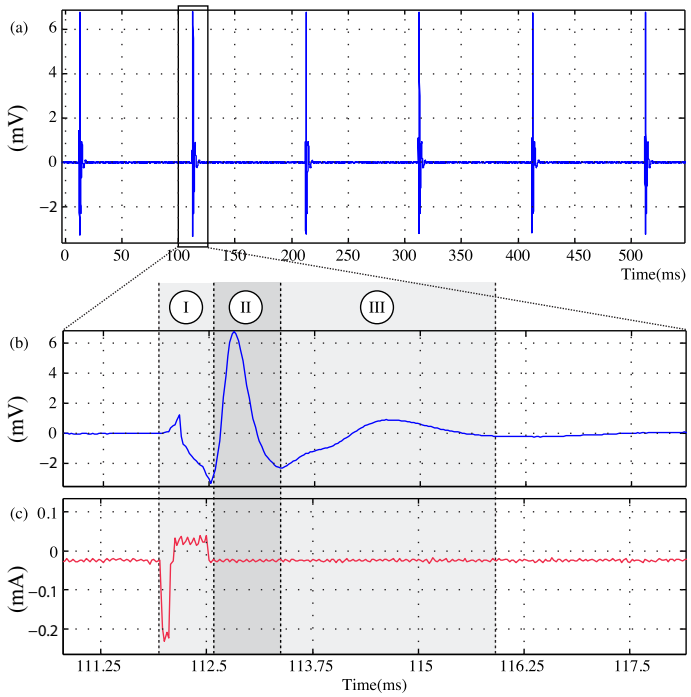


Figure 5.28: *ex-vivo* measured response to stimulation. Shown are: (a) action potentials generated in a peripheral nerve with the neural stimulator, (b) an enlargement of a single stimulated action potential, (c) the measured current stimulus that initiated the action potential.

5.5 Discussion and Future Work

This chapter has presented a neural stimulator that implements a novel approach to charge balancing - allowing asymmetric stimulation patterns to be used - and uses a fully integrated switched capacitor DC-DC converter to reduce system power consumption. Table 5.4 compares this work to other designs that achieve high energy-efficiency compared to basic current mode stimulators.

The work has demonstrated that dynamic voltage scaling using switched capacitor DC-DC conversion can be employed on current-mode stimulation to achieve power savings of up to 50%. The output currents (as seen in Fig. 5.23 (d)) are stable and show that the DC-DC converter has minimal impact on current stimulus output. The voltage ripple on the output of the converter does cause some current ripple through the electrodes but in simulations this is less than 2 μA (peak-to-peak) at the maximum stimulation current. Furthermore, this is at the DC-DC converter clock frequency (i.e. up to 3.3 MHz) and is thus unlikely to have a physiological impact on stimulation. Power reduction was not achieved at low stimulation currents, likely as a result of the quiescent system power consumption and overheads in operating the DC-DC converter. However, actual power waste in this region is expected to be reasonably small due to the low current levels involved and, assuming

Table 5.4: Comparison with other low-power neural stimulator designs.

	Arfin et Al [11]	Kelly et Al [6]	Sit et Al [4]	This work
CMOS Technology	0.35 μm	1.5 μm	0.7 μm HV	0.18 μm HV
Dynamic range	0–450 μA	0–136 μA	0–1 mA	0–504 μA
Voltage compliance	3 V	1.75 V	15 V	11.5 V
Stimulus control	Current	Voltage	Current	Current
Max power savings*	62 %	66 %	n/A	50 %
Fully integrated	✗	✗	✓	✓
Charge mismatch	n/A	n/A	≤0.4 %	≤0.45 %
Asymmetric waveforms	✓	✓	✗	✓
Channels	1	15	16	8

*Power savings relative to a typical current controlled stimulator

the stimulation patterns contain a mixture of high and low stimulus currents, it is likely these power losses will be more than compensated for by the power savings at higher power levels. There are also a number of possible mitigation strategies to avoid power loss at low current levels (e.g. modifying the system to simply use the 6 V supply at low load currents), however, these incur additional complexity. Unless the low load efficiency of the converter can be significantly improved, it seems unlikely that stimulators operating at currents below 100 μA will benefit from DC-DC converter integration.

Charge balanced stimulation pulses are important for patient safety and preventing electrode degeneration. DC current flows of 100 nA across an electrode have been correlated with tissue damage in animal models [30] and industry targets a DC error of < 25 nA [4]. The stimulator proposed here is capable of stimulating at over 1500 pulses per second, but will in practice only be used to deliver up to 80 stimulations per second per channel (based on maximum observed firing rates of human proprioceptors [31, 32]). Each stimulation delivers up to 50nC of charge and therefore this stimulator injects and extracts up to 4 μA from the tissue per channel. Measured results show the proposed system delivered charge imbalances of up to 5% (equivalent to 200nA) for a single stimulation and a worst case charge imbalance of 0.46 % (18nA) for a series of stimulations, with typical charge balancing performance in the 0.05 % - 0.15 % range. The proposed interleaving of current sinks therefore enables asymmetric waveforms while keeping charge balancing performance in the safe operating region.

5.5.1 Future Work

The stimulator presented here is a proof of principle prototype; planned alterations for a future iteration include increasing the number of channels to 16 and reducing the number of bond pads (by removing testing I/O pads and utilising serial rather than parallel data transmission). There are also a number of areas identified for further investigation including:

- The power consumption and issues associated with integrating a voltage regulator to reduce ripple.

- Alternate DC-DC converter control strategies and ripple rejection to improve low current stimulation efficiency.
- More comprehensive *in vitro* testing, including using electrodes of various impedances, to better determine real world efficiency and to investigate the increased current ripple observed in Figure 5.27.
- And finally a proposed system redesign to enable the system stimulation voltage (V_{stim}) to be set to 0 V (ground) in the anodic phase - allowing the energy stored in the electrode capacitance to be more efficiently recovered.

Bibliography

[1] K. Horch and G. Dhillon. *Neuroprosthetics: Theory and Practice*. Series on bioengineering and biomedical engineering. World Scientific, 2004. ISBN: 9789812380227.

[2] J. C. LaManna, K. A. McCracken, M. Patil, and O. J. Prohaska. "Stimulus-activated changes in brain tissue temperature in the anesthetized rat". *Metabolic brain disease* 4.4 (1989), pp. 225–237.

[3] D. Ni, R. K. Shepherd, H. L. Seldon, S.-A. Xu, G. M. Clark, and R. E. Millard. "Cochlear pathology following chronic electrical stimulation of the auditory nerve. I: Normal hearing kittens". *Hearing research* 62 (1992), pp. 63–81.

[4] J.-J. Sit and R. Sarpeshkar. "A Low-Power Blocking-Capacitor-Free Charge-Balanced Electrode-Stimulator Chip With Less Than 6 nA DC Error for 1-mA Full-Scale Stimulation". *Biomedical Circuits and Systems, IEEE Transactions on* 1 (2007), pp. 172–183.

[5] O. Macherey, A. van Wieringen, R. P. Carlyon, J. M. Deeks, and J. Wouters. "Asymmetric pulses in cochlear implants: effects of pulse shape, polarity, and rate." *Journal of the Association for Research in Otolaryngology : JARO* 7 (2006), pp. 253–66.

[6] S. K. Kelly and J. L. Wyatt. "A Power-Efficient Neural Tissue Stimulator With Energy Recovery". *Biomedical Circuits and Systems, IEEE Transactions on* 5 (2011), pp. 20–29.

[7] D. Tan, M. Schiefer, M. W. Keith, R. Anderson, and D. J. Tyler. "Stability and selectivity of a chronic, multi-contact cuff electrode for sensory stimulation in a human amputee". *Neural Engineering (NER), 2013 6th International IEEE/EMBS Conference on*. IEEE. 2013, pp. 859–862.

[8] K. H. Polasek, H. A. Hoyen, M. W. Keith, and D. J. Tyler. "Human nerve stimulation thresholds and selectivity using a multi-contact nerve cuff electrode". *Neural Systems and Rehabilitation Engineering, IEEE Transactions on* 15 (2007), pp. 76–82.

[9] K. H. Polasek, H. A. Hoyen, M. W. Keith, R. F. Kirsch, and D. J. Tyler. "Stimulation stability and selectivity of chronically implanted multicontact nerve cuff electrodes in the human upper extremity". *Neural Systems and Rehabilitation Engineering, IEEE Transactions on* 17.5 (2009), pp. 428–437.

[10] S. Ethier, M. Sawan, E. M. Aboulhamid, and M. El-Gamal. "A 9V fully integrated CMOS electrode driver for high-impedance microstimulation". 2009, pp. 192–195.

[11] S. K. Arfin and R. Sarpeshkar. "An Energy-Efficient, Adiabatic Electrode Stimulator With Inductive Energy Recycling and Feedback Current Regulation". *Biomedical Circuits and Systems, IEEE Transactions on* 6 (2012), pp. 1–14.

[12] V. Kursun and E. G. Friedman. *Multi-voltage CMOS circuit design*. John Wiley & Sons, Ltd, 2006.

[13] T. Van Breussegem and M. Steyaert. *CMOS Integrated Capacitive DC-DC Converters*. Analog Circuits and Signal Processing. Springer, 2012. ISBN: 9781461442806.

[14] G. V. Pique. "A 41-phase switched-capacitor power converter with 3.8 mV output ripple and 81% efficiency in baseline 90nm CMOS". *Solid-State Circuits Conference Digest of Technical Papers (ISSCC), 2012 IEEE International*. IEEE. 2012, pp. 98–100.

[15] D. El-Damak, S. Bandyopadhyay, and A. P. Chandrakasan. "A 93% efficiency reconfigurable switched-capacitor DC-DC converter using on-chip ferroelectric capacitors". *Solid-State Circuits Conference Digest of Technical Papers (ISSCC), 2013 IEEE International*. IEEE. 2013, pp. 374–375.

[16] H.-P. Le, J. Crossley, S. Sanders, and E. Alon. "A sub-ns response fully integrated battery-connected switched-capacitor voltage regulator delivering 0.19 W/mm 2 at 73% efficiency". *Solid-State Circuits Conference Digest of Technical Papers (ISSCC), 2013 IEEE International*. IEEE. 2013, pp. 372–373.

[17] L. G. Salem and P. P. Mercier. "4.6 An 85%-efficiency fully integrated 15-ratio recursive switched-capacitor DC-DC converter with 0.1-to-2.2 V output voltage range". *Solid-State Circuits Conference Digest of Technical Papers (ISSCC), 2014 IEEE International*. IEEE. 2014, pp. 88–89.

[18] L. Seung-Chul and L. Seung-Hoon. "A low-ripple switched-capacitor DC-DC up converter for low-voltage applications". *IEICE transactions on electronics* 84.8 (2001), pp. 1100–1103.

[19] T. Boretius, J. Badia, A. Pascual-Font, M. Schuettler, X. Navarro, K. Yoshida, and T. Stieglitz. "A transverse intrafascicular multichannel electrode (TIME) to interface with the peripheral nerve". *Biosensors and Bioelectronics* 26.1 (2010), pp. 62–69.

[20] K. H. Polasek, H. A. Hoyen, M. W. Keith, and D. J. Tyler. "Human Nerve Stimulation Thresholds and Selectivity Using a Multi-contact Nerve Cuff Electrode". *Neural Systems and Rehabilitation Engineering, IEEE Transactions on* 15 (2007), pp. 76–82.

[21] M. Schiefer, K. Polasek, R. Triolo, G. Pinault, and D. Tyler. "Selective stimulation of the human femoral nerve with a flat interface nerve electrode". *Journal of neural engineering* 7.2 (2010), p. 026006.

[22] R. J. Baker. *CMOS: Circuit Design, Layout and Simulation*. 2nd Edition. John Wiley & Sons, Inc, 2008.

[23] M. Ghovanloo and K. Najafi. "A compact large Voltage-compliance high output-impedance programmable current source for implantable microstimulators". *Biomedical Engineering, IEEE Transactions on* 52 (2005), pp. 97–105.

[24] M. Azin and P. Mohseni. "A high-output-impedance current microstimulator for anatomical rewiring of cortical circuitry". 2008, pp. 2502–2505.

[25] B. S. Wilson, C. C. Finley, D. T. Lawson, R. D. Wolford, and M. Zerbi. "Design and evaluation of a continuous interleaved sampling (CIS) processing strategy for multichannel cochlear implants". *Journal of Rehabilitation Research* 30 (1993), pp. 110–116.

[26] T. G. Constandinou, J. Georgiou, and C. Toumazou. "A Partial-Current-Steering Biphasic Stimulation Driver for Vestibular Prostheses". *Biomedical Circuits and Systems, IEEE Transactions on* 2 (2008), pp. 106–113.

[27] M. S. M. Wens. *Design and Implementation of Fully-Integrated Inductive DC-DC Converters in Standard CMOS, Analog Circuits and Signal Processing,* Springer Science and Business Media, 2011.

[28] V. M. Woods. "Stimulus Waveforms Based on Platinum Polarization for Efficient and Selective Nerve Stimulation". PhD thesis. Imperial College London, 2011.

[29] Z. Mou, I. F. Triantis, V. M. Woods, C. Toumazou, and K. Nikolic. "A Simulation Study of the Combined Thermoelectric Extracellular Stimulation of the Sciatic Nerve of the Xenopus Laevis: The Localized Transient Heat Block". *Biomedical Engineering, IEEE Transactions on* 59 (2012), pp. 1758–1769.

[30] R. K. Shepherd. "Chronic Electrical Stimulation of the Auditory Nerve using Non-charge-balanced Stimuli". *Acta Oto-laryngologica* 119.6 (1999), pp. 674–684.

[31] L. Jami. "Golgi Tendon Organs in Mammalian Skeletal Muscle: Functional Properties and Central Actions". *Physiological Reviews* 72 (1992), pp. 623–666.

[32] B. B. Edin and A. B. Vallbo. "Dynamic Response of Human Muscle Spindle Afferents to Stretch". *Journal of Neurophysiology* 63 (1990), pp. 1297–1306.

6 Vibratory proprioceptive feedback

6.1 Introduction

A key challenge in developing a proprioceptive, or indeed any sensory neural prosthesis, is testing the efficacy and acceptability of the artificial feedback patterns. A variety of animal experiments have been proposed for these purposes, but they present formidable challenges including: training the animals; uncertainty in the nature of the sensation elicited; and the difficulty of interpreting the animal's response to the feedback. Meanwhile experimentation with humans presents a completely different set of challenges – primarily related to safety and ethical considerations of electrode implantation (typically an invasive surgical procedure) and possible tissue damage – but can be just as problematic.

A method of conducting human testing with minimal ethical and safety concerns, could be of great benefit for neural prosthesis development and for sensory research. Non-invasive (low risk) proprioceptive feedback has previously been demonstrated using vibrating tactors applied to the skin above muscle bodies and tendons – the vibrations stimulate the proprioceptive neurons inside the muscle and tendon – generating the sensation of limb movement or displacement (a proprioceptive illusion). The application of vibration patterns to multiple muscles in a coordinated manner has been shown to provide the subject with the sensation of 3-dimensional limb movement, and with sufficient clarity that the shape traced by the illusory movement of the limb endpoints (e.g. fingertips) can be identified and distinguished.

It should be noted, however, that subjects are also able to interpret haptic vibratory feedback (i.e. sensory substitution feedback that does not generate a proprioceptive illusion) as representing artificial limb movement. It is currently unclear therefore, how much additional information a subject gains during proprioceptive rather than haptic vibratory feedback.

This chapter investigates the suitability of using this proprioceptive illusion as a safe and ethical method of inducing neural feedback patterns in humans. As well as aiming to compare proprioceptive and haptic vibratory feedback in terms of how well a subject can interpret them in trials involving the identification of a 2-dimensional illusory shape and in a control task.

This chapter is organised as follows: Section 6.2 presents background information on the proprioceptive and haptic vibratory feedback; Section 6.3 describes the mechanical devices used to generate the feedback; Section 6.4 describes the materials, algorithms and trials used; Section 6.5 describes the results; and finally Section 6.6 discusses the results and provides recommendations for future work.

6.2 Artificial feedback

6.2.1 Proprioceptive illusion

Applying vibration to tendons or muscle bodies has been shown to create the illusion of motion as well as systematic errors in the subject's ability to judge limb position [1]. Numerous experiments have identified that the vibration sensitivity of primary muscle spindles in the vibrated muscle is the main mechanism for this phenomenon [2] (indeed this illusion was a major piece of evidence justifying muscle spindles as key receptors for proprioception [3]).

Experiments investigating this illusion soon identified that the perceived rate of motion and perceived displacement in limb position are primarily dependent on the frequency of vibration and that once the amplitude of vibration exceeds a certain threshold amount required to generate the illusion, further increase in amplitude do not alter the sensations [4]. Perhaps unsurprisingly from what we know of muscle spindles, further experiments showed that the perceived limb displacement is in the direction the limb would move if the vibrated muscle was stretched [5]. This fits with a hypothesis that the CNS is interpreting the vibration induced muscle spindle signals as muscle stretch and is calculating limb position accordingly.

The direction of illusory limb motion associated with vibrating a particular muscle has been referred to as the muscle's Preferred Sensory Direction (PSD). Roll and Gilhodes [5] demonstrated that using simultaneous vibration of multiple muscles it was possible to generate 2-dimensional sensations of limb movement and illusory 'tracings' of geometric shapes and letters that subjects could readily discriminate. It should be noted that although muscle spindles are the primary conduit for the illusory movement during tendon vibration, the subject can also derive a significant quantity of haptic information from the vibration. It is unclear how much this haptic feedback contributes to enabling the subject to recognise and interpret the illusory movement.

Analysis of micro-neurographic recordings (from transcutaneously inserted electrodes into peripheral nerves) showed that the spindle firing rate is often at a 1:1 ratio (or sometimes a subharmonic) to the vibration frequency and identified a range of frequencies at which the spindles were most sensitive (60-100 Hz) [2]. Subsequent research by Fallon and Macefield [4] refined this using a more carefully controlled mechanical vibration setup and confirmed the finding of 1:1 spindle firing, but showed no significant frequency sensitivity (up to 120 Hz).

This vibration to action potential relationship potentially offers a non-invasive way of stimulating muscle spindles. Exploiting this to create a feedback mechanism for amputees has been considered, but many challenges exist, not the least of which is the likely absence or truncation of key muscles in the amputation process. However, an alternative application is as a tool both for proprioceptive prosthesis research – where it directly addresses the ethical and safety concerns for use with human subjects – and for investigating whether proprioceptive feedback offers any advantages over sensory substitution feedback.

6.2.2 Vibrotactile feedback

Vibrotactile stimulation involves the application of temporally modulated vibration to the surface of the skin in order to convey information. It was first conceived of in the 1960s as a feedback mechanism for people with vision or hearing impairment. Since then numerous other applications have been explored including: for rehabilitation, for motor learning support, for gaming, and most relevantly for feeding back information about prosthetic limb movement and forces to the amputee user [6–8].

Numerous feedback methods have been tried for these applications (e.g. electrocutaneous or tastebud stimulation), however, vibrotactile stimulation remains popular due to its low-cost, low-complexity, safe and non-invasive nature [7, 9]. However, achieving good performance with this feedback modality is a multi-dimensional problem and there still remains a lot of uncertainty regarding the best: placement of the vibration tactors; vibration frequencies; vibration amplitude; modulation techniques; and methods to assess the performance of these systems.

The sensitivity of human skin to vibration provides some constraints on the range of frequencies to be considered and the distribution of these receptors may in turn inform the placement of tactors. Table 6.1 shows data gathered on the sensitivity of key receptors in human skin. Meissner and Pacinian corpuscles are believed to be primarily responsible for vibrotactile perception in smooth, glabruous skin. Less is known about perception in hairy skin, although a significant reduction in the density of Pacinian corpuscles has been observed [10]. Previous work has typically involved the application of sets of tactors on the skin of the arm or hand and operation at frequencies centred either on 50 or 250 Hz. Alternative placements have been tried [7] as well as varying the orientation of arrays of tactors [8], but have not shown strong and consistent performance differences.

Table 6.1: Vibration sensitivity of skin receptors – adapted from Kaczmarek et al. [9]

Probable receptor	**Frequency range**	**Peak sensitivity**	**Sensation**
Pacinian corpuscle	40–800 (10–500)*	200–300	Tickle/vibration
Meissner corpuscle	10–200 (3–100)*	20–40	Touch/motion/flutter/tap
Ruffini ending	7 (15–400)*		Stretch/shear/tension
Merkel cell	0.4–100 (<5)*	7	Pressure

* Figures in brackets from [10].

Experiments reported in the literature demonstrate a preference for amplitude or location (i.e. changing the perceived location of vibration) modulation. Amplitude modulation is the simplest modulation technique, but suffers from significant variation from user-to-user as well as from vibration site-to-site, due to differences in the tactor contact area and the underlying tissue mechanics at each site. Pulse train modulation (i.e. frequency modulation) in theory avoids these variations and provides more consistent performance by keeping the amplitude constant, however, in practice it is more difficult to implement and its performance has been poor, making it unpopular [7, 11]. Location modulation was one of the first modulation techniques and it remains another popular choice, however,

it requires more devices and greater complexity than amplitude modulation (although the phantom-position phenomenon [12] provides a mechanism to increase the resolution without significantly increasing the number of devices). Ultimately the performance of all these modulation techniques has been mixed with most groups reporting some performance gain, but at inconsistent levels of effectiveness [8].

6.3 Vibration mechanisms

6.3.1 Vibrotactile devices

A multitude of different tactors have been used to provide vibrotactile feedback (some of which are pictured in Fig. 6.1). The most popular of these fall into two categories: 1) Linear Electromagnetic Actuators (LEAs) – based on an electromagnet surrounding a magnet/piece of ferromagnetic material (or vice-versa) combined with a spring or diaphragm to constrain motion; or 2) Eccentrically Rotating Mass (ERM) motors – based on a DC motor with an eccentric or imbalanced weight mounted on the shaft.



(a) Vibrotactile tactors. S – solenoids, Sp – loudspeakers, VC – voice coil, E – shafted ERM motors, P – pancake ERM motors, C2 & Haptuator & Tactaid – custom tactors

(b) Bruel Kjaer 4810 shaker external (reproduced from bksv.com)

(c) Bruel Kjaer 4810 shaker cut-through (reproduced from bksv.com)

Figure 6.1: (a) Tactors for vibrotactile applications (reproduced from Choi and Kuchenbecker [10]). (b) and (c) An LEA tendon vibrator.

LEA designs can be split into solenoids (ferromagnetic core) or voice-coils (permanent magnet core) [10]. Both types need to be driven by a time varying signal in order to vibrate, typically this will be a square wave for solenoid type devices and a sine wave for voice-coil devices.

Solenoid devices for haptic purposes typically require a spring to return the moving core to its rest position and as a result provide substantially greater amplitude vibration at the spring's mechanically resonant frequency. Voice-coils on the other hand are very similar to loudspeakers and designs exist with linear vibration dynamics over a wide range of frequencies, although in order to achieve good performance the driving waveform needs to be more carefully controlled.

ERM motors come in 3 types (two of which are depicted in Fig. 6.1) – shafted, enclosed shafted and shaftless (pancake). They are the most commonly used in the literature and of-

fer advantages such as being small, cheap, lightweight, easily controlled (a constant voltage induces vibration), and offering variable vibration frequency. However, they offer poorer control of vibration frequency compared to LEAs, increased latency especially on startup, and the amplitude is dependent on the vibration frequency.

6.3.2 Tendon vibration devices

Tendon vibration experiments have used a similar variety of mechanical set-ups to generate the required vibration. These have ranged from industrial vibration shakers (scaled up voice coil devices – see Fig. 6.1(b) and (c) to jigsaws with padding on the blades. However, the most common vibration sources in the literature have been vibration shakers and physiotherapy vibrating massagers (based on ERM motors).

The properties of these tendon vibrators mirror those of vibrotactile devices. Industrial shakers as voice coil devices enable accurate control of the vibration frequency and amplitude, but are typically large and cost thousands of pounds for a multiple motor setup. Due to their size and design – with only a small section designed to vibrate – their base must be mounted to a solid structure. Physiotherapy massagers on the other hand are much cheaper and can be smaller, but offer poor control of frequency and the amplitude of oscillation is a function of the rotation frequency and the eccentricity of the mounted weight's centre of mass. The entire device is vibrated by the movement of the weight and as such the whole device needs to be strapped to or held against the tendon.

6.4 Materials & Methods

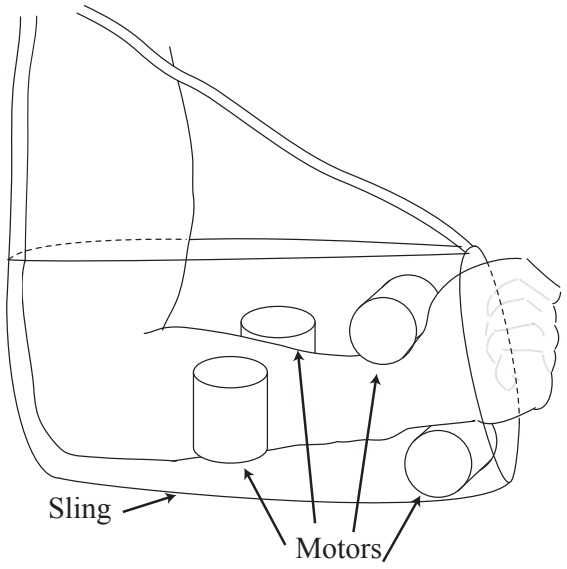


Figure 6.2: Example motor positioning in the arm sling.

6.4.1 Trial setup

The aims of the trials were to: 1) demonstrate the use of the non-invasive vibratory proprioceptive illusion for determining the effectiveness of neural feedback patterns; and 2) contrast the performance of vibrotactile feedback with two forms of illusory proprioceptive feedback.

To investigate these issues, 2 trials were conducted in which volunteers were asked to interpret feedback representing movement of their left hand (and in particular the illusory movement of their fingertip).

The trial setup placed volunteers in a seated position with their left arm in an arm sling and supported in a comfortable pose (see Fig. 6.2). Depending on the trial either four vibrotactile or four tendon vibration motors were placed in the sling – two on the forearm targeting the Flexor Carpii Radialis and Extensor Digitorum Profundus muscles (sensitive to flexion of the wrist), and two on the wrist targeting the tendons of the Extensor Carpii Ulnaris and Extensor Policis Brevis/Longus muscles (sensitive to deviation of the wrist) at the point they pass over the wrist bones. This motor placement meant that supra-threshold vibration of these four motors (with tendon vibration motors) could generate the illusion of wrist movement in two degrees of freedom (deviation and flexion), while sub-threshold vibration (with vibrotactile motors) conveyed similar information without the illusion.

The rest of this section describes the design of the vibration devices (Section 6.4.3), the modulation patterns (Section 6.4.4) and finally the detail of the trials (Section 6.4.5).

6.4.2 Subjects

Volunteers were required to have no neurological or physical impairments to the wrist or arm were reported. All volunteers gave their informed consent in accordance with the Helsinki declaration and the Imperial College Research Ethics Committee reviewed and approved all trial procedures.

6.4.3 Vibration devices

Tendon vibrator design

The target requirements for the tendon vibrator design were that it was capable of operation between 0 – 100Hz and that it provided sufficient amplitude to generate the proprioceptive illusion; control of frequency within a few Hertz was targeted as an achievable aim.

Solenoids, loudspeakers, commercial vibration shakers and vibration massage devices were investigated and rejected on the basis of cost, size or lack of control of vibration frequency. A number of off-the-shelf pancake and enclosed shafted ERM devices were tested and rejected on the basis that they produced insufficient vibration amplitude to induce the required illusion.

A search of the literature showed that Celik et al. [13] proposed a small purpose built version of an eccentrically weighted motor, with a sensor for measuring the speed of rotation and a modified Proportional Integral (PI) controller to adjust a Pulse Width Modulation (PWM) signal for controlling speed. A prototype based on this design was constructed –

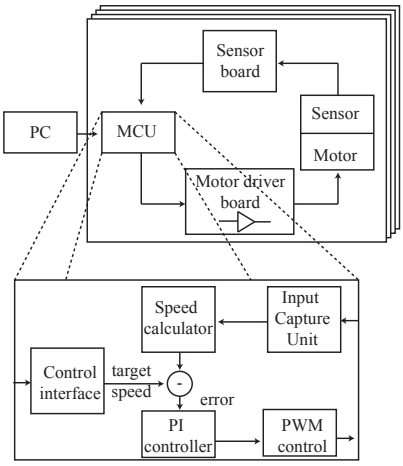
consisting of a DC motor with a weight with an adjustable centre of rotation – and tested. An approximately semi-circular mass of 33 g with a centre of mass offset of 3.5 mm from the axis of rotation, was found to generate the proprioceptive illusion even at lower frequencies, however, the prototype was unable to achieve the desired maximum speed of approximately 100Hz (6000rpm).



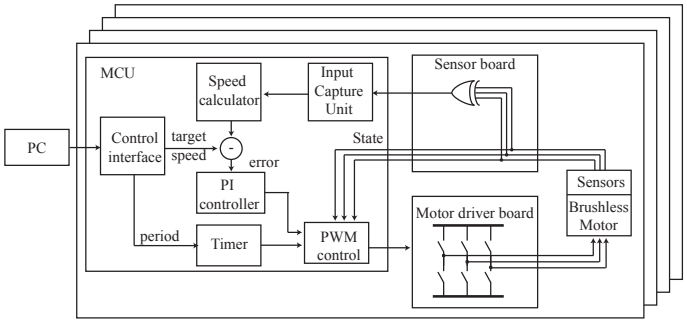
(a) Motor design (rev 1)



(b) Motor design (rev 2)



(c) Motor design (rev 1) control system



(d) Motor design (rev 2) control system

Figure 6.3: Tendon vibration motors and outline system designs.

A complete system including a more powerful DC motor, optical speed control sensor, microcontroller, and sensor & motor driver boards was created (see Fig. 6.3(a) and constituted Motor Design (rev. 1). Unfortunately, slow startup, large overshoot and speed control problems plagued this design. Initial attempts to address this focused on the speed sensor and the PI control, however, both increasing the rate of sensor feedback and modifications & tuning of the PI controller did little to address these issues.

The system was redesigned with a sensored brushless DC motor, providing increased torque and improved speed control at the expense of control complexity and slightly increased motor cost. The motor was a standard 540 type used in remote control cars with 3 integrated 180° Hall sensors positioned 120° out of phase. This formed Motor Design (rev. 2) and is shown in Fig. 6.3(b). Commutation was controlled by a microcontroller and was triggered by a timer with a period determined by the desired rotation speed. The microcontroller had two modes for determining the next commutation state: below 90% of the target speed the controller detected the current state of the rotor and applied the

appropriate commutation to move the rotor to the next state; or above 90% of the target speed the controller simply stepped through the various commutation states. The two modes of commutation control were implemented to reduce overshoot of the target speed and also to improve the accuracy of the speed lock when the motor was rotating at the target speed. In addition a PI controller (based on the error in the speed) was implemented to vary the PWM duty cycle applied to the motor coils.

Vibrotactile hardware

The vibration requirements for vibrotactile feedback in this study are simpler than for illusory motion, the key criteria for the selection of a vibrator for vibrotactile feedback were: the size; the cost; that the frequency range of operation was within the sensory range of the meissner & pacinian corpuscles; and that the strength of vibration was large enough to be easily felt but small enough not to evoke any illusory motion. An enclosed-shafted motor from Precision Microdrive (Uni-vibe model 325-100) was selected on the basis of its sub-threshold performance during earlier motor assessment.

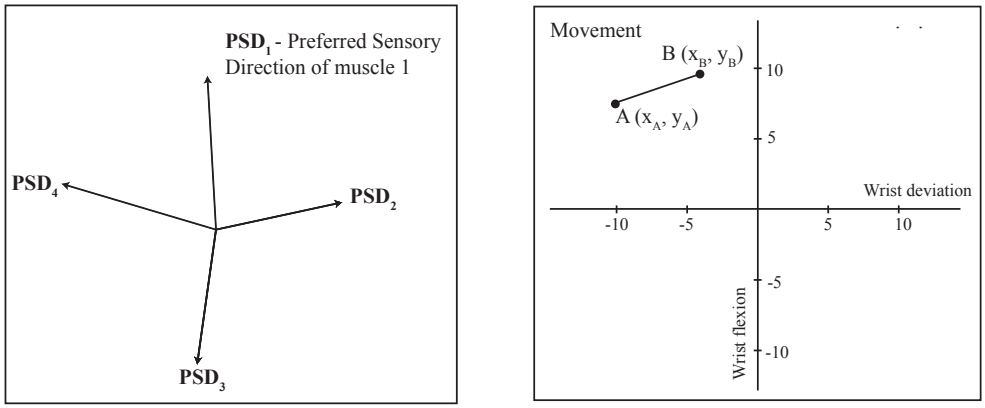
6.4.4 Vibration modulation

Proprioceptive feedback patterns

Two methods were used to estimate the muscle spindle firing patterns that are being induced. The first (denoted as PSD proprioceptive feedback) is as described in [14, 15], briefly: the expected Preferred Sensory Direction (PSD) of the 4 muscles being vibrated (i.e. the direction of hand movement from the neutral position that would most stretch each muscle) was estimated in the Opensim biomechanical modelling package and expressed as 4 unit vectors (see Fig. 6.4(a)). The illusory motion to be applied was likewise expressed as a vector (see Fig. 6.4(b)). The target vibration frequency of 2 of the 4 motors was then calculated as the illusory movement vector dot product multiplied with the relevant PSD vector e.g. for motion $\mathbf{AB} = \binom{x_B - x_A}{y_B - y_A}$ (see Fig. 6.4(b)), the two relevant vectors are PSD_1 and PSD_2 so the corresponding motor vibration frequencies (Motor_1 and Motor_2) are calculated as:

$$\begin{aligned} \text{Motor}_1 = &\quad \mathbf{PSD}_1 \bullet \mathbf{AB} \\ \text{Motor}_2 = &\quad \mathbf{PSD}_2 \bullet \mathbf{AB} \end{aligned} \tag{6.1}$$

The second method (referred to as Biomimetic proprioceptive feedback) was based on the biomechanical and proprioceptor modelling described in Chapter 4 and Williams and Constandinou [16]. In this method the range of motion of an extended finger (during wrist deviation and flexion) was mapped to a 2 dimensional on-screen grid as indicated in Figure 6.4(c). The illusory movement vector (**AB**) is therefore mapped to a change in wrist flexion and deviation. This movement is biomechanically modelled to determine the changes in muscle length of the 4 target muscles and these length changes are subsequently passed to the Mileusnic et al. [17] model of the muscle spindle to estimate firing patterns that would occur in a normal arm – and hence vibration patterns for the 4 motors (due to

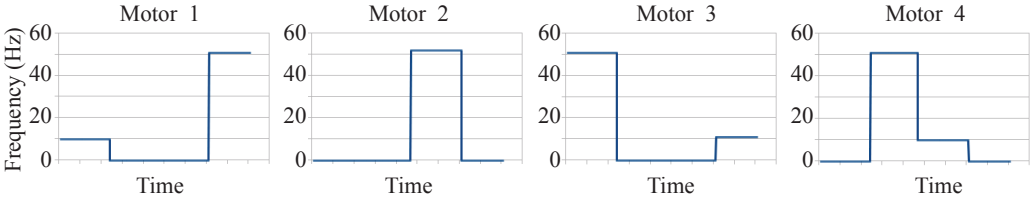


(a) Example Preferred Sensory Directions (b) Example motion from point A to B

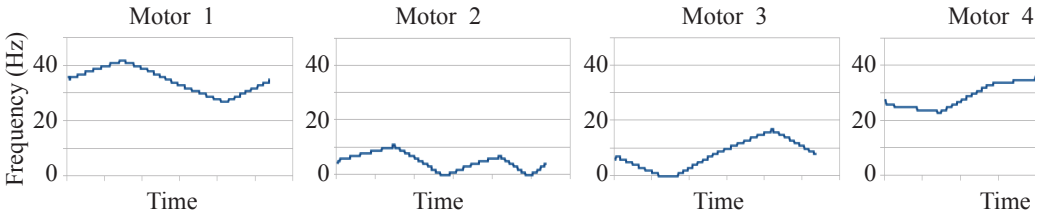
Figure 6.4: Proprioceptive feedback pattern calculation.

the 1:1 relationship between vibration and spindle firing).

It should be noted that these two methods of proprioceptive feedback generation differ substantially in what they are feeding back – the PSD approach provides only movement feedback (i.e. is purely determined by the instantaneous movement vector), whereas the spindle estimate approach also includes position and acceleration components. This difference is dmonstrated by looking at the output of each approach as illustrated in Figure 6.5 for a sequence of illusory motions tracing a square.



(a) Feedback patterns using the Preferred Sensory Direction approach



(b) Feedback patterns using the Biomimetic approach

Figure 6.5: Example outputs of the two proprioceptive feedback patterns representing the drawing of an illusory square over a period of 5 seconds. (a) The output of the Preferred Sensory Direction method [15], and (b) the output of the biomimetic spindle modelling.

Vibrotactile feedback patterns

Since we are investigating the difference between supra- and sub-threshold (i.e. comparing illusory proprioceptive feedback and haptic feedback) vibration we propose to apply the

vibrotactile tactors to the same sites as the proprioceptive illusion tactors (i.e. on non-glabrous skin over tendons) and to use frequencies in a similar range (<100Hz). Patterns of haptic feedback vibration were a scaled version of those generated by the PSD method for proprioceptive feedback, on the basis that these would be more easily consciously interpreted than the spindle feedback.

6.4.5 Trials

The trials were split into 3 phases: (1) calibration, (2) feedback for an imposed motion, and (3) feedback as support during a control task. The GUI for the trials was implemented using the Processing platform and motor control signals were sent to the microcontroller using a virtual serial port over USB.

Stage 1 – calibration

During this trial, patterns of vibration designed to generate illusions of hand movement, rotation and oscillation were used to identify: the best motor placements; the minimum levels of vibration causing a movement illusion and the maximum comfortable levels of vibration.

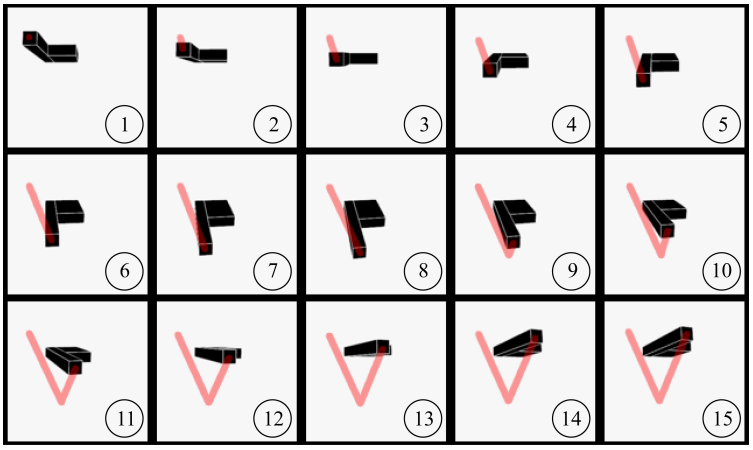
Trial 1 – imposed motion

The purpose of this trial was to assess how well a subject could interpret different forms of feedback by testing their ability to identify a symbol from each feedback modality. Volunteers were first briefly trained to identify symbols using on-screen visual feedback illustrating a hand and finger tracing the shape (see Fig. 6.6(a)). Training sets were then conducted with combinations of visual feedback and one of the 3 other feedback modalities under trial (vibrotactile feedback, PSD proprioceptive feedback and biomimetic proprioceptive feedback). The illusory motion vectors for these feedback modalities was generated by considering the wrist movements necessary to trace the shape on a screen starting at the top left.

Volunteers were then asked to identify symbols presented to them using just one of the 3 feedback modalities. Sets of 10 symbols (chosen at random from a pool of 21 symbols – consisting of letters, numbers and shapes – shown in Fig. 6.6(b)) were used for each modality. Each symbol was repeated twice and after each, the user was asked to select the symbol from the set of possible symbols. To reduce unwanted information cues, all symbols were designed to have a similar starting point (top left) and were designed to be of similar duration.

Trial 2 – control task

The purpose of this trial was to investigate the relative benefit gained from different forms of feedback in a control task. In this trial volunteers were asked to use keyboard cursor keys to guide an icon from its starting position to a target box under varying feedback

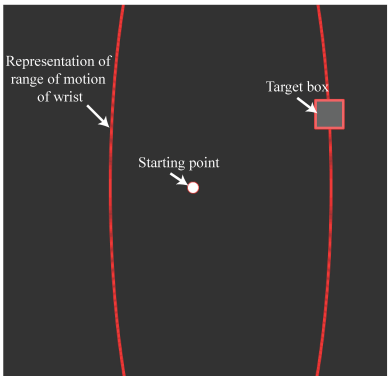


(a) Sequence of 15 screenshots of visual feedback showing a depiction of a hand tracing a 'v' symbol

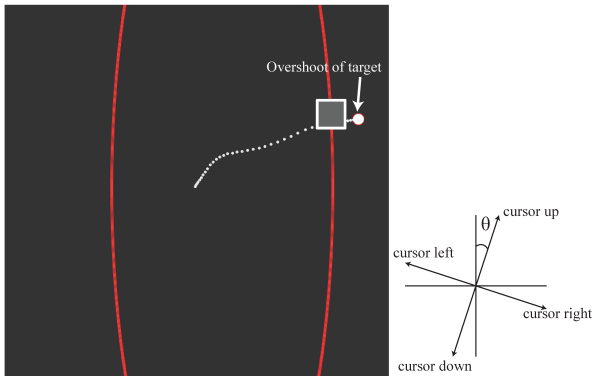


(b) The symbols used

Figure 6.6: Trial 1: (a) visual feedback and (b)symbols used.



(a) Starting configuration



(b) Near completion – target overshot

Figure 6.7: Trial 2 task.

conditions (see Fig. 6.7). The movement of this icon provided the motion vectors for the feedback modalities.

A training phase (in which the user could see the movement and location of the icon) was again conducted with each of the 3 feedback modalities. Following the training phase the user was deprived of visual feedback (about the movement and location of the icon) and was provided with either no feedback or with one of the 3 feedback modalities. Sets of 10 runs were conducted for each of the feedback conditions. A run was successfully completed if the user managed within 15 seconds to place the icon in the target box.

To prevent the user simply performing the task through learned skill, the acceleration and friction coefficients for the icon's movement were varied at random for each trial and an angle offset (θ) was introduced as depicted in Figure 6.7(b).

6.5 Results

6.5.1 Subjective sensations

This section presents observations of testing a number of vibration devices for their ability to generate the proprioceptive illusion as well as with different feedback patterns. It should be noted that these observations are the result of testing on a single subject and previous work has indicated that there may be significant variation in the sensitivity of users to this illusion [18].

The devices performed with varying degrees of success; no illusory motion was perceived with the solenoids and loudspeaker assemblies tested, while commercial ERM motors (similar to that used by Celik et al. [13]) were able to induce some sensation of motion (or impairment of the user's ability to judge hand position) at higher frequencies. In contrast the custom ERM motors developed here were able to generate illusory motion at low frequencies (<20Hz), but became uncomfortable at higher frequencies.

Generally the sensations of illusory motion were faint (the main sensation being of vibration) and were weakened further if the user visually monitored the limb under test. The preponderance of vibration as the perceived sensation, likely resulted from the high required amplitude of vibration and the difficulties associated with precisely targeting a particular tendon while mounting the devices to the body.

During initial device testing the simpler PSD proprioceptive feedback patterns appeared to be substantially more easy to interpret than the biomimetic patterns, although this may have resulted from the vibration devices being unable to follow the target vibration profile.

6.5.2 Tendon vibrator performance

Prior to the conduct of full trials, the performance of the custom vibration devices was tested and tuned in benchtop experiments. The primary aim of this step was to characterise and optimise the vibration control performance. Tests were conducted with the motors initially clamped in a vice on the bench before being tested in the sling.

Unfortunately technical issues plagued the ERM tendon vibrator designs. Many of these were minor and readily solvable such as: vibration induced connection failures, interference from motors & PWM signals, and repeated tuning of the PI controllers used. However, other issues were more fundamental and prevented the conduct of the proposed trials.

Motor Design (rev 1) suffered from numerous problems with speed control (see Fig. 6.8(a) for an example speed plot). Startup suffered from inertia leading to windup of the PI controller and overshoot; there was significant fluctuation in the motor speed which at low speeds (<15Hz) resulted in stalling; and the motor's top speed fell well short of the desired 100Hz. Modifications to the PI controller were implemented to improve the speed control (especially on startup), but showed limited success.

Motor Design (rev 2) was intended to address these issues, by using a larger and brushless motor. When clamped in a vice the results for this device seemed encouraging (see Fig. 6.8(b). However, even clamped in a vice the signs of a resonance issue are visible (between around 20 – 40Hz) resulting in speed fluctuations. When mounted in the sling the

motor appeared to undergo a change in vibration mode at the higher end of these speeds and subsequently exhibited a variety of problems. This both prevented good speed control and severely limited the top speed the motor could attain (see Fig. 6.8(c)). It was observed that the motor attained near it's top speed (unclamped) with a PWM duty cycle of just 10–15%; while high duty cycle ratios (controlled by the PI controller) did not substantially increase the top speed.

Also shown are the results from previous work demonstrating a low cost tendon vibrator for comparison (Figure 6.8(d)) which shows the results reported in [13]).

6.6 Discussion

The system described here was unable to investigate the primary research questions on: the suitability of the technique for non-invasive proprioception research; and comparing the performance of proprioceptive feedback with vibrotactile. intended goal of providing non-invasive proprioceptive feedback. However, this section briefly reviews the limited results obtained, the approach taken, the issues encountered and discusses the feasibility of the concept.

6.6.1 Results discussion

The work conducted here identified several substantial challenges to the use of tendon vibration for non-invasive feedback including: 1) difficulty mounting the devices to the body; 2) poor frequency control at low frequencies; 3) high amplitude at high frequencies (causing discomfort); 4) resonance preventing the devices achieving high frequencies and impairing frequency control; 5) insufficient acceleration of the devices to follow the desired frequency profile; and 6) vibration of non-target muscles and tissue. Mostly these issues can be traced back to the use of ERM motors to generate the vibration and the suitability of these devices for this application is discussed below. However, alternative LEA devices come with their own challenges such as mounting and, as previously noted, high performance devices are also orders of magnitude more expensive.

It was noted in preliminary testing that the PSD feedback appeared more easy to interpret than the Biomimetic feedback. Possible reasons for this may have been:

- Poor vibration control – due to challenges mounting the vibration devices and controlling the motor speed, the actual vibration pattern applied to the muscles may have been substantially different to the desired pattern.

- Conflicting proprioceptive feedback – previous tendon vibration experiments have noted that the primary sensation reported by subjects is that of motion rather than altered position. However, experiments show that subjects perception of limb position has also been affected with some subjects struggle to identify the position of their limb [18], possibly as a result of conflicting feedback from other proprioceptive sources which are unaffected by the vibration illusion (e.g. skin or unvibrated muscles). The PSD feedback therefore plays to the strengths of the tendon vibration technique.

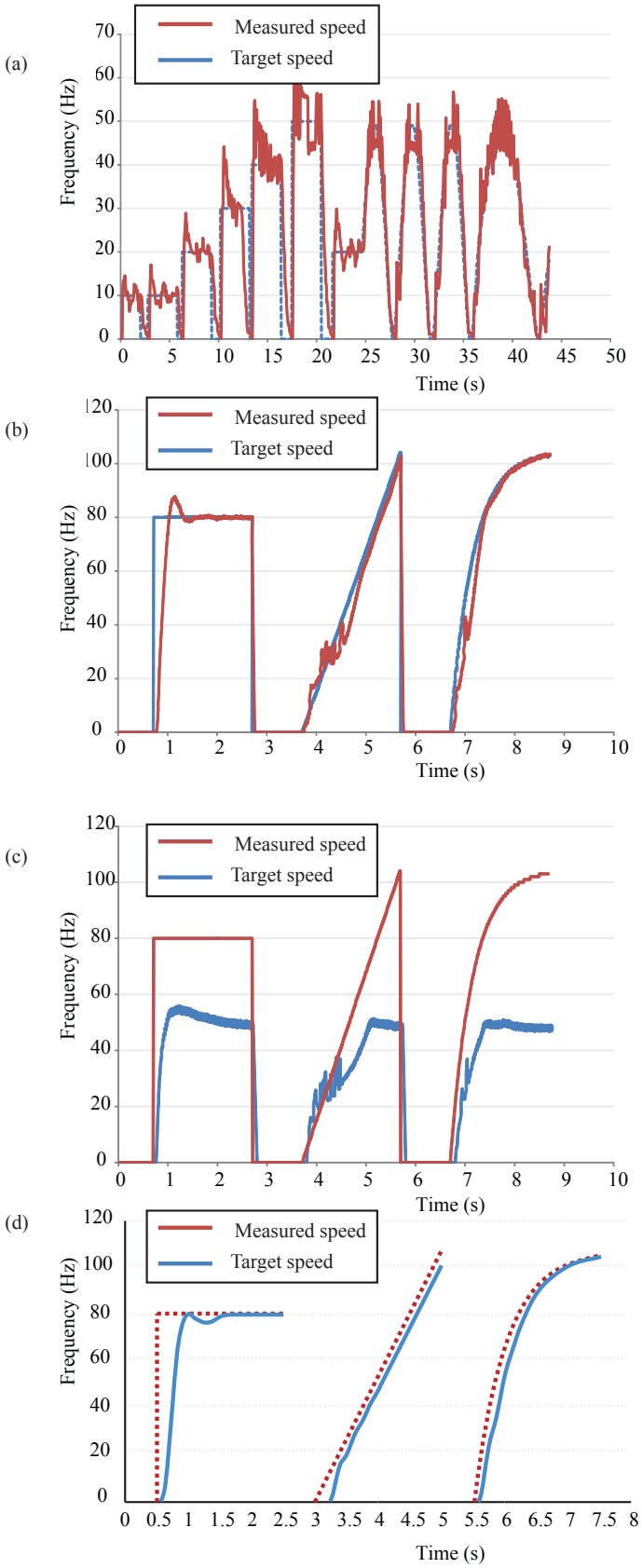


Figure 6.8: Results of trials of vibration frequency control. (a) Motor design 1, (b) Motor design 2 (tested in a vice), (c) Motor design 2 (tested unclamped), (d) results from Celik et al. [13].

Focusing on the more-perceptible motion sensation and not altering the feedback based on where in space the illusory limb should be (thereby reducing the conflict between proprioceptive sources), may well make feedback provided in this way more comprehensible to the user than the spindle mimicking feedback proposed.

Suitability of ERM motors for non-invasive proprioceptive feedback

Four substantial challenges to using ERM motors were noted that appear to make them largely unsuitable for this application:

- ERM motors are examples of forced harmonic vibration, where the term 'harmonic' refers to the way the system is vibrated at the frequency of excitation (i.e. the rotating unbalanced mass). Mathematical analysis of these systems is challenging unless constraints on the systems degrees of freedom can be assumed (which is not the case here). However, it is generally estimated that the amplitude of vibration increases with the square of the frequency. In the experiments, both motor designs presented here were capable of generating illusory motion at lower speeds, but struggled to achieve the target top speed of 100Hz (N.B. use at this speed range would likely have been uncomfortable), whereas smaller commercial devices did achieve the high speeds, but failed to generate illusory motion at lower speeds. This link between frequency and amplitude may be a fundamental obstacle to the use of ERM motors as a proprioceptive feedback tool, due to the challenge it presents for achieving a system that is strong enough to generate illusory motion at low frequencies and remains comfortable at high frequencies.

- In early development of the system presented here, the attachment of ERM motors to the body rather than mounted to a frame (as you would for an LEA) was considered a positive feature (due to its simplicity and flexibility). However, this approach leads to highly variable damping of the motor vibration, with associated impacts on vibration amplitude and dynamics. The mounting here also prevented close targeting of specific muscles and it is likely that numerous ones were simultaneously stimulated.

- The acceleration of the ERM devices used here was insufficient to track the rapid changes in vibration frequency required for the Biomimetic proprioceptive feedback – making them an unsuitable mechanism for conveying the spikes observed in proprioceptive neural signals.

- In order to obtain sufficient vibration amplitude the eccentric weight needs to be a sizeable fraction of the weight of the motor – this increases the risk of a resonance issue occurring and presents challenging torque requirements for the motor on startup and at low speeds.

6.6.2 Feasibility of non-invasive proprioception and recommendations

This chapter presented the development of a trials setup to investigate the feasibility of non-invasive biomimetic proprioceptive feedback and its performance compared to previously

proposed non-invasive feedback.

Recommendations for future work:

- The obstacles encountered in this work were largely a result of the mechanical vibration mechanism chosen. A key recommendation is therefore that future work should focus on use of an alternative device such as an LEA based tendon vibrator. Previous proprioceptive illusion experiments with LEA based vibrators have often used square waveforms to drive the LEA [5, 15], but a more accurately controlled sinusoidal drive mechanism was proposed by Fallon and Macefield [4] and is recommended.

- Non-invasive feedback using PSD modulation has previously been successfully demonstrated in healthy subjects. The possibility of using it to provide feedback to amputees (where key muscles have been relocated or reinnervated) could be an area worth future investigation – although miniaturising and mounting the vibration devices in a portable manner would likely be a substantial obstacle.

This work has been inconclusive about the feasibility and performance of tendon vibration for non-invasive biomimetic proprioceptive feedback, but hopefully the ideas, structure and issues presented here will be of benefit to future researchers. The ability to non-invasively test proprioceptive feedback would be a major advantage in the development of a proprioceptive neural prosthesis and potentially proprioception research.

Bibliography

[1] G. M. Goodwin, D. I. McCloskey, and P. B. Matthews. "Proprioceptive illusions induced by muscle vibration: contribution by muscle spindles to perception?" *Science* 175.4028 (1972), pp. 1382–1384.

[2] J.-P. Roll, J.-P. Vedel, and E. Ribot. "Alteration of proprioceptive messages induced by tendon vibration in man: a microneurographic study". *Experimental Brain Research* 76.1 (1989), pp. 213–222.

[3] P. B. C. Matthews. "Evolving views on the internal operation and functional role of the muscle spindle." *The Journal of physiology* 320 (1981), p. 1.

[4] J. B. Fallon and V. G. Macefield. "Vibration sensitivity of human muscle spindles and Golgi tendon organs". *Muscle & nerve* 36.1 (2007), pp. 21–29.

[5] J.-P. Roll and J. Gilhodes. "Proprioceptive sensory codes mediating movement trajectory perception: human hand vibration-induced drawing illusions". *Canadian journal of physiology and pharmacology* 73.2 (1995), pp. 295–304.

[6] A. Alahakone and S. A. Senanayake. "Vibrotactile feedback systems: Current trends in rehabilitation, sports and information display". *Advanced Intelligent Mechatronics, 2009. AIM 2009. IEEE/ASME International Conference on*. IEEE. 2009, pp. 1148–1153.

[7] C. E. Stepp and Y. Matsuoka. "Object manipulation improvements due to single session training outweigh the differences among stimulation sites during vibrotactile feedback". *Neural Systems and Rehabilitation Engineering, IEEE Transactions on* 19.6 (2011), pp. 677–685.

[8] C. E. Stepp and Y. Matsuoka. "Vibrotactile sensory substitution for object manipulation: Amplitude versus pulse train frequency modulation". *Neural Systems and Rehabilitation Engineering, IEEE Transactions on* 20.1 (2012), pp. 31–37.

[9] K. A. Kaczmarek, J. G. Webster, P. Bach-y-Rita, and W. J. Tompkins. "Electrotactile and vibrotactile displays for sensory substitution systems". *Biomedical Engineering, IEEE Transactions on* 38.1 (1991), pp. 1–16.

[10] S. Choi and K. J. Kuchenbecker. "Vibrotactile display: Perception, technology, and applications". *Proceedings of the IEEE* 101.9 (2013), pp. 2093–2104.

[11] A. Chatterjee, P. Chaubey, J. Martin, and N. Thakor. "Testing a prosthetic haptic feedback simulator with an interactive force matching task". *JPO: Journal of Prosthetics and Orthotics* 20.2 (2008), pp. 27–34.

[12] R. W. Mann and S. D. Reimers. “Kinesthetic Sensing for the EMG Controlled” Boston Arm””. *Man-Machine Systems, IEEE Transactions on* 11.1 (1970), pp. 110–115.

[13] O. Celik, M. K. O’Malley, R. B. Gillespie, P. A. Shewokis, and J. L. Contreras-Vidal. “Compact and low-cost tendon vibrator for inducing proprioceptive illusions.” *WHC*. 2009, pp. 623–624.

[14] C. Thyrion and J.-P. Roll. “Predicting any arm movement feedback to induce three-dimensional illusory movements in humans”. *Journal of neurophysiology* 104.2 (2010), pp. 949–959.

[15] J.-P. Roll, F. Albert, C. Thyrion, E. Ribot-Ciscar, M. Bergenheim, and B. Mattei. “Inducing any virtual two-dimensional movement in humans by applying muscle tendon vibration”. *Journal of neurophysiology* 101.2 (2009), pp. 816–823.

[16] I. Williams and T. G. Constandinou. “Computationally Efficient Modelling of Proprioceptive Signals in the Upper Limb for Prostheses: a Simulation Study”. *Frontiers in Neuroscience* 8 (2014), p. 181.

[17] M. P. Mileusnic, I. E. Brown, N. Lan, and G. E. Loeb. “Mathematical Models of Proprioceptors. I. Control and Transduction in the Muscle Spindle”. *Journal of Neurophysiology* 96 (2006), pp. 1772–1788.

[18] D. McCloskey. “Differences between the senses of movement and position shown by the effects of loading and vibration of muscles in man”. *Brain research* 61 (1973), pp. 119–131.

7 Conclusion

In recent years there have been exciting developments in prosthetic limb functionality [1] and in myoelectric feedforward control [2]. However, this progress has highlighted the fundamental limitations of open loop prosthetic control.

A device capable of giving an amputee a sense of feeling back from their prosthetic limb could close this loop and help millions of people live happier, more productive lives [3, 4]. Ideally such a device would mimic all natural proprioceptive patterns and apply neuromodulation to the correct neurons to generate these patterns in the body – creating natural percepts and intuitively comprehensible feedback – but such a system remains a distant prospect.

The work presented here is aimed at identifying the challenges in the road ahead and moving a few steps closer to this goal.

7.1 Summary

7.1.1 Introductory and background information chapters

Chapter 1 identified the need for a proprioceptive feedback for upper limb amputees, outlined the aspirations for such a device and described the research approach to delivering on these aspirations.

Chapter 2 reviewed normal human proprioception, the impact of amputation on the proprioceptive system, and previous attempts at artificial proprioception – ultimately identifying that a high performance neural prosthesis is required, as well as identifying previous work indicating the feasibility of this approach.

7.1.2 Design of a proprioceptive neural prosthesis

Chapter 3 looked at the design of a proprioceptive neural prosthesis. The end to end system was broken down into constituent parts and a process for guiding decisions was proposed. Options and requirements were considered for each component part and challenges were identified.

Three key challenges were targeted to address in the remainder of this research: a) generating real time naturalistic feedback patterns (Chapter 4); b) efficient, safe neural stimulation (Chapter 5); and c) non-invasive human testing of feedback patterns (Chapter 6).

7.1.3 Real time naturalistic patterns

Chapter 4 presented a real time model capable of generating ensemble average estimates of muscle spindle and GTO signals for 17 muscles in a human upper limb system with 7 degrees of freedom. This was achieved using a combination of extant and novel approximations to four previously proposed biomechanical and proprioceptor models.

On the biomechanics side, the Holzbaur musculoskeletal model [5] of the human upper limb was loaded in the 3D biomechanical modelling software OpenSim and surfaces were fitted to describe the way muscle lengths and moment arms varied with joint angles around the 7 degrees of freedom. This was combined with a static optimisation implementation (using a Simplex linear programme solver and a min-max optimisation criteria [6]) to estimate muscle activations.

Proprioceptive modelling was based on the Houk and Simon model for the GTO [7], and the Mileusnic model for the muscle spindles [8]. A stiff approximation to the Mileusnic model was proposed based on assuming all the stretch occurs in the more flexible polar regions of the spindles, allowing the model to be expressed without differential equations. Modifications to both models were suggested to fit them to human receptors rather than the feline receptors that both models were originally based on.

Results showed a number of discrepancies due to the approximations. These differences were generally small and recommendations for future systems and workarounds were suggested to mitigate potential issues. The results also highlighted some potential limitations of the spindle model in predicting human receptor responses. However, ultimately the results indicated that real time operation should be feasible and achievable on a portable processing platform.

7.1.4 Efficient neural stimulation

Chapter 5 presented an 8 channel energy-efficient neural stimulator for generating charge-balanced asymmetric pulses.

Power consumption was reduced by implementing a fully-integrated DC-DC converter that uses a reconfigurable switched capacitor topology to provide 4 output voltages for Dynamic Voltage Scaling (DVS).

A novel charge balancing method was implemented which has a low level of accuracy on a single pulse and a much higher accuracy over a series of pulses. The method used was robust to process and component variation and does not require any initial or ongoing calibration.

Measured results indicate that the charge imbalance was typically between 0.05 % - 0.15 % of charge injected for a series of pulses. Results also showed DC conversion efficiencies of up to 82 % are achieved using integrated capacitances of under 1 nF and that the DVS approach offers power savings of up to 50 % compared to the front end of a typical current controlled neural stimulator. However, power efficiences were not achieved at low amplitude stimulations due to the overhead involved in the DC converter and current control.

Ex-vivo experiments demonstrated the viability in using this circuit for neural activation. The circuit was implemented in a commercially-available 0.18 μm HV CMOS technology

and occupied a core die area of approximately 2.8 mm^2 for an 8 channel implementation.

7.1.5 Non-invasive proprioceptive feedback

Chapter 6 looked at addressing another major obstacle to developing a proprioceptive prosthesis – the difficulty in testing feedback patterns. The proposed approach here was a low cost tendon vibrator design with improved speed control and increased effectiveness compared to previous designs. However, issues related to resonance and with the chosen type of vibration device prevented successful trials being conducted.

7.2 Contributions

The main contributions produced during this PhD and presented in this Thesis were:

- Chapter 3:
  1. A review of neuromodulation techniques – identifying the opportunities and limitations presented by the various methods.
  2. A review of the design of a proprioceptive neural prosthesis – proposing a design process and identifying component options, system issues and a possible low risk, near term implementation.
- Chapter 4:
  1. Novel integration of biomechanical tools and proprioceptive receptor models (with proposed modifications to fit these to human data) to create a system capable of translating prosthetic limb sensor data into estimates of human neural firing patterns.
  2. Novel approximations to enable computationally efficient models for biomechanical and proprioceptor modelling – potentially enabling the processing for a proprioceptive prosthesis to be run in real time on portable, low power hardware.
  3. Identification of issues relating to the fitting of proprioceptor models to different musculature and species, as well as issues relating to the computationally efficient static optimisation approach used.
- Chapter 5:
  1. Creation of a fully integrated DC-DC converter and current controlled stimulator that uses up to 50% less power than standard while maintaining good current control.
  2. A novel technique enabling fully integrated accurate charge balancing (in the presence of mismatch and process variation) with an asymmetric waveform – this enables lower amplitude stimulation with benefits for power consumption and tissue safety.
- Chapter 6:

1. Identification of low cost components capable of inducing the proprioceptive illusion and a test setup for investigating user performance interpreting this illusion.
2. Identification of issues and challenges present in the use of Eccentric Rotating Mass motors for a vibration induced proprioception illusion targeted at a wide range of vibration frequencies.

7.3 Future directions

Looking to the future there is still a long way to go before a proprioceptive neural prosthesis becomes practically and commercially viable. This section identifies areas of future work and potential technologies to take the device forward towards this goal. It should be noted that in each of chapters 4 - 6, a number of recommended improvements to the work presented here have been proposed and these are not repeated here. Nor will this section consider almost inevitable incremental technological improvements, e.g. battery performance or portable processing capability.

Instead this section looks first at several possible disruptive technologies, before considering key remaining challenges and a way forward for a proprioceptive prosthesis.

7.3.1 Disruptive technologies

Certain key assumptions are guiding much of the current research into a proprioceptive neural prosthesis, however, developments in related fields may undermine some of these assumptions such as:

- **Transcutaneous connectors suitable for chronic use** A break in the skin barrier is associated with a high risk of infection over time. As a result transcutaneous connectors or wires are typically only used for acute human experiments. However, advances in osseointegration, plastic surgery and biomimetic surfaces (inspired by deer antlers) have led to chronic transcutaneous implants for prosthesis attachment – with low associated infection rates and improved prosthesis mounting [9, 10]. Recent research has started to look at the possibility of integrating electronic connectors into these implants. If successful then it has major implications for the electronic system design. In particular it potentially enables the stimulator to remain outside the body and thereby: greatly relaxes size weight and power (and heat) constraints; removes the need for implanted batteries and wireless links; and enables easy stimulator upgrades or modifications.

- **Purely capacitive electrodes** Electrode materials in common use today exhibit significant Faradaic current flow when a DC offset is applied across the electrode-electrolyte interface. Purely capacitive electrode designs exist, but are generally not considered suitable for stimulation as they currently have low safe charge capacity for a given electrode size and are therefore substantially less effective at safely stimulating neurons. This expectation of Faradaic current flow leads to strict requirements for

biphasic waveforms, careful charge balancing and electrode-electrolyte voltage limitations. However, developments in nano-structure electrode surface technology (e.g. using carbon nanotubes [11, 12]) have the potential to create small but high capacity electrodes which could significantly change stimulator requirements.

- **Neural manipulation** Non-genetic biological manipulation of neuronal growth or sensitivity (e.g. altering myelin or ion channel expression) offers a potential alternative method of increasing the selectivity of neuromodulation, and may be a more viable (ethically) alternative to optogenetics [13–15]. If feasible it could have a major impact on neural stimulator and electrode design.

7.3.2 Way ahead

The technologies listed above all have the potential to have a big impact on proprioceptive prosthesis design. However, by themselves, they do little to address key issues that are specific to a proprioceptive neural prosthesis, or to address the numerous challenges to make such a device commercially viable.

Instead there broadly appears to be a requirement for two interrelated avenues of development a) experimental investigation and b) system development.

Experimentation is required in order to demonstrate benefit and to clarify key areas of uncertainty, such as how performance and intuitiveness vary depending on:

- The neural signal patterns applied – e.g. whether mimicking natural patterns is superior to simple linear modulation or whether there is a better alternative.
- The selectivity of stimulation – e.g. the level of impact that co-stimulation of non-target neurons has.
- The comprehensiveness of the feedback – e.g. the impact of stimulating more neurons or adding more channels providing feedback from other muscles, tendons, joints, or skin.
- The descending signals – e.g. the role of fusimotor efferent commands and whether modelling of these is required.
- The impact of feedback loops – e.g. inappropriate proprioceptive feedback could have a detrimental reflex effect on the efferent signals (neural or myoelectric) that are used to control the prosthesis, or even cause loop instability.

Commercial viability of a proprioceptive prosthesis depends not only on maximising benefit, but also acceptability to the patient and minimising whole life costs to the healthcare provider. System development needs to address issues for each of these 3 areas including:

- Enhancing function – good integration between recording and stimulation hardware; development of the prosthesis as a system (e.g. an open architecture approach); and tools and techniques for managing stimulation settings and determining stimulus percepts.

- Safe and comfortable operation – fail safe stimulation control; lightweight hardware; and minimal surgical requirements & invasiveness.
- Minimising maintenance – high durability, reliability, stability (with automatic or patient driven calibration or configuration) and low power operation.

7.4 Concluding Remarks

Interest in proprioceptive neural feedback has been present but muted for much of the last 40 years. However, over the last decade there has been a substantial increase in focus on this little known sense. Likely triggers for this have been: the commercial success of cochlear implants; the key concept work conducted by Dhillon and Horch; and the high trauma survival rate of young soldiers in the Iraq and Afghanistan wars which was instrumental in inspiring the DARPA funded "Revolutionizing Prosthetics" programme which has demonstrated a major leap in prosthesis functionality. These developments have underlined the feasibility and need for feedback to improve prosthetic limb control. Researchers and research programmes have responded and in just the last few years: numerous proprioceptive prosthesis concept papers have been published [16–22]; DARPA has launched the $40 million HAnd Proprioception and Touch Interfaces (HAPTIX) programme; and at the start of 2014 two teams separately released footage of closed loop prosthesis control with neural feedback (albeit with unnatural feedback patterns).

The next five years promise to be an exciting period for the development of a proprioceptive prosthesis. I hope that the work presented here – the design of a proprioceptive prosthesis [23]; power efficient and novel charge balanced stimulation [24]; real time proprioceptive signal generation [25]; and efforts to create an affordable non-invasive proprioceptive feedback device – will prove to be a significant contribution to these efforts.

Bibliography

[1] B. Lee, F. J. Attenello, C. Y. Liu, M. P. McLoughlin, and M. L. Apuzzo. "Recapitulating Flesh with Silicon and Steel: Advancements in Upper Extremity Robotic Prosthetics". *World neurosurgery* 81.5 (2014), pp. 730–741.

[2] T. A. Kuiken, G. Dumanian, R. Lipschutz, L. Miller, and K. Stubblefield. "The use of targeted muscle reinnervation for improved myoelectric prosthesis control in a bilateral shoulder disarticulation amputee". *Prosthetics and Orthotics International* 28 (2004), pp. 245–253.

[3] A. Blank, A. M. Okamura, and K. J. Kuchenbecker. "Identifying the Role of Proprioception in Upper-Limb Prosthesis Control: Studies on Targeted Motion". *ACM Transactions on Applied Perception* 7 (2010).

[4] D. J. Weber, R. Friesen, and L. E. Miller. "Interfacing the Somatosensory System to Restore Touch and Proprioception: Essential Considerations". *Journal of Motor Behavior* 44 (2012), pp. 403–418.

[5] K. R. Holzbaur, W. M. Murray, and S. L. Delp. "A model of the upper extremity for simulating musculoskeletal surgery and analyzing neuromuscular control". *Annals of biomedical engineering* 33 (2005), pp. 829–840.

[6] J. Rasmussen, M. Damsgaard, and M. Voigt. "Muscle recruitment by the min/max criterion: a comparative numerical study". *Journal of Biomechanics* 34 (2001), pp. 409–415.

[7] J. Houk and W. Simon. "Responses of Golgi tendon organs to forces applied to muscle tendon." *Journal of neurophysiology* 30 (1967), pp. 1466–1481.

[8] M. P. Mileusnic, I. E. Brown, N. Lan, and G. E. Loeb. "Mathematical Models of Proprioceptors. I. Control and Transduction in the Muscle Spindle". *Journal of Neurophysiology* 96 (2006), pp. 1772–1788.

[9] C. J. Pendegrass, A. E. Goodship, and G. W. Blunn. "Development of a soft tissue seal around bone-anchored transcutaneous amputation prostheses". *Biomaterials* 27.23 (2006), pp. 4183–4191.

[10] R. Branemark, O. Berlin, K. Hagberg, P. Bergh, B. Gunterberg, and B. Rydevik. "A novel osseointegrated percutaneous prosthetic system for the treatment of patients with transfemoral amputation A prospective study of 51 patients". *Bone & Joint Journal* 96.1 (2014), pp. 106–113.

[11] E. Jan, J. L. Hendricks, V. Husaini, S. M. Richardson-Burns, A. Sereno, D. C. Martin, and N. A. Kotov. "Layered carbon nanotube-polyelectrolyte electrodes outperform traditional neural interface materials". *Nano letters* 9.12 (2009), pp. 4012–4018.

[12] J. J. Pancrazio. “Neural interfaces at the nanoscale” (2008).

[13] P. Lotfi, K. Garde, A. K. Chouhan, E. Bengali, and M. I. Romero-Ortega. “Modality-specific axonal regeneration: toward selective regenerative neural interfaces”. *Frontiers in neuroengineering* 4 (2011).

[14] L. A. Pfister, M. Papaloizos, H. P. Merkle, and B. Gander. “Nerve conduits and growth factor delivery in peripheral nerve repair”. *Journal of the Peripheral Nervous System* 12.2 (2007), pp. 65–82. ISSN: 1529-8027.

[15] D. L. Sherman and P. J. Brophy. “Mechanisms of axon ensheathment and myelin growth”. *Nature Reviews Neuroscience* 6.9 (2005), pp. 683–690.

[16] S. S. Hsiao, M. Fettiplace, and B. Darbandi. “Sensory feedback for upper limb prostheses.” *Progress in brain research* 192 (2011), p. 69.

[17] D. J. Weber, R. Friesen, and L. E. Miller. “Interfacing the Somatosensory System to Restore Touch and Proprioception: Essential Considerations”. *Journal of Motor Behavior* 44 (2012), pp. 403–418.

[18] A. E. Schultz and T. A. Kuiken. “Neural interfaces for control of upper limb prostheses: the state of the art and future possibilities”. *PM&R* 3.1 (2011), pp. 55–67.

[19] C. Antfolk, M. D’Alonzo, B. Rosen, G. Lundborg, F. Sebelius, and C. Cipriani. “Sensory feedback in upper limb prosthetics” (2013).

[20] P. Zhang, Q. Xu, and J. P. He. “Review and Perspective: Sensory Feedback in Upper Limb Prosthesis”. *Applied Mechanics and Materials* 303 (2013), pp. 261–265.

[21] D. Farina, W. Jensen, and M. Akay. *Introduction to Neural Engineering for Motor Rehabilitation*. IEEE Press Series on Biomedical Engineering. Wiley, 2013, pp. 311–326. ISBN: 9781118628492.

[22] J. S. Schofield, K. R. Evans, J. P. Carey, and J. S. Hebert. “Applications of sensory feedback in motorized upper extremity prosthesis: a review”. *Expert Review of Medical Devices* (2014), pp. 1–13.

[23] S. Luan, I. Williams, T. G. Constandinou, and K. Nikolic. “Neuromodulation: present and emerging methods”. *Frontiers in Neuroengineering* 7 (2014), p. 27.

[24] I. Williams and T. G. Constandinou. “An energy-efficient, dynamic voltage scaling neural stimulator for a proprioceptive prosthesis”. *IEEE Trans. BioCAS* 7 (2013).

[25] I. Williams and T. G. Constandinou. “Computationally Efficient Modelling of Proprioceptive Signals in the Upper Limb for Prostheses: a Simulation Study”. *Frontiers in Neuroscience* 8 (2014), p. 181.